MEASUREMENT OF THE INCLUSIVE JET AND DIJET CROSS SECTIONS USING 2010 DATA FROM THE ATLAS DETECTOR AND CALIBRATION STUDIES AND SIMULATION OF THE ATLAS FORWARD CALORIMETER

by

Peter Thompson

A thesis submitted in conformity with the requirements
for the degree of Doctor of Philosophy
Graduate Department of Physics
University of Toronto

Abstract

Measurement of the inclusive jet and dijet cross sections using 2010 data from the ATLAS detector and calibration studies and simulation of the ATLAS forward calorimeter

Peter Thompson
Doctor of Philosophy
Graduate Department of Physics
University of Toronto
2013

Data collected during the 2003 beam test of the `ATLAS` Forward Calorimeter has been analysed, and results for the energy resolution and response of the calorimeter are presented. The effect of inactive material placed in the beamline on the detector performance has also been studied. A Monte Carlo simulation of the Forward Calorimeter has also been constructed, and results obtained from this simulation are compared to data, with generally good agreement found between the two. The inclusive jet and dijet cross sections have also been measured using 37 pb^{-1} of data collected at `ATLAS` during 2010. The kinematic reach of this measurement extends into the forward region of the `ATLAS` detector, covering rapidities that have not previously been studied at a hadron-hadron collider. This is accomplished through a sophisticated triggering scheme, in which jets in the transition region were selected provided they satisfied either the forward jet trigger or the central jet trigger conditions. The results are compared to theoretical predictions obtained using NLO event generators (NLOJet++ and `POWHEG`), which generally agree with the measured data.

Acknowledgements

First of all, I would like to express my gratitude to my supervisor, Peter Krieger, for providing me with this opportunity. I have found his insights, guidance and feedback to be extremely valuable, and have enjoyed working with him during this time.

I would also like to thank members of the Carleton TB03 group: J.P. Archambault, Dag Gillberg, Louise Heelan, Tom McCarthy, Gerald Oakham and Manuella Vincter. There are many intricacies associated with the FCal, the testbeam, and its simulation, and I've had many fruitful discussions about these things with all of you.

I have also enjoyed working with members of the 2010 inclusive jet analysis, especially Eric, Mario, Chris, Justin and Dag. While it was fairly hectic trying to get things done before the numerous deadlines, it was extremely satisfying to see the results at the end of it.

I've also enjoyed spending this time in the company of other ATLAS Toronto students: Behi, Bin, Cristen, Dominique, Gabe, Hass, Pier-Olivier, Reyhanneh, Saminder, Sing, Teresa, Travis, and Trisha. You've all been very helpful over the years.

I would also like to thank my family, especially my parents, my sister, Ted and Smudge. The regular care packages from all of you have been greatly appreciated. I'd also like to thank my Toronto family: Anne, Duncan, Hailey, Hannah, Heather and Hugh. You've made me feel very welcome here, and I've enjoyed spending time with all of you.

Finally, I would like to thank Heather, for all her love and support (and tolerance). This would not have been possible without you.

Contents

List of Tables

List of Figures

Chapter 1

Introduction

This thesis will describe the measurement of the inclusive jet and dijet cross section using 2010 data obtained from ATLAS detector, as well as data and simulation results related to the 2003 beam test of the ATLAS forward calorimeter. Chapter 2 discusses the Standard Model of particle physics, focusing on aspects of QCD that are relevent for jet production and Monte Carlo event generators. Chapter 3 covers the LHC and the `ATLAS` detector. As the calorimeters are used for jet reconstruction, these are discussed in detail. Particular attention is paid to the forward calorimeter, as it is also the subject of chapter 4, which describes the 2003 beam test. This chapter details measurements of the intrinsic response and resolution of the calorimeter, as well as measuring the effects of additional material placed upstream of the calorimeter. Monte Carlo simulations of the beam test have also been carried out, and the results of these simulations are compared to data. The testbeam offers a clean environment in which the FCal can be calibrated and where data can be compared to Monte Carlo. As the tracking coverage at `ATLAS` does not cover the region occupied by the forward calorimeter, direct comparisons of data and Monte Carlo using particles of known energy are difficult to perform in-situ. It is particularly important to validate the simulation in this environment, as all of the hadronic calibration schemes used at `ATLAS` are derived from Monte Carlo. Calibration factors derived from these testbeam data form the basis of the forward calorimeter calibration used by `ATLAS`. The forward calorimeter also plays an important role in the measurement of the inclusive jet and dijet cross sections. These measurements are discussed in chapter 5, and are made using data collected with `ATLAS` during 2010. The analysis presented here expands upon earlier measurements, as data from the forward calorimeter is included in order to enlarge the kinematic reach of the measurements.

Chapter 2

The Standard Model

2.1 Overview

The Standard Model (SM) describes the particles present in nature and the interactions between them. It has existed in its current form since 1974, and has been validated by numerous experiments since then [1, 2]. All of the particles described in the Standard Model have been observed experimentally. Most recently, the observation of a particle "consistent" with the Higgs boson was announced on July 4th of 2012 [3, 4]. The cross-sections at the LHC's design specifications are shown in Figure 2.1 for several standard model processes. The cross-section for jet production is several orders of magnitude greater than many of the other processes of interest, and so they are produced in copius quantities at the LHC. Because of this, jets are studied extensively at `ATLAS`, and are used to make measurements of QCD.

Elementary fermions in the Standard Model are divided into two groups: the quarks and leptons. These particles represent the fundamental building blocks of matter, and there are six "flavours" of each. For the quarks these are the up (u), down (d), charm (c), strange (s), top (t), and bottom (b). These may be organised into generations of

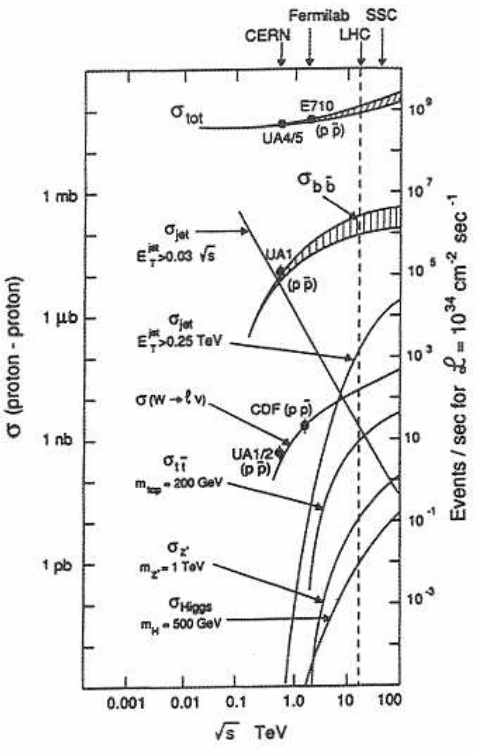

Figure 2.1: Cross-sections for several SM processes as a function of the centre of mass energy of the pp collision [5]. The dashed line corresponds to the design energy of the LHC, while the production rates on the right are obtained using the LHC's design luminosity.

increasing mass, as follows,

$$\begin{pmatrix} u \\ d \end{pmatrix} \begin{pmatrix} c \\ s \end{pmatrix} \begin{pmatrix} t \\ b \end{pmatrix}, \tag{2.1}$$

where the upper members of each generation (the "up type" quarks) have electric charge $+2e/3$ and the lower members ("down type") have charge $-e/3$, where e is the absolute value of the charge on an electron. The leptons may be arranged in the same way, giving

$$\begin{pmatrix} \nu_e \\ e \end{pmatrix} \begin{pmatrix} \nu_\mu \\ \mu \end{pmatrix} \begin{pmatrix} \nu_\tau \\ \tau \end{pmatrix}, \tag{2.2}$$

where the lower members are the electron, muon, and tau, respectively, each having electric charge -1e. Each of these is paired with a neutrino (ν), which is neutral and almost massless. All quarks and leptons have a spin of 1/2.

The strong, weak, and electromagnetic forces are also described by the Standard Model[*]. These are described by gauge theories, such that the SM Lagrangian exhibits $SU(3)_c \otimes SU(2)_L \otimes U(1)_Y$ symmetry. The doublets listed in equations 2.1 and 2.2 reflect the way in which the quark and lepton fields transform under the $SU(2)_L$ symmetry group, where the subscript L denotes that only the left handed components of the fields take part in this interaction. The $SU(2)_L$ and $U(1)_Y$ symmetries together describe the electroweak sector of the Standard Model, with the subscript Y referring to weak hypercharge[†]. Quantum Chromodynamics (QCD) is the gauge theory that describes the strong (or colour) force and $SU(3)_c$ is the symmetry group associated with it, where the subscript C refers to colour charge.

Interactions between particles may occur via the strong force, the weak force or the electromagnetic force. All types of particles interact via the weak force, but only quarks interact via the strong force. Quarks and electrically charged leptons interact via the electromagnetic force, but neutrinos cannot. All of these interactions are mediated by gauge bosons, which are excitations of the gauge fields and act as force carriers. The strong force is carried by gluons, which are massless. There are eight types of gluon, corresponding to the 8 generators of the $SU(3)_c$ symmetry associated with the strong force. There would be four massless bosons arising from the electroweak ($SU(2)_L \otimes U(1)_Y$) symmetry, however these symmetries are broken down to a single $U(1)_{EM}$ symmetry by the Higgs mechanism[6]. This $U(1)_{EM}$ symmetry describes electromagnetic interactions, and the corresponding gauge boson is the massless photon. The other three gauge bosons

---

[*] Gravity is not included in the SM, but its effects are negligible at the energy scales of interest.

[†] The weak hypercharge of a particle is the sum of its electric charge and the third component of its weak isospin (T_3). Up-type quarks and neutrinos have T_3 = 1/2, while down-type quarks and charged leptons have T_3 = -1/2.

associated with the broken symmetries are the W^+/W^- bosons which have a mass of (80.385 ± 0.015) GeV* , and the Z boson which has a mass of (91.188 ± 0.002) GeV[7].

In addition to the weak gauge bosons, the Higgs field also allows fermionic particles to posses mass in a way that doesn't violate the gauge invariance of the SM Lagrangian. There is a potential associated with the Higgs field which causes it to spontaneously take a non-zero vacuum expectation value, breaking the electroweak symmetry mentioned earlier. Fermions interact with the Higgs field via a Yukawa coupling, and so when the Higgs field takes a vacuum expectation value these couplings act as mass terms in the Lagrangian while retaining their gauge invariance.

2.2 Quantum ChromoDynamics

Quantum ChromoDynamics (QCD) is a non-Abelian gauge theory based on $SU(3)_c$. It is the strongest of the three interactions in the Standard Model, but only affects colour charged particles. As the LHC collides beams of protons, QCD is the dominant interaction. The remainder of this chapter will focus on QCD as it is the interaction responsible for jet production, which is the subject of the analysis presented in Chapter 5.

Feynman diagrams for the three fundamental QCD vertices are shown in Figure 2.2. A major difference of QCD compared to quantum electrodynamics (QED) is that gluons carry colour charge and thus couple to one another, while the photon is uncharged. Gluon-gluon couplings can occur via the three gluon or four gluon vertices, which are depicted in Figures 2.2(b) and 2.2(c).

The coupling constant, α_s, describes the strength of QCD interactions. This varies as a function of the transferred momentum, such that the strength of the coupling at two

---

[*] For simplicity, masses and momenta are listed with units of eV in this thesis, even though the eV is a unit of energy. In cases where a mass or momentum value is given in terms of eV, the unit should be understood to be eV/c^2 or eV/c, respectively.

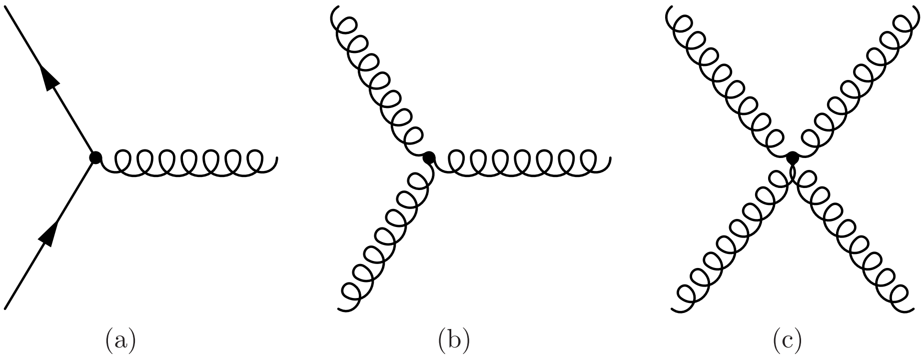

Figure 2.2: Feynman diagrams depicting the vertices of QCD.

different momentum scales, p^2 and Q^2, are related by

$$\alpha_s(p^2) = \frac{\alpha_s(Q^2)}{1 + \frac{11-(2/3)N_f}{4\pi}\alpha_s(Q^2)\log(\frac{p^2}{Q^2})} \tag{2.3}$$

where N_f is the number of quark flavours with mass less than p^2. The "QCD scale", Λ_{QCD}, is defined as the scale at which the denominator of equation 2.3 vanishes, i.e.

$$\frac{11-(2/3)N_f}{4\pi}\,\alpha_s(Q^2)\,\log(\frac{\Lambda^2_{QCD}}{Q^2}) = -1. \tag{2.4}$$

Using this definition, equation 2.3 becomes

$$\alpha_s(p^2) = \frac{4\pi}{(11-(2/3)N_f)\log(\frac{-p^2}{\Lambda^2_{QCD}})}. \tag{2.5}$$

The value of Λ_{QCD} is around 200-300 MeV. This does not mean that the coupling constant is infinite at Λ_{QCD}, merely that the perturbative calculations used in the derivation of equation 2.3 are no longer valid in this regime. When measured at the mass of the Z boson, $\alpha_s(M_Z) = 0.1184$ [7], indicating that perturbation theory is reliable at this energy scale.

A leading order diagram for a $qq \rightarrow qq$ process is shown in Figure 2.3(a), where four-momentum is exchanged between two quarks via a gluon. At next to leading order

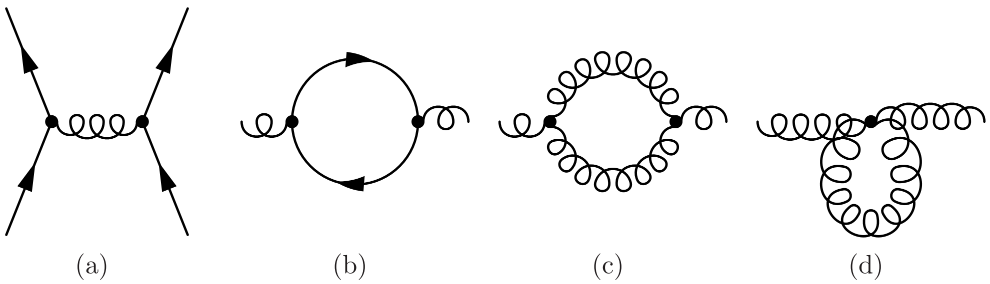

Figure 2.3: Tree level $qq \rightarrow qq$ scattering, and vacuum polarisation diagrams.

(NLO), the gluon propagator in Figure 2.3(a) may be replaced by the vacuum polarisation diagrams shown in Figures 2.3(b)-2.3(d). The first of these diagrams, Figure 2.3(b), causes the vacuum to effectively screen colour charge, such that at large distances the strength of the interaction is diminished. A similar effect occurs in Quantum ElectroDynamics (QED), the quantum field theory describing the electromagnetic interaction. A diagram analogous to Figure 2.3(b) exists in QED, which gives rise to the running of the electromagnetic coupling constant.

The three and four gluon vertices in Figure 2.2 give rise to the diagrams in Figures 2.3(c) and 2.3(d). The gluon loops in these diagrams cause an anti-screening effect, such that the strength of the interaction decreases as the exchanged four-momentum increases. This is the opposite effect to that seen for the quark loop, however in QCD it is this effect that dominates.

The anti-screening effect is characteristic of $SU(N)$ gauge theories. An $SU(4)$ theory would contain four colours and 15 gluon fields ($N^2 - 1$), increasing the contribution of the gluon loop diagrams in Figure 2.3 and thus increasing the anti-screening effect. Conversely, a QCD-like theory based on $SU(2)$ would contain 3 gluons (like the three gauge bosons of the weak force), which would result in a smaller anti-screening effect. The screening effect, however, increases with the number of quark fields contained in the theory. For example, in $SU(3)$ gauge theories that contain 17 or more quark flavours the screening effect is dominant and the strength of the interaction increases as the exchanged four-momentum increases, as can be seen from equation 2.5.

2.2.1 Factorisation

Theoretical descriptions of proton-proton collisions are complicated, as different energy scales are involved in the problem. The four-momentum exchanged between partons can be at the TeV scale for collisions at the LHC, while the physics describing the arrangement of the partons within the proton is determined at a much lower scale, Λ_{QCD}. QCD is a strongly coupled theory at low energies, whereas at higher energies it is weakly coupled and perturbative methods may be used. Fortunately, factorisation allows the physics at these different scales to be separated [8]. The low-momentum, non-perturbative physics describing the structure of the proton may be isolated from the high momentum, parton-parton scattering.

The structure of the proton may thus be described using Parton Distribution Functions (PDFs), $q_i(x, Q^2)$, $G(x, Q^2)$, and $\overline{q}_i(x, Q^2)$. The functions $q_i(x, Q^2)$ describe the probability of a probe (such as an electron or parton) with momentum Q^2 finding a quark of flavour i within the proton, with said quark carrying a fraction x of the proton's momentum[6]. Similarly, the distribution functions $\overline{q_i}(x, Q^2)$ and $G(x, Q^2)$ describe the probability of finding an anti-quark or gluon, respectively, within the proton. While a proton is typically thought of as containing two up quarks and one down quark, it also contains gluons, which together carry about half of the proton's momentum [6]. Gluons may also split into quark-antiquark pairs, referred to as "sea" quarks. Because of this, the probabilities of finding antiquarks (or quarks with flavours other than up or down) are non-zero, and vary as a function of Q^2[9]. The number of valence quarks is conserved, however, giving the conditions

$$\int_0^1 dx \left[q_{\mathrm{up}}(x,Q^2) - \overline{q}_{\mathrm{up}}(x,Q^2)\right] = 2 \tag{2.6}$$

$$\int_0^1 dx \left[q_{\mathrm{down}}(x,Q^2) - \overline{q}_{\mathrm{down}}\}(x,Q^2)\right] = 1 \tag{2.7}$$

$$\int_0^1 dx \left[q_j(x,Q^2) - \overline{q}_j(x,Q^2)\right] = 0 \quad , \quad j \in \{c,s,t,b\} \tag{2.8}$$

While the parton distribution functions must be determined from experiment, their Q^2 dependence can be calculated in a similar fashion to that of the coupling constant, α_s. The dependence of the PDFs on Q^2 is given by the Dokshitzer - Gribov - Lipatov - Altarelli - Parisi (DGLAP) equations [6, 10]:

$$\frac{\mathrm{d}q_i(x,Q^2)}{\mathrm{d}\log Q^2} = \frac{\alpha_s}{2\pi}\int_x^1 \frac{\mathrm{d}y}{y}\left[P_{qq}(y)q_i(\frac{x}{y},Q^2) + P_{qG}(y)G(\frac{x}{y},Q^2)\right] \tag{2.9}$$

$$\frac{\mathrm{d}\overline{q_i}(x,Q^2)}{\mathrm{d}\log Q^2} = \frac{\alpha_s}{2\pi}\int_x^1 \frac{\mathrm{d}y}{y}\left[P_{qq}(y)\overline{q_i}(\frac{x}{y},Q^2) + P_{qG}(y)G(\frac{x}{y},Q^2)\right] \tag{2.10}$$

$$\begin{aligned}\frac{\mathrm{d}G(x,Q^2)}{\mathrm{d}\log Q^2} = \frac{\alpha_s}{2\pi}\int_x^1 \frac{\mathrm{d}y}{y}\Bigg[&P_{Gq}(y)\sum_i\left(q_i(\frac{x}{y},Q^2) + \overline{q_i}(\frac{x}{y},Q^2)\right) \\ &+P_{GG}(y)G(\frac{x}{y},Q^2)\Bigg],\end{aligned} \tag{2.11}$$

where the P_{xx} are splitting functions. While a probe at Q^2 may see a quark or gluon within the proton, a probe with higher momentum may be able to resolve finer structures that are only present for a short time. For example, a given probe may be able to resolve a quark, while a probe with higher momentum may be able to interact with a collinear gluon emitted by this quark (Figure 2.4(a)). Similarly, a high momentum probe may be able to resolve a quark or antiquark (Figure 2.4(b)), or another gluon (Figure 2.4(c)), which are produced by a gluon. The splitting function $P_{Gq}(y)$ describes the probability for a quark to emit a colinear gluon, with the gluon carrying a fraction y of the quark's momentum. The complementary function $P_{qq}(y)$ describes the probability that the quark will retain a fraction y of its momentum after this emission. The function $P_{qG}(y)$ describes the probability for a gluon to split into a quark/anti-quark pair, with one of the products carrying a fraction y of the gluon's momentum, while $P_{GG}(y)$ is the probability for a gluon to emit another gluon that carrys a fraction y of its momentum.

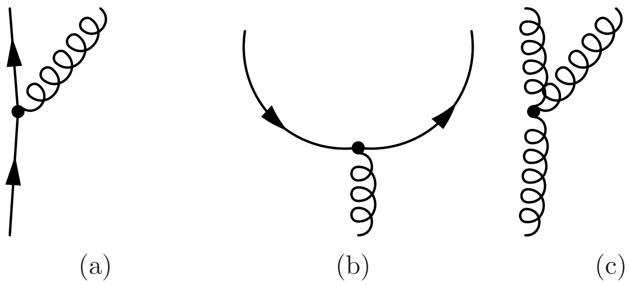

Figure 2.4: Processes described by the splitting functions. In (a), a colinear gluon is emitted by a quark, while in (b) a gluon splits into a quark antiquark pair. In (c), a gluon emits another gluon.

The PDFs derived by the CT10 group [11] are plotted in Figure 2.5, for $Q^2 = 1$ TeV. These are derived from a global analysis of data collected from many experiments. Most recently, the results of fixed target deep inelastic scattering experiments carried out at HERA [12], as well as data obtained from proton-proton collisions at the Tevatron [13], have been included in the CT10 analysis. At small x the gluon PDF is dominant, and consequently the sea quark contributions are also significant in this regime, whereas the valence quarks dominate at higher values of x.

2.2.2 Perturbative QCD

The cross-section for producing a final state, X, from two protons with four-momentum p_A and p_B may be written as [15]

$$\sigma_{pp\to X} = \sum_{i,j} \int_0^1 \mathrm{d}x_1 \int_0^1 \mathrm{d}x_2\, f_{i,A}(x_1, Q^2)\, f_{j,B}(x_2, Q^2)\, \hat{\sigma}_{i,j\to X}(x_1 p_A\,, x_2 p_B), \qquad (2.12)$$

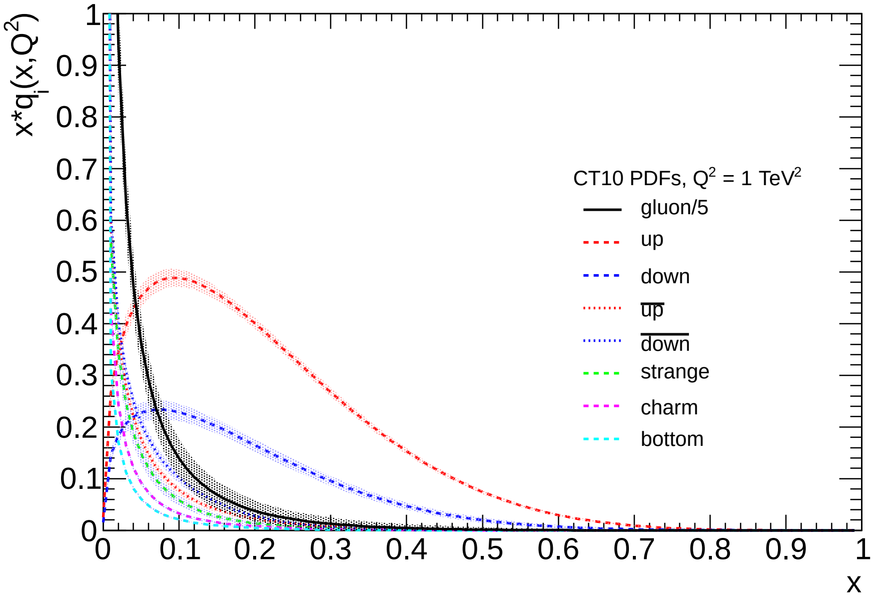

Figure 2.5: CT10 PDFs, obtained at a Q^2 scale of 1 TeV [11, 14]. Note that the y axis shows the product of the PDF and x. The area under a given curve thus corresponds to the relative amount of the proton's momentum carried that type of parton. The up and down quark curves show the valence quark contributions only: the contributions from sea quarks are equal to the antiquark curves.

where $f_{i,A}$ is the parton distribution function describing the probability of finding a parton of flavour i within proton A, and the sum runs over all parton types. The partonic cross-section, $\hat{\sigma}_{i,j\to X}$, describes the probability of producing the final state X from the incoming partons of flavour i and j, and may be calculated order by order in perturbation theory.

A leading order (LO) diagram for a 2 → 2 process is shown in Figure 2.6(a). Leading order contributions are the easiest to calculate, but are generally only correct to within an order of magnitude for QCD processes [16]. Theoretical predictions that are to be compared with experimental measurements usually need to be made at next-to-leading order (NLO) or higher.

At NLO, virtual corrections arising from loop diagrams (such as the one shown in Fig-

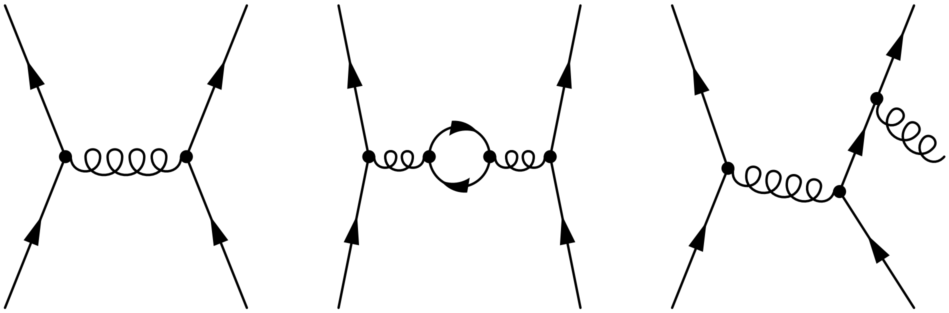

(a) (b) (c)

Figure 2.6: Diagrams for $qq \rightarrow qq$ scattering. The tree diagram in (a) contributes at leading order, while the virtual correction in (b) and the real correction in (c) contribute at NLO.

ure 2.6(b)) must be considered. These virtual corrections contain ultraviolet divergences, which may be removed through renormalisation. However, there are also infrared divergences present, such that the result diverges in cases where the energy of an incoming or outgoing parton vanishes ("soft" divergence), or in cases where the separation between two of the initial or final state partons vanishes (a "collinear" divergence). These infrared divergences cannot be removed, and so any calculation carried out to a fixed order in perturbation theory that considers a specific number of partons in the final state will diverge [17]. In order to obtain a physical result at fixed order in perturbation theory, real corrections must be considered. These real corrections include cases where an additional parton is emitted by one of the incoming or outgoing partons, such as that shown in Figure 2.6(c). The real corrections also include collinear and soft divergences, but of the opposite sign to those present in the virtual corrections. In fixed order calculations in which both real and virtual contributions are considered, the infrared divergences cancel to give a finite result[16].

2.2.3 Soft Processes in Proton-Proton Collisions

The products of hard scatterings between partons are usually considered the most interesting parts of proton-proton collisions. However, there are other important processes involved in these collisions. Partons entering or leaving the hard scattering may undergo bremsstrahlung emission, producing initial (or final) state radiation.

There are also underlying event (UE) effects associated with the proton remnants, i.e. other partons that were constituents of the initial protons but were not involved in the hard scattering. These partons may undergo soft scatterings amongst themselves (multiple parton interactions), and may also radiate before/after these interactions.

"Pile-up" is another issue affecting the LHC*. The LHC collides bunches containing $\sim 10^{11}$ protons. At the LHC's design specifications, it is rare for only a single scattering to occur during bunch crossings, with (on average) ~ 23 collisions occuring between different pairs of protons every bunch crossing. The majority of these collisions are soft, producing low p_{T} products. However, the energy deposited in the calorimeter by pile-up needs to be accounted for when measuring other high p_{T} objects, particularly jets.

2.2.4 Hadronisation and Jet Production

After the hard scattering and emission of any final state radiation, partons will continue to interact via the colour force. As the separation between these partons increases, the strength of the interaction also increases.

The confinement hypothesis states that colour charged partons do not exist in isolation; they must be confined within colourless hadrons[6]. All hadrons observed in nature consist of quarks and gluons arranged in colour singlet (i.e. colour neutral) states. If a given quark were to be separated from the other constituents in its parent hadron in order to "isolate" it, the energy required to achieve this would increase with the separation distance. At a certain point it becomes energetically favourable for a quark-antiquark pair to be produced from the vacuum, such that the remnants of the parent hadron form a bound state with one member of the new pair, while the separated quark binds with

---

*While pileup is a significant issue at the LHC's design luminosity (and at present), it was not a major concern during 2010. At the end of the 2010 data-taking period, there were ~ 3.5 collisions occuring during each bunch crossing the other member of the pair. It is thus not possible to observe a free quark in isolation, as new hadrons are formed instead using partons created from the vacuum.

Partons emerging from the collision thus organise themselves into collimated sprays of hadrons, which are referred to as “jets”. The showering and hadronisation of particles are non-perturbative processes, and so it is difficult to predict the way in which a parton produced in a collision will evolve into a jet. Jets will be discussed further in chapter 5, which describes the experimental measurement of the inclusive jet cross-section.

2.2.5 Monte Carlo Event Generators

Event generators are Monte Carlo (MC) programs that simulate high energy physics events, and thus may be used to obtain theoretical predictions for the results of a given analysis. In the context of ATLAS, these programs are used to simulate proton-proton collisions, incorporating initial state radiation, final state radiation, and underlying event effects. The output of an event generator consists of a list of stable particles, which may then be passed to a detector simulation program such as `GEANT4` (discussed in Section 4.3.1). Results obtained from the simulation may then be analysed in the same manner as real data, allowing theoretical and experimental results to be compared.

Parton Shower Monte Carlo programs, such as `PYTHIA` [18] and `HERWIG` [19], factorise the collision into different stages. These consist of the hard scattering between partons, and initial (final) state radiation emitted by incoming (outgoing) partons, as illustrated in Figure 2.7. The hard scattering is determined first, using the leading order cross-section for the hard process. As the hard process involves a large four-momentum transfer, it is possible for the scattering to occur between partons that are off the mass shell [20]. The incoming and outgoing partons are then “showered” in order to produce the initial/final state radiation. Outgoing partons undergo a series of time-like emissions in which additional partons are radiated. These emissions reduce the p^2 of the involved partons, such that final state partons end up on the mass shell. The probability that an emission will occur is given by the relevant splitting function, $P_{\rm xx}$, (introduced in Section 2.2.1) multiplied by a Sudakov form factor. The Sudakov factor is essentially a resummation of virtual corrections at leading logarithmic (LL) level [20, 21] and conserves probability such that the chance for a series of emissions to occur never exceeds unity.

Initial state radiation is treated similarly to final state radiation, but in reverse. As the hard scattering is computed first, the properties of the partons just prior to the scattering have already been determined. These incoming partons are then evolved backwards in time, undergoing repeated emission until they become on-shell constituents of the colliding protons.

Parton shower Monte Carlo generators typically include methods to model multiple parton interactions in order to describe the underlying event. For events generated by `HERWIG`, this is handled by the `JIMMY` library [22], whereas `PYTHIA` has built-in routines to handle this. These models depend on a number of parameters (such as a minimum $p_{\rm T}$ threshold for scattered partons). The values of these parameters define a specific "tune" of the generator. The `ATLAS` Minimum Bias Tunes (AMBT1 and AMBT2B for `PYTHIA`, and AMBT2 for `HERWIG`) and `ATLAS` Underlying Event Tunes (AUET2 for `HERWIG` and AUET2B for `PYTHIA`) [23] are derived from `ATLAS` minimum bias and underlying event analyses, respectively. These are used in some of the theoretical predictions presented in Section 5.7.1, as is the Perugia 2011 [24] tune for `PYTHIA`.

While parton shower MC generators calculate the hard scattering process at LO, matrix element generators such as `POWHEG` [25] and NLOJET++[26] treat the hard scattering at NLO in perturbative QCD. These generators use a subtraction[16] technique, in which a term is subtracted from the real corrections and added to the virtual corrections such that both sets of corrections may be evaluated numerically. This allows the cross-section for the hard scattering to be calculated at full NLO accuracy.

Parton shower MC generators are good at handling soft emissions, whereas matrix element generators are accurate to NLO and are capable of generating events containing

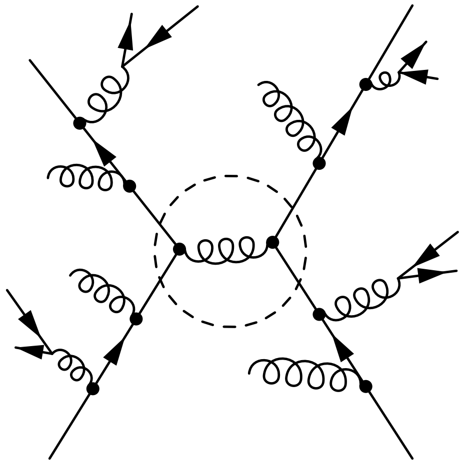

Figure 2.7: In shower Monte Carlo programs, the hard scattering (inside the dashed circle) is computed first at leading order. The partons entering (exiting) this scattering are then showered to produce the initial (final) state radiation.

multiple well-separated jets. Matrix element generators may be used to compute the hard scattering before passing the incoming and outgoing partons to shower MCs to model the soft emissions. However, this has to be done carefully, as some contributions at NLO are included within the LL resummation used by the shower MCs, and so simply showering the output from an NLO ME would double count these contributions. Recently the `POWHEG` box [27] formalism has been applied to 2→2 parton scattering [28], which allows the shower MCs to appropriately interface with the ME calculation. The contribution from the shower MC is subtracted during the ME calculation, so that the calculation is done consistently. `POWHEG` is used in this fashion for some of the theoretical predictions presented in Sections 5.7.1 and 5.7.2.

Chapter 3

The LHC and the ATLAS Detector

3.1 The Large Hadron Collider

The Large Hardon Collider (LHC)[29] is a particle collider situated near Geneva, Switzerland. It is 27km in circumference and is located between 45m and 170m underground, crossing the Swiss-French border four times. It is designed to accelerate two beams of protons to energies of 7 TeV, and to collide these beams at four points along its circumference with instantaneous luminosities of up to $10^{34}\text{cm}^{-2}\text{s}^{-1}$. At present protons in the LHC are being accelerated to 4 TeV per beam, which is a slightly more than half of the design energy, while the maximum instantaneous luminosity being achieved is currently around $\sim 8 \times 10^{33}\text{cm}^{-2}\text{s}^{-1}$. The LHC is also capable of accelerating heavy ions to high energy. The ALICE experiment is focused on analysing these heavy ion collisions, while both `ATLAS` and `CMS` also have heavy ion programs.

The injection chain for beam particles is shown in Figure 3.1. Hydrogen gas is used as a source of protons. Gas molecules are ionised in a duoplasmotron[30], which emits protons at an energy of 90 keV. The protons are then accelerated to 750 KeV in a Radio Frequency Quadrupole (RFQ) before being accelerated to 50 MeV in a linear accelerator (LINAC2). A series of synchrotrons (the Proton Synchrotron Booster (PSB), Proton

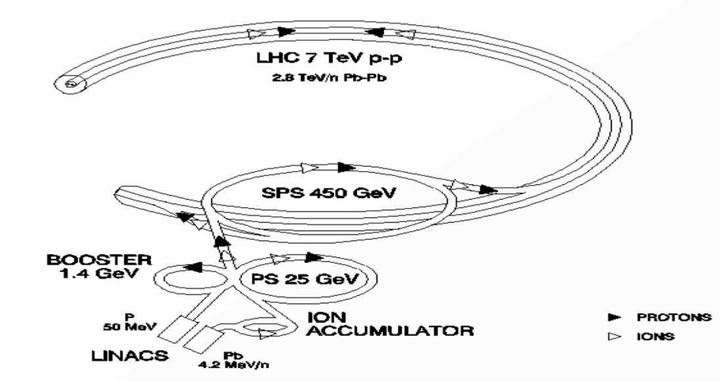

Figure 3.1: Injection chain for protons and ions feeding the LHC.

Synchrotron (PS), and Super Proton Synchrotron (SPS)) are then used to accelerate protons to energies of 1.4 GeV, 25 GeV and 450 GeV, respectively. After acceleration by the SPS, beams are injected into the LHC. Superconducting Radio-Frequency (RF) cavities are then used to accelerate the protons to their final energy. Each LHC beam is designed to hold up to 2808 bunches[*], each containing $\sim 10^{11}$ protons, which are separated in time by 25 ns.

3.2 The ATLAS Detector

The `ATLAS` detector[31] (shown in Figure 3.2) is a multi-purpose detector used to analyse collisions at the LHC. It is one of two multi-purpose detectors, the other being the Compact Muon Solenoid (CMS)[32]. `ATLAS` consists of sophisticated particle tracking systems, a system of calorimeters, and a Muon Spectrometer, each of which will be discussed below. The Inner Detector (ID) and Muon Spectrometer (MS) will be discussed only briefly, as they play little role in the analyses discussed in this thesis. This chapter will focus on the calorimeters of `ATLAS`, as these are used to reconstruct jets. Particular attention is paid to the forward calorimeters, as one of these was the subject of the beam

---

[*] Currently only half of these bunches are being filled, such that bunch crossings are seperated by 50 ns.

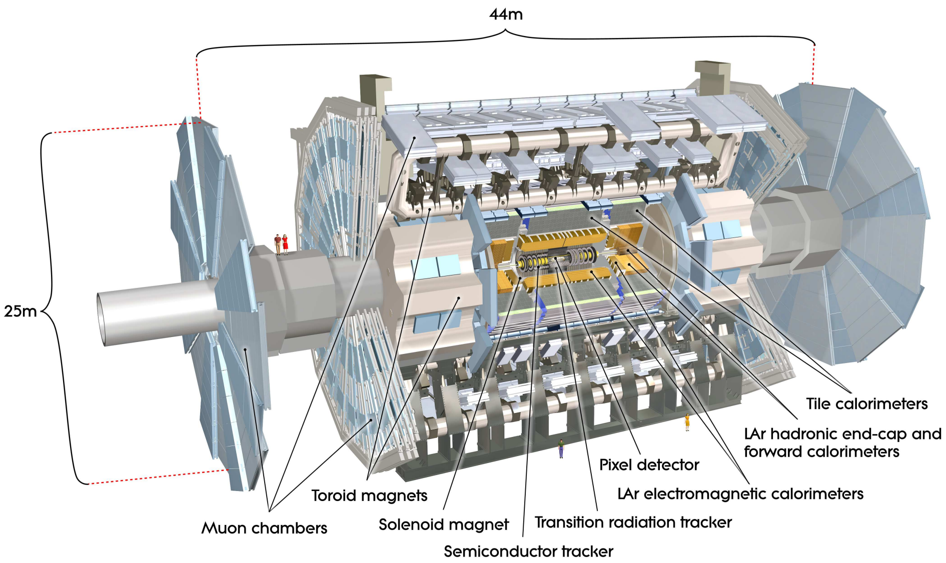

Figure 3.2: Diagram of the ATLAS detector.

test discussed in Chapter 4, and also because the forward calorimeters are responsible for the large kinematic coverage achieved in the inclusive jet and dijet cross-section measurements that are described in Chapter 5.

3.2.1 Coordinates

`ATLAS` uses a right-handed Cartesian coordinate system. The nominal interaction point at the centre of `ATLAS` is defined to be the origin of this coordinate system, with the beams running along the z axis. The positive x axis points towards the centre of the LHC ring, while the positive y axis is perpendicular to the other two, and points upwards. Parts of the detector are labelled according to which side of the interaction point they are located on. The “A-side” refers to objects located at positive values of z, while objects located at negative z are said to be on the “C-side”. `ATLAS` is divided into a barrel and two end-cap sections. Each of these sections contains a cryostat, as (most of) the `ATLAS` calorimetry is based on liquid argon technology.

The polar angle θ defines the angle from the beam axis, while the azimuthal angle ϕ

defines the angle around the beam axis. The direction $\theta = 0$ points along the positive z axis, while $\phi = 0$ corresponds to the positive x axis. The pseudorapidity, η, is defined using the polar angle θ, such that

$$\eta = -\log\left(\tan\left(\frac{\theta}{2}\right)\right). \tag{3.1}$$

Pseudorapidity is an approximation to rapidity, y. The rapidity of an object with energy E is given by

$$y = \frac{1}{2}\log\left(\frac{E + p_z}{E - p_z}\right), \tag{3.2}$$

where p_z is the z component of the objects momentum. The rapidity may be used to define a boost along the z axis, such that in the boosted frame of reference the object's momentum will be perpendicular to the beam direction. In the limit where the mass of the object is negligible, pseudorapidity and rapidity are equivalent. Detector regions are typically described in terms of η, due to the one-to-one correspondence with θ. Rapidity is often used when discussing kinematics, as differences in rapidity are invariant with respect to boosts in the direction of the beam.

3.2.2 Inner Detector

The Inner Detector (ID) is used to reconstruct the trajectories (tracks) of charged particles produced during proton-proton collisions. It is comprised of three systems: the pixel detector, the SemiConductor Tracker (SCT), and the Transition Radiation Tracker (TRT). These three components are contained within a cylindrical region of length 3.5m and radius 1.15m centred on the `ATLAS` interaction point. The `ATLAS` solenoid is a superconducting magnet located just outside of the ID, in the barrel cryostat, and generates a 2T magnetic field oriented along the z axis in the region occupied by the ID. The applied field gives rise to curvature in the trajectories of charged particles, such that measurements of particle trajectories can be used to determine the transverse momentum (p_{T})

of those particles. The ID is also used for vertex reconstruction at `ATLAS`. The primary vertex is associated with the location of the hard inelastic collision, while other soft collisions may produce additional secondary vertices. The accuracy with which a given vertex position may be reconstructed is dependent on the number of tracks associated with the vertex and the p_{T} of those tracks. In cases where there are at least 70 tracks emerging from the primary vertex and the quadratic sum of track p_{T} values exceeds 8 GeV, the primary vertex can be determined with an accuracy of ~30 μm in the transverse plane and ~50 μm in the longitudinal direction[33].

The inner detector consists of a barrel section (shown in Figure 3.3) and two end-cap sections (Figure 3.4).

The pixel detector uses sensors formed from 250μm thick wafers of silicon. The barrel section consists of three cylindrical layers, and three disc-like layers are used to form each end-cap. All together there are $\sim 8 \times 10^7$ pixel channels, which are designed to provide a hit resolution of 10 μm in the $R - \phi$ plane and 115 μm in the z direction in the barrel section.

The SCT is located beyond the pixel detector, and consists of 4 cylindrical layers in the barrel section and 9 disc layers in each end-cap. Each SCT module has semiconducting microstrip sensors mounted on both sides that are oriented at an angle of 40 mrad to each other. As a single microstrip sensor only provides a position measurement in one dimension, orienting two at a slight angle allows the position of the hit to be measured in two dimensions, by correlating hits in the two sensors. The SCT is designed to have a resolution of 17 μm in the $R - \phi$ plane and 580 μm in z.

The TRT is the outermost section of the inner detector, and is formed from straw-shaped drift tubes. The barrel section contains ~52,500 tubes, while ~123,000 tubes are contained in each end-cap section. Straws are made from layers of polyimide, aluminium, polyurethane and graphite-polyimide. Each straw is 4mm in diameter, with a gold-plated tungsten wire (of diameter 31μm) located in the centre of the tube that serves as an

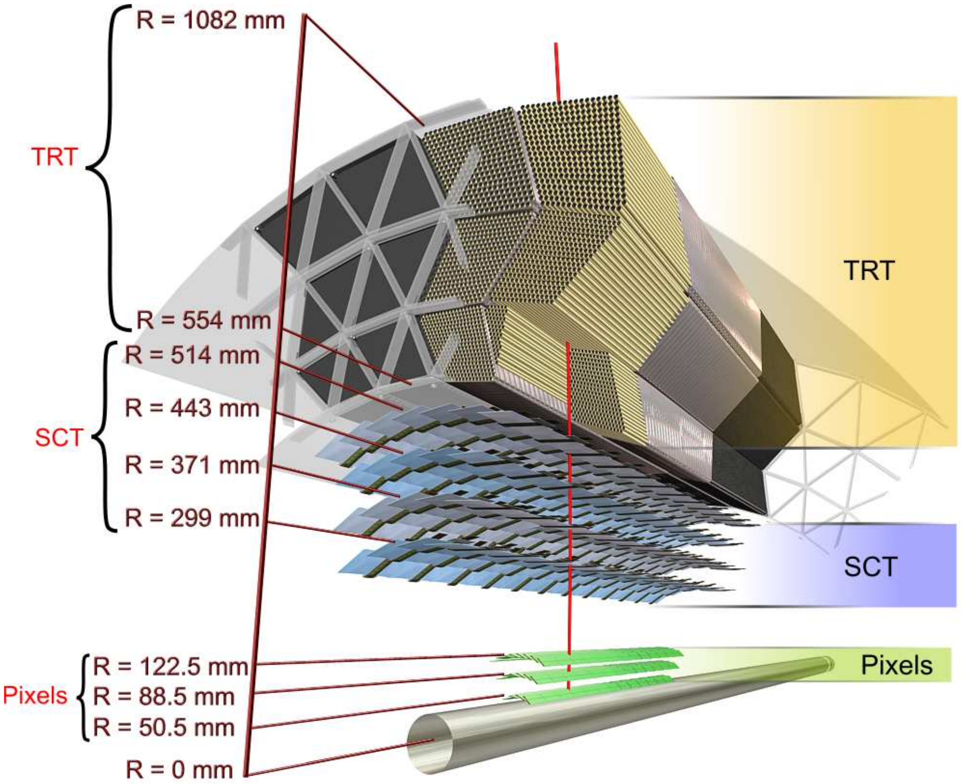

Figure 3.3: Diagram of the barrel section of the inner detector.

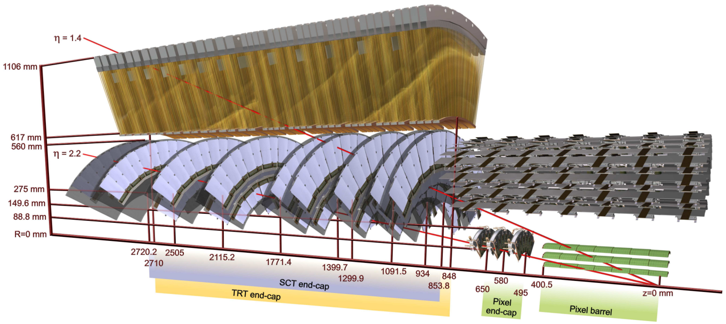

Figure 3.4: Diagram of the inner detector, showing the elements traversed by particles at pseudorapidities of 1.4 and 2.2.

anode. The gas in the tubes is 70% Xe, 27% CO_2 and 3% O_2. Charged particles entering the tube ionise the gas, with the resulting electrons drifting towards the anode in the centre. Measurement of the electron drift time allows the distance of the particle track from the wire to be determined with a resolution of 130μm. The straw tubes are housed within a volume filled with CO_2 and a matrix of polypropylene fibres (in the barrel section) or foils (in the end-caps). Electrons moving between the CO_2/polypropylene interfaces emit transition radiation. This radiation (and the original electron) will then ionise the gas inside the tubes, inducing a signal on the tube anodes. Xenon is used because it efficiently absorbs the transition radiation photons, emitting photoelectrons in the process. Charged pions produce less transition radiation than electrons, and thus generate smaller signals. This difference in signal size allows the TRT to perform particle identification, discriminating electrons from charged pions.

3.2.3 Muon Spectrometer

The Muon Spectrometer is the outermost system of the `ATLAS` detector, and is illustrated in Figure 3.5. It is designed to measure muons in the region $|\eta| < 2.7$ with a momentum resolution of $\sim 10\%$ at 1 TeV. However, during 2010 running muons were measured with a resolution of $\sim 5\%$ at 100 GeV in the barrel region[34]: when the fit to this data is extrapolated, it corresponds to a resolution of $\sim$25% at 1 TeV. The Muon Spectrometer is also capable of triggering on muons in the region $|\eta| < 2.4$. The Muon Spectrometer is comprised of four types of detectors: Monitored Drift Tubes (MDTs), Cathode Strip Chambers (CSCs), Resistive Plate Chambers (RPCs) and Thin Gap Chambers (TGCs). The MDTs and CSCs are referred to as “precision chambers” and are used to measure the kinematics of muons, while the TGCs and RPCs are used for triggering and measuring the ϕ coordinates of muon tracks.

Superconducting toroidal magnets (the barrel toroid and two end-cap toroids) are located beyond the calorimeters. These produce a toroidal field (i.e. one in which the field

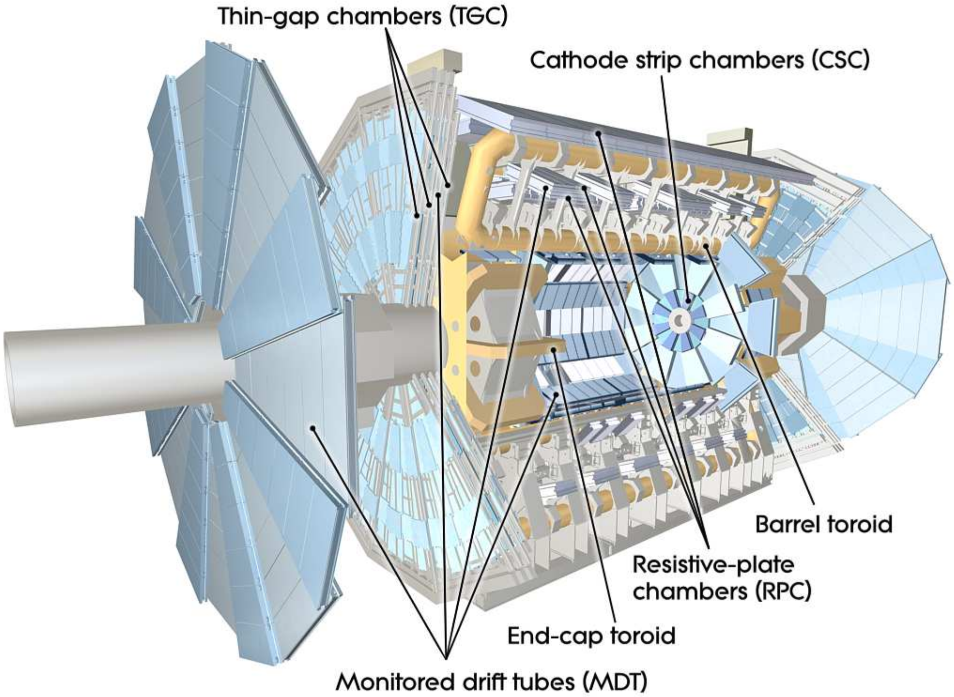

Figure 3.5: The different components of the Muon Spectrometer. The MDT and CSC components are used for measuring muon momenta, while the RPCs and TGCs are used primarily for triggering.

lines run in the azimuthal direction), which causes charged particles to bend in the $R-z$ plane. In order to measure track momenta with high resolution, the relative alignment of the MDT and CSC chambers must be well known. A high precision optical system is used to monitor the positions and mechanical deformations of the measurement chambers, which must be known to within 30 μm in order to achieve the desired momentum resolution.

MDTs are comprised of cylindrical drift tubes of diameter 29.97mm, with a central anode wire of diameter 50μm. A mixture of Argon (93%) and CO_2 (7%) is used to fill the tubes. Each drift tube is capable of measuring the distance of a muon track from the anode wire with a resolution of 80μm. The tubes are grouped together to form chambers. There are three (roughly) cylindrical layers of chambers in the barrel (at radii of 5 m, 7.5 m and 10 m), and four layers in each end-cap.

MDTs are used in all four layers of the end-cap sections. However, in the forward region ($|\eta| > 2.0$) of the innermost layer (located at $z \approx 7.4$ m) CSCs are used instead, as the MDTs are unable to operate in the high levels of radiation present in this region. The CSCs are multi-wire proportional chambers (MWPCs), filled with a mixture of Argon (80%) and CO_2 (20%), and are capable of measuring hit positions to within 60 μm in the bending plane.

For triggering purposes, RPCs are used in the barrel region ($|\eta| < 1.05$) while TGCs (which are a form of MWPC) are used in the end-cap region ($1.05 > |\eta| > 2.4$). The intrinsic response time of these detectors is on the order of a few nanoseconds, enabling them to reliably identify the bunch crossing in which any detected muons were produced.

3.2.4 Calorimetry

3.2.4.1 Sampling Calorimeters

All of the calorimeters used at `ATLAS` are sampling calorimeters, which consist of active regions and passive (absorbing) regions. The active layers are sensitive: energy deposited in these regions produces a signal which is then read out. The passive regions are made from a denser absorbing material, which is used to regulate the shower size. Sampling calorimeters are less expensive to produce than homogenous calorimeters.

Sampling calorimeters may be characterised by their sampling fraction, which is defined as the energy deposited in the active regions by a minimum ionising particle (MIP) divided by the total energy deposited in the active and passive regions by the MIP [35].

Most of the `ATLAS` calorimeters are based on liquid argon (LAr) technology, i.e. LAr is used to form the active regions of the calorimeter. Charged particles passing through these active regions ionise the liquid argon. The liberated electrons then drift in an applied electric field, resulting in an induced current pulse. This current is then used as a signal.

The `ATLAS` Tile calorimeter uses tiles of scintillating polystyrene as the active material. These are positioned between layers of steel (the passive material). Charged particles passing through these tiles excite the scintillating material, which then produces photons. This scintillation light is then wavelength shifted in order to prevent it from being reabsorbed by the scintillating material, and then carried by optical fibres to photomultiplier tubes (PMTs), which absorb the light and produce an electrical signal.

3.2.4.2 Electromagnetic Shower Development

Photons and electrons interact with the calorimeter via electromagnetic (EM) processes. The dominant processes by which electrons (or positrons) lose energy while traversing the material of the calorimeter are ionisation and Bremsstrahlung. At high energies Bremsstrahlung dominates, while at lower energies ionisation is the dominant process. The critical energy, ϵ_c, is defined as the value of an electron's energy at which the rate of energy loss via ionisation is equal to the rate of energy loss from Bremsstrahlung. This value is material dependent, but an approximation for solids and liquids is given by[35]

$$\epsilon_c = \frac{610\text{MeV}}{Z + 1.24} \tag{3.3}$$

where Z is the atomic number of the element being traversed.

The longitudinal extent of an EM shower may be expressed in terms of the radiation length, which is the distance over which an electron loses $\sim 63\%$ $(1 - e^{-1})$ of its energy via Bremsstrahlung. The radiation length of a material may be approximated by[36]

$$X_0 = \frac{716.4\,A}{Z(Z+1)\log(287/\sqrt{Z})} \quad \text{gcm}^{-2}, \tag{3.4}$$

where Z is the atomic number of the element. Note that the expression has units of g cm^{-2}, and so should be divided by the density of the material in order to obtain a value with dimensions of length. In cases where the material is comprised of multiple elements, then the radiation length of the compound is given by

$$\frac{1}{X_0} = \sum_j \frac{w_j}{X_{0,j}}, \tag{3.5}$$

where the $X_{0,j}$ and w_j are, respectively, the radiation length and fraction (by mass) of the j-th element.

A similar quantity exists to describe the lateral extent of an EM shower. The Molière radius, ρ_M, is given by

$$\rho_M = X_0 \frac{21.2\text{MeV}}{\epsilon_c}. \tag{3.6}$$

Unlike the radiation length, the Molière radius doesn't have a strict physical meaning, although roughly $80 - 90\%$ of an EM shower's energy is generally deposited within a cylinder of radius ρ_M [35].

The dominant processes for photons are pair production, Compton scattering and the photoelectric effect. At higher energies ($\gtrsim 10$ MeV) pair production is the most likely, though as the photon's energy decreases Compton scattering becomes more prevalent, while the photoelectric effect dominates at the lowest energies ($\lesssim 1$ MeV). The average distance that a high energy photon travels before undergoing pair production is $9/7\ X_0$.

Typically, EM showers consist of successive Bremsstrahlung and pair production interactions. An initial electron will radiate, producing a photon. The photon will then undergo pair production, yielding an electron-positron pair in addition to the original electron. This process then repeats, with electrons and positrons radiating photons that then convert into additional electron-positron pairs. This continues until the electron/positron energies fall below the critical energy, at which point they are more likely to lose energy via ionisation than through further radiation. The energy of the initial electron is thus divided between all the electrons and photons produced during the shower, with the electrons then depositing their energy in the calorimeter via ionisation. Ionisation in the active layers of a calorimeter is used to generate a signal: in the LAr calorimeters the ionisation induces a current in the electrode, which is used as a signal, while in the Tile it produces photons via scintillation, which are then guided to a photomultiplier tube and used to produce an electrical signal.

3.2.4.3 Hadronic Shower Development

While EM showers tend to be dominated by only a few processes, there are many more processes that may take place in a hadronic shower, making them more complex.

The longitudinal development of hadronic showers is characterised by the nuclear interaction length, λ_{int}, which describes the average distance that a hadron will travel in a material before interacting with a nucleus. In general, λ_{int} scales as $A^{1/3}$, where A is the mass number of the element being traversed.

Hadronic showers have an EM component and a non-EM component. Of the π mesons produced in hadronic interactions, roughly 1/3 are π^0 mesons. The decay $\pi^0 \rightarrow \gamma\gamma$ occurs very quickly (at rest, the π^0 has a lifetime of 8.5×10^{-17}s), with a branching fraction of 99% [7]. Thus, almost all the π^0's produced in hadronic showers go on to induce EM showers. At each interaction, some of the energy carried by the non-EM component is redirected into the EM component. As the energy of the initial hadron increases, the number of interactions (and thus the fraction of energy carried by the EM component) increases also. The energy carried by the EM component thus scales non-linearly with the energy of the initial hadron.

A feature of the non-EM component of hadronic showers is that some of the energy deposited in the active layers is invisible to the calorimeter. For instance, when a showering hadron interacts with a nucleus and frees a number of nucleons, the binding energy required to release those nucleons is essentially lost: it is invisible to the calorimeter. Neutrons are produced in large quantities during nuclear interactions, and while these may undergo further nuclear interactions they will not ionise the active region of the calorimeter, and so in that sense are invisible. Furthermore, hadronic interactions with nuclei may produce particles that decay to muons and/or neutrinos. Muons (unlike electrons) deposit a minimal amount of energy via ionisation before leaving the calorimeter, while neutrinos (almost always) leave the calorimeter without interacting at all.

A calorimeter will have a lower response to a hadronic shower than it would to an EM shower of the same initial energy, unless it somehow corrects for this invisible energy. This correction is referred to as compensation. The most effective way to achieve compensation is by increasing the calorimeter's response to the non-EM shower component. This response may be boosted if the active material contains hydrogen (as is the case with scintillating materials). In this case, the neutrons produced in nuclear interactions can scatter off hydrogen nuclei. The active material is then sensitive to the recoiling proton [37]. Alternatively, using fissile material as an absorbing material can boost the non-EM response. Energy released in fission reactions can compensate for invisible energy losses. The ZEUS[38] calorimeter is based on uranium/scintillator technology, and is an example of a compensating calorimeter.

The `ATLAS` calorimeters are all non-compensating, and thus the response of the calorimeters to hadrons is lower than for electrons of the same energy. Software-based methods are used during offline reconstruction to correct for this effect, as described in sections 4.5.2 and 5.3.2

3.2.4.4 Calorimeter Energy Resolution

The performance of a sampling calorimeter may be characterised in terms of its resolution, $\sigma/\bar{E}$, where $\bar{E}$ is the mean reconstructed energy and σ is the RMS of the calorimeter response. The resolution is typically parameterised by a function of the form

$$\frac{\sigma}{\bar{E}} = \frac{A}{\sqrt{\bar{E}}} \oplus B \oplus \frac{C}{\bar{E}}, \tag{3.7}$$

where A, B, and C are called the stochastic, constant, and noise terms, respectively, and $\oplus$ denotes addition in quadrature.

The stochastic term arises from variations in the sampled energy, for example, an incident particle may shower in a way that deposits a large amount of energy in the active regions of the calorimeter, or in a way that deposits less energy in these regions. These sampling fluctuations are governed by Poisson statistics, and thus give rise to a term proportional to $\bar{E}^{-1/2}$ in the resolution[39].

The constant term arises from effects that are independent of energy deposited in the detector, such as non-uniformities in the calorimeter response. These non-uniformities may be caused by uninstrumented material in front of the calorimeter, irregularities in the calorimeter structure, or damage caused by radiation or aging, or a calorimeter design in which the response is dependent on the impact point of the incident particle. This impact point dependence forms the dominant contribution to the constant term for the forward calorimeters of `ATLAS`, which is discussed further in section 4.5.1.

The noise term is associated with electronic noise in the readout chain. For the liquid argon calorimeters used at `ATLAS`, the majority of this noise is introduced in the preamplifiers which are located on the front end boards. The noise contribution is independent of the signal being read out of the channel, and so the noise term in the resolution scales as $\bar{E}^{-1}$.

3.2.5 The ATLAS Calorimeters

`ATLAS` contains five distinct calorimeters, shown in Figure 3.6. The Electromagnetic Barrel (EMB) Calorimeter is located in the central "barrel" section of `ATLAS`, while the Electromagnetic End-cap Calorimeter (EMEC), Hadronic End-cap Calorimeter (HEC) and Forward Calorimeters (FCal) are located within the end-caps at either end. The Tile calorimeter consists of barrel section, and two extended barrel sections that surround the end-cap cryostats.

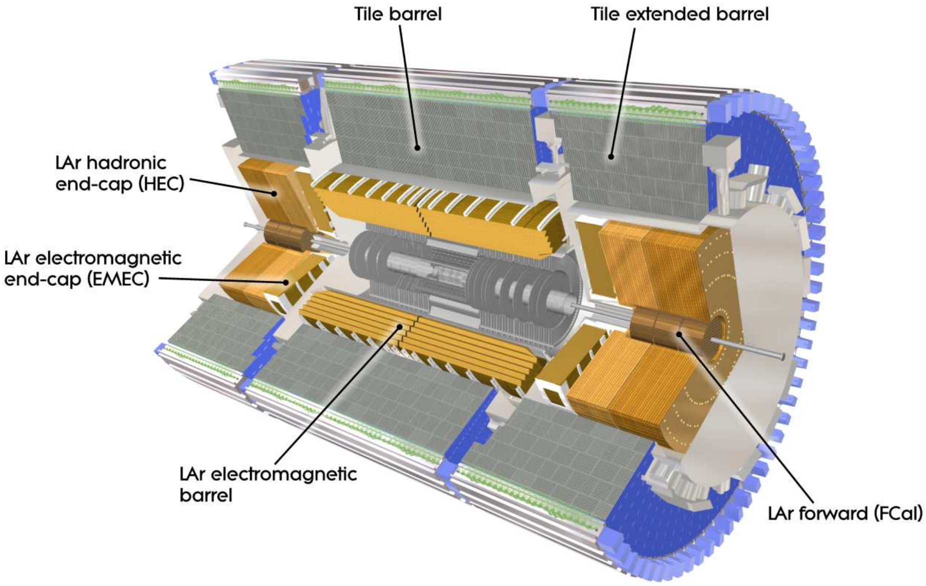

Figure 3.6: The calorimeters of the ATLAS detector.

3.2.5.1 Barrel Calorimeters

The EMB calorimeter is a lead/liquid argon sampling calorimeter covering the pseudorapidity range $|\eta| < 1.475$. Liquid argon was chosen for the active medium because it can be used to obtain a fast, linear response while also being resistant to radiation [31]. The absorber plates are folded into a distinctive accordion shape, as shown in Figure 3.7. The shape of the absorber plates gives the EMB calorimeter a structure that is completely symmetric in the azimuthal direction, with no gaps in detector coverage. The linearity and resolution of the response are thus uniform in ϕ.

The absorber plates are made of lead, with stainless steel sheets glued on each side in order to increase their mechanical strength. The plates are then folded into the accordion shape, with the folding angle increasing with depth (radius) in order to maintain the size of the LAr gap (and hence the sampling fraction) throughout the calorimeter. The lead plates are 1.5mm thick for $|\eta| < 0.8$ and 1.1 m thick for $|\eta| > 0.8$. Thinner sheets are used at higher $|\eta|$ in order to control the depth of the calorimeter[40], which varies from

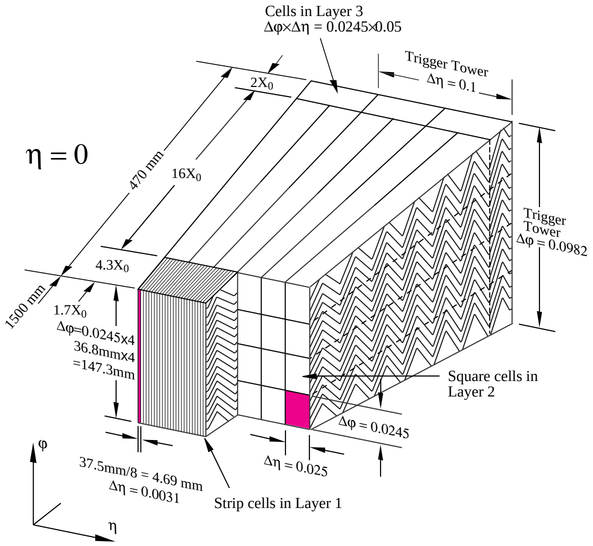

Figure 3.7: Section of the electromagnetic barrel calorimeter, showing the accordion shape of the absorber plates.

22 - 30 X_0 in the region $0 < |\eta| < 0.8$, and from 24 to 33 X_0 in the region $0.8 < |\eta| < 1.3$.

Flexible Printed Circuit Boards (PCBs) are used to form the electrodes, which consist of three layers of copper separated by polyimide. The electrodes are positioned in between layers of the absorber, with honeycomb spacers being used to keep the electrodes in the centre of these gaps. The absorber layers are grounded, while the two outer layers of copper on each electrode are connected to an HV supply at +2kV [31]. This creates two active liquid argon gaps of thickness 2.1 mm on either side of the electrode. The inner layer of copper on each electrode is used to read out the signal, as it is capacitively coupled to both the outer layers.

The readout of the EM Barrel calorimeter [41] is divided longitudinally (i.e. in depth) into three layers. The first and third layers are each a few X_0 in depth and only contain the beginning and end of the shower, while most of the energy is deposited in the second layer which has a depth of ∼17-20 X_0. The readout granularity in $\Delta\eta \times \Delta\phi$ is 0.003×0.1, 0.025×0.0245, and 0.05×0.0245 in layers 1, 2 and 3, respectively. A diagram of the readout layer of the electrode is shown in Figure 3.8, in which the different readout granularities are visible. The first layer has a very fine segmentation in η, which allows

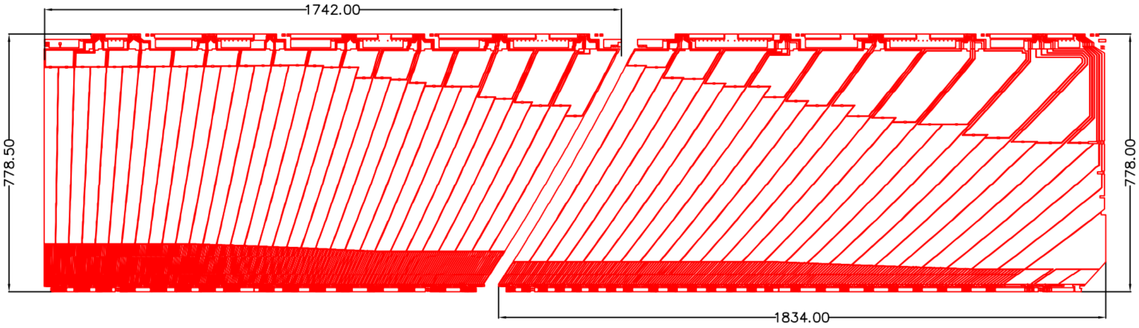

Figure 3.8: Schematic view of the readout layer of an EM Barrel electrode, prior to folding. The piece on the left is used to read out signals from $0 < \eta < 0.8$, while the piece on the right covers the region $0.8 < \eta < 1.475$ [41].

decaying π^0 particles to be distinguished from individual photons.

A steel/scintillator "Tile" calorimeter [42] is used to measure the energy of hadronic particles in the barrel region. It consists of a central barrel section covering the pseudorapidity range $|\eta| < 0.8$, and two extended barrel sections that enclose the LAr end-caps. The Tile calorimeter receives less radiation than the EM Barrel, and so alternatives to liquid argon based calorimetry are viable in this region. A steel/scintillator calorimeter was chosen as it was the most cost effective way of building a hadronic calorimeter with a large depth[31]. The total depth of the Tile calorimeter is about 7.4 interaction lengths.

Each section of the Tile calorimeter is divided into 64 modules, each of which covers an azimuthal angle of 5.625°. The absorbing material of the calorimeter is formed from a series of steel "master" plates, which are 5mm thick and run the full radial depth of the Tile calorimeter (2.0m). A series of smaller, 4mm thick spacer plates are positioned in between layers of master plates. The spacer plates are used to create gaps between adjacent master plates, and it is within these gaps that the scintillating tiles are located, as shown in Figure 3.9. The scintillating tiles are made of polystyrene, which produces scintillation light in the ultra-violet range when excited by the passage of showering particles. The polystyrene is doped with fluors that shift the wavelength of this light into the visible spectrum. Optical fibres are coupled to two sides of each scintillator tile,

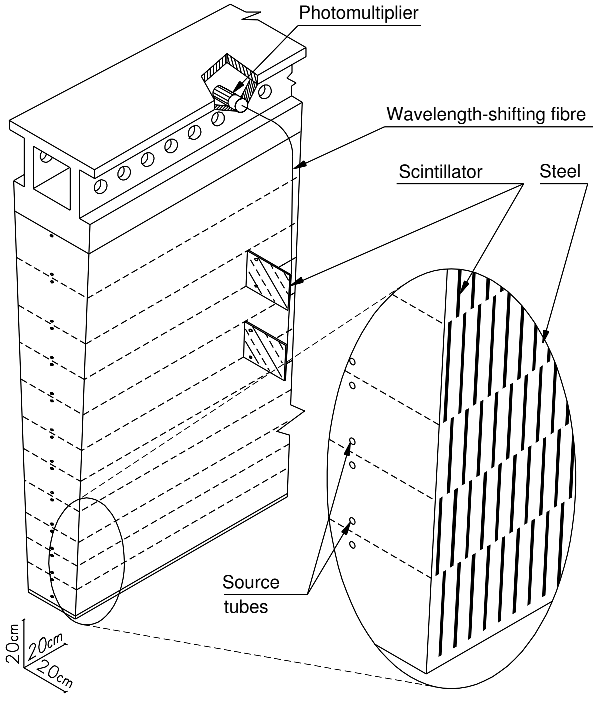

Figure 3.9: Schematic of a tile calorimeter module. Alternating layers of master plates and spacer plates are glued together, with scintillating tiles positioned in the gaps in this structure.

and are used to carry light from the tiles to the Photomultiplier tubes (PMTs), which are housed within the mechanical support structure of the calorimeter. The PMTs then convert the scintillation light to an electronic signal.

3.2.5.2 End-Cap Calorimeters

The Electromagnetic End-Cap (EMEC) and Hadronic End-Cap (HEC) Calorimeters are liquid argon calorimeters housed within the end-cap cryostats at either end of the detector.

The EMEC covers the pseudorapidity range $1.375 < |\eta| < 3.2$, and has a similar design to the EM Barrel calorimeter. As with the barrel, the absorber is formed from accordion shaped layers of lead sheets, while the active regions consist of the liquid argon gaps between these layers. Honeycomb spacers are used to keep the electrodes positioned

Figure 3.10: photograph of an EMEC module, showing the accordion structure of the absorbers. The boundary between the inner wheel and the outer wheel can be seen towards the left, where the shape of the absorber plate changes.

in the centres of these gaps. A module of the EMEC is shown in Figure 3.10.

The EMEC consists of two coaxial wheels, with the boundary between wheels located at $|\eta| = 2.5$, matching the acceptance of the ID. The inner wheel uses absorber sheets of thickness 2.2mm, giving the calorimeter a depth of $26-36X_0$ in the region $2.5 < |\eta| < 3.2$, while the absorber plates in the outer wheel are thinner (1.7mm) giving the calorimeter a depth of $24 - 34X_0$ in this region. Each wheel is subdivided into eight wedge-shaped modules. Due to the accordion shape of the absorber layers, there are no discontinuities in the calorimeter between adjacent modules. As with the EM barrel, the structure of the EMEC is completely symmetric with respect to azimuthal angle. The number of readout layers and their granularities are dependant on pseudorapidity; this information is summarised in Table 3.1.

The HEC calorimeters [43] utilise a parallel plate geometry, which consists of alternating layers of copper and liquid argon oriented at right angles to the beam. Each side of the HEC consists of front wheel and a rear wheel, each of which is divided azimuthally

pseudorapidity	layer 1	layer 2	layer 3
$1.375 < \|\eta\| < 1.425$	0.050×0.1	0.050×0.025	-
$1.425 < \|\eta\| < 1.5$	0.025×0.1	0.025×0.025	
$1.5 < \|\eta\| < 1.8$	0.0031×0.1		0.050×0.025
$1.8 < \|\eta\| < 2.0$	0.0042×0.1		
$2.0 < \|\eta\| < 2.4$	0.0063×0.1		
$2.4 < \|\eta\| < 2.5$	0.025×0.1		
$2.5 < \|\eta\| < 3.2$	0.1×0.1	0.1×0.1	-

Table 3.1: Readout granularity for the EMEC [31], expressed as $\Delta\eta \times \Delta\phi$.

into 32 wedge-shaped modules. The front wheel is comprised of a front plate which is 12.5 mm thick, as well as 24 copper plates, each of which is 25mm thick. The rear wheel contains a front plate that is 25mm thick, and is followed by 16 plates of thickness 50mm.

In both wheels, the liquid argon gaps formed between the absorber plates have a depth of 8.5mm. These gaps are divided into four sub-gaps of thickness ∼2mm by a set of three parallel electrodes, forming an electrostatic transformer [44]. This makes it easier to match the impedance of the calorimeter channel to the readout electronics. The signal is read off a central pad in the middle electrode, with shapes etched into these pads determining the read-out structure. Cells in the HEC have a granularity of 0.1×0.1 in $\Delta\eta \times \Delta\phi$ for $|\eta| < 2.5$, and 0.2×0.2 at higher $|\eta|$.

3.2.6 Forward Calorimeters

The `ATLAS` Forward Calorimeters (FCal) are located just outside the beampipe, with their front faces situated 4.7 m on either side of the `ATLAS` interaction point. These are liquid argon based calorimeters, and are located within a support tube inside the end-cap cryostat (Figure 3.12). They cover the pseudorapidity region $3.1 < |\eta| < 4.9$.

Each FCal consists of three modules, one electromagnetic module (FCal1) and two hadronic modules (FCal2 and FCal3). Each module has a cylindrical shape, with an outer radius of 449 mm and a depth of 444 mm. A plug made of a brass alloy has a similar shape and is located behind the hadronic modules in order to provide additional

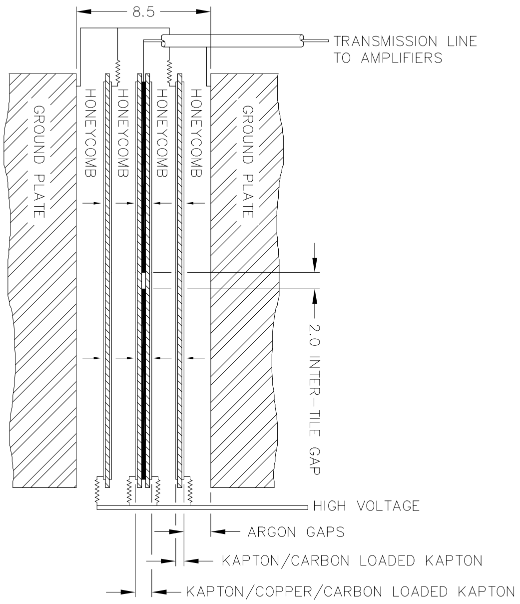

Figure 3.11: Electrode structure in the HEC. Electrodes are arranged to form an electrostatic transformer

shielding for the muon chambers behind it. As the FCal operates at a temperature just below 90K in `ATLAS`, “cold” values will be used in the following when quoting dimensions, densities, or other temperature-dependent quantities.

The electromagnetic modules of the FCal were produced by the University of Arizona. Each module consists of a stack of circular copper plates with an inner radius of 72 mm and an outer radius of 449 mm. Each plate is drilled with a hexagonal array of holes into which the electrodes were inserted. This was done in a way that established a good electrical connection between the outside of the electrode and one of the copper end-plates. Each electrode consists of a copper tube (the cathode) containing a copper rod (anode) around which a radiation-hard PEEK fibre is wrapped. The inner radius of the copper tubes is 2.62 mm while the radius of the copper rods is 2.35mm, thus leaving a gap of 267 μm which is filled with liquid argon. The PEEK fibre has a diameter of 250 μm,

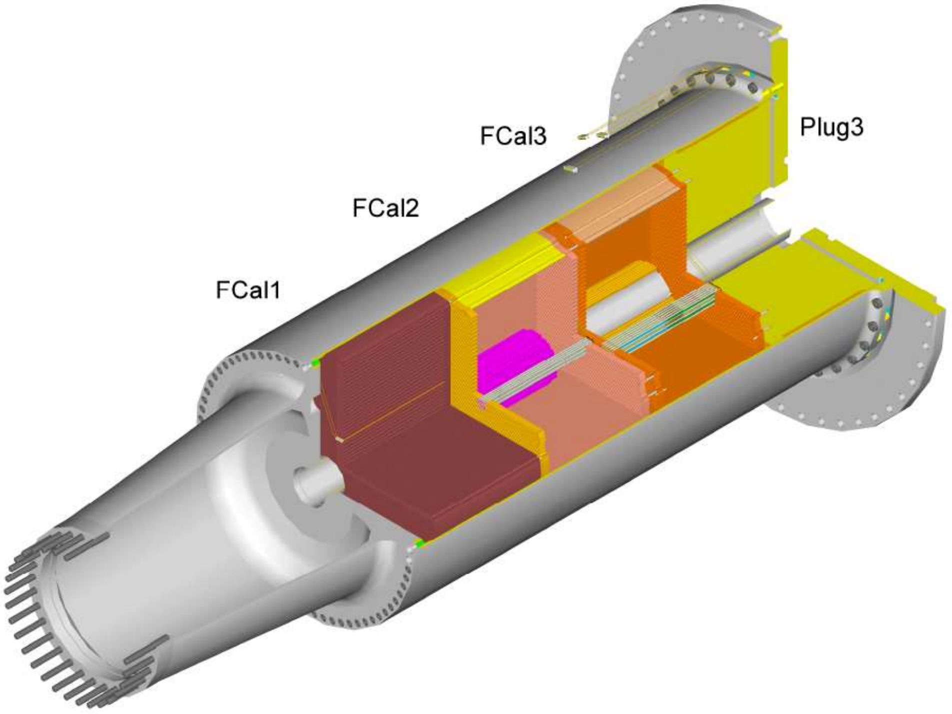

Figure 3.12: Cut-away view showing the FCal within its support tube[45]. The region inside the support tube and just upstream of the calorimeter is evacuated in ATLAS.

and is present to keep the rod positioned in the centre of the tube, thus maintaining the uniformity of the LAr gap throughout the electrode and keeping the rod electrically isolated from the tube. Typical gap sizes used in traditional LAr calorimeters are on the order of a few millimetres, as is the case for the EM Barrel, EMEC and HEC calorimeters. However, as the FCal is located at high pseudorapidity, minimum bias events will deposit energy in it at a very high rate. The smaller gap size is required in order to reduce the drift time across the gap, and thus preventing the high rate of ionisation from causing a build-up of positive ions in the liquid argon. Positive ion buildup can distort the electric field in the LAr gap, thus distorting the signal from the electrode. The distance between electrodes in FCal1 is similar to the Molière radius for copper. EM showers in the FCal should thus spread across several electrodes, allowing the calorimeter to sample the shower effectively. Copper also allows the FCal1 module to conduct heat efficiently.

The cryostat temperature is kept at about 88.5K, while the boiling point for liquid argon within the cryostat is 92.7K. With the LHC running at design luminosity, minimum bias events are expected to heat the FCal at a rate of about 45W, with about half of that power going into FCal1. A finite element analysis estimated that this heating would cause a temperature increase within the FCal of no more that 1.5K, which is not enough to cause the liquid argon to boil[45].

The hadronic modules of the FCal were produced at the University of Toronto (FCal2) and at Carleton University in Ottawa (FCal3). They have a similar design to the electromagnetic module, however tungsten is used as the absorber material instead of copper. Each of the hadronic modules uses two copper end plates drilled with a hexagonal array of holes, each of which holds an electrode. The electrodes use copper tubes for their cathodes and rods made of pure tungsten (with density 19.2 g/cm^3) for the anodes. The absorber matrix is formed from small slugs of tungsten alloy ("WFeNi" - 97% Tungsten/2% Iron/1% Nickel) positioned in the gaps between the electrode tubes, as shown in Figure 3.13. The material composition and density of the calorimeter components are important factors when establishing a description of the calorimeter to be used by simulations. By themselves, the WFeNi slugs have a measured mean density of 18.3 g/cm^3. When considering the WFeNi slugs, the copper electrode tubes, and any spaces in the absorber matrix that are filled with liquid argon, the average density of absorbing material (excluding electrode rods) in the hadronic modules is estimated to be 14.33 g/cm^3 for FCal2 and 14.45 g/cm^3 for FCal3 [46].

3.2.6.1 FCal Electronics

An electric field of ∼1KV/mm is conventional for liquid argon calorimeters. In order to provide this the rods of each electrode are supplied with high voltage while the tubes are grounded. Showering particles ionise the liquid argon, leaving free electrons and Ar$^+$ ions in the gap. The electric field in the gap then causes this charge to drift resulting in

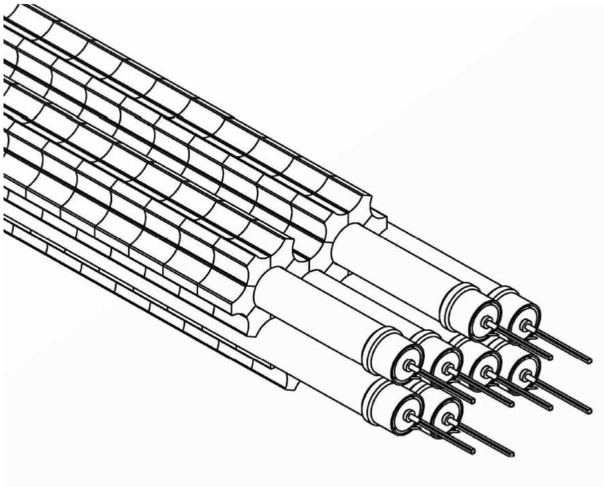

Figure 3.13: Diagram showing the arrangement of electrodes and slugs in the hadronic modules [45].

Quantity	FCal1	FCal2	FCal3
Absorber material	Copper	Tungsten	Tungsten
Module inner diameter	72 mm	79 mm	86 mm
Electrode Separation	7.5mm	8.62 mm	9.0mm
Rod Diameter	2.35 mm	2.47 mm	2.75 mm
Tube inner diameter	2.62 mm	2.84 mm	3.25 mm
LAr Gap	267 μm	375 μm	500 μm
Distance from IP to front face	4668.5mm	5128.3 mm	5602.8
Number of electrodes	$\sim$ 12,000	$\sim$ 10,000	$\sim$ 8000

Table 3.2: Dimensions of the FCal modules.

a current pulse. This pulse is triangular in shape, having a fast rise time ($\sim$1 ns) and taking $\sim$61 ns (in FCal1) to return to zero [45]. The height of the pulse peak depends on the amount of charge deposited in the liquid argon, and is thus proportional to the amount of energy deposited in the liquid argon [*].

The signal is read out via a coaxial cable that also supplies the electrodes with high voltage. Electrodes in the FCal are ganged together on interconnect boards to form "tube groups". Tube groups are formed from four electrodes in FCal1, six electrodes in FCal2, and nine electrodes in FCal3. Gold-plated signal pins connect the rods from these

---

[*] The energy required to ionise an atom of argon is 15.8 eV.

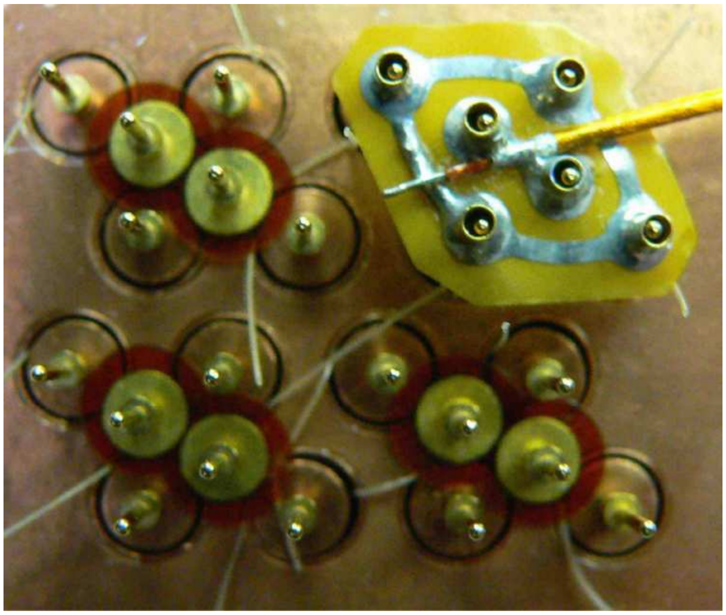

Figure 3.14: Photo of an endplate of FCal1, taken during assembly, showing the interconnect board and the coaxial cable used for HV delivery and readout [45]. Also visible are the PEEK fibres used to keep the rods centred within the tubes. The two central pins in each group are used to ground the end plate, and thus the tubes, while the four exterior pins provide HV to the rods and carry the signal off the electrode.

electrodes to the interconnect board, which is supplied with HV via a coaxial cable as shown in Figure 3.14. The tubes are also grounded through this coax: each interconnect board is connected (via grounding pins) to the FCal end plate. As the interconnect board connects electrodes in parallel, the signal carried off the interconnect board is the sum of the current pulses in each electrode of that tube group.

The readout lines are then fed out to summing boards, which are located on the rear of the HEC (i.e. inside the end-cap cryostats) as shown in Figure 3.15. On each summing board, signals from four interconnect boards are further combined to form a single readout channel. A typical FCal channel thus corresponds to four tube groups, which is equivalent to 16/24/36 electrodes in FCal1/FCal2/FCal3. The summing is carried out through a transmission line transformer, which serves to match the impedance of the readout coax to that of the "pigtail" cable used to carry the signal away from the

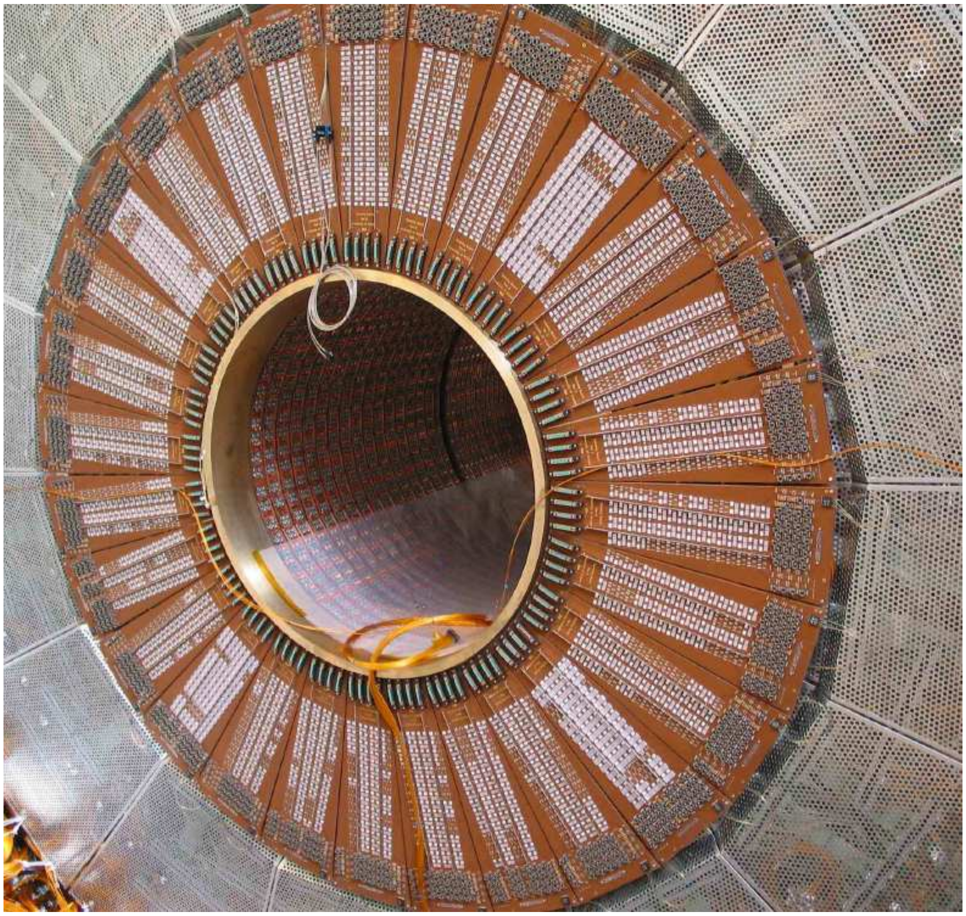

Figure 3.15: The FCal summing boards mounted on the rear of the HEC[45]

summing board (Figure 3.16). A different HV source is used to supply each tube group in a given channel, so that if one source fails then the other three tube groups in the channel should still be powered. This has occurred in `ATLAS`: one of the lines supplying HV to the A-side FCal was severed during installation. This line supplies HV to one quadrant of FCal3, leaving one quarter of the tube groups in the affected area without HV. The remaining tube groups still contribute signal to the channels in this area, and so the effect of the severed HV line is corrected for during reconstruction.

Near the inner and outer edges of the FCal the tube groups are irregularly shaped. It is not practical to sum these channels in a coherent manner, and these “unsummed” channels also provide better readout granularity at high $|\eta|$.

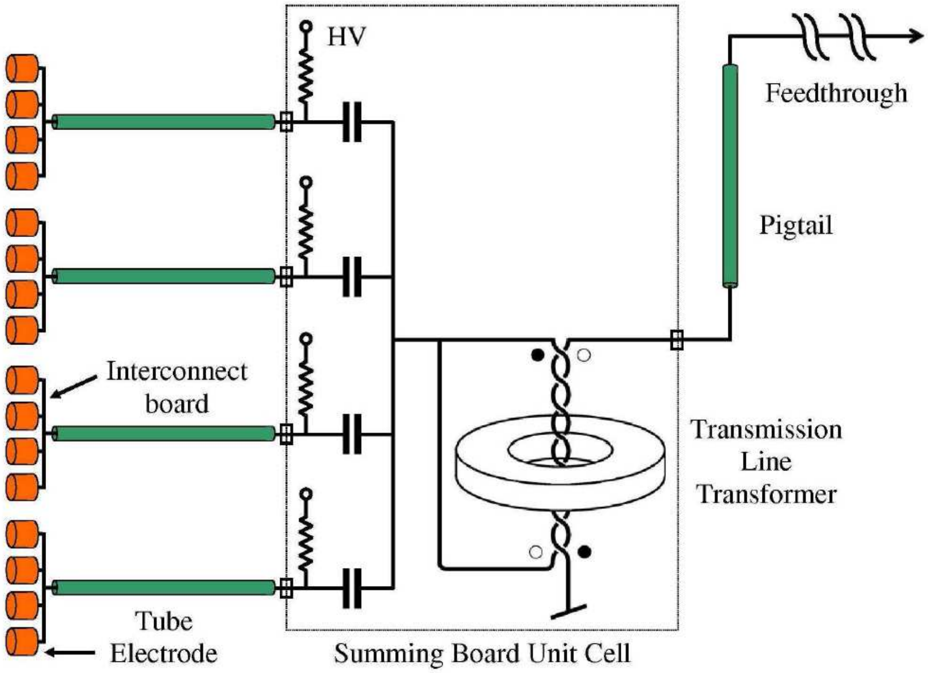

Figure 3.16: Diagram of the FCal readout chain for a single summed channel. Summed channels are composed of four tube groups, which each consist of 4/6/9 electrodes in FCal1/FCal2/FCal3.

“Pigtail” cables are used to carry the signal from the summing boards to the cryostat feedthrough. Outside the cryostat, a stripline cable is used to carry the signal from the feedthrough to the Front End Boards.

3.2.6.2 Front End Boards

Front End Boards (FEBs)[47] are used in the electronics chains of all liquid argon calorimeters. Much of the following discussion applies to the electronics associated with all of these calorimeters, however some of the details mentioned here are specific to the electronics chain of the FCal.

On the FEB, the signal is amplified and then shaped. The shaping consists of one differentiation and two integration steps (CR-RC^2) resulting in a bipolar pulse shape. This is done in order to optimise the signal with respect to pileup and electronics noise[40, 47]. In the other LAr calorimeters it takes much longer for the triangular current pulse to drop from its peak value back to zero due to the larger gap size*. In these cases the shaping also allows the signal to be read out much faster, as the relevant information can be obtained from the first ~ 125 ns of the shaped pulse. Three different gains (low, medium, and high) are used when amplifying the signal. The amplification used for high gain is about 10 times as much as that used for medium gain, which in turn is about 10 times higher than that used for low gain. Each shaping chip processes the signals from four channels. An additional output on this chip sums the four inputs and then shapes the result. This output is used in the formation of trigger towers, which are discussed in section 3.2.7.

Timing on the FEB is managed by a Trigger Timing Control (TTC) chip, which distributes clock pulses every 25ns. The signal (at each gain) is sampled at every 25ns, and stored (as an analog voltage) on a Switched Capacitor Array (SCA) circuit. The pulse shapes for the three FCal modules are illustrated in Figure 3.17, showing the times at which the signals are sampled. Each pulse consists of an initial positive lobe followed by a longer negative lobe, the start of which can be seen in the Figure.

When a trigger signal indicates that an event should be read out, the pulse samples are read off the SCA and fed to an ADC (Analog to Digital Converter). For each sample the ADC then outputs a 12-bit signal. Under normal operation only a single gain is read out of the SCA and digitised; a gain selector chip is used to determine which gain will yield the largest pulse height without saturating the ADC output. This is done by digitising a sample near the peak of the pulse at medium gain, and comparing the result to two pre-defined thresholds. If the value of the digitised sample lies between the thresholds then medium gain is used for the digitisation, otherwise low gain is used if the sample exceeds the upper threshold or high gain is used if the sample is smaller than the lower threshold. In order to allow for negative values, e.g. samples taken on the negative lobe

---

[*] This time is $\sim$400 ns in the EM barrel but only ~ 60 ns in FCal1 [45]

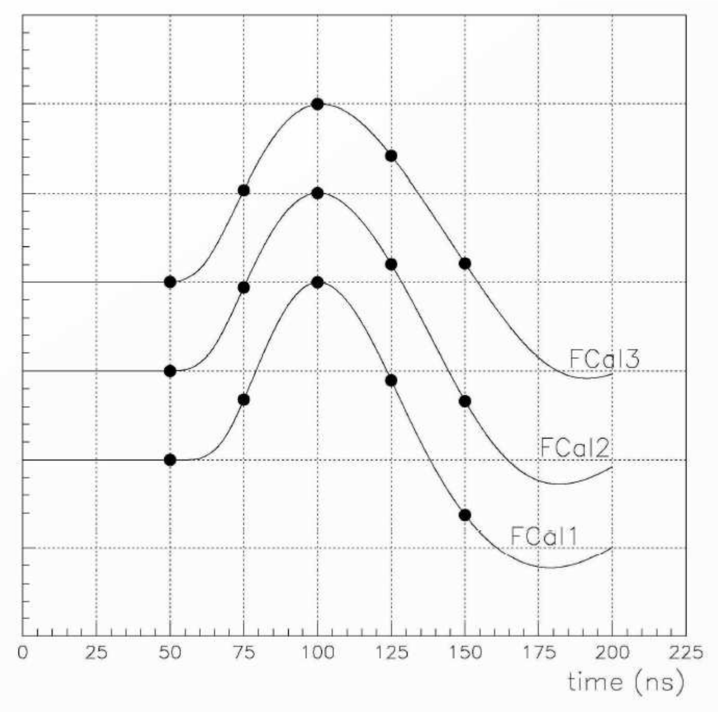

Figure 3.17: Pulse shapes for each module. The dots indicate the times at which they are sampled and digitised.

of the pulse, a "pedestal" value is subtracted from the digitised output. An offset voltage is added to the samples read from the SCA just prior to their digitisation [47]. This offset voltage is chosen such that the pedestal value is around 1,000 ADC counts, leaving around 3,000 ADC counts to represent the positive lobe of the pulse. For example, the negative lobe of a pulse may be sampled, and stored as a negative voltage in the SCA. Prior to digitisation, the sample is read from the SCA, and the offset voltage is added, such that the voltage to be digitised is positive. The digitised sample will then have a value of less than 1,000 ADC counts. When used to compute the channel energy (as discussed below), the pedestal value (∼1,000 ADC counts) is first subtracted, such that the value associated with this sample is negative.

For the testbeam studies discussed in chapter 4 the pedestal values were obtained from physics data on a run by run basis. For each channel, the first sample of each pulse was averaged over the entire run, and this value was used as the pedestal during reconstruction. Note that the first sample is taken before the pulse starts to rise, as illustrated in figure 3.17. In `ATLAS`, the pedestal values for each channel are obtained from electronic calibration runs.

3.2.6.3 Signal Reconstruction/Optimal Filtering Method

Offline reconstruction of the energy deposited in the calorimeter is done through the use of optimal filtering coefficients (OFCs) [48]. These coefficients are used to reconstruct the amplitude of the signal pulse and its timing in such a way that the effect of the noise on the reconstruction is minimised.

The OFC method produces two sets of coefficients, a_i and b_i, which on average correctly produce the pulse amplitude A and time shift τ:

$$\begin{aligned} A &= \left\langle \sum_i a_i S_i \right\rangle \qquad (3.8) \\ A\tau &= \left\langle \sum_i b_i S_i \right\rangle, \qquad (3.9) \end{aligned}$$

where S_i is the value of the i-th signal sample, after pedestal subtraction. Given that the pulse shape, $g(t)$ is known, these samples may be expressed as

$$S_i = Ag(t_i - \tau) + n_i = Ag(t_i) - A\tau g'(t_i) + n_i, \qquad (3.10)$$

where g' is the derivative of the pulse shape and n_i is the noise present in the i-th sample. Equations 3.8 and 3.9 may then be rewritten as

$$\begin{aligned} A &= \sum_i a_i Ag(t_i) - a_i A\tau g'(t_i) + a_i \langle n_i \rangle \qquad (3.11) \\ A\tau &= \sum_i b_i Ag(t_i) - b_i A\tau g'(t_i) + b_i \langle n_i \rangle \qquad (3.12) \end{aligned}$$

The coefficients should be chosen in such a way that the variances of A and $A\tau$ are minimised. As the mean value of the noise is zero, these variances may be written as

$$\mathrm{Var}(A) = \sum_{i,j} a_i a_j \langle n_i n_j \rangle \tag{3.13}$$

$$\mathrm{Var}(A\tau) = \sum_{i,j} b_i b_j \langle n_i n_j \rangle, \tag{3.14}$$

where $\langle n_i n_j \rangle$ is simply the autocorrelation matrix of the noise between samples. This minimisation may be carried out using the method of Lagrange multipliers, with constraints

$$\begin{array}{ll} \sum_i a_i g_i = 1, & \sum_i a_i g_i' = 0 \\ \sum_i b_i g_i = 0, & \sum_i b_i g_i' = -1 \end{array}$$

obtained from equations 3.11 and 3.12.

For the testbeam studies discussed in chapter 4, a SPICE [49] simulation of the FCal electronics chain was used to obtain an initial estimate of the pulse shape used in the OFC calculation. This estimate was then improved using an iterative procedure that incorporated data taken from testbeam runs. The data used in this procedure are taken from events in which have a large pulse amplitude, in order to ensure that the signal is coming from a physical energy deposit.

3.2.6.4 Electronic Calibration

After reconstructing the pulse amplitude, an “ADC2MeV” factor is applied in order to convert the pulse amplitude (in ADC counts) to the energy deposited in the calorimeter cell. For the FCal, the ADC2MeV value used during reconstruction is based on testbeam measurements (see section 4.5.1), and will be discussed further on page 51. For the other LAr calorimeters (EMB, EMEC and HEC), the ADC2MeV factor is obtained using an electronic calibration procedure. The ADC2MeV factor may be written as the following product:

$$F_{\mathrm{ADC}\to\mathrm{MeV}} = F_{\mu\mathrm{A}\to\mathrm{MeV}}\, F_{\mathrm{DAC}\to\mu\mathrm{A}}\, \frac{1}{M_{\mathrm{phys}}/M_{\mathrm{calib}}}\, R. \tag{3.15}$$

The factors $F_{\mathrm{DAC}\rightarrow\mu\mathrm{A}}$, R, and $\frac{1}{M_{\mathrm{phys}}/M_{\mathrm{calib}}}$ are derived from electronic calibration studies of the calorimeter, and will be discussed below. The factor $F_{\mu\mathrm{A}\rightarrow\mathrm{MeV}}$ describes the amount of energy that must be deposited in the calorimeter cell in order for the signal current in the calorimeter electrodes to have a peak value of 1 μA. Note that $F_{\mu\mathrm{A}\rightarrow\mathrm{MeV}}$ is related to the sampling fraction, f_{samp}, of the calorimeter, such that

$$\frac{1}{F_{\mu\mathrm{A}\rightarrow\mathrm{MeV}}} = \frac{f_{\mathrm{samp}}}{\tau_{\mathrm{drift}} E_{\mathrm{ion}}}, \tag{3.16}$$

where E_{ion} is the ionisation energy of argon (15.8 eV) and τ_{drift} is the electron drift time in the calorimeter cell.

All of the liquid argon calorimeters in `ATLAS` make use of a calibration board, which injects a calibration pulse into the readout chain. In the FCal, this pulse is injected at the input to the FEB[45], and so serves to monitor the electronic gain. In the EMEC, EM Barrel and HEC the pulse is injected at the calorimeter electrodes, and is also used to predict pulse shapes, channel by channel.

Between LHC fills, electronic calibration studies of the LAr calorimeters may be performed. There are three types of calibration runs that may be undertaken during these studies: delay runs, ramp runs, and pedestal runs. Pedestal runs are used to record samples in the absence of any signal, and thus can be used to obtain the RMS of the electronics noise in the channel and the autocorrelation function of the noise. The noise autocorrelation function is used in the derivation of the OFCs, while the noise RMS is taken as the pedestal value, which is subtracted from pulse samples during reconstruction of the pulse peak.

The calibration pulse is controlled by a 16-bit Digital-to-Analog Converter (DAC)[50]. In ramp runs, the amplitude of the injected calibration pulse is varied ("ramped"), and OFCs are then applied in order to reconstruct the pulse peak. This allows the relationship between the input current signal (in DAC) and the reconstructed pulse peak (in ADC)

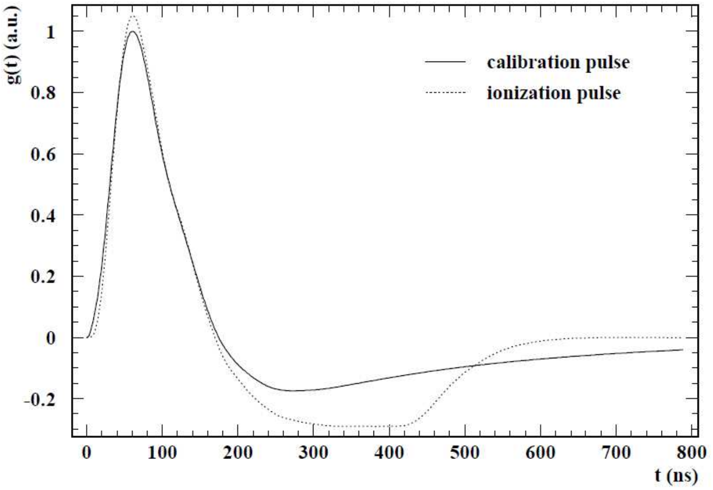

Figure 3.18: Calibration and ionisation pulse shapes for an EMB channel, after shaping. Prior to shaping, the peak current of the two pulses were equal [51].

to be measured. A linear fit is performed to the (ADC,DAC) data, and the slope, R (in units of DAC/ADC), is extracted. Thus, the factor of R in equation 3.15 functions as an ADC→DAC conversion factor. The amplitude of the DAC signal and the peak value of the injected current pulse are related by the factor $F_{\mathrm{DAC}\rightarrow\mu\mathrm{A}}$, which depends on the specifics of the calibration board. The product $F_{\mathrm{DAC}\rightarrow\mu\mathrm{A}}\,R$ thus acts as an ADC→ μA conversion factor for calibration pulses.

However, signal pulses arising from ionisation have different shapes to the injected calibration pulses. Ionisation pulses are triangular, having a peak proportional to the number of ionisation electrons produced in the active region of the calorimeter cell and dropping to zero after the drift time has elapsed. The injected calibration pulses are shaped like decaying exponentials in order to approximate this triangular shape. This difference has an effect during the shaping. For example, in the case where an injected calibration pulse and an ionisation pulse both have the same initial peak current, the amplitude of the calibration pulse after shaping will be slightly lower than that of the ionisation pulse (as illustrated in Figure 3.18).

Delay runs allow the pulse shapes to be measured. In delay runs, the calibration pulse is delayed (with respect to the TTC clock) by multiples of 1 ns. This effectively allows the shaped calibration pulse to be sampled at 1 ns intervals, which gives an accurate measurement of the shape of the calibration pulse. This information may then be used to infer the final shape of pulses originating from ionisation[51], which may then be used (together with the noise autocorrelation information obtained from pedestal runs) to derive the OFCs used for data taking at ATLAS. The factor $M_{\mathrm{phys}}/M_{\mathrm{calib}}$ describes the ratio of the shaped ionisation pulse amplitude to that of the shaped calibration pulse amplitude, for cases in which both pulses have the same peak current prior to shaping. This factor corrects for the effect of pulse shaping, and thus allows the calibration factors (which are derived from calibration pulses) to be used for the calibration of ionisation pulses.

For the FCal, the calibration is based on testbeam studies rather than derived using calibration pulses. The factor $F_{\mu\mathrm{A}\rightarrow\mathrm{MeV}}$ may be calculated for each module from the geometry of the FCal electrodes and the other properties of the detector. The ADC2MeV value obtained from testbeam can then be used to derive a value of $F_{\mathrm{DAC}\rightarrow\mu\mathrm{A}}$ that is appropriate for the electronics used in ATLAS. As the calibration is not derived from calibration pulses, the factor $\frac{1}{M_{\mathrm{phys}}/M_{\mathrm{calib}}}$ is not needed. Pedestal runs are used to measure noise in the electronics, but pulse shapes from testbeam data are used in the calculation of the OFCs (delay runs are not taken for the FCal). Ramp runs are still used to obtain R, and can thus be used to correct for any variations in the electronic gains.

3.2.7 Trigger and Data Acquisition

Collisions between proton bunches occur at ATLAS at a design rate of 40 MHz, however, the maximum rate at which events can be recorded is limited by computing resources and is presently $\sim$ 400 Hz. The trigger system is designed to ensure that as many interesting events are recorded as possible, while rejecting less interesting events that occur at high rates, as shown in Figure 2.1. The ATLAS trigger system consists of three consecutive levels: level one (L1), level 2 (L2), and the Event Filter (EF). The L1 trigger selects candidate events at a maximum rate of 75 kHz. Most of these events are subsequently rejected at L2, reducing the acceptance rate to 3.5 kHz. The final level of event rejection is done by the EF, which accepts events at the desired rate of $\sim$ 400 Hz.

The L1 trigger utilises custom-built hardware that is located off the detector, and needs to decide whether to accept or reject the event within 2.5 μs of the corresponding bunch crossing. While this decision is being made, information from detector channels is stored in pipeline memories, which are located on or near the detector. The level 1 trigger consists of three of three parts, L1 Calo, L1 Muon, and the Central Trigger Processor (CTP). The L1 Calo trigger is used to select electrons, jets, taus, and other high p_{T} objects (excluding muons), while the L1 muon trigger processes signals from the RPCs and TGCs of the Muon Spectrometer.

The CTP decides whether an event is accepted or rejected at L1. Trigger conditions are specified in a "menu", each item of which is some combination of trigger items from L1 Calo and/or L1 Muon. The CTP also handles the "prescales" on these menu items, which are used to control the bandwidth allowed for each item and keep the L1 acceptance rate at the desired level. For a menu item with a prescale of 50, one event will be accepted at L1 for every fifty events that satisfy the trigger conditions associated with that menu item. Menu items associated with a rare or particularly interesting event topology may be given a prescale of one, in which case the event is accepted every time the trigger conditions are met. Frequently occurring or less interesting topologies (such as those containing low-p_{T} jets) are given higher prescales.

The CTP also receives input from specialised detectors, such as ALFA (Absolute Luminosity For ATLAS), LUCID (Luminosity measurement using a Cherenkov Integrating Detector), the Beam Conditions Monitor (BCM) and the Minimum Bias Trigger Scintillators (MBTS). LUCID [52] and ALFA [53] are luminosity detectors located 17m and 240m from the ATLAS interaction point, respectively, and were used to measure the luminosity delivered to `ATLAS` during 2010. The BCM [54] is designed to monitor the condition of the beams and identify situations in which beams may be harmful to `ATLAS` detectors (triggering a beam abort). It also provides a real time measurement of the luminosity at `ATLAS`. The MBTS is used to select "minimum bias" events: the thresholds required to accept these events are very low, and so collision events are selected with minimal bias. These events are typically soft inelastic scatterings. The MBTS consists of tiles of scintillating polystyrene that are 2cm thick. There are 16 of these tiles mounted on the outer wall of each end-cap cryostat (on the side closest to the interaction point), covering the pseudorapidity range $2.09 < |\eta| < 3.84$. Early studies of the MBTS showed it to be very efficient, with an efficiency of over 99% for selecting events in which there were at least 3 tracks with $p_{\mathrm{T}} > 100\mathrm{MeV}$ [55]. Because of its high efficiency and low bias, the MBTS trigger was used as a reference when determining the efficiency of the jet triggers used in the inclusive jet and dijet cross section measurements, as discussed in section 5.4.1. The distribution of charged particles obtained from minimum bias events recorded at `ATLAS` is plotted in Figure 3.19 [56]. Note that the distribution is roughly uniform in η. Due to the nonlinear relationship between η and the polar angle, θ, a fixed interval $\Delta\eta$ corresponds to a smaller angular interval at high $|\eta|$ than at low $|\eta|$. For example, one side of the EM Barrel has a length of 3.2 metres and covers the region $0 < \eta < 1.475$, while the FCal has an outer radius of $\sim 450\mathrm{mm}$ and covers the region $3.2 < \eta < 4.9$: the FCal covers a larger pseudorapidity interval in a much smaller area. As the distribution of particles produced in minimum bias events varies slowly in η, detectors covering higher values of η will be subject to a higher flux of particles than detectors located at low η. The effects of pile up are thus more significant for the FCal and end-cap calorimeters than for the barrel calorimeters.

The time available for the L1 decision is too short for L1 Calo to consider the information from individual calorimeter cells. Cell information is stored in the detector electronics, and only read out when an L1 accept signal is received from the CTP. Of

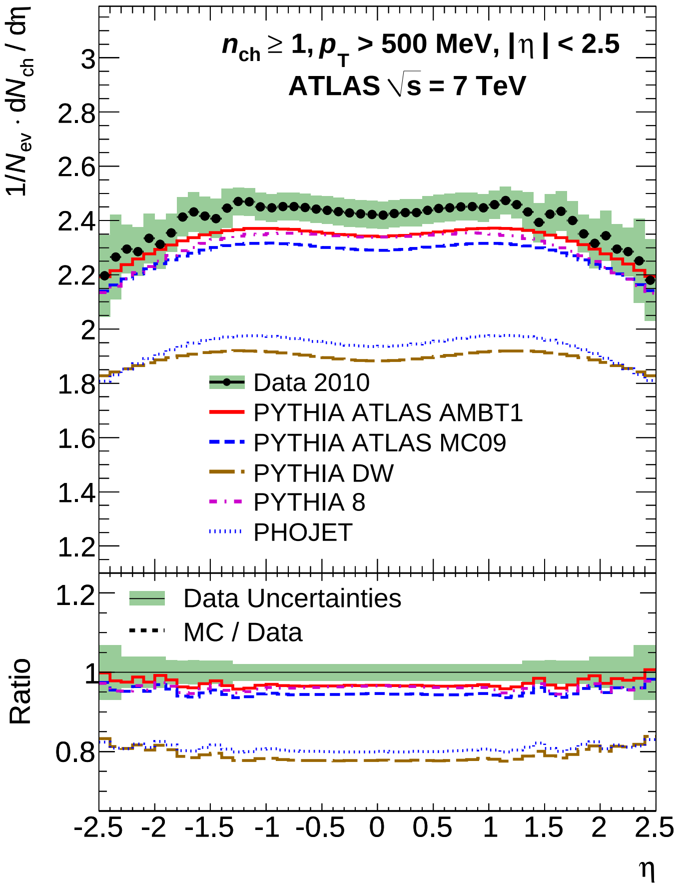

Figure 3.19: Distribution of charged particles produced in minimum bias events[56]. The plot shows data measured at ATLAS, as well as predictions obtained from Monte Carlo simulations using a variety of tunes. Note that the plot only covers the region $-2.5 < \eta < 2.5$, as Inner Detector coverage is limited to this interval.

the 2.5 μs available at L1, the decision is usually made within 2.1μs. However, a large fraction of this time is taken up by the transit time for signals to propagate between the trigger hardware and the detector, while L1 Calo processes events in less than 1 μs. Instead of relying on cell information, calorimeter signals are instead processed into "trigger towers", which are then sent as input to L1 Calo. Trigger towers are formed from analog sums of readout channel signals, as discussed in Section 3.2.6.2. In the Tile calorimeter, a trigger tower is formed by summing the signals from five channels. In the LAr calorimeters, the first two stages of summation are carried out on the FEBs, while the remaining addition is carried out on dedicated Tower Builder Boards (for the EMB and EMEC) or Tower Driver Boards (for the HEC and FCal)[57]. In the barrel and end-cap regions ($|\eta| < 3.2$), the trigger towers have a granularity 0.1×0.1 in η and ϕ, whereas in the FCal the trigger towers have a granularity of approximately 0.4×0.4.

3.2.7.1 Jet Triggers

The level 1 central jet trigger combines 2×2 blocks of trigger towers to form "jet elements", which then have a granularity of 0.2×0.2 in $\eta - \phi$ space. A sliding window algorithm[58] is then used to identify jets. The window consists of a 4×4 grid of jet elements, and a jet is identified if the total transverse energy within the window exceeds a given threshold. For example, the "L1_J10" algorithm requires the transverse energy (at the EM scale) in the window to exceed 10 GeV. Additionally, the 2×2 cluster of jet elements in the centre of the window is required to be a local maximum; that is, the central cluster must have a transverse energy greater than that of any other 2×2 block of jet elements within the window.. If these criteria are met, then the event is accepted by the jet algorithm. The 0.4×0.4 area of $\eta - \phi$ at the centre of the window is then identified as a "Region of Interest" (ROI), and is passed on to any relevant L2 trigger algorithms.

The forward jet trigger is used to identify jets in the region $|\eta| > 3.2$, and operates independently of the central jet trigger. While the central jet trigger uses information from the EM Barrel, Tile, EMEC and HEC calorimeters, only the forward jet trigger uses information from the FCal. Trigger towers in the FCal have a granularity of $\sim$0.4 $\times$ 0.4 in $\eta - \phi$, which is coarser than in other calorimeters. A jet element is then formed by summing all FCal trigger towers in η, such that the jet element has dimensions 1.6×0.4 in η and ϕ, respectively[58]. Jets are then identified using the same sliding window algorithm that is used by the central jet trigger[59].

At L2, the trigger decision needs to be made within 40ms. This interval is sufficient for cell-based methods to be used, although only cells within the region of interest (typically about 2% of the detector) are read out. A cone-based algorithm is used for jet identification: a cone of fixed radius $\Delta R = \sqrt{\Delta\eta^2 + \Delta\phi^2}$ is positioned at the centre of the RoI. Energy weighted values of η and ϕ are obtained by summing cells within the cone, and the centre of the cone is then moved to these coordinates. This process is carried out a predetermined number of times.

At the EF level, 4.0s of processing time is available, and so algorithms similar to those used for offline reconstruction (described in section 5.3.1) may be used at the trigger level. Note that EF algorithms for jet triggers were not online while the data used in this thesis were being recorded, and so the trigger studies presented in section 5.4.1 focus on jet triggers at L1 and L2.

Chapter 4

Beam Test studies of the ATLAS Forward Calorimeter

4.1 Introduction

The first testbeam studies of the ATLAS Forward Calorimeter were carried out in 1993, using an early prototype of the FCal1 module[60]. This study provided proof of principle of the novel calorimeter design, and based on the results the design was adopted by the ATLAS collaboration [60]. The prototype used in these studies was made of brass instead of copper and had a depth of 25 cm, approximately half the depth of the FCal1 module presently being used in ATLAS. A subsequent beam test was carried out in 1995 using a full-depth FCal1 prototype [61]. In 1998 further beam tests were carried out at CERN using full-depth “module 0” prototypes of FCal1 and FCal2, which allowed the response of the hadronic modules to be investigated for the first time [62, 63]. The 2003 testbeam utilised all three of the C-side FCal modules presently operating in ATLAS, and will be discussed in detail in this chapter. Following this, a 2004 combined testbeam studied the behaviour of the combined end-cap calorimeter system[64]. This utilised the refurbished “module 0” FCal1 and FCal2 prototypes used in the 1998 testbeam, as well as modules

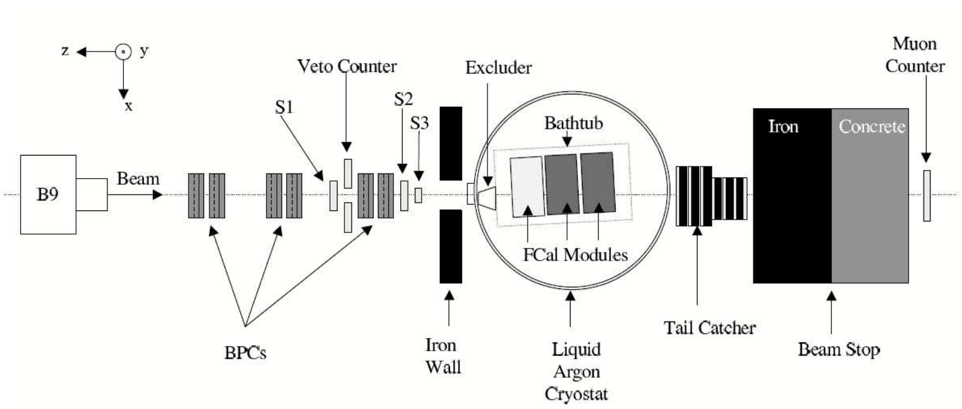

Figure 4.1: Diagram showing the setup used for the 2003 FCal beam test (not to scale).

from the EMEC testbeam [65, 66] and purpose-built HEC modules. The remainder of this chapter will focus exclusively on the 2003 beam test.

The 2003 testbeam studies were carried out in the H6 beamline at CERN, which is fed by the SPS. Protons from the SPS were directed at fixed targets in order to produce secondary beams of the desired particles (electrons/positrons or charged pions) at the available energies (10-200 GeV).

A diagram of the beamline is shown in Figure 4.1. Beam particles emerge from the B9 magnet, travelling a distance of 32 metres and passing through several sets of instruments before reaching the FCal. The B9 magnet was used to control the vertical inclination of the beam, and thus the vertical position of the beamspot on the FCal face. The cryostat containing the FCal was able to be translated horizontally and rotated slightly, providing control over the horizontal position of the beamspot and the angle at which the beam particles struck the front face of the calorimeter. A total of 5 beamspots were used, labelled 1,2,3, 4L and 4H, as illustrated in Figure 4.2. Positions 1,2 and 3 were used to study the effects of energy leakage down the beampipe from particles impacting close to the inner edge of the detector. High energy (∼200 GeV) beams of electrons and pions were used to provide data at these positions, and the results of these studies can be found in [67, 68]. Position 4L was used to study the intrinsic response of the FCal

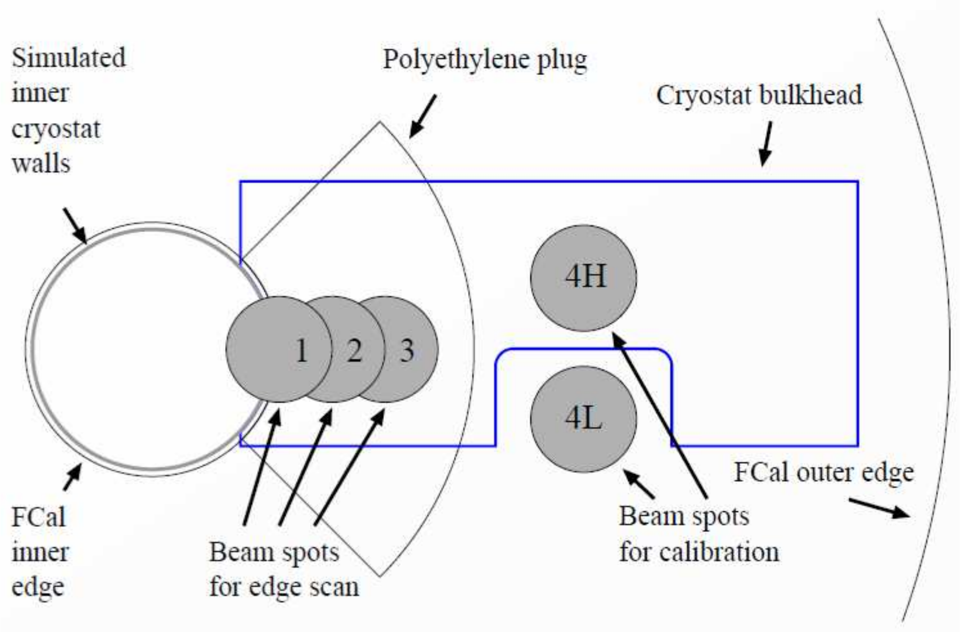

Figure 4.2: Beamspots studied in the testbeam.

with a minimal amount of material between the calorimeter and the incoming particles, whereas position 4H was used to simulate a more `ATLAS`-like environment with additional dead (i.e. uninstrumented) material introduced into the beamline. Electrons and pions at energies from 10-200 GeV were used at these beamspots. This chapter will discuss the analysis of data taken at positions 4L and 4H, and the comparison of these results to those obtained from Monte Carlo simulations carried out using the `ATLAS` software framework, `Athena`, and `GEANT4`, which simulates the interactions of the beam particles with the calorimeter.

4.2 Beamline Instrumentation

Eight beam positioning chambers (BPCs) were used to provide tracking information on beam particles. Four of these BPCs were of a more sophisticated design, one pair of which was located about 1.6 metres downstream of the B9 magnet while the other pair was situated 3 metres upstream of the FCal, on an adjustable table described below.

These chambers each contain two readout planes, oriented at right angles such that measurements of both transverse coordinates may be made. Each readout plane covered an area of 120mm × 120mm, and had an average resolution of around 130 μm. The other four BPCs were of an older design and were able to measure a single track coordinate with a resolution of about 325 μm. These were positioned in the middle of the beamline (about 20m from the FCal), with two BPCs measuring the x coordinate of the beam particles and the other two the y coordinate. In total, the eight BPCs provide six independent measurements of the x and y coordinates of the beam particle tracks.

A mapping between BPC and calorimeter coordinate systems was established through analysis of electron data [69]. The track measured by the BPCs was projected on to the calorimeter in order to obtain the beam impact point in the BPC coordinate system. This was then associated with the barycentre of the energy deposited in FCal1 using the calorimeter coordinate system. However, the finite granularity of the calorimeter readout tended to bias the position of the energy barycentres towards the centre of the readout cells. This mapping was improved by considering the ratio E_{max}/E_1, where E_1 was the total energy deposited in FCal1 and E_{max} was the largest energy value contained in a single channel. This ratio was plotted as a function of (BPC) x and y, with minimal values in the ratio corresponding to cases where energy was shared evenly between multiple channels. The positions of the minima could thus be associated with cell boundaries in the calorimeter coordinate system, which then allowed the mapping between BPC and calorimeter coordinate systems to be determined with greater precision. The uncertainty associated with this mapping is ±0.12 mm in the x coordinate and ±0.25mm in the y coordinate [67].

The adjustable table was positioned about 2 metres upstream from the cryostat, on which three scintillators (S1, S2, S3) were positioned. These scintillators were polystyrene-based, and were used for triggering and “beam cleaning”, which is discussed in Section 4.4. All three scintillators were 1 cm thick, with S1 and S2 having cross-sectional dimensions

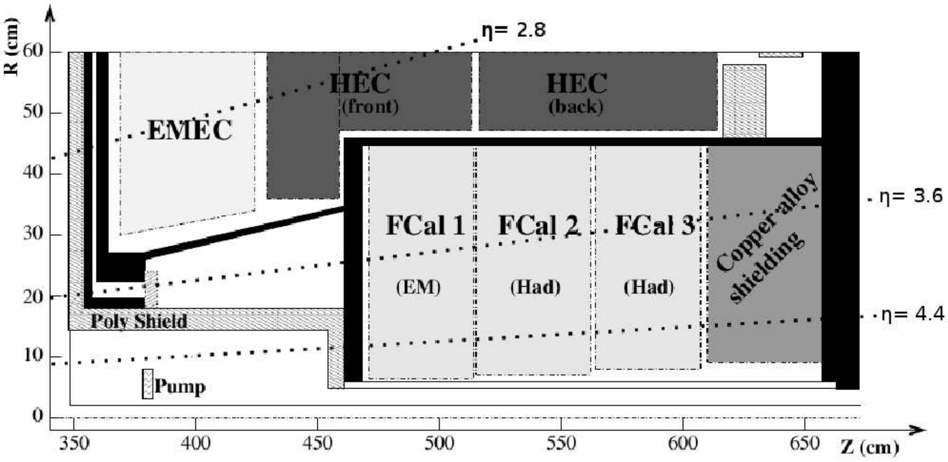

Figure 4.3: Cross-section of FCal positioned within the end-cap cryostat, showing the inactive material present in this region. The material in black is associated with the end-cap cryostat.

of 10cm × 10cm, while S3 had dimensions 7cm × 7cm. A veto counter was also present on the table, consisting of rectangular piece of scintillator (63cm × 63cm × 5cm) with a circular hole 65mm in diameter that the beam passed through. The height of the table could be varied such that the beam instruments were in the appropriate position for the beamspot under study.

As the liquid argon gaps in the FCal are much smaller than those used in typical liquid argon calorimeters, FCal channels are susceptible to shorts should any conductive debris find its way into the liquid argon. Because it was particularly difficult to clean the interior of the cryostat, the FCal was housed inside a "bathtub" which sat inside the cryostat. This was made from stainless steel 1.5 mm thick, and had a rectangular shape. Holes were present on its sides to allow the liquid argon to flow in as the cryostat was filled, but these were covered with a fine mesh to keep any debris out.

In order to simulate a more ATLAS-like environment for data taken at positions 1,2,3 and 4H, additional material was inserted into the beamline. A cross-section of part of the ATLAS end-cap is shown in Figure 4.3, showing the uninstrumented (or "dead") material present in this region. An aluminium plate 50.8 mm thick was bolted to the inside of the bathtub to model the cryostat bulkhead (i.e. the cryostat material located just in front of FCal1 in Figure 4.3), with a slot cut out of the plate such that the material would not affect beams at position 4L. The area covered by this plate is labelled as “Cryostat bulkhead” in Figure 4.2.

The `ATLAS` JM shielding [31] (labelled “Poly Shield” in Figure 4.3) is made of boronated polyethylene and is present in `ATLAS` to prevent albedo radiation from scattering back into the inner detector. This was modelled in the beam test by placing a wedge shaped piece of polyethylene on the outside of the bathtub such that it covered positions 1, 2, and 3, simulating the toroidal “plug” part of the shielding that lies close to the beam pipe and adjacent to the cryostat bulkhead. Figure 4.4 shows a photograph of the bathtub with this polyethylene attached to its exterior wall. An iron wall was located between the adjustable table and the cryostat. This wall had a 10cm x 10cm slot cut into it to allow the beam to pass through. When taking data at position 4H, a rectangular piece of polyethylene with dimensions 5 cm × 20 cm × 1 m was placed at an angle in this slot. This was done in order to model the tube shaped part of the JM shielding that runs parallel to the beam axis. When running at position 1, a small piece of aluminium was instead placed in this slot, simulating the ion pump present close to the beampipe in `ATLAS` (labelled “Pump” in Figure 4.3).

In `ATLAS`, the area within the cone-shaped part of the FCal support tube (just in front of the FCal, as shown in Figures 4.3 and 3.12) is evacuated. The support tube used in `ATLAS` was not present during the testbeam, and the FCal modules were instead mounted on a purpose-built stand within the cryostat. An “excluder” made of RohaCell was attached to the outside of the bathtub, in order to prevent the region of space corresponding to the evacuated region in `ATLAS` from being filled with liquid argon. The density of RohaCell is 0.011 g/cm^3 whereas that of liquid argon is 1.43 g/cm^3, so the RohaCell provides a relatively good approximation of a vacuum. A hollow stainless steel cylinder was also placed inside the FCal during the beam test to simulate the beampipe,

Figure 4.4: Photograph of the FCal being lowered into the bathtub used for the beam test. The polyethylene used to simulate the plug portion of the ATLAS JM shielding is visible on the front of the bathtub, while the summing boards can be seen on the left side.

and also to exclude liquid argon from this region.

Note that in `ATLAS`, there is additional material upstream of the FCal that has not been considered here. The additional material described above was intended to model only the upstream material associated with the end-cap cryostat and the JM shielding. At the time of the beam test, the amount of material associated with the inner detector and its services was not well known, and so no attempt was made to simulate it. However, in `ATLAS`, particles reaching the FCal will first have to pass through this material.

A tail-catcher calorimeter comprised of layers of steel and scintillator was positioned downstream of the cryostat. Behind this was a beamstop of iron and concrete, and beyond that a muon counter was located. The tail-catcher and muon counter were only used for muon identification: energy deposited in the tail catcher was not considered when measuring the response of the FCal, or in the derivation of any weights used for hadronic reconstruction in the analysis presented here.

A CEDAR (Cherenkov Differential counter with Achromatic Ring focus, [70]) detector was located upstream of the B9 magnet and used for particle identification. The CEDAR detector consists of a chamber filled with gas (He) at high pressure. As beam particles pass through this chamber, they emit Cherenkov radiation at an angle that depends on their velocity and mass. The optics of the CEDAR collect this light and focus it into a ring-shaped image, with different types of particles giving rings of different radii. An adjustable annular aperture is positioned in front of a series of photomultipliers, such that these detect light only from rings of a given radius. The radius selected by the aperture may be tuned such that signal from the photomultipliers corresponds to a beam particle of the desired mass.

4.2.1 Timing and Pulse Shapes

Reconstruction of the calorimeter signals was carried out using the OFC method described in Section 3.2.6.3. Pulse shapes were sampled in time with the TTC clock on the FEBs (described in Section 3.2.6.1). Seven samples were recorded for each pulse during physics runs, with the timing adjusted such that, on average, the fourth sample was coincident with the pulse peak. The first sample could thus be used to monitor noise, as it was recorded before the signal pulse started to rise. In `ATLAS` the TTC system is synchronised to the LHC clock, such that samples are taken in time with each bunch crossing. This was not the case during the beam test, as beam particles arrived at random times with respect to the TTC clock. Timing for the event was taken from the S1 scintillator. A LeCroy 2228A Time to Digital Converter (TDC) with a timing resolution of 50 ps was used to measure the phase difference between the event trigger and the TTC clock, with the trigger from the S1 scintillator used as a start signal and the clock pulse from the TTC system used as a stop signal. The TDC only measured a phase difference between the start and stop signals, and so readings close to 0 or 25 ns were ambiguous. To resolve this a second TDC was used in which the stop signal was delayed by 10 ns, which allowed the time interval between the beam trigger and the TTC pulse to be determined uniquely.

While the OFC method is capable of handling time differences between pulse peaks and sample times, the Taylor expansion used in equation 3.10 becomes invalid when this time, τ, becomes large. To avoid this issue, events are binned according to the phase time measured by the TDC, using 25 bins of width 1 ns. A set of OFCs is calculated for each bin using a pulse shape that has been shifted in time by the relevant amount. During event reconstruction, the amplitude of each pulse is obtained by using the set of OFCs corresponding to the TDC phase time for that event. Only a single set of OFCs is required at `ATLAS`, as in this case the TTC clocks are synchronised with that of the LHC, and so the samples are recorded in time with the LHC clock.

4.2.2 Offline Reconstruction

Offline reconstruction of the beam test data is carried out using `Athena`. A flowchart depicting the data structures and algorithms used in the reconstruction of data and simulation events is shown in Figure 4.5. For each event, the LArRawChannelBuilder algorithm retrieves the pulse samples (which are stored as LArDigits), and fetches the appropriate set of OFCs from a database. The pedestal is then subtracted from these samples and the OFCs are applied, giving the amplitude of the pulse in ADC counts. This amplitude is then converted to an energy using a factor (the ADC2MeV value discussed in Section 3.2.6.4) that depends on the channel and gain. The energy of the channel, in MeV, is then stored as a LArRawChannel object. Another algorithm is then used to create a CaloCell object from this LArRawChannel. From the CaloCell, the position, time, energy, quality, and four-momentum of the channel may be retrieved, making CaloCells suitable objects for use in data analysis. Because of this, CaloCell information is recorded by default in Event Summary Data (ESD) files, one of the standard file formats used by `ATLAS`. CaloCells are also used as input during the formation of topological clusters (discussed in Section 4.6), which in turn are used as input for jet-finding and missing-energy algorithms.

For initial studies of the testbeam data, the ADC2MeV factors used in the reconstruction were set to 1, so that the final energies were obtained in terms of ADC counts. This was done so that the actual ADC2MeV values could be extracted from the data more easily. However, the LArRawChannel class used in `Athena` stores channel energies as an integer number of MeV, as energies less than 1 MeV are deemed insignificant. An unforeseen consequence of this was that in earlier versions of the testbeam analysis, cell energies were truncated (rounded down) to an integer number of ADC counts. This rounding meant that energy was effectively lost during the reconstruction process, up to ∼80 MeV per cell in FCal1 and ∼160 (∼185) MeV in FCal2 (FCal3). This had a small effect on the electron results, but a more significant effect on the hadron results due to

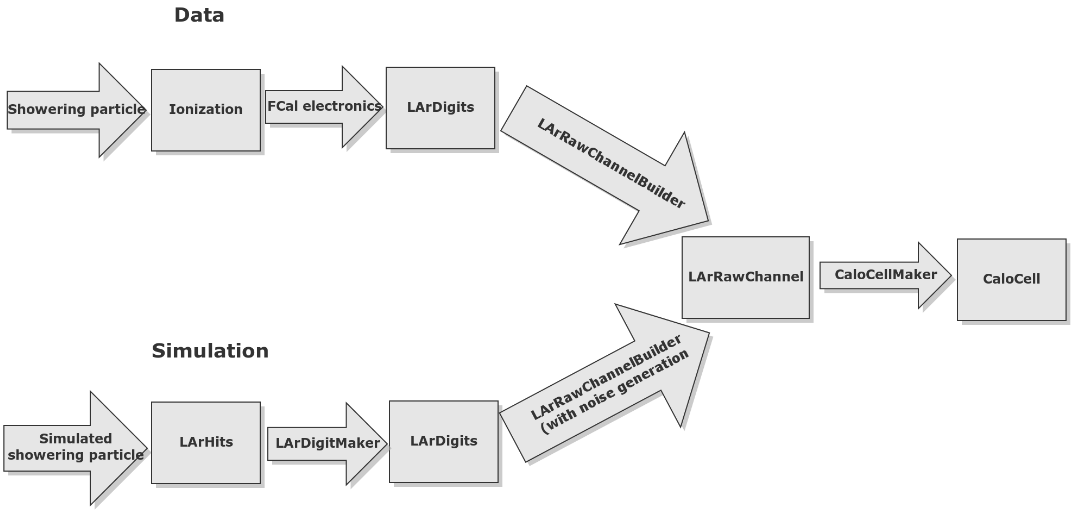

Figure 4.5: Flowchart showing the processes/algorithms and data structures involved in the reconstruction of testbeam data and simulation results.

the broader showers and higher ADC2MeV factors associated with the hadronic modules. The bug has since been fixed, and none of the results presented here are affected by it. The effect that this bug had on the previously published results [69] was small, and will be discussed further later in this chapter.

4.3 Monte Carlo Simulation

A Monte Carlo simulation of the testbeam setup has been developed within the `Athena` framework. `GEANT4.9.2` [71] is used to simulate interactions of the beam particles with beamline elements and the calorimeter. The results of this simulation are then reconstructed and analysed in the same manner as the data. The forward calorimeter beam test provides a clean environment in which the results from data may be compared to those obtained from simulations. As all of the hadronic calibration schemes used at `ATLAS` are derived from Monte Carlo, it is important to understand the how well these simulations agree with data.

4.3.1 GEANT4 Simulation of the Forward Calorimeter Beam Test

Geometry in `GEANT4` is described in terms of volumes. A "solid volume" is first created to describe the shape of a given object. This is then used to derive a logical volume, which inherits the shape of the solid and is associated with a material. A material type is defined by specifying the relative mass fractions of its constituent elements and the density of the material. Logical volumes are then used to construct physical volumes, which inherit the shape and material information from the logical volume. A physical volume also has a position and orientation assigned to it, and it is by positioning these physical volumes that the geometry of the simulation is defined. A special physical volume, the world volume, is created first. All subsequent physical volumes are then placed either inside the world, or inside another physical volume.

The description of the beamline used in the simulation contains all beamline elements downstream of the B9 magnet, including all scintillators, BPCs, cryostat material, beampipes, the tailcatcher and the muon counter. Most of these objects are defined from scratch, however the description of the FCal is taken from that used in the full `ATLAS` simulation (although this is modified slightly as discussed below), while the H6 cryostat description has been taken from another testbeam simulation. Elements upstream of the B9 magnet, such as the CEDAR detector, have not been included. The scintillators and BPCs that are included in the simulation are only treated as dead material, no (simulated) signals are obtained from them.

Small modifications to the FCal definition used in the simulation were made in order to improve some aspects of the material description. In the default definition of the FCal, WFeNi is the material used for the rods in the hadronic modules, whereas they are actually made of pure tungsten which has a slightly higher density. The correct materials and densities (given in Section 3.2.6) have been used in the testbeam simulation.

In `GEANT4`, physics is defined in terms of processes. Particles are propagated through the simulation in a step-by-step fashion, with continuous processes (such as ionisation) acting on the particle during the step while discrete processes (such as decays, pair production) take place at the end of a step. After each step, the particle's kinematics are updated. Secondary particles are only produced if their energy exceeds a "range cut": if a process would produce a secondary particle with energy less than the range cut, this energy is instead deposited in the material. Range cuts are specified as a distance, but `GEANT4` converts this distance to an energy based on the material the particle is travelling through at the time. A range cut of 30μm has been used for testbeam simulations, and is also used in full `ATLAS` simulations involving the FCal. This value is appropriate given the narrow width of the active liquid argon gaps. In the full simulation of the `ATLAS` detector, range cuts of 100μm are used in the EM barrel and EMEC calorimeters, while a cut value of 1mm is used in the HEC.

Electromagnetic showers are generally well understood and relatively straightforward to model. Hadronic showers are more complex, and a variety of processes are used to describe the shower development. Hadronic "physics lists" are used to define the specific set of processes available and the energy ranges in which they are used. Three physics lists have been used in the simulation of the test beam, and are outlined below:

- QGSP_BERT: Quark Gluon String Precompound with Bertini cascade. This is the default physics list used for `ATLAS` simulations. The Quark Gluon String model [72] is used to simulate hard inelastic scattering for hadrons with energies from 12 GeV to 100 TeV. One or more strings are formed between between partons of the colliding hadrons, one of which belongs to a nucleus in the material while the other is a hadron in the shower. These strings are then "cut" by inserting quark/anti-quark pairs. One member of the pair becomes the new "end" of the string, while the other forms a hadron with the parton that was the old end. This process repeats until the string has insufficient energy to form new pairs. The precompound model is then used to de-excite what remains of the nucleus. Between 9.5 and 25 GeV, a Low Energy parameterisation (LEP) is used to describe inelastic scattering [73]. For particles with energy less than 10 GeV, a Bertini intra-nuclear cascade model [74, 75] is used to describe inelastic scattering with nuclei. The incoming hadron is classically scattered within the nucleus, using cross-sections and angular distributions taken from experiment.

- QGSP_BERT_HP: This physics list is essentially the same as QGSP_BERT, but includes high precision modelling for low energy neutrons (<20 MeV). This method relies extensively on cross-sections obtained from experiment. It was reported in [76] that the high precision neutron tracking had a significant effect on the development of hadronic showers in tungsten, and so it was considered worthwhile to investigate this physics list.

- FTFP_BERT: This physics list uses the Fritiof string model [77] to model high energy inelastic interactions. The Fritiof model can be applied over a wide range of energies, and is used for hadrons with energies between 4 GeV and 100TeV. As with the QGSP_BERT physics list, the precompound model is used to de-excite the nucleus following the Fritiof interaction. The Bertini Cascade model is also used at energies below 5 GeV.

4.3.2 Reconstruction of Simulation Results

The reconstruction chain used for Monte Carlo simulations is, with a few exceptions, the same as that used for reconstruction of testbeam data. In `GEANT4`, when a showering particle deposits energy through ionisation in a liquid argon gap, a "hit" is produced. The hit describes the size, time and location of the energy deposited in the liquid argon. A digitisation step then collects these hits and simulates the electronics chain to in order to produce digitised samples of the pulse shape, which are again stored as LArDigits.

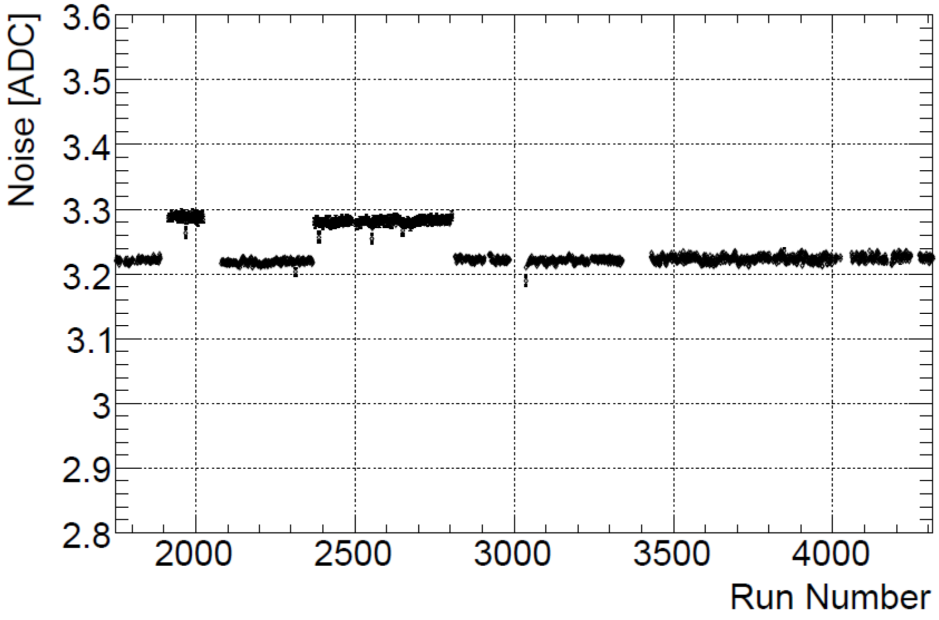

Figure 4.6: Plot showing variation in the pedestal RMS, as a function of run number (covering the full duration of the beam test). The pedestal RMS is an indication of the level of noise present in the electronics, showing that this varied with time.

These are then processed into LArRawChannels and CaloCells in the same manner as is used for data, as shown in Figure 4.5.

Electronic noise must also be modelled in the simulation. For the FCal, most of this noise arises in the preamplifiers on the FEBs. Noise can be quantified by studying the RMS of the pedestal values, which gives a value of 3.2 ADC counts per sample* when averaged over all channels and all runs. In addition to physics data, some randomly triggered events were recorded during data taking, in between spills. The data taken by these random triggers is essentially all noise, and allows correlations in the noise between channels to be studied.

The default method for modelling noise in the simulation is done during the digitisation step, where the autocorrelation matrix for the noise is retrieved from a database. It

---

*Note that this value is specific to the electronics used for the testbeam. The preamplifiers used in `ATLAS` are of a slightly different design, and thus have a different level of noise.

is then used to randomly generate the noise contributions that are added to each sample. However, during data taking, the level of electronic noise present was seen to vary, as is shown in Figure 4.6. After the second period of high noise, the source of the problem was discovered and fixed. However, data for different beam configurations (i.e. particle type/beam energy/beamspot location) were taken at various times, so the average noise present for data taken with a given beam configuration (e.g. 200GeV pions at 4L) differs from that present in data taken with a different beam configuration (e.g. 10 GeV pions at 4L). To account for this effect in the simulation, randomly triggered data (taken from the same runs as the physics data) are used to determine the amount of noise that is added into the simulation, using a procedure that will be discussed below. This method allows different beam configurations to be simulated with different levels of noise, whereas the default method of noise generation would apply the same level of noise to all simulation results, and this noise would not include correlations between channels.

4.3.3 Noise Generation and Application

The noise added into the simulation is derived from the randomly triggered data. A covariance matrix is generated by running over the randomly triggered data taken with a specific beam configuration (e.g. 200 GeV pions at position 4L), such that

$$M_{ij} = \frac{1}{N_{\text{events}}} \sum_{n}^{N_{\text{events}}} e_{i,n}\, e_{j,n} \tag{4.1}$$

where $e_{i,n}$ is the noise reconstructed from the i-th channel of the n-th event, in ADC counts. The matrix M_{ij} is then diagonalised, such that it can be written as

$$\mathbf{M} = \mathbf{U}^T\, \mathbf{D}\, \mathbf{U} \tag{4.2}$$

where $\mathbf{U}$ is a unitary matrix with columns equal to the eigenvectors of $\mathbf{M}$, and $\mathbf{D}$ is a diagonal matrix which has the eigenvalues of $\mathbf{M}$ as its entries. The matrix $\mathbf{U}^T$ thus acts as a transformation matrix, transforming information from the "channel" basis to the eigenvector basis. The eigenvectors and eigenvalues are written to a file, and then retrieved during the reconstruction.

The noise is applied in the LArRawChannelBuilder algorithm, after the pulse peak has been found through application of the OFCs. The matrix elements U_{ij} and eigenvalues D_{ii} are first read from file. For each event a vector of noise, N_i is then generated. This is done in the eigenvector basis using a normal distribution, such that $\sigma(N_i) = D_{ii}$. This noise is then transformed back into channel basis, such that

$$N'_i = \sum_j U_{ij}\, N_j \tag{4.3}$$

which builds in all the correlations between channels. The noise N'_i is then added to the reconstructed pulse peak of the i-th channel.

The default method relies on an autocorrelation matrix, such that a correlations between samples are present but each channel is considered independently. The alternative method described above avoids dealing with the noise on individual samples and instead considers the total noise on the reconstructed pulse peak, while also incorporating correlations in the noise between different channels. These correlations are significant, as without them the estimations of the noise contribution in a given cluster are too low. This is important when studying the energy resolution of the FCal, which will be discussed later.

4.4 Event Selection

The three scintillators located on the adjustable table (labelled S1, S2, and S3 in Figure 4.1) were used for triggering. Coincident signals were required from all three in order for the event to be accepted. Any signal from the veto counter indicated that the beam particle had scattered off the upstream material, and in these cases the event was rejected. When analysing data taken from electron beams, events were rejected if there was any signal in either the tail-catcher or the muon counter, as this implied that a muon was present in the event. Showering electrons should have been fully contained within the FCal, so any energy present in the tail-catcher was attributed to muons. It is possible for muons to be produced during hadronic showers, and so these cuts were not applied to data taken from pion beams.

A series of “Beam Cleaning” cuts were also applied, which used information from the scintillators as well as the BPCs. These are intended to remove events in which multiple beam particles were present and events in which the beam particle had scattered off the upstream material. In order to remove events in which multiple particles were present, the signal from each scintillator was compared to that expected for a minimum ionising particle (MIP). If a single scintillator produced a signal consistent with 5 times that of a MIP, or at least two scintillators gave signals over twice the MIP threshold, the event was rejected.

While the primary purpose of the BPCs was to provide tracking information on the beam particles, they were also used in the beam cleaning in a similar way to the scintillators. A key feature of MWPCs is that the total charge arriving at an anode is proportional to the total number of electron-ion pairs produced in the chamber, and from this the number of ionising particles that passed through the active areas could be inferred. Events were rejected if a single BPC produced a signal five times greater than that expected for a single MIP, or if at least two BPCs generated a signal twice that expected for a single MIP.

Particle tracks were reconstructed by performing a linear fit to the data from the BPCs. The $x-z$ and $y-z$ planes were reconstructed separately, with the BPCs providing six measurements of the track in each plane. If the sum of the χ^2 values for these fits exceeded 40.0 (for 8 degrees of freedom), the event was rejected. The reconstructed tracks were then used to define "beam-envelope" cuts, which were intended to remove events containing undesired particles. The beams delivered to the testing area were not completely pure, and so hadrons were sometimes present in the electron beams and protons sometimes present in the pion beams. The magnet systems in the H6 beamline tended to separate electrons and hadrons into different areas of phase space, due to differences in their charge to mass ratios. The x intercept of the track, c_x, was measured using the BPC closest to the FCal ("BPC 5"). This intercept was then used to determine an "ideal" slope in the $x-z$ plane for the desired particle type, $m_{x,\text{ideal}}(c_x)$, as well as a width parameter, $\Delta m_x(c_x)$. Similarly, the intercept c_y, was used to define an ideal slope, $m_{y,\text{ideal}}(c_y)$, and width, $\Delta m_y(c_y)$, in the $y-z$ plane. The quantity

$$\Delta S = \left(\left(\frac{m_{x,\text{ideal}}(c_x) - m_{x,\text{measured}}}{\Delta m_x(c_x)} \right)^2 + \left(\frac{m_{y,\text{ideal}}(c_x) - m_{y,\text{measured}}}{\Delta m_y(c_y)} \right)^2 \right)^{1/2} \tag{4.4}$$

was then calculated, where $m_{x,\text{measured}}$ and $m_{y,\text{measured}}$ are the measured track slopes in the x and y directions, respectively. The quantity ΔS describes how much the measured track direction deviates from the ideal track direction for the desired particle type. If ΔS exceeded a specified threshold (1.25 in this analysis), the measured track was deemed to lie outside the beam-envelope for the desired particle type, and the event was rejected.

As mentioned in Section 4.2.1, two TDCs were used to measure the time interval between the trigger signal and the clock pulse from the TTC, at which time the signals from the calorimeter were sampled. Output from the TDC is given as an integer number of TDC counts, between ~ 300 and ~ 800, which covers a time interval of 25 ns and thus gives the TDC a time resolution of 50 ps. There are three regions where a mismeasurement of the TDC can be problematic: near the TDC's minimum value, its maximum value, and in the "wrap-around" region. The wrap-around point is where the phase jump occurs, such that the time interval measured by a TDC jumps suddenly from 0 ns to 25 ns. The TDC phase quality is defined as the smallest difference between the TDC reading and one of the problematic regions. Event timing was determined using the TDC which had the highest phase quality. Events were rejected in cases where the readout from the highest quality TDC was within 1 ns of a problematic region.

The CEDAR detector (described in Section 4.2) was also used to improve the beam purity. It was mainly used to eliminate proton events when analysing data taken with π^+ beams, by rejecting events containing beam particles that the CEDAR did not identify as charged pions. However, the CEDAR information was also used when analysing electron data at 60 GeV, as the electron beams had a low purity at this energy.

4.5 Results Obtained Using Cylindrical Cell Clustering

4.5.1 Analysis of Electron Data

Using the tracking information from the BPCs, the point at which the beam particles strike the front face of the calorimeter can be determined (with accuracy on the order of 1 mm). Cylindrical clusters are then formed by collecting all cells within a certain distance of the impact point. For the analysis of data taken with electron beams, only calorimeter cells in FCal1 are considered. For the analysis of data taken with hadron beams, calorimeter cells from all three FCal modules are included in the cylindrical cluster. As the FCal was oriented at an angle with respect to the incoming beam particles, the beam particle track is projected through the FCal to give a slightly different impact point for each module. This impact point changes by $\sim$ 2cm between neighbouring modules.

On average, about 80-90% of the energy deposited by an electromagnetic shower is contained within a cylinder of radius ρ_M (the Molière radius). In FCal1 the Molière radius is about 17 mm, and $\sim 99\%$ of the energy is contained within a cylindrical cluster of radius 8 cm, as can be seen in Figure 4.7. Clusters with radii 12 cm and 16 cm are also generated during event reconstruction. These larger clusters capture about 1% more energy than the 8 cm cluster, however the noise contained within the cluster increases by $\sim 50\%$ at a radius of 12 cm and $\sim 100\%$ at a radius of 16 cm. For this reason 8 cm clusters are used in the analysis of electron data. Note that both positron and electron beams were available during the beam test. No distinction was made between these particles during this analysis, and so both particles will be referred to as "electrons" in this Section*.

The energy reconstructed for a given particle has some dependence on the position at which that particle impacts the calorimeter, as an electron striking the centre of an electrode rod deposits less visible energy in the calorimeter than one that hits close to the liquid argon gap [60, 63]. As the diameter of the beamspot (65 mm) is an order of magnitude larger than the spacing between adjacent electrodes (7.5 mm in FCal1), many different impact points are sampled. This leads to a non-Gaussian distribution in the response, as this is essentially the sum of many different Gaussian distributions. A good fit to the data is obtained using a double Gaussian function,

$$F(E) = a_0 \exp\left(-\frac{(E-a_1)^2}{2a_2^2}\right) + a_3 \exp\left(-\frac{(E-a_4)^2}{2a_5^2}\right) \tag{4.5}$$

where the parameters a_0 and a_3 describe the amplitudes, a_1 and a_4 describe the means, and a_2 and a_5 describe the widths of the component Gaussians. When fitting the response distributions with the double Gaussian, some constraints are imposed on the parameters.

---

*The distinction between electrons and positrons is made later in this Section during some of the discussion on systematic effects, but this is the only case in which they are treated separately

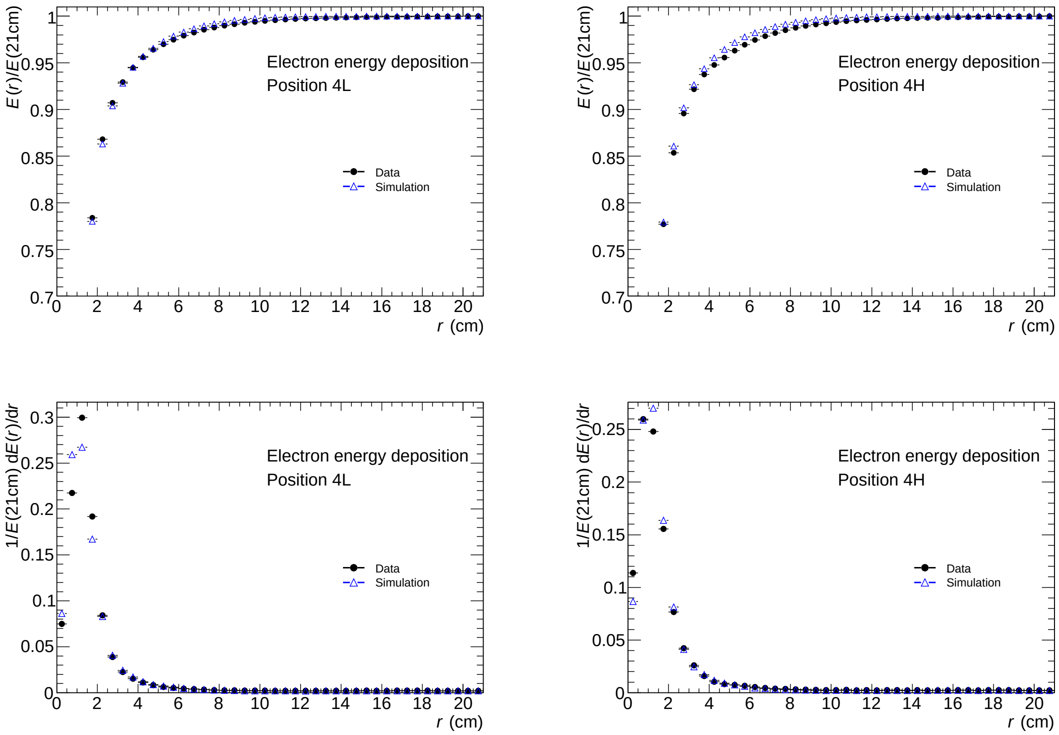

Figure 4.7: Fraction of energy contained within a cylinder of radius r centred on the beam impact point. Figures (a) and (b) show the fraction of energy contained within a cylinder of radius r compared to a cylinder of radius 21cm, for showers initiated by 193.1 GeV electrons at position 4L and 4H, respectively. Figures (c) and (d) show the fractional energy deposited between r and $r + \mathrm{d}r$ as a function of r, for position 4L and 4H respectively. The value of 21cm was chosen because as cylinders of larger radii are not entirely contained within the FCal.

The non-Gaussian shape of the response is determined by the geometry of the calorimeter, as this determines which impact points are closer to a liquid argon gap (yielding a higher response), and which impact points are further from the gap (giving a lower response). This suggests that the shape of the response should be independent of the beam energy, which allows some constraints to be imposed on the fit parameters in equation 4.5. The ratios of the populations and the means of the two Gaussians are held fixed, such that

$$\frac{a_0 a_2}{a_3 a_5} = C_1 \tag{4.6}$$

$$\frac{a_1}{a_4} = C_2, \tag{4.7}$$

where C_1 and C_2 are constants obtained from an unconstrained double Gaussian fit on the 193 GeV electron data (or 200 GeV hadron data). These values are then used to apply constrained fits to the responses at lower beam energies. The constrained fits tend to have better agreement with the peak of the distribution, and so these have been used to obtain the results presented in this chapter, though the unconstrained fits have been considered in systematic studies.

The mean response, $\bar{E}$, is taken as the first moment of $F(E)$, where the i-th moment, μ_i, is given by

$$\mu_i = \frac{\int_{E_{\mathrm{min}}}^{E_{\mathrm{max}}} E^i F(E)\mathrm{d}E}{\int_{E_{\mathrm{min}}}^{E_{\mathrm{max}}} F(E)\mathrm{d}E}, \tag{4.8}$$

where the limits of the integral, E_{min} and E_{max}, are obtained from the response histogram. The lower limit, E_{min}, is taken from the low edge of the lowest energy bin that is not empty, while E_{max} is the upper edge of the highest non-empty histogram bin.

The width of the response, σ, is determined from the first and second moments of $F(E)$, such that

$$\sigma = \left(\mu_2 - \mu_1^2\right)^{1/2}. \tag{4.9}$$

Statistical uncertainties on these quantities may be written in terms of higher order moments. However, for simplicity, a (single) Gaussian fit is made to the response, and the moments of this Gaussian are used to compute the statistical uncertainties. The statistical uncertainties on $\bar{E}$ and σ are then

$$\begin{aligned} \Delta\bar{E} = \Delta\mu_1 &= \frac{\sigma_g}{\sqrt{N_g}} && (4.10) \\ \Delta\sigma &= \frac{\sigma_g}{\sqrt{2N_g}}, && (4.11) \end{aligned}$$

where σ_g and N_g are the width and population from the (single) Gaussian fit.

The response of the FCal to electrons (for all beam energies) is plotted in Figures 4.8 and 4.9, for positions 4L and 4H, respectively. The results of the fits to these distributions are summarised in Tables 4.1 and 4.2.

A double Gaussian is fit to the electron peak in the response distribution. While the beam envelope cuts improve the purity of the electron sample, some of these events still contain showers initiated by hadrons. Hadronic showers are broader then EM showers (and so are not contained within 8 cm clusters), and not all of the energy they deposit is visible to the calorimeter (as discussed in Section 3.2.4.3). The response to hadrons is thus lower than that for electrons. The response plots in Figures 4.8 and 4.9 contain some events at lower energy due to the hadron contamination in addition to the higher energy peak corresponding to the electron response. The high tail of the hadron distribution overlaps with the low tail of the electron peak, and so this effect is accounted for when analysing the data. This is accomplished by using data taken from hadron runs to model this tail in the electron response. The total function fitted to the distributions shown in Figure 4.8 is given by

$$G(E) = F(E) + w\, H_{\pi}(E), \tag{4.12}$$

where $F(E)$ is the double Gaussian function described in equation 4.5. The "function" $H_{\pi}(E)$ is derived from data taken during pion runs at (approximately) the same beam energy. Cylindrical clusters with radius 8 cm are formed for each pion event, and used to fill a histogram with the same binning as is used for the electron response. The energy E is then converted to a bin number, and the number of entries in this bin is taken as the value of $H_{\pi}(E)$. The parameter w corresponds to a normalisation for the hadron data and is allowed to freely vary in the fitting. The parameters of the double Gaussian are also allowed to vary, but are subject to the constraints in equations 4.6 and 4.7.

The effects of the electronics noise are estimated by creating clusters from randomly triggered events ("random events"), which are recorded in the absence of any beam particles. Each physics event is associated with a random event obtained from the same run. The beam impact point from the physics event is used to form a cylindrical cluster in the random event as well as the physics event, such that the same calorimeter cells are

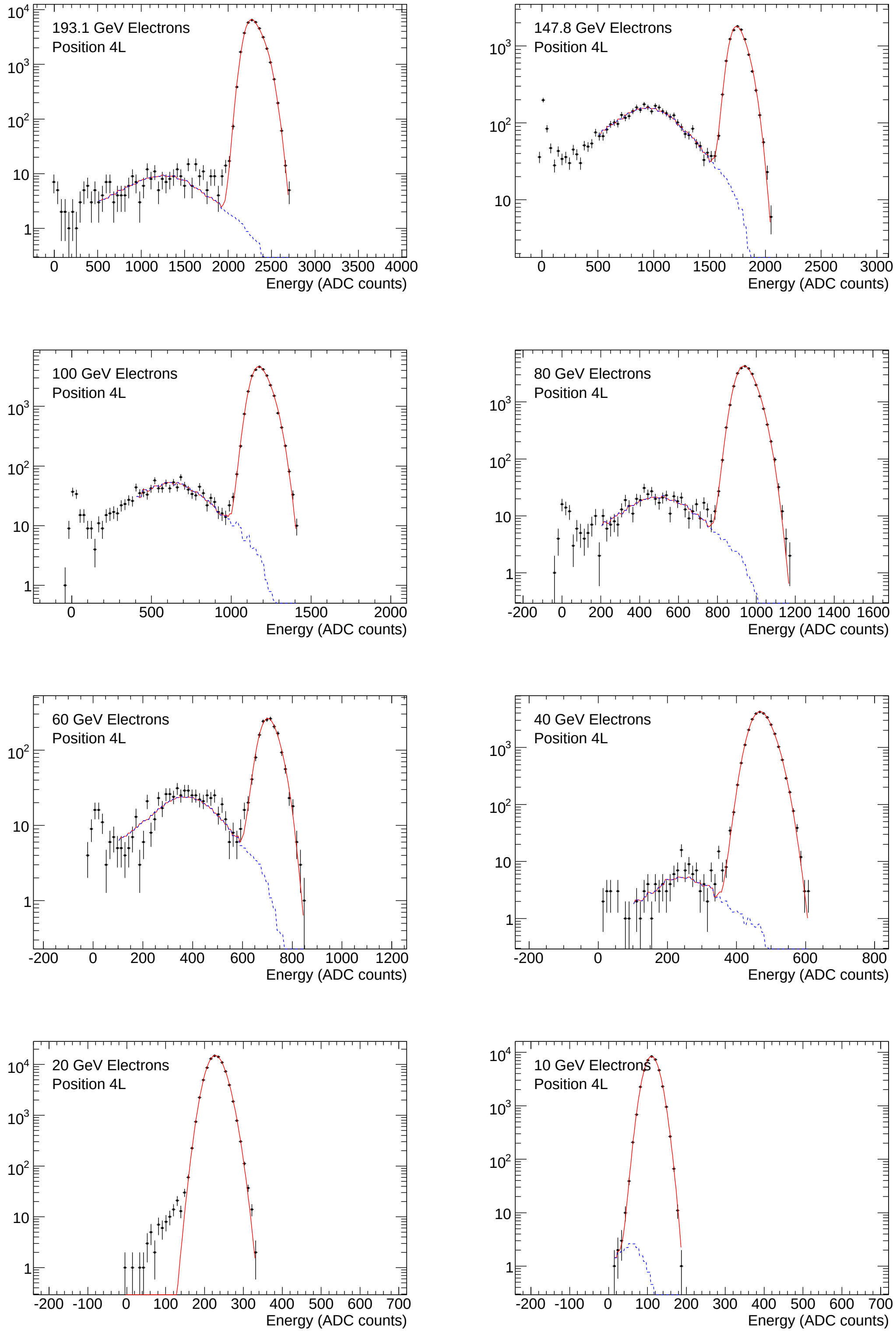

Figure 4.8: Response of the FCal to electrons at position 4L. The red curve is the total fit to the data, which consists of a double Gaussian fit to the electron peak as well as the fit to the hadron contribution (blue dashed line).

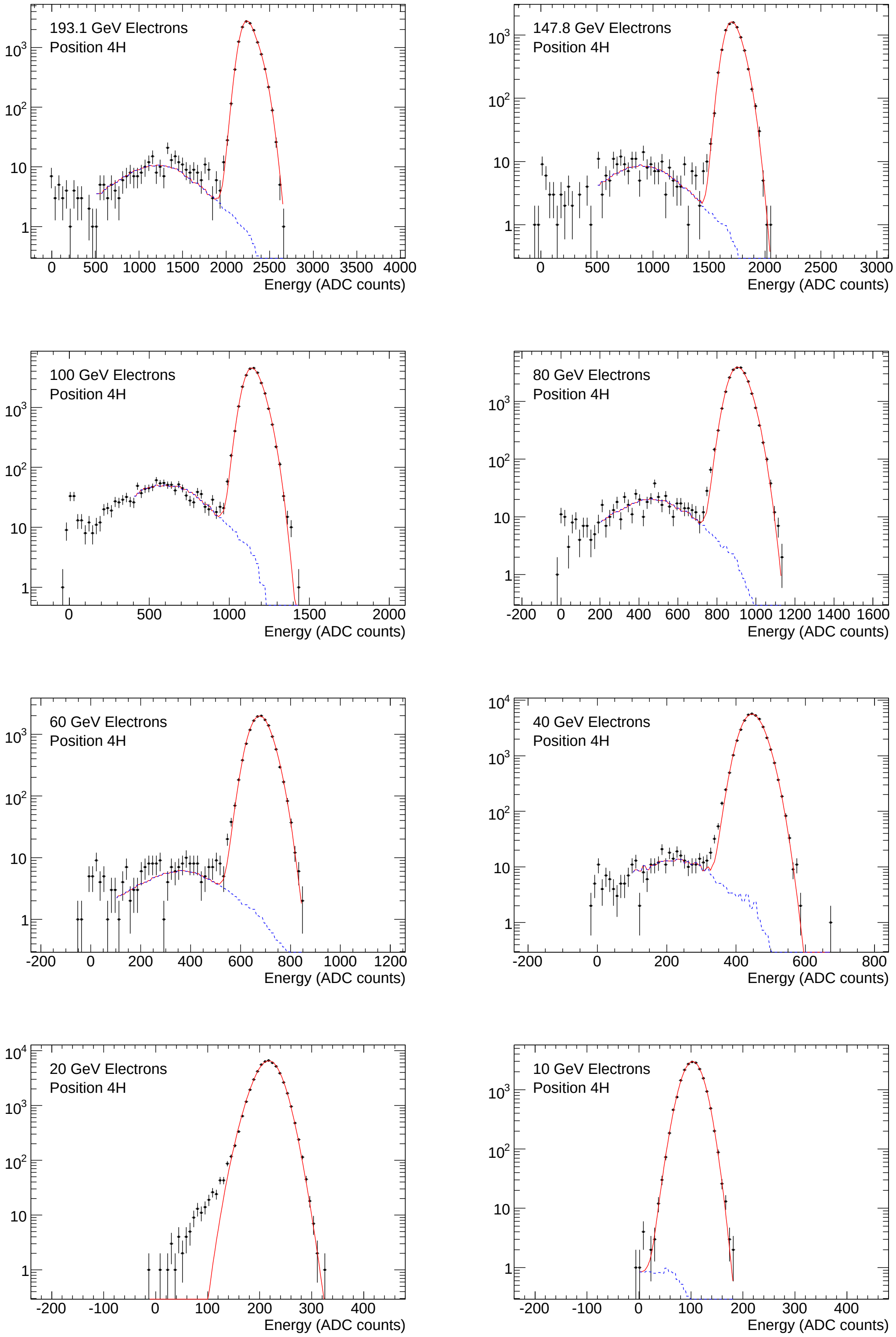

Figure 4.9: Response of the FCal to electrons at position 4H. The red curve is the total fit to the data, which consists of a double Gaussian fit to the electron peak as well as the fit to the hadron contribution (blue dashed line).

Beam Energy (GeV)	Fitted Mean (ADC)	Fitted Width (ADC)	Noise (ADC)
193.1 GeV	2300.6 ± 0.5	94.4 ± 0.3	15.1 ± 0.1
147.8 GeV	1763.4 ± 0.8	75.9 ± 0.5	17.2 ± 0.1
100 GeV	1186.4 ± 0.3	56.8 ± 0.2	17.5 ± 0.1
80 GeV	946.9 ± 0.3	47.9 ± 0.2	17.4 ± 0.1
60 GeV	708.1 ± 0.9	36.6 ± 0.7	13.9 ± 0.2
40 GeV	472.4 ± 0.2	29.9 ± 0.1	14.6 ± 0.1
20 GeV	229.3 ± 0.1	21.7 ± 0.1	14.53 ± 0.04
10 GeV	110.9 ± 0.1	17.7 ± 0.1	14.5 ± 0.1

Table 4.1: Results for the FCal response to electrons, at position 4L. Quantities are obtained from the double Gaussian fit discussed in the text, and quoted uncertainties are statistical only.

Beam Energy (GeV)	Fitted Mean (ADC)	Fitted Width (ADC)	Noise (ADC)
193.1 GeV	2263.9 ± 0.7	90.9 ± 0.5	15.7 ± 0.1
147.8 GeV	1718.3 ± 0.8	72.1 ± 0.5	15.6 ± 0.1
100 GeV	1150.8 ± 0.3	55.1 ± 0.2	17.1 ± 0.1
80 GeV	912.1 ± 0.3	48.8 ± 0.2	17.1 ± 0.1
60 GeV	680.1 ± 0.4	40.5 ± 0.2	15.9 ± 0.1
40 GeV	448.1 ± 0.2	30.9 ± 0.1	15.2 ± 0.1
20 GeV	215.8 ± 0.1	23.1 ± 0.1	14.85 ± 0.05
10 GeV	102.7 ± 0.1	18.5 ± 0.1	14.3 ± 0.1

Table 4.2: Results for the FCal response to electrons, at position 4H. Quantities are obtained from the double Gaussian fit discussed in the text, and quoted uncertainties are statistical only.

clustered in each case. A Gaussian fit is then performed on the cluster energies obtained from the random events, and the width of this is used as an estimate of the electronics noise contribution to cluster energies in physics events. This width is then used in the computation of the energy resolution, which is described below.

The simulated response to electrons is shown in Figure 4.10 for position 4L and Figure 4.11 for position 4H, while the fit results and clustered noise are listed in Tables 4.3 and 4.4. All of the physics lists described in Section 4.3.1 model electromagnetic showers in the same way, so no distinction between physics lists is made for the simulation results for electrons.

The linearity of the FCal response to electrons is shown in Figures 4.12(a) (for position 4L) and 4.12(b) (position 4H), depicting the mean reconstructed energy (in ADC counts) as a function of beam energy. In each case the results of a linear fit have been overlaid, the results of which are given in Table 4.5. The y intercept was not fixed to zero when performing the fit. The negative result for the intercept is attributed to energy losses in the upstream material, with the additional material at 4H resulting in an intercept larger in magnitude than that at 4L. As the simulation only modelled beamline components downstream of the B9 magnet, energy losses in materials upstream of this point would not be reflected in the simulation results. This is a possible explanation as to why the simulation results have a less negative intercept than those obtained from data. The effects of the additional material in front of position 4H appear to be well modelled by the simulation, as can be seen by comparing the values of the intercepts at position 4L and 4H. In data, the intercept at 4H is 8.3 ADC counts lower than that measured at position 4L, while in the simulation results there is a difference of 9.0 ADC counts.

One of the larger sources of systematic uncertainty on the response linearity is due to effects related to the beam polarity. The electron beams used in this study were secondary or tertiary beams produced by directing proton beams from the SPS at a fixed target. At higher energies a secondary beam was used, the polarity of which (e^+ or e^-)

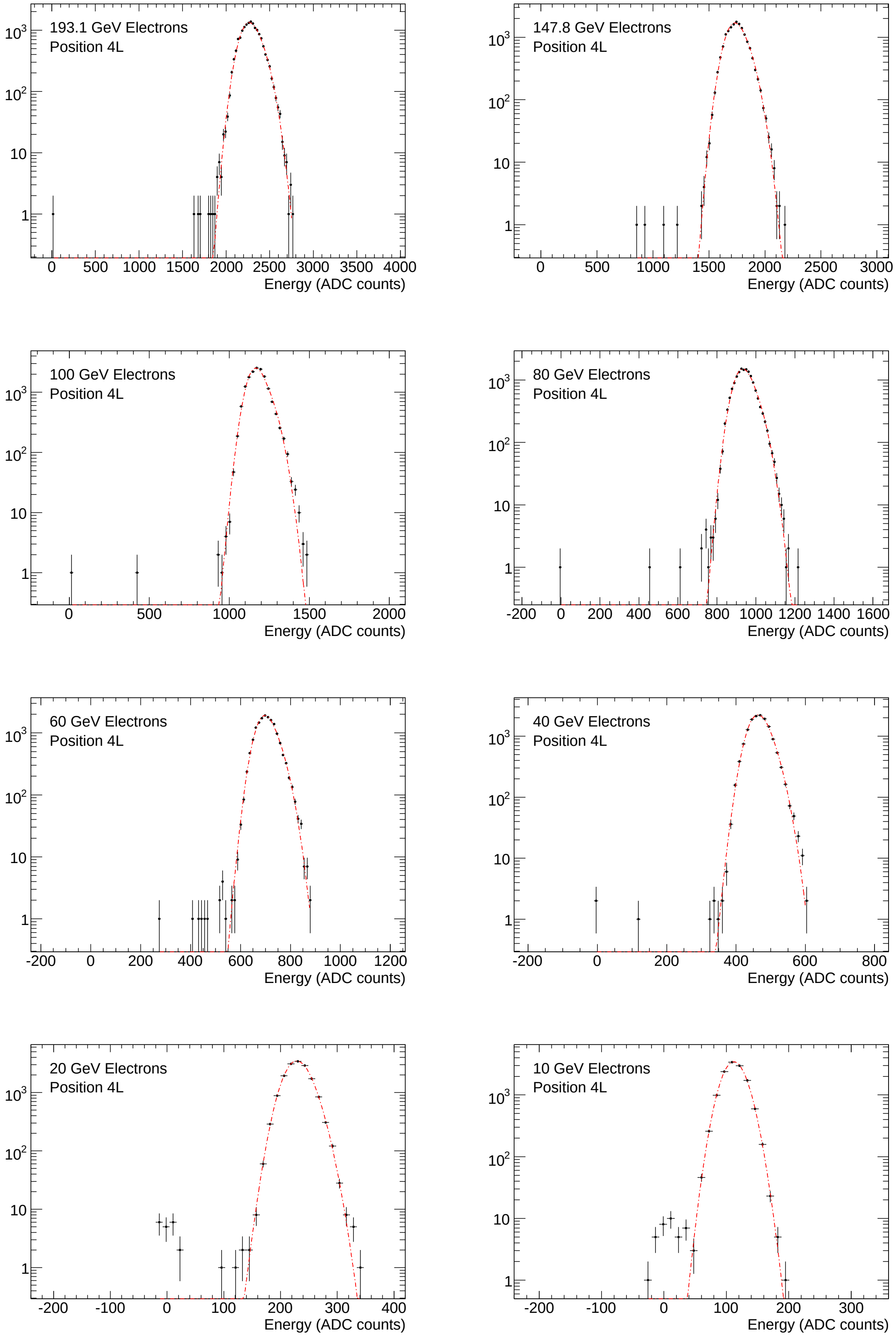

Figure 4.10: Monte Carlo results for electrons at position 4L. The red curve shows the double Gaussian fit to the response.

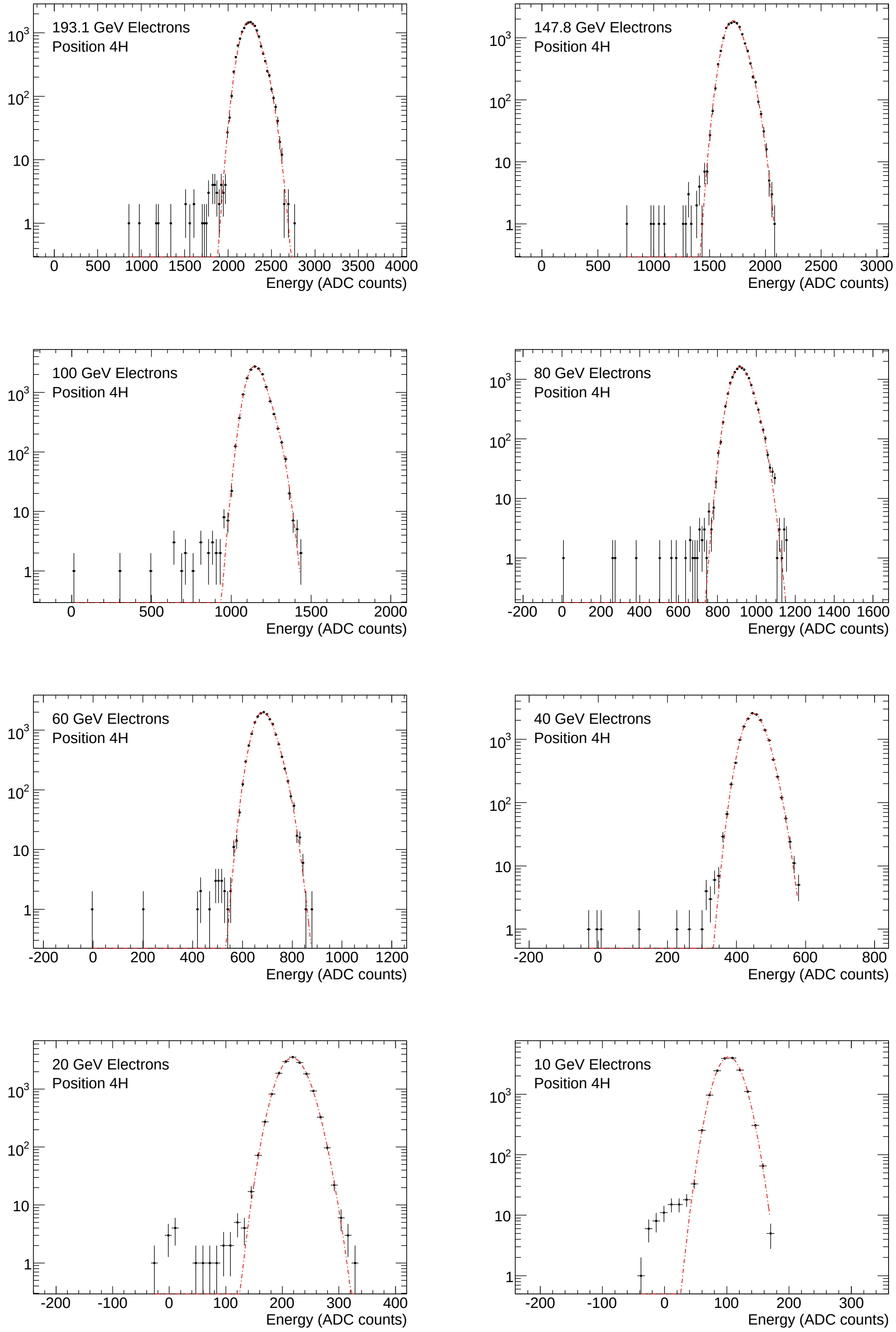

Figure 4.11: Monte Carlo results for electrons at position 4H. The red curve shows the double Gaussian fit to the response.

Beam Energy (GeV)	Fitted Mean (ADC)	Fitted Width (ADC)	Noise (ADC)
193.1 GeV	2285.2 ± 0.9	114.3 ± 0.7	14.2 ± 0.1
147.8 GeV	1747.4 ± 0.7	91.3 ± 0.5	17.0 ± 0.1
100 GeV	1180.2 ± 0.5	62.5 ± 0.3	17.4 ± 0.1
80 GeV	942.8 ± 0.4	51.7 ± 0.3	14.1 ± 0.1
60 GeV	705.3 ± 0.3	40.9 ± 0.2	14.2 ± 0.1
40 GeV	467.9 ± 0.3	31.6 ± 0.2	14.5 ± 0.1
20 GeV	230.5 ± 0.2	22.2 ± 0.1	14.3 ± 0.1
10 GeV	112.5 ± 0.2	18.0 ± 0.1	14.3 ± 0.1
5 GeV	53.1 ± 0.1	16.9 ± 0.1	14.1 ± 0.1

Table 4.3: Simulated response of the FCal to electron beams at position 4L. Quoted uncertainties are statistical only.

Beam Energy (GeV)	Fitted Mean (ADC)	Fitted Width (ADC)	Noise (ADC)
193.1 GeV	2259.7 ± 0.8	103.2 ± 0.6	15.9 ± 0.1
147.8 GeV	1723.5 ± 0.7	82.8 ± 0.5	15.6 ± 0.1
100 GeV	1159.5 ± 0.4	58.4 ± 0.3	17.0 ± 0.1
80 GeV	923.0 ± 0.4	48.2 ± 0.3	17.1 ± 0.1
60 GeV	687.7 ± 0.3	39.3 ± 0.2	16.1 ± 0.1
40 GeV	452.4 ± 0.2	30.7 ± 0.2	15.0 ± 0.1
20 GeV	218.8 ± 0.2	22.3 ± 0.1	14.6 ± 0.1
10 GeV	103.5 ± 0.1	18.4 ± 0.1	14.3 ± 0.1

Table 4.4: Simulated response of the FCal to electron beams at position 4H. Quoted uncertainties are statistical only.

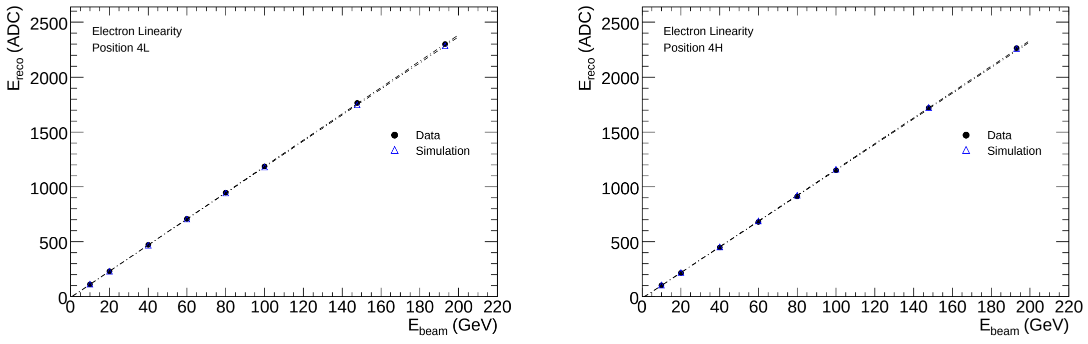

(a) (b)

Figure 4.12: Linearity of the response to electrons at position 4L (a) and 4H (b).

was determined based on the needs of experiments in the neighbouring H8 beamline. At lower energies a tertiary beam was used, the polarity of which could be chosen freely.

Data was taken at position 4L using both e^- and e^+ beams at energies of 10 GeV and 20 GeV. Electromagnetic showers induced by electrons should on average deposit the same energy as those initiated by positrons. The 10 GeV and 20 GeV results in Figure 4.8 combine data obtained from both e^+ and e^- beams. When beams of opposite polarity were considered separately, the response to 10 GeV positrons was found to be on average $(1.7 \pm 0.1)\%$ higher than the response to electrons. At 20 GeV, the response to positrons was found to be (1.01 ± 0.05) % higher than the response to electrons. This variation in response is attributed to conditions in the magnet systems. The magnets were not systematically de-Gaussed during data taking, and so it is possible that hysteresis effects may have led to some small variations in the beam energy. These variations in the beam energy are considered as a source of systematic uncertainty.

linearity result	slope (ADC/GeV)	Intercept (ADC)
Data (4L)	11.966 ± 0.002	-9.26 ± 0.07
Simulation (4L)	11.865 ± 0.003	-6.45 ± 0.13
Data (4H)	11.693 ± 0.002	-17.53 ± 0.10
Simulation (4H)	11.747 ± 0.003	-15.44 ± 0.13

Table 4.5: Linearity results for electron data. Quoted uncertainties are statistical.

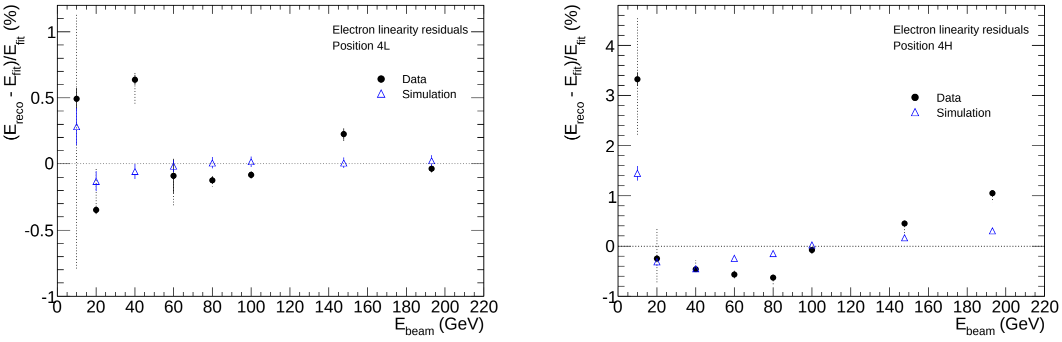

(a) (b)

Figure 4.13: Residuals obtained from the linearity fit for electrons at position 4L (a) and 4H (b). Solid lines in the error bars represent the statistical uncertainties, while the systematic uncertainties are represented by dotted lines.

For the 10 GeV and 20 GeV data points in Figure 4.12(a), events from both e^+ and e^- beams are used. The linear fit obtained in this case is considered the “nominal” result. The systematic uncertainty on the linearity due to variations in the beam energy was obtained by varying the data used at 10 GeV and 20 GeV, i.e. using events from only e^+ or only e^- runs at each energy. For each of these cases, the linear fit was repeated, and the fit result was compared to the nominal case. The largest difference observed for each parameter has been taken as the systematic uncertainty due to variations in the beam energy.

At position 4H only a single beam polarity was used at each energy, with e^+ beams being used at 10 GeV and 20 GeV. The response to e^- beams at 4H was estimated by calculating the ratio of the e^+ to e^- responses at position 4L, and then scaling the response to e^+ beams at 4H by this ratio. After obtaining estimates of the response to e^- beams, the uncertainty associated with variations in the beam energy was determined using the same procedure as was done for position 4L.

Other systematic effects considered include the binning used in histograms, whether or not the pion response is included in the electron fit, the signal parameterisation used for the fit, and the event selection criteria. These effects were all found to be small, while the beam energy variations were the most significant source of systematic uncertainty. Systematic uncertainties from different sources were summed in quadrature in order to obtain the final uncertainty on the results.

The linearity at position 4L is best described by a line with slope 11.97 ± 0.06 ADC/GeV and intercept -9.3 ± 1.1 ADC counts, where the quoted uncertainties are dominated by systematic effects. The statistical uncertainties are given in Table 4.5. At position 4H, the linearity is described by a line with slope 11.69 ± 0.06 ADC/GeV and intercept -17.5 ± 1.3 ADC counts, where the uncertainties are again dominated by systematic effects.

Previous studies of the FCal pulse shapes [78, 79] and a SPICE simulation of the FCal electronics chain enabled a prediction of the ADC2GeV calibration factor to be made prior to the beam test. This initial prediction agreed to within 5% of the value measured at position 4L. However, some impedance mis-matches that had not been accounted for were subsequently identified by analysing pulse shapes recorded when taking data[69]. These . When the simulation was modified to include these effects, the predicted value of the calibration factor became 12.0 ADC/GeV, improving the agreement with the results presented here.

The residuals obtained from the linearity fits are plotted in Figure 4.13. From the plot in Figure 4.30(a), it can be seen that the response at position 4L is linear to within 1%. This is also the case at position 4H for energies of 20 GeV and above. Some of the residuals in these figures are still not consistent with zero after including the systematic effects discussed above. It is therefore possible that an unidentified source of systematic uncertainty may contribute at the ∼0.5% level, though this has not been included in the quoted results.

The energy resolution of the FCal response to electrons is plotted in Figure 4.14, for both data and simulation. The randomly triggered events provide information on the

	Stochastic Term (% GeV$^{1/2}$)	Constant Term (%)
Data (4L)	27.0 ± 0.2	3.58 ± 0.02
Simulation (4L)	24.7 ± 0.3	4.56 ± 0.03
Data (4H)	33.7 ± 0.2	3.11 ± 0.03
Simulation (4H)	28.1 ± 0.3	3.96 ± 0.03

Table 4.6: Fit parameters for energy resolution to electrons. Quoted uncertainties are statistical only.

amount of noise present in the electronics, and so this information is used to subtract (in quadrature) the noise contribution from the width of the response. This is done because the level of noise was observed to vary over time, such that data collected at different beam energies are affected by different levels of noise. The resolution is thus defined as $\sigma_E/\bar{E}$, where

$$\sigma_E = \sqrt{\sigma^2 - \sigma_N^2} \tag{4.13}$$

where σ_N is the width of the noise distribution reconstructed from randomly triggered events. The width of the electron peak, σ, and the mean response, $\bar{E}$, are obtained from the double Gaussian fit as described by equations 4.8 and 4.9. The values of these quantities are listed in in Tables 4.1 and 4.2, for positions 4L and 4H, respectively. As noted earlier, the amount of noise present in the electronics varied over time, but the RMS of the noise contribution to 8 cm clusters was generally around 14-17 ADC counts (1.2-1.4 GeV). The RMS of the noise contribution to the cluster energy has been plotted as a function of beam energy in Figure 4.15.

The resolution is fit to a function of the form

$$\frac{\sigma_E}{\bar{E}} = \frac{A}{\sqrt{E}} \oplus B \tag{4.14}$$

which is the same as that given in equation 3.7 but with the noise term omitted (as the noise contribution to the resolution has been subtracted). The fit results are listed in Table 4.6.

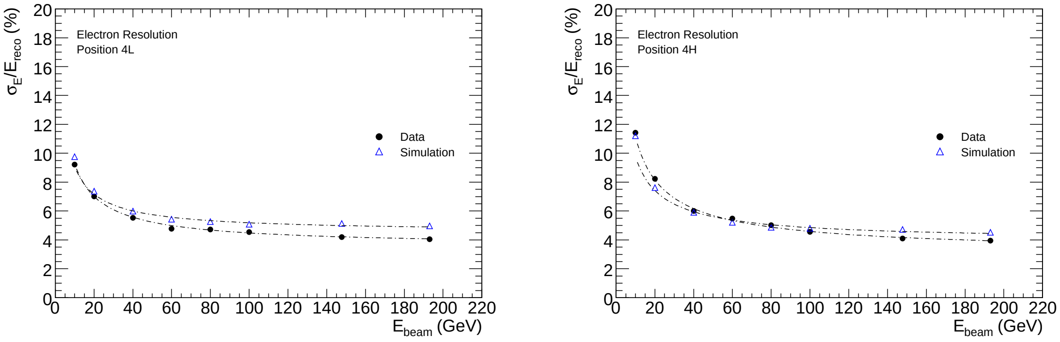

(a) (b)

Figure 4.14: Energy resolution of the FCal to electrons, using data taken from position 4L (a) and 4H (b). A noise subtraction procedure has been applied, as described in the text.

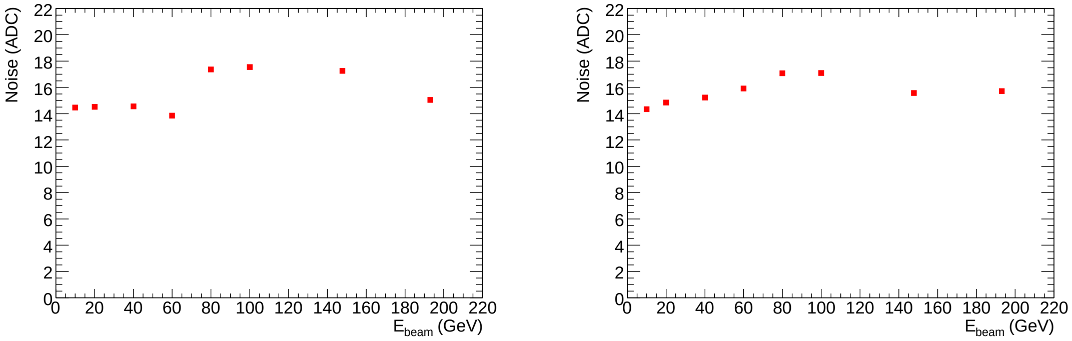

Figure 4.15: RMS of the electronics noise clustered at different energies, for electron beams at position 4L (a) and position 4H (b).

The constant term of the electron energy resolution is influenced by the impact point dependence of the response [61]. The additional upstream material present for data taken at position 4H can cause the beam particles to begin showering earlier. In such cases, the energy in the shower is then distributed over a larger area by the time it reaches the FCal, decreasing the impact point dependence and resulting in a lower constant term for the resolution measured at position 4H. This effect is seen in both the data and simulation results.

The simulation results for electrons give a higher (i.e. worse) resolution than that seen in data at higher beam energies, although the discrepancy is smaller at position 4H

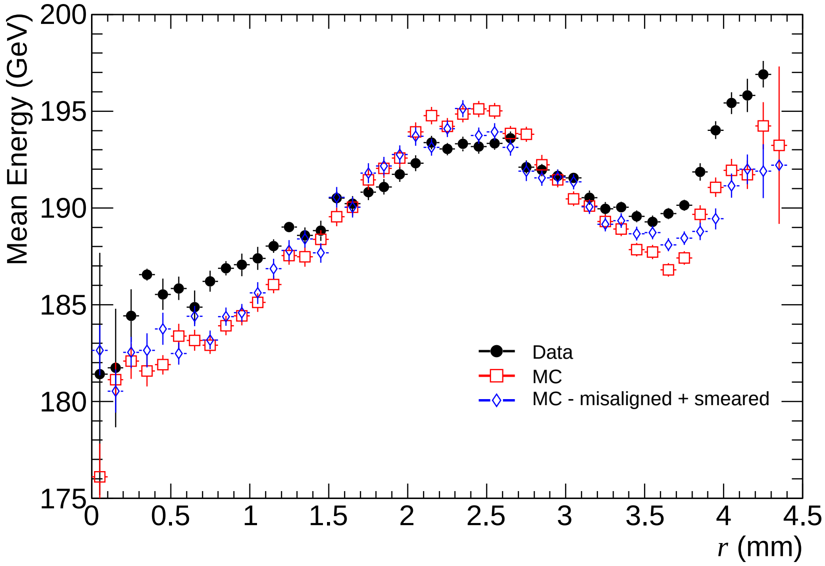

Figure 4.16: Electron response plotted as a function of r, for 193 GeV electrons at position 4L. Note that the liquid argon gap is centred at $r = 2.5$mm. The red squares represent simulation results in which there is no uncertainty in the impact point position, whereas the blue diamonds represent simulation results in which the impact point has been smeared in a manner consistent with the uncertainties present in the data, as discussed in the text.

than 4L. Again, the effects of the additional material at position 4H are well modelled by the simulation. The constant term at position 4L is 15% higher than that seen at 4H, in both data and simulation, indicating that the effects of the additional material at position 4H are well modelled by the simulation.

The constant term for the resolution is significantly higher in the simulation than in data. This discrepancy is also present in comparisons between `GEANT4` simulations and data taken during the 1998 and 2004 testbeams [63, 64], with the constant term for the electron resolution obtained from simulations being consistently higher than that seen in data.

As mentioned above, the impact point dependence of the response contributes to the constant term of the resolution. Figure 4.16 shows the mean response of the FCal as a function of r, which is the radial distance from the impact point to the centre of the closest electrode, for 193 GeV electrons at position 4L. For FCal1, the liquid argon gap covers the region 2.375 mm $< r <$ 2.625 mm, and thus the response is higher near this region. Smaller values of r mean that the electron is striking the copper rod located at the centre of the electrode, leading to a lower response. Note that the simulation results show a larger variation with r than is observed in data, indicating that the impact point dependence of the response is stronger in the simulation than in data.

When analysing data, the impact point is determined from the beam particle track, which is reconstructed from BPC measurements. The uncertainty on the measured impact point associated with the position resolution of the BPCs is 0.26mm in the x and y coordinates. There is also an uncertainty associated with the alignment between the BPC and FCal coordinate systems, which is ± 0.12 mm in the x coordinate and ± 0.25mm in the y coordinate [67]. In the simulation, the trajectories of the beam particles and the precise position of the FCal are known exactly. In order to better compare data and simulation results, the blue diamonds in Figure 4.16 represent simulation results in which the impact points have been artificially smeared in a way that is consistent with the uncertainties present in the data. That is, a shift equal to the alignment uncertainty and a random smearing with RMS equal to the track reconstruction uncertainty were applied to the impact points in the simulation results.

The noise subtracted electron resolution at 193 GeV is $(4.05 \pm 0.02)\%$ in data, whereas the resolution obtained from simulations is $(4.97 \pm 0.03)\%$, where the quoted uncertainties are statistical only. In order to estimate how much of this discrepancy could be attributed to the greater impact point dependence seen in the simulation, weights were assigned to the simulated events. Simulated events were binned in r[*], and the clustered energy was compared to the mean response observed for that bin in data. If the clustered energy for an event was greater than the mean response seen in data, then the event was assigned a weight w_i (where the index i refers to the r-bin being considered), otherwise the event was assigned a weight $1/w_i$. The weight w_i was then determined such that the

---

[*] The "smeared" value of r was used for this binning

weighted average response for simulation results in the i-th bin was equal to the mean response obtained from the same bin in data. After weighting the simulation events, the resolution was recalculated and found to be (4.86 ± 0.01%), which is still significantly higher than the resolution seen in data. The greater impact point dependence seen in the simulation is thus not sufficient to fully account for the higher resolution seen in the simulation results.

The sources of systematic uncertainty considered for the electron energy resolution are the same as those considered for the response linearity, although the choice of cluster radius is also considered. As mentioned earlier, a larger clustering radius captures a slightly larger fraction of the showering particle's energy. However, this also significantly increases the amount of noise present in the cluster, as the noise contribution scales with the number of cells in the cluster. The choice of clustering radius is thus taken as a source of systematic uncertainty on the energy resolution of the FCal. This uncertainty was estimated by calculating the resolution using both 12cm and 16cm clusters. The stochastic term obtained using these larger clusters was then compared to that obtained using 8cm clusters, with the largest difference being taken as the systematic uncertainty on the stochastic term. The systematic uncertainty on the constant term was obtained in the same way.

The systematic uncertainties are dominated by beam energy variations and the choice of cluster size, with other effects providing a smaller contribution. The resolution at position 4L is best described by a stochastic term of $(27.0 \pm 0.9)\% \cdot (\mathrm{GeV})^{1/2}$ and a constant term of $(3.58 \pm 0.09)\%$, while the resolution at position 4H is best described by a stochastic term of $(33.7 \pm 0.8)\% \cdot (\mathrm{GeV})^{1/2}$ and a constant term of $(3.11 \pm 0.09)\%$. These uncertainties are again dominated by systematic effects, with the statistical uncertainties being listed in Table 4.6.

The resolution at 4L presented here has a stochastic term of $(27.0 \pm 0.9)\% \cdot (\mathrm{GeV})^{1/2})$, which is slightly lower than the published result of $(28.5 \pm 1.0)\% \cdot (\mathrm{GeV})^{1/2})$ [69]. This difference is due to the rounding error discussed in Section 4.2.2, which has been corrected in these results but was undiscovered at the time of publication. The constant term presented here $(3.58 \pm 0.09)\%$ is slightly larger than the published value $(3.5 \pm 0.1)\%$, but these values are consistent within the uncertainties.

4.5.2 Analysis of Hadron Data

In the analysis of hadron data, the signal from each FCal module is first calibrated to the electromagnetic (EM) scale by applying the ADC2MeV factors. The values used to reconstruct signals from the FCal are 83.3 MeV/ADC for FCal1, 163.9 MeV/ADC for FCal2 and 185.2 MeV/ADC for FCal3. These are the same values used in the published analysis[69], which were originally obtained using the results of a SPICE simulation of the FCal electronics and calculations pertaining to the FCal's geometry and material. As discussed above, the predicted value for FCal1 is in good agreement with the value obtained from the linear fit to the FCal1 response to electrons. During a previous beam test[63], the response to electrons was studied separately for prototypes of the FCal1 and FCal2 modules. The ratio of these responses was measured from this data, and used to validate the predictions for the EM scale factors of the hadronic modules.

Figure 4.17 shows the transverse shower profile (at the EM scale) for 200 GeV hadron data at positions 4L and 4H. Figures 4.17(a) and 4.17(b) show the integrated energy contained within a cylinder of radius r centred on the impact point, normalised to the energy contained within a cylinder of radius 21 cm[*] for positions 4L and 4H, respectively. Figures 4.17(c) and 4.17(d) show the derivatives of Figures 4.17(a) and 4.17(b), respectively, and show in detail the relative amounts of energy deposited as a function of r. Each bin shows the amount of energy contained within a cylindrical shell of thickness 0.5 cm, normalised to the total energy contained within a cylinder of radius 21cm. The

---

[*] Any energy that propagates (transversely) further than 21cm from the centre of the beamspot is not contained within the FCal.

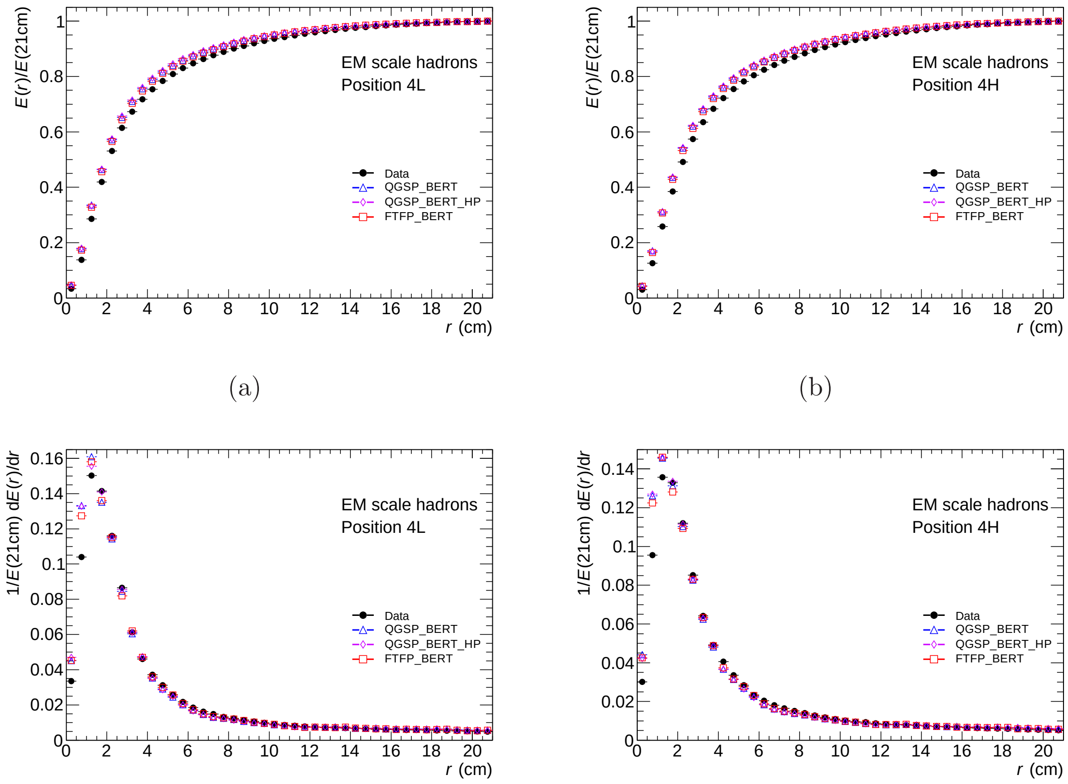

(a) (b)

(c) (d)

Figure 4.17: Energy distribution within the FCal as a function of the transverse distance (r) from the projected beam impact point. Figures (a) and (b) show the cumulative energy distribution at position 4L and 4H, respectively, while Figures (c) and (d) show the derivatives of these plots.

simulation results (for all physics lists studied) show that a slightly larger fraction of the energy is contained within smaller transverse distances, indicating that the simulated showers are narrower than those observed in data. This is consistent with other `ATLAS` data/simulation comparisons[64, 80, 81]. Cylindrical clusters of radius 16cm are used for analysis of the hadron data: these contain $\sim$ 99% of the energy deposited in the calorimeter.

The longitudinal shower profiles for 200 GeV hadrons are shown in Figure 4.18. These show the amount of energy (at the EM scale) clustered within each module as a fraction of the total energy clustered in all modules. The simulation results show more energy

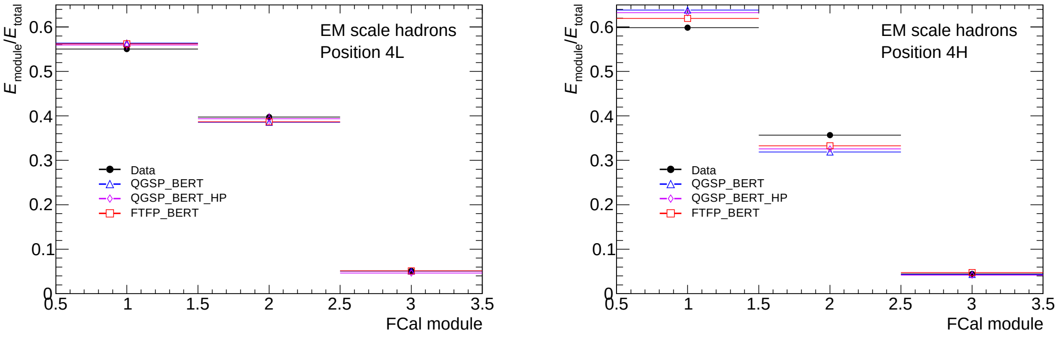

(a) (b)

Figure 4.18: Longitudinal distributions of energy (EM scale) deposited in the FCal. These show the relative amounts of energy clustered in each module, for beams at position 4L (a) and 4H (b).

deposited in FCal1 and less energy in FCal2, indicating the simulated showers are shorter than those observed in data. This has also been seen in other ATLAS data/simulation comparisons [64, 80, 81].

The shower maximum is the longitudinal depth at which the particle shower contains the largest number of particles, and thus corresponds to the depth at which the energy deposition is greatest. The additional material in front of position 4H can sometimes cause the shower to start earlier, and thus move the location of the shower maximum back towards the front of the FCal. This results in a larger fraction of energy being deposited in FCal1 at position 4H compared to position 4L, which can be seen in Figure 4.18 for both the data and simulation results.

The mean response of the FCal to hadrons is plotted in Figure 4.19, as a function of the beam energy. The response here is again taken at the EM scale. The response is fit to the double Gaussian parameterisation given in 4.5, and the constraints for the four parameter fit given in equations 4.6 and 4.7 are derived from hadron data at 200 GeV.

As discussed in Section 3.2.4.3, the relative amount of energy contained in the EM part of a hadronic shower scales nonlinearly with the energy of the incident hadron. This feature of hadronic showers gives rise to the nonlinear behaviour seen in Figure 4.19: as the beam energy increases, the EM component of the shower also increases, giving a higher relative response at the EM scale.

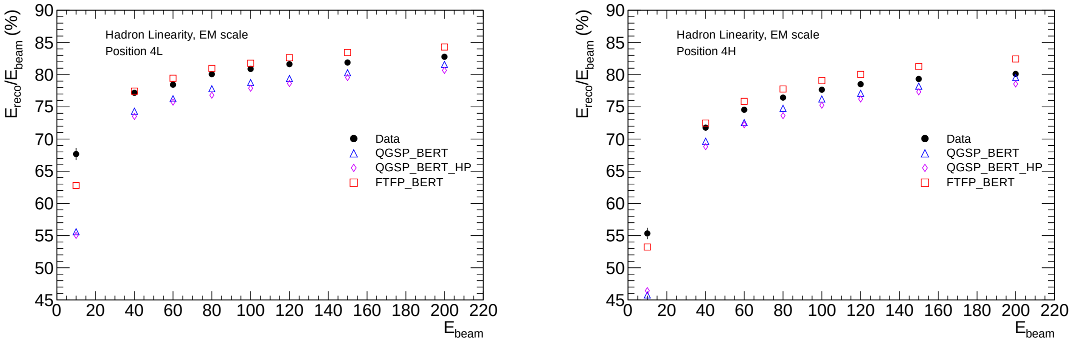

(a)

(b)

Figure 4.19: Ratio of energy reconstructed at the EM scale to the beam energy, for hadrons at position 4L (a) and 4H (b).

As hadrons deposit less visible energy in the calorimeter than electrons, the reconstructed energy needs to be corrected from the EM scale to the hadronic scale. For the test beam analysis, this is accomplished using a simple flat weighting scheme, whereby a single weight is assigned to each module. The calibrated energy is then given by

$$E_{\mathrm{reco}} = g_1 E_1^{\mathrm{EM}} + g_2 E_2^{\mathrm{EM}} + g_3 E_3^{\mathrm{EM}} \tag{4.15}$$

where E_1^{EM}, E_2^{EM}, and E_3^{EM} are the EM scale energies clustered in FCal1, FCal2 and FCal3, respectively, and g_1, g_2, and g_3 are the flat weights for the three modules.

The weights are derived at a given beam energy, as energy dependent weights can not be used at ATLAS. They are obtained by minimising the function

$$\chi^2 = \sum_{i}^{N_{\mathrm{events}}} \left(g_1 E_{1,i}^{\mathrm{EM}} + g_2 E_{2,i}^{\mathrm{EM}} + g_3 E_{3,i}^{\mathrm{EM}} - E_{\mathrm{beam}} \right)^2 \tag{4.16}$$

where E_{beam} is the beam energy and the sum runs over all events taken at this energy. The weights are constrained such that the mean reconstructed energy is equal to the beam energy. This constraint is implemented by assigning g_3 the value

$$g_3 = \frac{E_{\mathrm{beam}} - g_1\langle E_1^{\mathrm{EM}}\rangle - g_2\langle E_2^{\mathrm{EM}}\rangle}{\langle E_3^{\mathrm{EM}}\rangle}, \tag{4.17}$$

where the angled brackets denote the average taken over all events. With this constraint applied, the χ^2 in equation 4.16 becomes equal to the variance of the reconstructed energy, and so minimising χ^2 minimises the width of the distribution of reconstructed energy.

The flat weights have been calculated at each beam energy, and are plotted in Figure 4.20, for beams at position 4L (a,c,e) and 4H (b,d,f). Weights derived using Monte Carlo results are also shown for comparison. Note that weights derived from 200 GeV data are used to calibrate all data and simulation results to the hadronic scale. Some of the weights derived from data at beam energies below 200 GeV are used to estimate systematic effects (which will be discussed later). Note that the agreement between weights derived from MC and weights derived from data implies that the MC derived weights should provide reasonable results when used to reconstruct data. This is the case at `ATLAS`, where hadronic calibration schemes are derived from Monte Carlo results. To illustrate this, results in which test beam data have been calibrated using weights derived from MC are shown in Appendix B. As the beam energy decreases the relative amount of energy deposited in FCal1 and FCal2 increases, while that deposited in FCal3 decreases. Consequently, the weights g_1 and g_2 increase with decreasing beam energy, while g_3 decreases. The uncertainty on g_3 is found by propagating the statistical uncertainties on g_1 and g_2. As FCal3 contains only a small fraction of the total energy deposited in the FCal, even at the highest beam energies available during the beam test, this results in an uncertainty on g_3 that is much larger than the uncertainties on the other two weights.

The calibrated response of the FCal to hadron beams of various energies is plotted in Figure 4.21 for position 4L and Figure 4.22 for position 4H. The responses obtained from

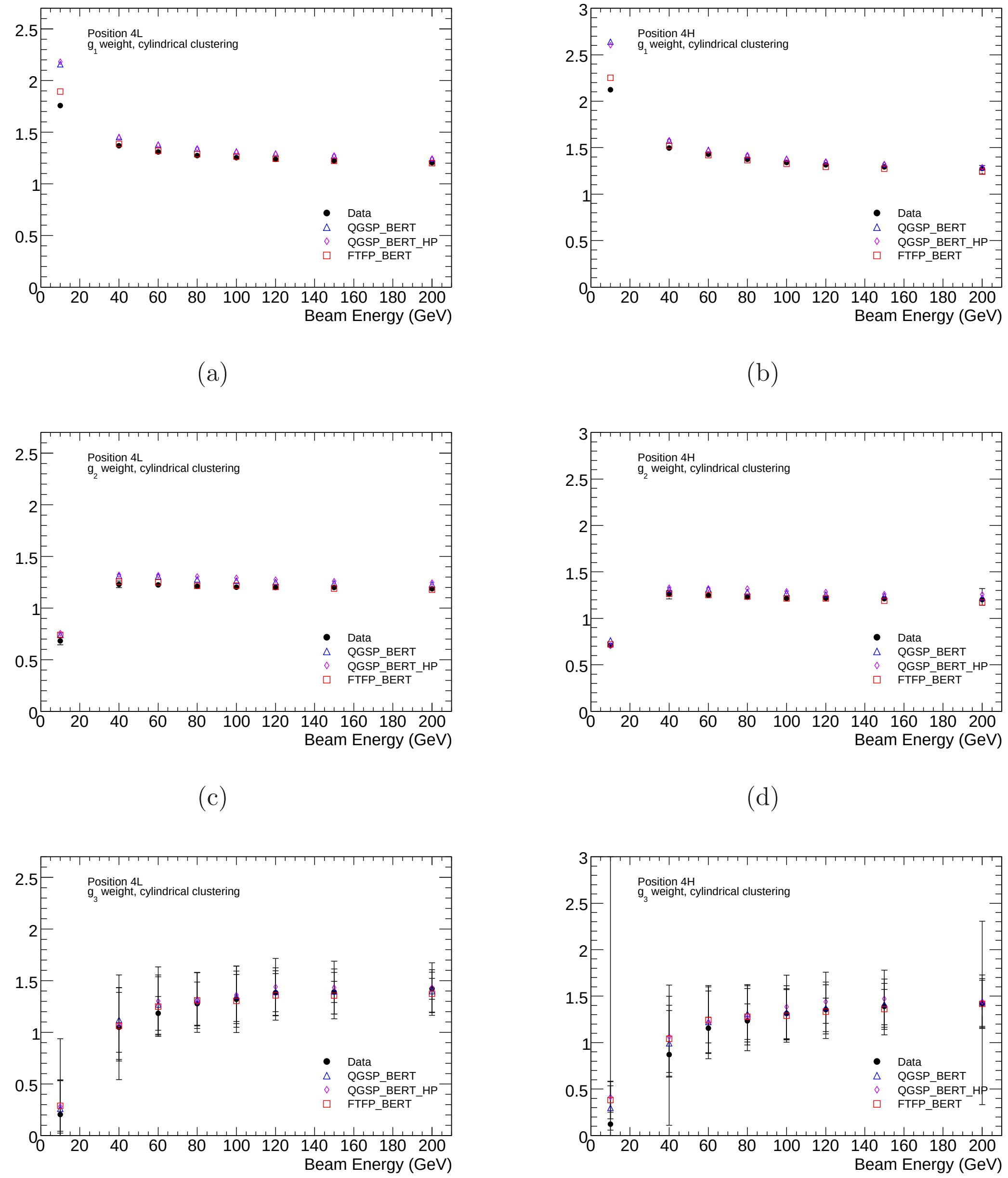

(a) (b)

(c) (d)

(e) (f)

Figure 4.20: Flat weights for hadronic calibration, as a function of the energy at which they are derived. Only the weights derived using 200GeV are used in the analysis, although weights derived at beam energies greater than 100 GeV are used in systematic studies. Figures (a), (c) and (e) show the weights g_1, g_2, and g_3, respectively, for position 4L, while figures (b), (d), and (f), respectively, show g_1, g_2, and g_3 for 4H.

simulation are shown in Appendix A, for all three of the physics lists considered. The mean and width of the response are extracted from the double Gaussian fit to the signal, as was done in the electron analysis. The results obtained from the fitting are summarised in Tables 4.7 and 4.8. When the weights g_1 and g_2 are varied by their uncertainties and g_3 is subsequently determined by the constraint (equation 4.17), the observed variation in the fit results is negligible. The statistical uncertainties associated with the hadronic weights have thus been neglected here. The noise contribution to the clustered energy was estimated from randomly triggered events, using the same method as in the electron analysis. This noise is plotted as a function of beam energy in Figure 4.23.

Beam Energy (GeV)	Fitted Mean (GeV)	Fitted Width (GeV)	Noise (GeV)
200 GeV	200.08 ± 0.06	19.46 ± 0.04	6.41 ± 0.01
150 GeV	148.39 ± 0.04	16.05 ± 0.03	6.55 ± 0.01
120 GeV	118.27 ± 0.05	14.24 ± 0.03	6.76 ± 0.02
100 GeV	97.6 ± 0.1	13.37 ± 0.08	7.29 ± 0.05
80 GeV	77.29 ± 0.06	11.31 ± 0.04	6.53 ± 0.03
60 GeV	56.74 ± 0.03	9.59 ± 0.02	6.08 ± 0.01
40 GeV	37.2 ± 0.1	8.49 ± 0.07	6.12 ± 0.05
10 GeV	8.2 ± 0.1	6.60 ± 0.08	6.17 ± 0.08

Table 4.7: Results for the FCal response to hadrons at position 4L. Quoted errors are statistical only.

Beam Energy (GeV)	Fitted Mean (GeV)	Fitted Width (GeV)	Noise (GeV)
200 GeV	200.05 ± 0.07	23.07 ± 0.05	6.48 ± 0.01
150 GeV	148.57 ± 0.05	19.00 ± 0.03	6.48 ± 0.01
120 GeV	117.82 ± 0.05	16.92 ± 0.04	7.15 ± 0.02
100 GeV	97.05 ± 0.09	15.71 ± 0.07	7.64 ± 0.03
80 GeV	76.40 ± 0.06	14.00 ± 0.04	7.63 ± 0.02
60 GeV	55.90 ± 0.03	11.65 ± 0.02	6.72 ± 0.01
40 GeV	35.9 ± 0.1	9.93 ± 0.09	6.48 ± 0.06
10 GeV	6.9 ± 0.1	7.23 ± 0.08	6.41 ± 0.07

Table 4.8: Results for the FCal response to hadrons at position 4H. Quoted errors are statistical only.

The ratio of the mean reconstructed energy at the hadronic scale to the beam energy

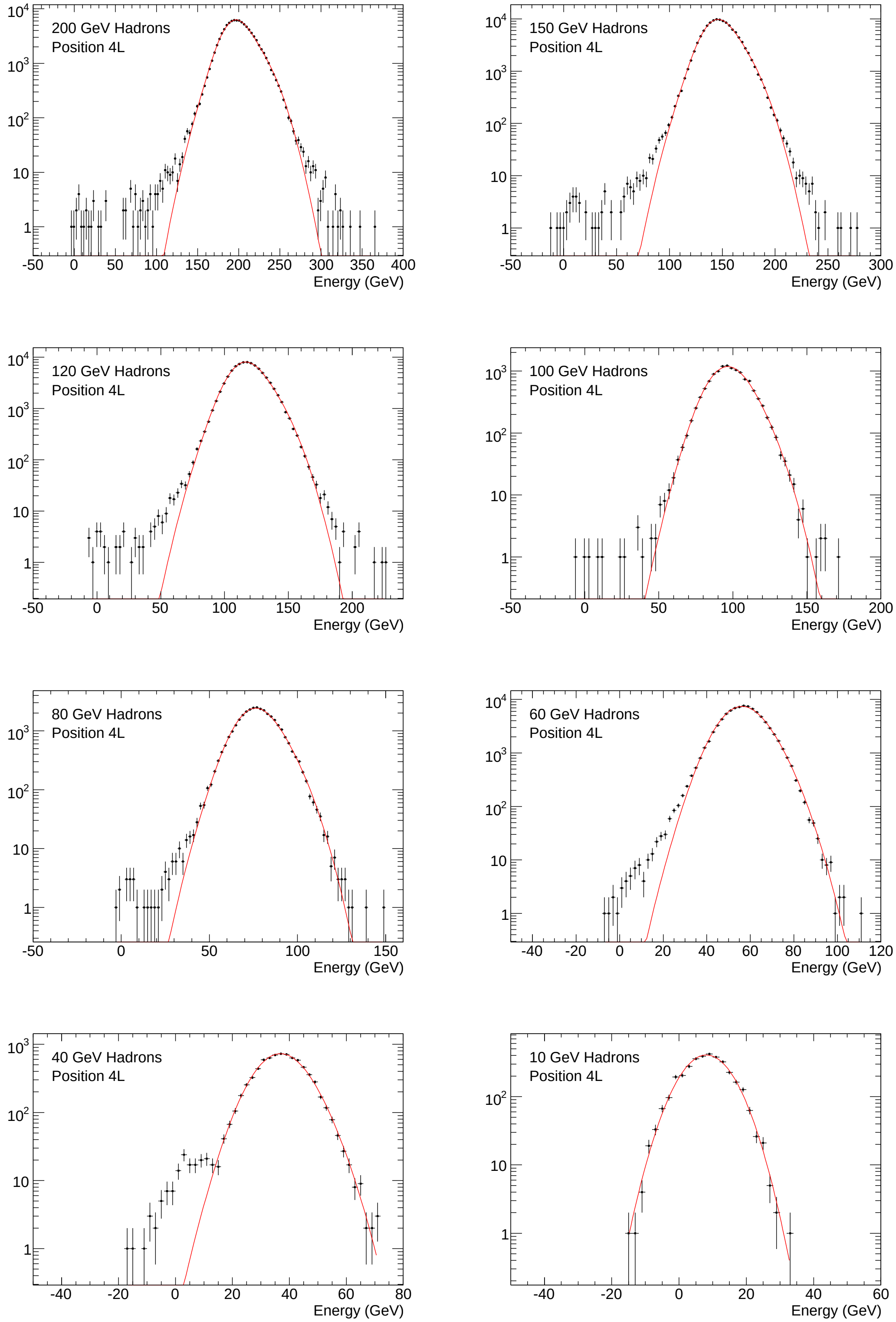

Figure 4.21: FCal response to hadron beams at position 4L. The red curve shows the double Gaussian fit, from which the mean energy and width of the response are derived.

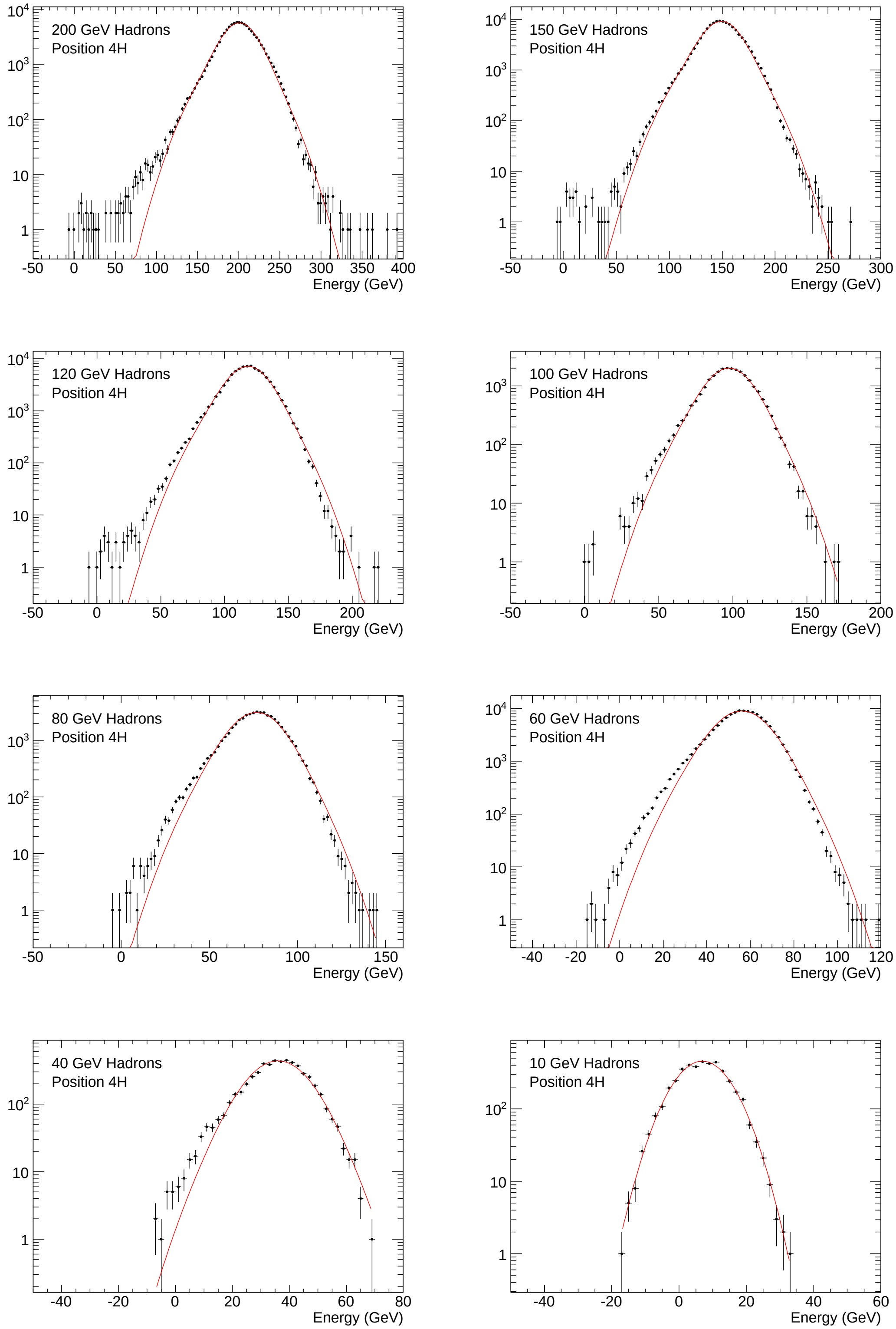

Figure 4.22: FCal response to hadron beams at position 4H. The red curve shows the double Gaussian fit, from which the mean energy and width of the response are derived.

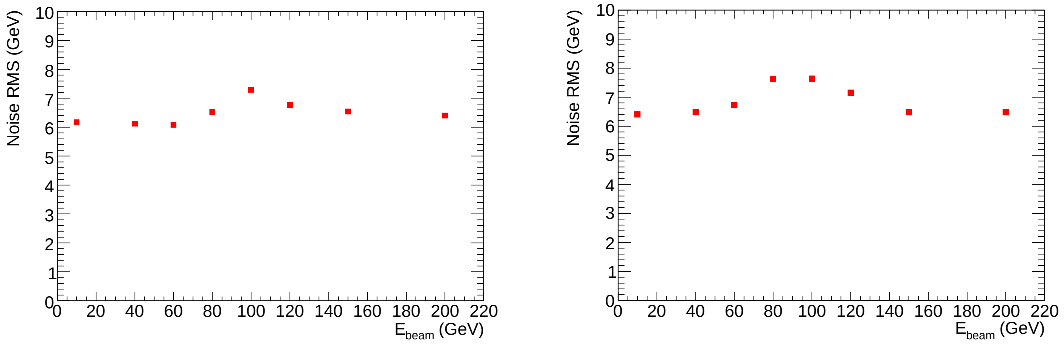

Figure 4.23: RMS of the electronics noise contribution to cylindrical clusters at position 4L (Fig. 4.23(a)) and position 4H (Fig. 4.23(b)).

is plotted in Figure 4.24, for data taken at both 4L and 4H. As most of the energy is deposited in FCal1 and FCal2, which have similar weights at 200 GeV, the shape of these plots are very similar to those shown in Figure 4.19. As the hadronic weights used are derived from data at beam energies of 200 GeV, and the optimisation requires that the mean reconstructed energy be equal to the beam energy, the data curves all reach a plateau of 100% at 200 GeV.

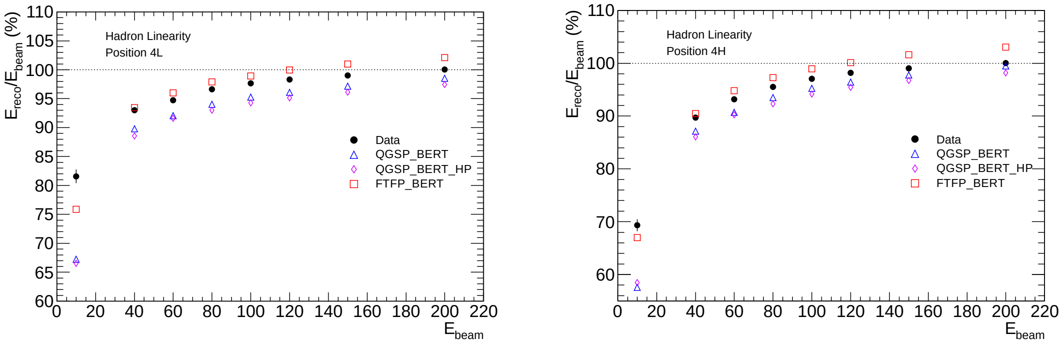

(a) (b)

Figure 4.24: Ratio of reconstructed energy to beam energy for hadrons at position 4L (a) and 4H (b). Hadronic calibration is accomplished through flat weights, which are derived from the 200 GeV data.

The energy resolution of the calibrated FCal response to hadrons is plotted in Figure 4.25. At higher energies the data and simulation results agree to within 1-2% (absolute), with the simulation results predicting a slightly better resolution than is seen in data. The resolution is fit to the same function used for electrons, with the results listed in Table 4.9.

Systematic effects related to the fitting procedure, histogram binning, event selection criteria, and the choice of hadronic weights are considered as sources of uncertainty, with uncertainties arising from different sources being summed in quadrature. The weights derived at 100 GeV, 120 GeV and 150 GeV are used to estimate the uncertainty associated with the weights; at these energies the weights show little variation with respect to the beam energy. Each set of weights is used to calibrate the data to the hadronic scale (for all beam energies), and then a fit is performed on the resolution. The largest deviation seen between the resolution fit parameters obtained using these weights and the fit parameters obtained using the nominal set of weights (derived from the 200 GeV data) is taken as the systematic uncertainty. Of the sources considered, the systematic uncertainty associated with the choice of weights is the largest, with other sources of uncertainty providing much smaller contributions.

The values for the stochastic and constant term of the resolution at position 4L are thus $(88 \pm 2)\ \%\cdot\mathrm{GeV}^{1/2}$ and $(6.8 \pm 0.4)\ \%$, respectively, while the stochastic and constant terms describing the resolution at position 4H are $(121 \pm 7)\ \mathrm{GeV}^{1/2}$ and $(7.1 \pm 1.2)\ \%$, respectively. The quoted uncertainties are dominated by systematic effects, with the statistical uncertainties on these parameters being listed in Table 4.9.

For the electron energy resolution, the additional material in front of position 4H gave rise to a lower constant term than at position 4L. This is not the case for the hadron resolution. For the data, the constant term at position 4H is slightly higher than at 4L (although the two values are consistent when their systematic uncertainties are considered). In the simulation results the constant terms at 4H are higher than those at 4L, although these are also consistent if systematic uncertainties of 0.5-1% (absolute) are associated with the simulation results, based on the variation seen in the constant term across the different physics lists.In all cases (data and simulation) the stochastic term at position 4H is 30-40% $\cdot$ (GeV)$^{1/2}$ higher than at position 4L.

The published values for the pion energy resolution for hadrons at position 4L were (94.2 ± 1.6) % $\cdot$ GeV$^{1/2}$ for the stochastic term and (7.5 ± 0.4)% for the constant term. The resolution presented here is a significant improvement over the published result, which is due to the correction of the rounding error described in Section 4.2.2. This error was rounding cell energies down to an integer number of ADC counts. The high MeV/ADC factors in the hadronic modules (163.9 MeV/ADC for FCal2 and 185.2 MeV/ADC for FCal3) caused this error to have a larger effect on energy reconstruction in the hadronic modules than in the EM module (which has a scale factor of 83.3 MeV/ADC). Additionally, hadronic showers extend further (both longitudinally and transversely) than EM showers, meaning that a more cells were affected. For these reasons, the rounding error had a greater effect in the analysis of hadron data than in the analysis of electron data, and so after correcting the error there is a greater improvement in the hadron resolution than was observed for the electron resolution.

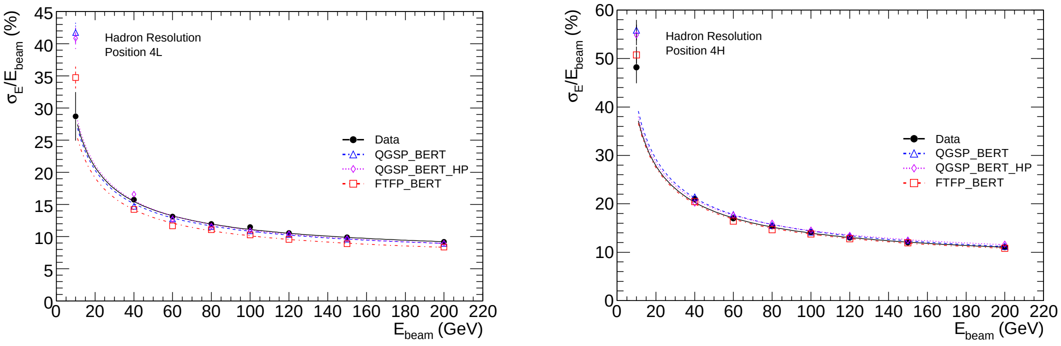

(a) (b)

Figure 4.25: Energy resolution of the FCal response to hadrons, using data taken at position 4L (a) and 4H (b). A noise subtraction procedure has been applied, as described in the text. The data is fit to the function described in equation 4.14, and the resulting fit parameters are listed in table 4.9

	Stochastic Term (% GeV$^{1/2}$)	Constant Term (%)
Data (4L)	88.0 ± 0.6	6.79 ± 0.06
QGSP_BERT (4L)	86.2 ± 1.1	6.54 ± 0.18
QGSP_BERT_HP (4L)	90.5 ± 1.1	6.22 ± 0.13
FTFP_BERT (4L)	81.2 ± 1.1	6.04 ± 0.11
Data (4H)	120.7 ± 0.6	6.98 ± 0.07
QGSP_BERT (4H)	127.6 ± 1.1	6.62 ± 0.17
QGSP_BERT_HP (4H)	123.3 ± 1.2	7.58 ± 0.16
FTFP_BERT (4H)	119.2 ± 1.1	6.77 ± 0.15

Table 4.9: Fit parameters for energy resolution to hadrons. Quoted uncertainties are statistical only.

4.6 Topological Cell clustering

In `ATLAS`, the tracking detectors do not cover the pseudorapidity region in which the FCal is located. The cylindrical clustering method thus cannot be used in `ATLAS`, as knowledge of the trajectories of incident particles is required in order to determine the point at which the particle impacts the calorimeter and thus form cylindrical clusters. Instead, `ATLAS` uses a topological clustering scheme ("topoclustering") for the reconstruction of hadronic energy deposits, in which neighbouring calorimeter cells are grouped together based on their signal to noise ratios [82]. Cluster seeds are found by searching for calorimeter cells that have an energy greater than some multiple, t_{seed}, of their noise RMS.

Neighbour cells are then added to the cluster provided they are adjacent to the seed cell and that their signal to noise ratio exceeds the neighbour threshold, $t_{\text{neighbour}}$. This step is then repeated, with additional neighbour cells being added to the cluster if they are adjacent to an existing neighbour cell and their signal to noise ratio exceeds $t_{\text{neighbour}}$. This procedure is iterated until no new neighbour cells are found. Finally, boundary or perimeter cells are added to the cluster by taking all cells that are adjacent to clustered cells and that have a significance greater than t_{cell}.

Hadronic clusters are reconstructed using a "420" scheme, i.e. t_{seed}, $t_{\text{neighbour}}$ and t_{cell} have values of 4,2 and 0, respectively. In this case, the signal is defined as the absolute value of the energy reconstructed in the calorimeter cell when searching for seed and neighbour cells. This ensures that contributions from noise are handled symmetrically. A high value of t_{seed} makes it unlikely that a cluster will be seeded purely from noise, while a low t_{cell} means that low energy cells around the periphery of the shower are still clustered. A "633" scheme is also used in ATLAS to cluster electromagnetic objects, and testbeam data has been used to investigate other clustering schemes[67].

The topoclustering software in `Athena` contains a splitting step [82], which is enabled by default. The splitter is intended to divide existing clusters into smaller clusters, such that there is a single cluster associated with each incident particle. New clusters are formed around local maxima, which are cells that satisfy the following conditions:

- The cell has an energy that is greater than the energies of any neighbouring cells.
- The cell has at least 4 neighboring cells that also belong to the original cluster.
- The cell has an energy that is greater than 500 MeV.

As the RMS of the noise in the hadronic modules of the FCal is close to 500 MeV, the splitter was turned off for the analysis of testbeam data in order to prevent noise fluctuations from creating new clusters.

4.6.1 Analysis of Electron Data

In addition to cylindrical clusters, topological clusters ("topoclusters") are formed during the reconstruction of each testbeam event. The cell-level noise values used to define these thresholds are obtained from analysis of randomly triggered testbeam data.

The response of the FCal to electrons (obtained using topological clustering) is shown in Figures 4.26 and 4.27, for beams at position 4L and 4H respectively. As with the results obtained using cylindrical clustering, the response is fit to the sum of a double Gaussian (for the electron peak) and a contribution derived from hadron data in order to account for any residual beam contamination. The results of the fits are listed in Tables 4.10 and 4.11. The noise contribution to the clusters is plotted as a function of the beam energy in Figure 4.28, for data taken at both position 4L and position 4H. This is estimated using randomly triggered events, as was done for the cylindrical clustering. For each physics event, a randomly triggered event is chosen. A cluster is formed in the randomly triggered event from all the cells that are clustered in the physics event. The clustered energy of the randomly triggered event is then taken as an estimate of the noise contribution to the cluster in the physics event. The clustered noise generally increases with the beam energy, as the clusters formed at higher beam energies tend to contain more cells.

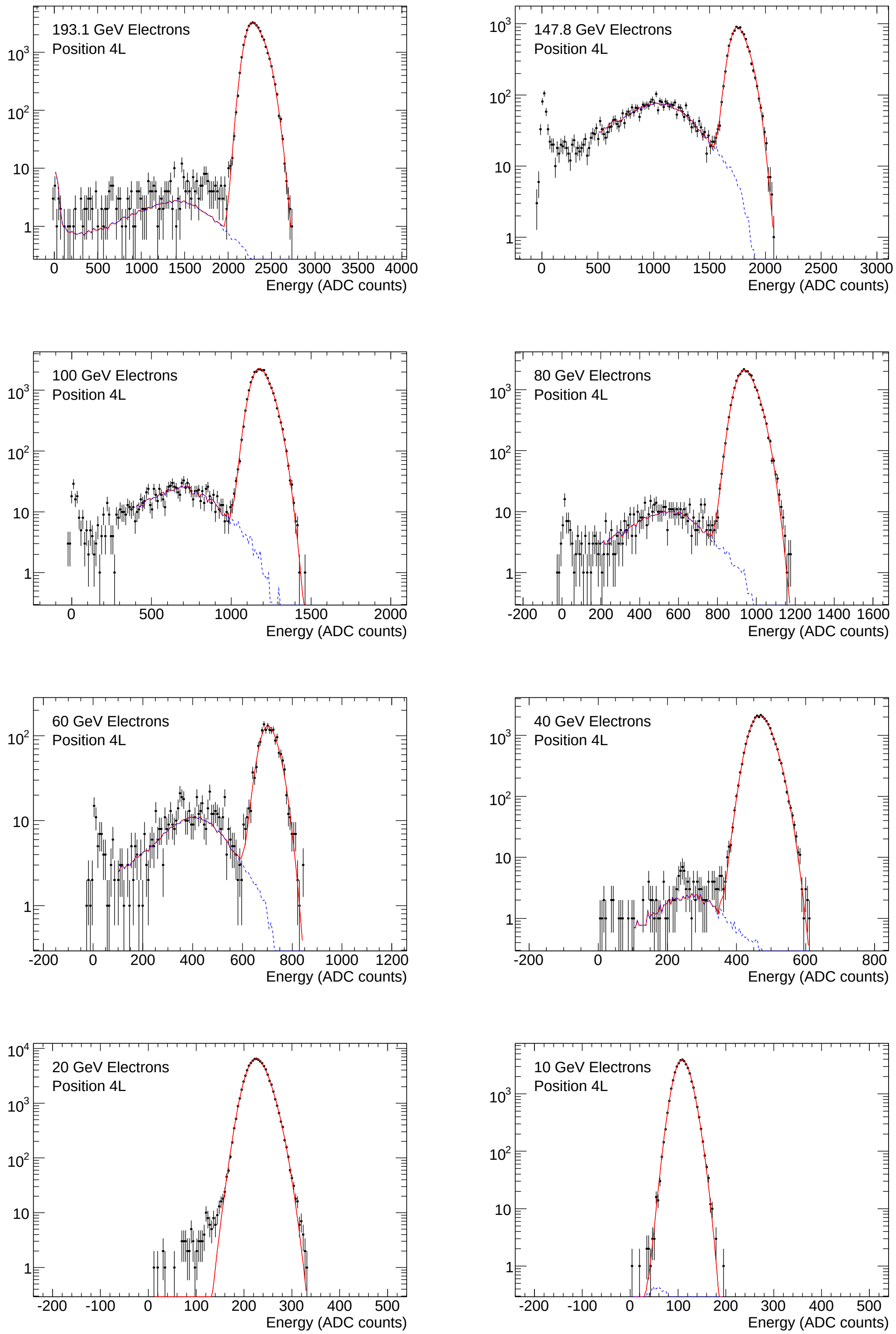

Figure 4.26: Response of the FCal to electrons at position 4L. The blue dashed curve shows the fit to the hadron contamination present in the data sample. The red curve is the total fit to the data, which consists of a double Gaussian fit to the electron peak as well as the fit to the hadron contamination.

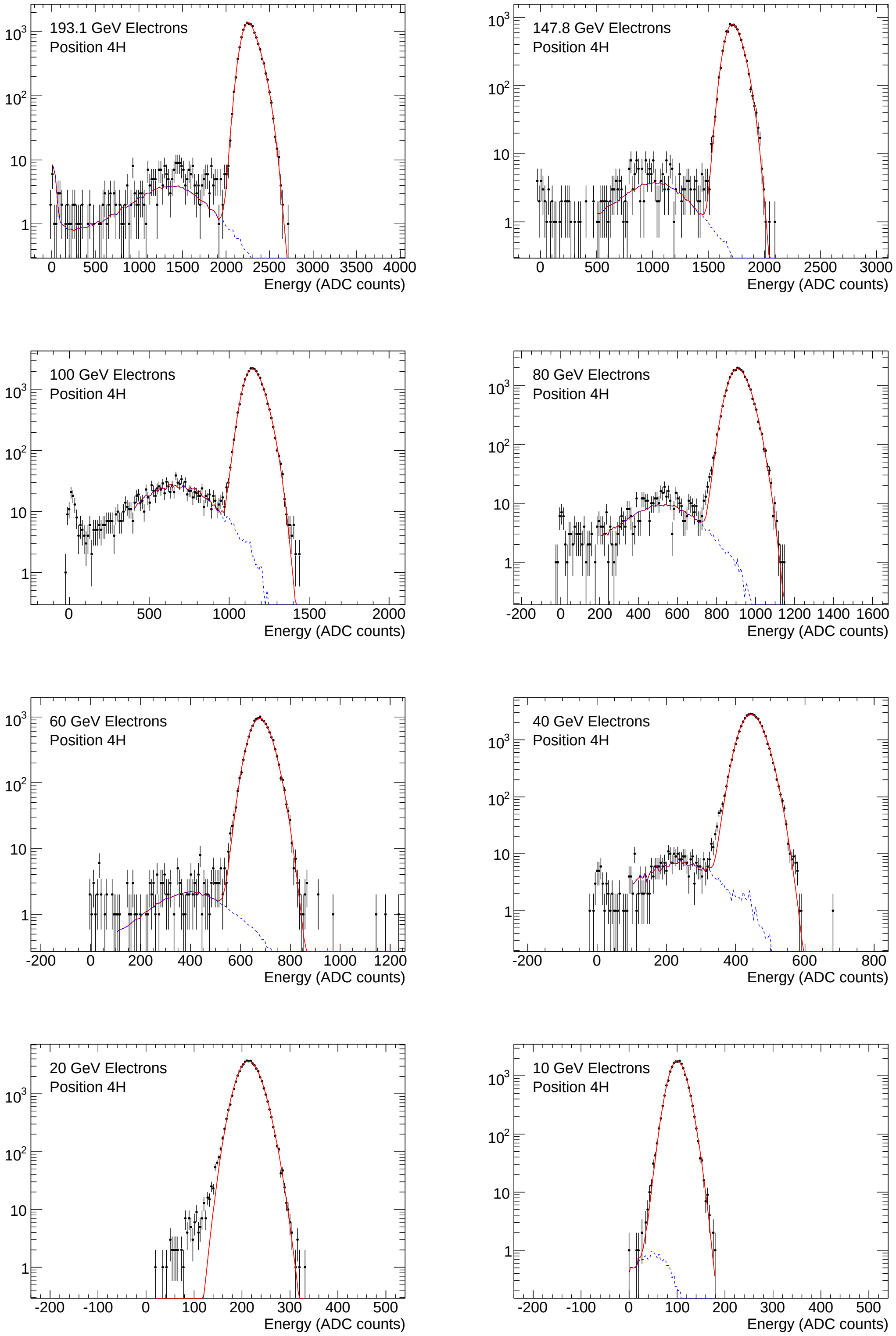

Figure 4.27: Response of the FCal to electrons at position 4H. The blue dashed curve shows the fit to the hadron contamination present in the data sample. The red curve is the total fit to the data, which consists of a double Gaussian fit to the electron peak as well as the fit to the hadron contamination.

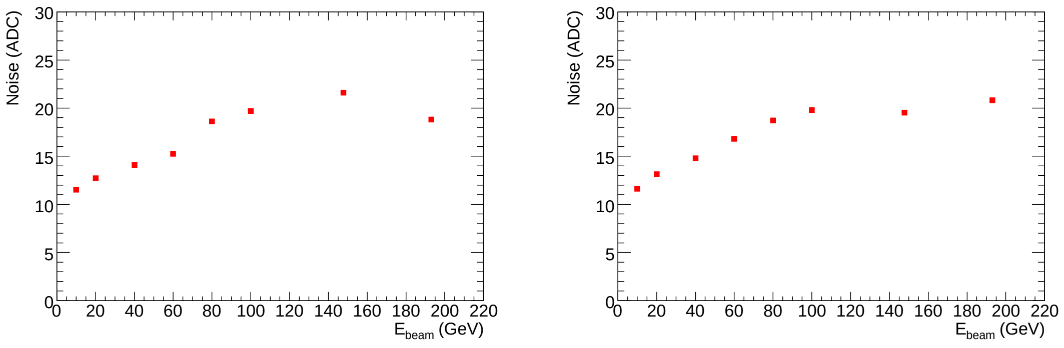

(a)

(b)

Figure 4.28: Clustered noise vs beam energy, for topologically clustered electrons at position 4L (a) and 4H(b).

The linearity of the FCal response obtained using topological clusters is shown in Figure 4.29, and the residuals obtained after fitting are plotted in Figure 4.30. The slopes obtained from these results are marginally higher than those obtained using cylindrical clustering, while the intercepts are slightly lower. Cells containing low amounts of energy may be excluded from the topoclusters in cases where they would be included in a cylindrical cluster, giving the topoclusters a lower energy than the cylindrical clusters. This effect is more significant at lower energies, and may be the cause of the lower intercept and higher slope seen in the topoclustered results. The difference between the intercepts measured at position 4H and position 4L in data is similar to the difference

Beam Energy (GeV)	Fitted Mean (ADC)	Fitted Width (ADC)	Noise (ADC)
193.1 GeV	2312.4 ± 0.5	95.4 ± 0.3	18.8 ± 0.1
147.8 GeV	1769.8 ± 0.8	77.5 ± 0.5	21.6 ± 0.1
100 GeV	1189.3 ± 0.3	58.0 ± 0.2	19.7 ± 0.1
80 GeV	948.1 ± 0.3	49.2 ± 0.2	18.6 ± 0.1
60 GeV	708 ± 1	37.0 ± 0.7	15.3 ± 0.2
40 GeV	471.2 ± 0.2	30.2 ± 0.1	14.1 ± 0.1
20 GeV	227.8 ± 0.1	20.9 ± 0.1	12.72 ± 0.03
10 GeV	109.6 ± 0.1	15.9 ± 0.1	11.54 ± 0.04

Table 4.10: Results for the FCal response to electrons, using topologically clustered data from beams at position 4L. Quoted uncertainties are statistical only.

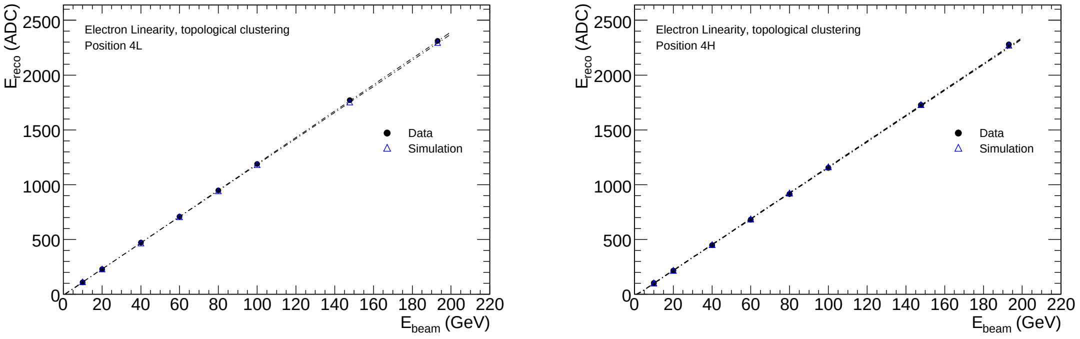

(a) (b)

Figure 4.29: Mean response as a function of beam energy, for electrons at 4L (a) and 4H (b).

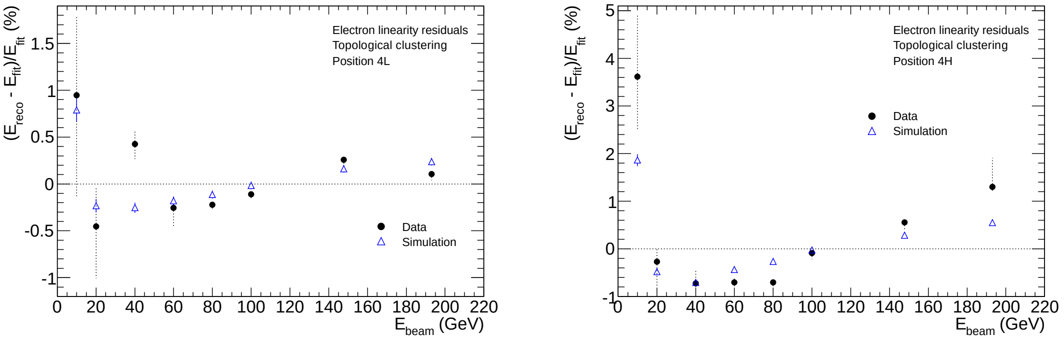

(a) (b)

Figure 4.30: Residuals obtained from the linearity fit for electrons at position 4L (a) and 4H (b). Solid lines in the error bars represent the statistical uncertainties, while the systematic uncertainties are represented by dotted lines.

Beam Energy (GeV)	Fitted Mean (ADC)	Fitted Width (ADC)	Noise (ADC)
193.1 GeV	2278.5 ± 0.7	91.9 ± 0.5	20.8 ± 0.1
147.8 GeV	1726.5 ± 0.8	73.2 ± 0.5	19.5 ± 0.1
100 GeV	1154.2 ± 0.3	56.5 ± 0.2	19.8 ± 0.1
80 GeV	913.8 ± 0.3	50.0 ± 0.2	18.7 ± 0.1
60 GeV	680.4 ± 0.4	41.1 ± 0.3	16.8 ± 0.1
40 GeV	446.9 ± 0.2	31.2 ± 0.1	14.8 ± 0.1
20 GeV	214.6 ± 0.1	22.1 ± 0.1	13.13 ± 0.04
10 GeV	101.2 ± 0.1	17.0 ± 0.1	11.6 ± 0.1

Table 4.11: Results for the FCal response to electrons, using topologically clustered data from beams at position 4H. Quoted uncertainties are statistical only.

linearity result	slope (ADC/GeV)	Intercept (ADC)
Data (4L)	12.023 ± 0.002	-11.67 ± 0.07
Simulation (4L)	11.905 ± 0.003	-7.96 ± 0.12
Data (4H)	11.751 ± 0.002	-19.86 ± 0.09
Simulation (4H)	11.789 ± 0.003	-16.74 ± 0.12

Table 4.12: Linearity results for electron data. Quoted uncertainties are statistical.

seen in the simulation results. In data, the intercept for position 4L is 8.2 ADC counts higher than the intercept for position 4H, while this difference is 8.8 ADC counts in the simulation results. These differences are similar to those seen in the cylindrically clustered results. Systematic uncertainties are estimated using the same methods employed for cylindrical clustering. The slope and intercept for the fit to the linearity at position 4L are (12.02 ± 0.06) GeV/ADC and (-11.7 ± 1.2) ADC counts, respectively, where the quoted uncertainties are dominated by systematic effects. At position 4H, the slope is (11.75 ± 0.07) GeV/ADC and the intercept is (-19.9 ± 2.3) ADC counts. Statistical uncertainties on these quantities are given in Table 4.12.

The energy resolution is plotted in Figure 4.31, with fit results listed in Table 4.13. The noise subtraction procedure is done in the same way as for the cylindrically clustered case. To estimate the systematic uncertainty associated with the choice of clustering method, a “430” clustering scheme was also used and compared with the results of the

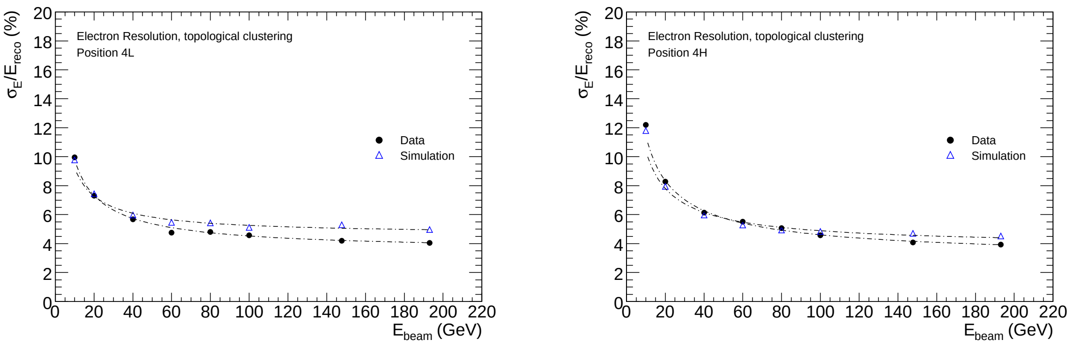

(a)

(b)

Figure 4.31: Energy resolution of the FCal to electrons at position 4L (a) and position 4H (b).

"420" method. The beam energy fluctuations and choice of clustering are again the dominant effects, with other sources of uncertainty providing much smaller contributions to the uncertainty.

The resolution at position 4L has a stochastic term of $(28.8 \pm 0.6)\ \% \cdot \mathrm{GeV}^{1/2}$ and a constant term of $(3.49 \pm 0.05)\ \%$, while at 4H the stochastic term is $(34.8 \pm 1.0)\ \% {\cdot} \mathrm{GeV}^{1/2}$ and the constant term is $(3.02 \pm 0.20)\ \%$. The quoted uncertainties are again dominated by systematic effects. The resolution results for topological clusters are quite similar to those obtained from cylindrical clusters (c.f. table 4.6), with the simulation results having a slightly worse resolution than that seen in data. The topoclustering procedure tends to exclude cells with low energy, which reduces the number of cells sampled and thus causes a slight increase in the stochastic term compared to the case for cylindrical clustering. The constant term from the simulation results is 21% higher at position 4L than at 4H, whereas in data this increases by (16 ± 8%), and so these ratios are consistent when the systematic uncertainties associated with the data are considered.

4.6.2 Analysis of Hadron Data

The ratio of the mean (EM scale) response of the FCal to the beam energy is plotted in Figure 4.32, for hadron events in which the response has been obtained using topological

	Stochastic Term (% GeV$^{1/2}$)	Constant Term (%)
Data (4L)	28.8 ± 0.1	3.49 ± 0.02
Simulation (4L)	25.2 ± 0.3	4.62 ± 0.02
Data (4H)	34.8 ± 0.2	3.02 ± 0.03
Simulation (4H)	30.5 ± 0.3	3.82 ± 0.03

Table 4.13: Fit parameters for energy resolution to electrons. Quoted uncertainties are statistical only.

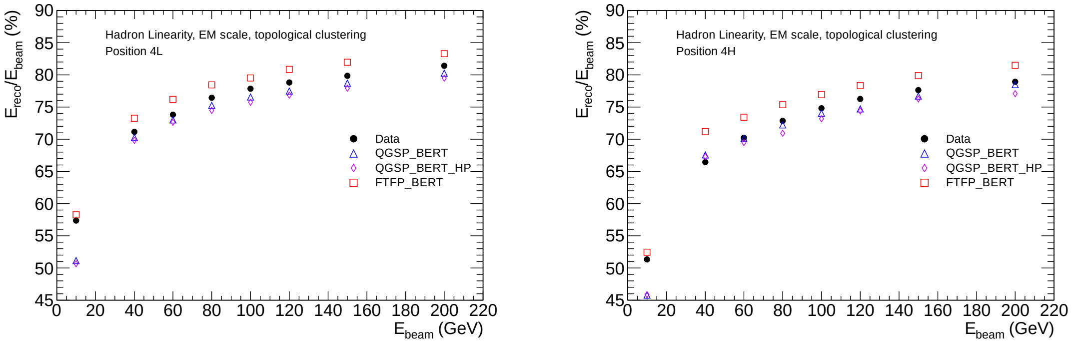

(a) (b)

Figure 4.32: Ratio of energy reconstructed at the EM scale to the beam energy, for hadrons at position 4L (a) and 4H (b).

clusters. These plots exhibit the same behaviour seen using cylindrical clustering (c.f. Figure 4.19), although there is better agreement between data and simulation at lower energies. This may be due to the shorter and narrower shower shapes seen in the simulation results. The more compact showers give rise to a higher energy density, which leads to a larger fraction of the deposited energy being included in the cluster. The topocluster thus contains a larger fraction of the shower's energy in the simulation than in data.

The weights used for hadronic calibration are derived for topoclusters using the same method as for cylindrical clusters, and are plotted in Figure 4.33. At high energy, the weights are very similar to those obtained for cylindrical clusters, and there is good agreement between data and MC. At lower energies less energy is contained within the topological clusters, and so the derived weights in FCal1 and FCal2 are larger than for the cylindrically clustered case. Again, only the weights derived from data at 200 GeV

Beam Energy (GeV)	Fitted Mean (GeV)	Fitted Width (GeV)	Noise (GeV)
200 GeV	200.07 ± 0.06	19.57 ± 0.04	5.13 ± 0.01
150 GeV	147.15 ± 0.05	16.01 ± 0.03	4.72 ± 0.01
120 GeV	116.09 ± 0.06	13.88 ± 0.05	4.31 ± 0.01
100 GeV	95.6 ± 0.1	12.95 ± 0.08	4.76 ± 0.03
80 GeV	75.06 ± 0.06	10.97 ± 0.04	4.09 ± 0.02
60 GeV	54.33 ± 0.03	9.10 ± 0.02	3.58 ± 0.01
40 GeV	34.89 ± 0.09	7.59 ± 0.06	3.13 ± 0.03
10 GeV	7.03 ± 0.06	3.27 ± 0.04	1.91 ± 0.03

Table 4.14: FCal response to hadrons at position 4L, obtained from fits to topologically clustered data.

Beam Energy (GeV)	Fitted Mean (GeV)	Fitted Width (GeV)	Noise (GeV)
200 GeV	200.24 ± 0.07	22.53 ± 0.05	5.21 ± 0.01
150 GeV	147.51 ± 0.05	18.63 ± 0.03	4.87 ± 0.01
120 GeV	116.05 ± 0.05	16.54 ± 0.04	4.94 ± 0.01
100 GeV	94.99 ± 0.09	15.23 ± 0.06	4.85 ± 0.02
80 GeV	74.03 ± 0.05	13.28 ± 0.04	4.60 ± 0.01
60 GeV	53.54 ± 0.03	10.82 ± 0.02	3.83 ± 0.01
40 GeV	33.8 ± 0.1	8.62 ± 0.08	3.13 ± 0.03
10 GeV	6.52 ± 0.06	3.41 ± 0.04	1.91 ± 0.02

Table 4.15: FCal response to hadrons at position 4H, obtained from fits to topologically clustered data.

have been used to calibrate data and simulation results to the hadronic scale, although weights derived from data at other beam energies have been used to estimate systematic uncertainties. Results in which the data has been reconstructed using weights derived from MC are given in Appendix B.

The calibrated responses are plotted in Figures 4.34 and 4.35, and the contributions to clusters from noise are plotted in Figure 4.36. The fit results are summarised in Tables 4.14 and 4.15. When compared to the cylindrically clustered results, the mean responses obtained using topological clustering are slightly lower. However, the noise contribution to the topological clusters is significantly lower than that seen for cylindrical clusters due to the noise suppressing properties of the topological clustering procedure.

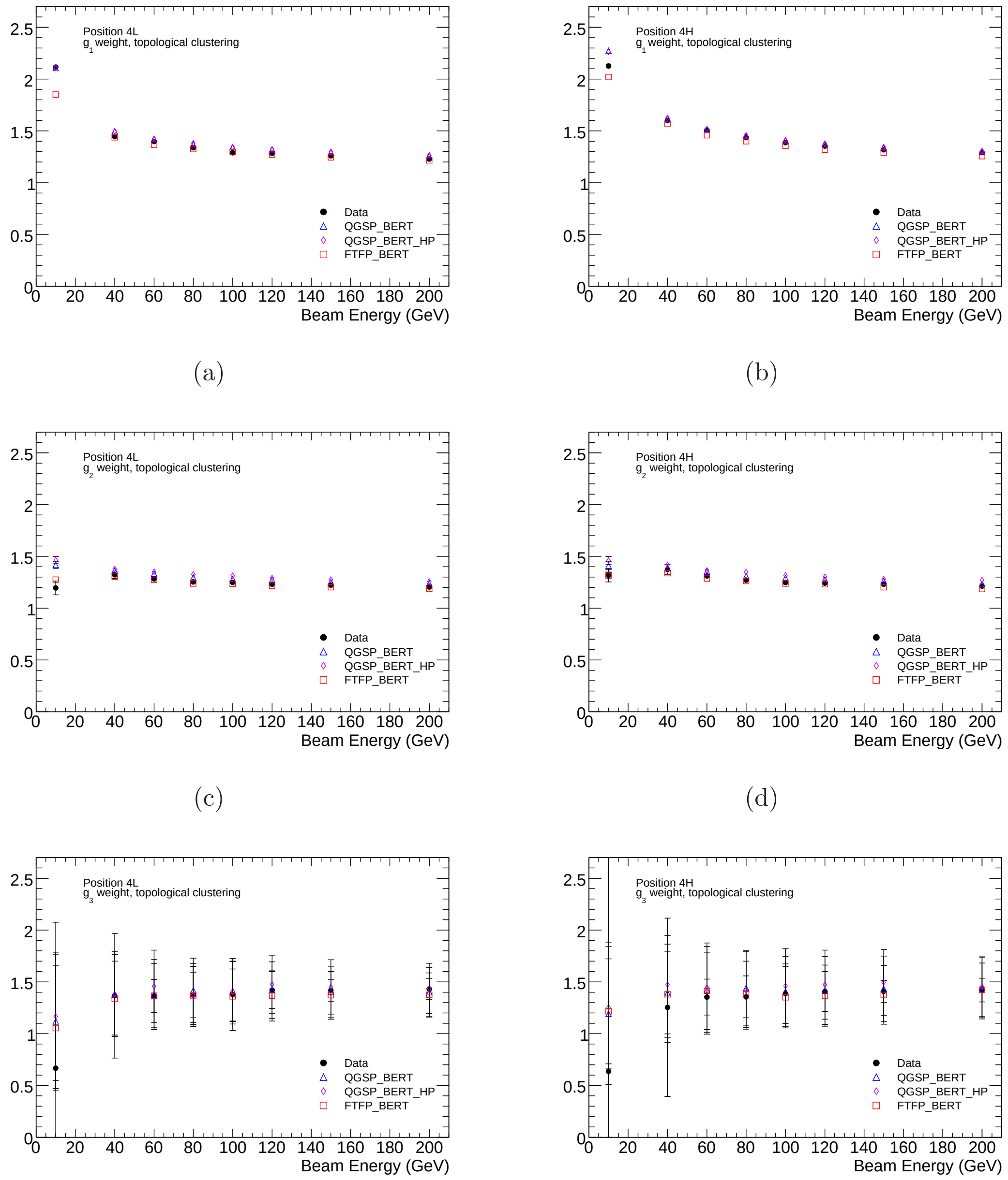

(a) (b) (c) (d) (e) (f)

Figure 4.33: Flat weights used in hadronic calibration, as a function of the energy at which they are derived. Only the weights derived using 200GeV are used in the analysis. Figures (a), (c) and (e) show the weights g_1, g_2, and g_3, respectively, for position 4L, while figures (b), (d), and (f), respectively, show g_1, g_2, and g_3 for 4H.

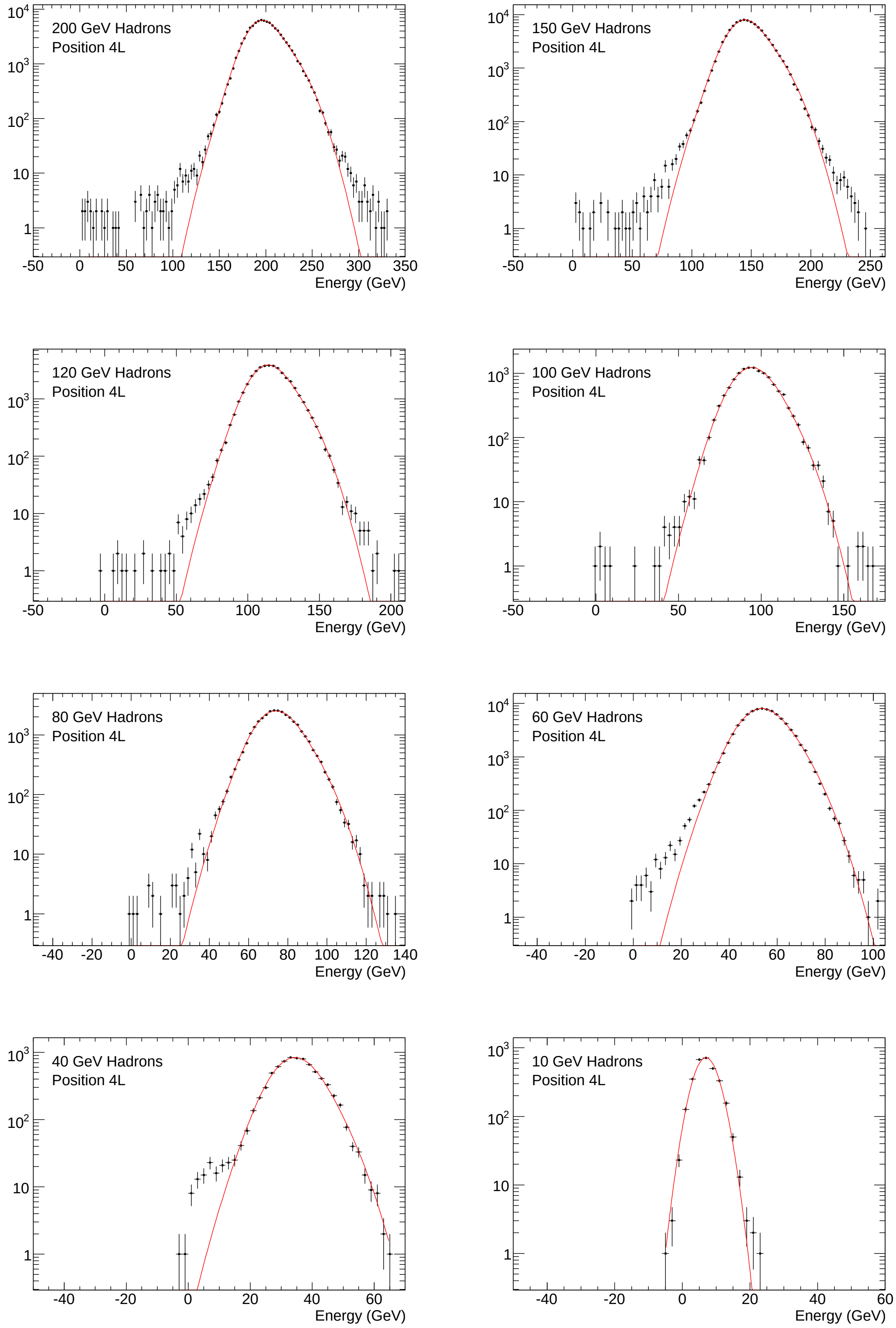

Figure 4.34: Response of the FCal to hadrons at position 4L. The response is obtained using a topological clustering method.

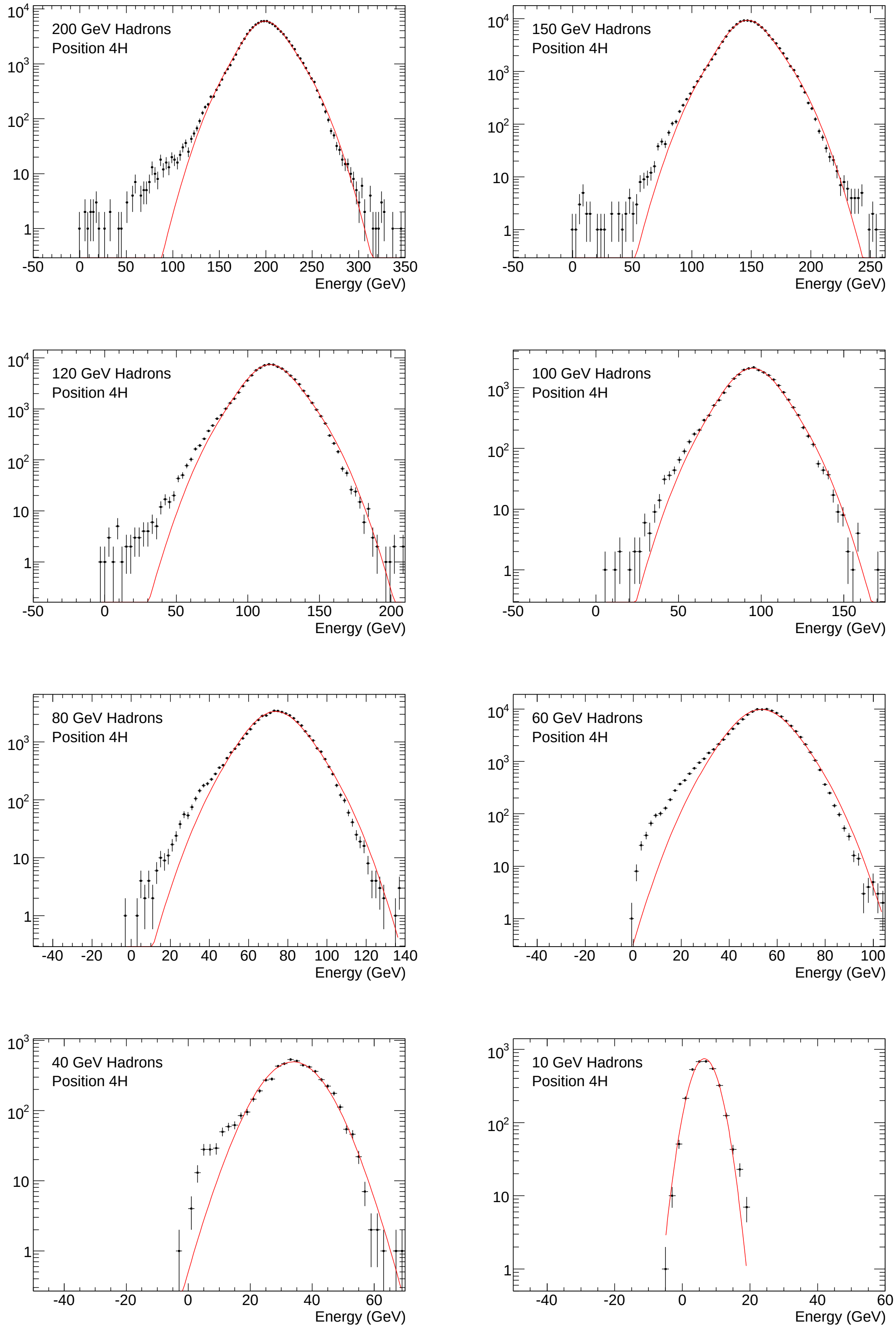

Figure 4.35: Response of the FCal to hadrons at position 4H. The response is obtained using a topological clustering method.

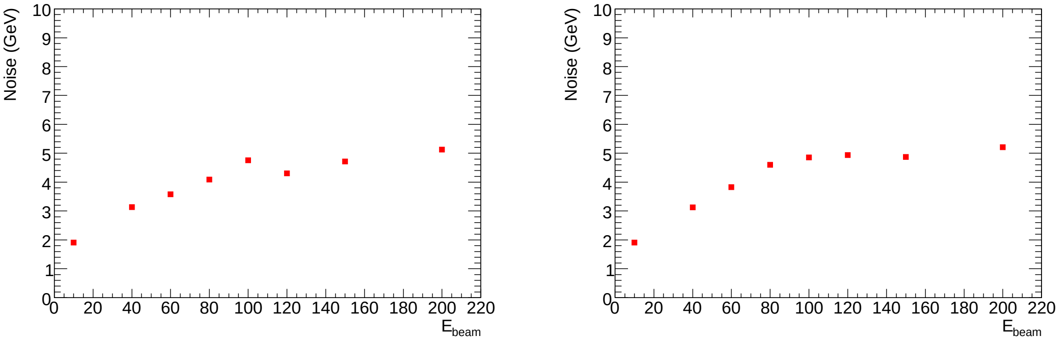

(a)

(b)

Figure 4.36: Clustered noise vs beam energy, for topologically clustered hadrons at position 4L (a) and 4H (b).

The mean response at the hadronic scale is plotted in Figure 4.37 as a function of beam energy. Again, as most of the energy is deposited in FCal1 and FCal2, which have similar weights, the shape of this plot is very similar to that seen at the EM scale in Figure 4.32. Simulations using the QGSP_BERT and QGSP_BERT_HP physics lists tend to deposit slightly less energy in the calorimeter than seen in data, whereas those using the FTFP_BERT physics list deposit slightly more.

At lower beam energies, the mean response obtained using topological clusters is lower than that obtained using cylindrical clusters, as can be seen by comparing Figures 4.24 and 4.37. The topological clustering algorithm excludes cells from the cluster if their energy is lower than the relevant threshold*. Because of this, at lower beam energies a larger fraction of the shower's energy is excluded from the topocluster. This results in the mean response being somewhat lower at energies below 200 GeV when compared to the cylindrically clustered case.

The resolution is plotted in Figure 4.38, and fit results are listed in Table 4.16. Again, as less energy is included in the topological clusters the stochastic term is substantially increased compared to the resolutions obtained from cylindrical clustering, by ∼ 20% at

---

*Note that more sophisticated calibration schemes include "out of cluster" corrections, which correct for energy lost in this way.

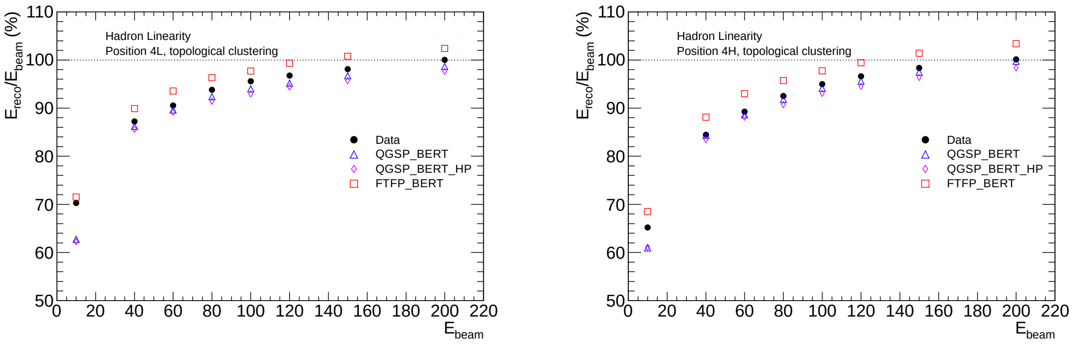

(a) (b)

Figure 4.37: Ratio of reconstructed energy to the beam energy, for hadrons at position 4L (a) and 4H (b). Flat weights have been applied to calibrate the reconstructed energy to the hadronic scale.

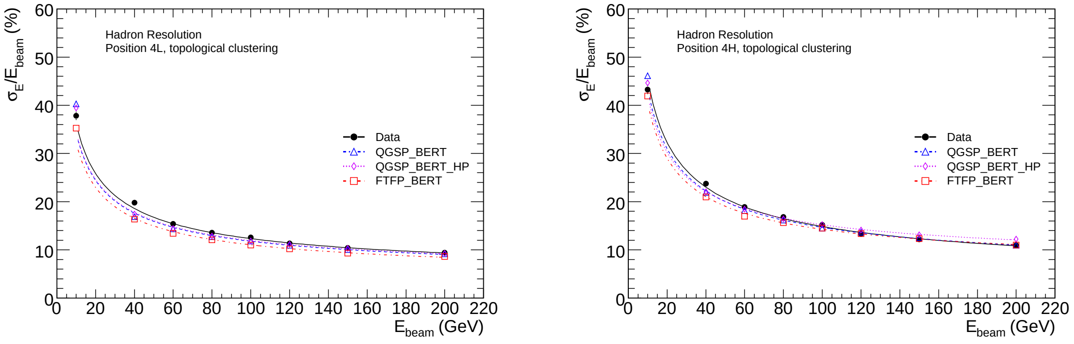

(a) (b)

Figure 4.38: Energy resolution of the FCal to hadrons at position 4L (a) and position 4H (b). Flat weights have been applied to calibrate the reconstructed energy to the hadronic scale.

position 4L and by 10-20 % at position 4H. In spite of this increase in the stochastic term, the resolution at 200GeV (and hence the constant term) is relatively unchanged.

The systematic effects considered when using topological clusters are the same as those that were considered for the resolution to hadrons obtained using cylindrical clustering, with “430” clusters again being used to estimate the uncertainty associated with the choice of clustering method. These uncertainties are again dominated by the choice of hadronic weights, giving values of (114 ± 2) % $\cdot$ GeV$^{1/2}$ for the stochastic term and (4.9 ± 0.3%) for the constant term at position 4L. At position 4H the stochastic term is

(137 ± 6) $\% \cdot \mathrm{GeV}^{1/2}$while the constant term is (3.8 ± 1.3%).

	Stochastic Term (% $\mathrm{GeV}^{1/2}$)	Constant Term (%)
Data (4L)	113.5 ± 0.4	4.86 ± 0.08
QGSP_BERT (4L)	107.0 ± 0.7	4.97 ± 0.12
QGSP_BERT_HP (4L)	107.6 ± 0.7	5.18 ± 0.12
FTFP_BERT (4L)	100.7 ± 0.6	4.59 ± 0.12
Data (4H)	143.6 ± 0.4	3.80 ± 0.12
QGSP_BERT (4H)	136.6 ± 0.8	5.30 ± 0.17
QGSP_BERT_HP (4H)	130.1 ± 0.8	7.77 ± 0.12
FTFP_BERT (4H)	126.4 ± 0.7	6.62 ± 0.13

Table 4.16: Fit parameters for energy resolution for hadrons, obtained using topologically clustered data. Quoted uncertainties are statistical only.

4.6.3 Cluster moments

Local Hadronic Calibration is one of the main methods for calibrating energy deposits to the hadronic scale used at `ATLAS` [83]. This method is applied to topological clusters, and makes use of various moments that describe the shape of the shower in order to distinguish between electromagnetic and hadronic energy deposits. Weights are then applied to clusters that are classified as hadronic, in order to calibrate their energy to the hadronic scale. This technique differs from other weighting schemes, such as the flat weights used in this analysis and the EM+JES method described in chapter 5, which apply an average weight to all energy deposits.

A cluster's shape may be be described in terms of "cluster moments", which may then be used to classify the cluster. As EM showers are on average shorter and narrower than hadronic showers, a good understanding of the shower shape allows the cluster to be classified as EM or hadronic. It is important to understand the level of agreement between data and Monte Carlo for this, as the hadronic calibration schemes used at `ATLAS` are derived entirely from Monte Carlo simulations.

The shower centre, $\vec{c}$, and the shower axis, $\hat{s}$ are two vector quantities that are used

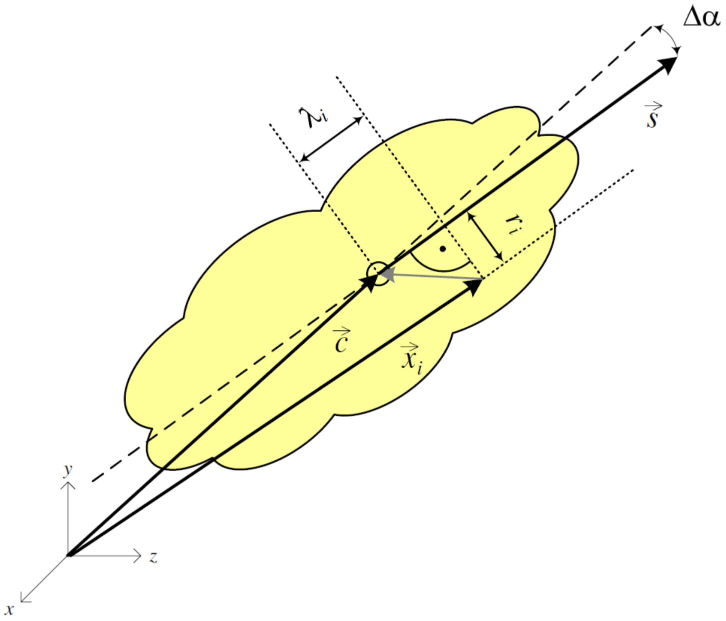

Figure 4.39: Illustration of some of the quantities used in the computation of cluster moments[81].

when defining certain moments. The shower centre is the energy weighted barycentre of the cluster, such that

$$\vec{c} = (c_x, c_y, c_z) \tag{4.18}$$

where

$$c_x = \frac{\sum_i E_i x_i}{\sum_i E_i} \tag{4.19}$$

$$c_y = \frac{\sum_i E_i y_i}{\sum_i E_i} \tag{4.20}$$

$$c_z = \frac{\sum_i E_i z_i}{\sum_i E_i} \tag{4.21}$$

where E_i and $\vec{x_i} = (x_i, y_i, z_i)$ are the energy and position of the position of the i-th cell, respectively, and the sums run over all cells in the cluster. Note that the coordinate system used for the moment calculations is defined with respect to the FCal and its nominal position in `ATLAS`. In `ATLAS`, the origin of the coordinate system is the interaction point, and the front face of FCal1 lies in the plane z = -4.7m. For the testbeam, the

FCal has been oriented such that beam particles will pass (approximately) through the origin [*].

The shower axis is a unit vector that describes the direction in which the shower propagates through the calorimeter. Because the beam particles are passing through the origin (or, in `ATLAS`, emerging from the interaction point), $\hat{s}$ should have a similar direction to $\vec{c}$. The shower axis is found by diagonalising the matrix

$$C = \begin{pmatrix} C_{xx} & C_{xy} & C_{xz} \\ C_{yx} & C_{yy} & C_{yz} \\ C_{zx} & C_{zy} & C_{zz} \end{pmatrix} \tag{4.22}$$

where, for example, the elements C_{xx} and C_{xy} are given by

$$C_{xx} = \frac{\sum_i E_i^2 (x_i - c_x)^2}{\sum_i E_i^2} \tag{4.23}$$

$$C_{xy} = \frac{\sum_i E_i^2 (x_i - c_x)(y_i - c_y)}{\sum_i E_i^2} \tag{4.24}$$

and other elements are defined analogously. The matrix C thus describes spatial correlations in the energy deposited by the shower. The eigenvector of C with direction closest to $\vec{c}$ is then normalised to obtain $\hat{s}$. However, in cases where the angle $\Delta\alpha$ between $\hat{s}$ and $\vec{c}$ exceeds $30°$, $\hat{s}$ is instead taken as $\vec{c}/|\vec{c}|$. Because all cell positions in FCal1 have the same z value, the energy deposited by an electron shower may have very little spread in z. This can result in eigenvectors that lie mainly in the $x - y$ plane, and thus in large values of $\Delta\alpha$.

The quantity λ_i is defined as the distance of the i-th cell from the cluster centre,

---

[*] The vertical inclination of the beams mean that particle coordinates have a non-zero y component when $x = z = 0$. The beamspot also has a finite radius.

projected onto the shower axis, such that

$$\lambda_i = (\vec{x_i} - \vec{c}) \cdot \hat{s}, \tag{4.25}$$

as illustrated in Figure 4.39. Similarly, r_i describes the component of the distance from the i-th cell to the cluster centre that is perpendicular to $\hat{s}$, and is given by

$$r_i = |(\vec{x_i} - \vec{c}) \times \hat{s}|. \tag{4.26}$$

These quantities are used to compute the moments $\langle r^2 \rangle$ and $\langle \lambda^2 \rangle$, which characterise the transverse width and longitudinal length of the shower, respectively. These moments are the energy weighted second moments of r_i and λ_i, and are given by

$$\langle r^2 \rangle = \frac{\sum_i E_i r_i^2}{\sum_i E_i} \tag{4.27}$$

$$\langle \lambda^2 \rangle = \frac{\sum_i E_i \lambda_i^2}{\sum_i E_i} \tag{4.28}$$

The distributions of $\langle r^2 \rangle$, for both data and simulation results (for electrons and pions at positions 4L and 4H), are plotted in Figure 4.40, while $\langle \lambda^2 \rangle$ is plotted in Figure 4.41.

The quantity λ_c, while not strictly a “moment”, describes the distance from the face of the calorimeter to the cluster centre, measured along the shower axis. For the FCal, the calorimeter front face is perpendicular to the z axis and so λ_c is given by

$$\lambda_c = (c_z - f_z)/s_z, \tag{4.29}$$

where f_z = -4.7m. Distributions of λ_c are plotted in Figure 4.42.

The final moment considered here is the energy weighted energy density of the cluster.

The energy density in the i-th cell in the cluster is given by

$$\rho_i = E_i / V_i, \tag{4.30}$$

where V_i is the cell volume. The moment $\langle \rho \rangle$ is then given by

$$\langle \rho \rangle = \frac{\sum_i E_i \rho_i}{\sum_i E_i}, \tag{4.31}$$

and is plotted in Figure 4.43.

Generally, for electrons the data and simulation results agree very well at both positions 4L and 4H. These results are also consistent with those obtained from analysis of the 2004 combined testbeam[84], in which a prototype FCal module was used. For hadrons there are some slight differences between the data and simulation results, which are most significant in the $\langle r^2 \rangle$ distributions. The simulation gives results for $\langle r^2 \rangle$, $\langle \lambda^2 \rangle$, and λ_c that are lower than those seen in data. These effects can be attributed to the observed size of the hadronic showers in simulation, which are shorter and narrower than those seen in data (as can be seen from Figures 4.17 and 4.18). The energy density is slightly higher in the simulation results than in data, but this is also attributed to the more compact shower size produced by the simulation. Again, the cluster moments from hadronic showers presented here are consistent with those obtained from the 2004 testbeam analysis[84]. The shower moments obtained from Monte Carlo agree well with those obtained from data, validating the use of Monte Carlo in the derivation of the local hadronic calibration.

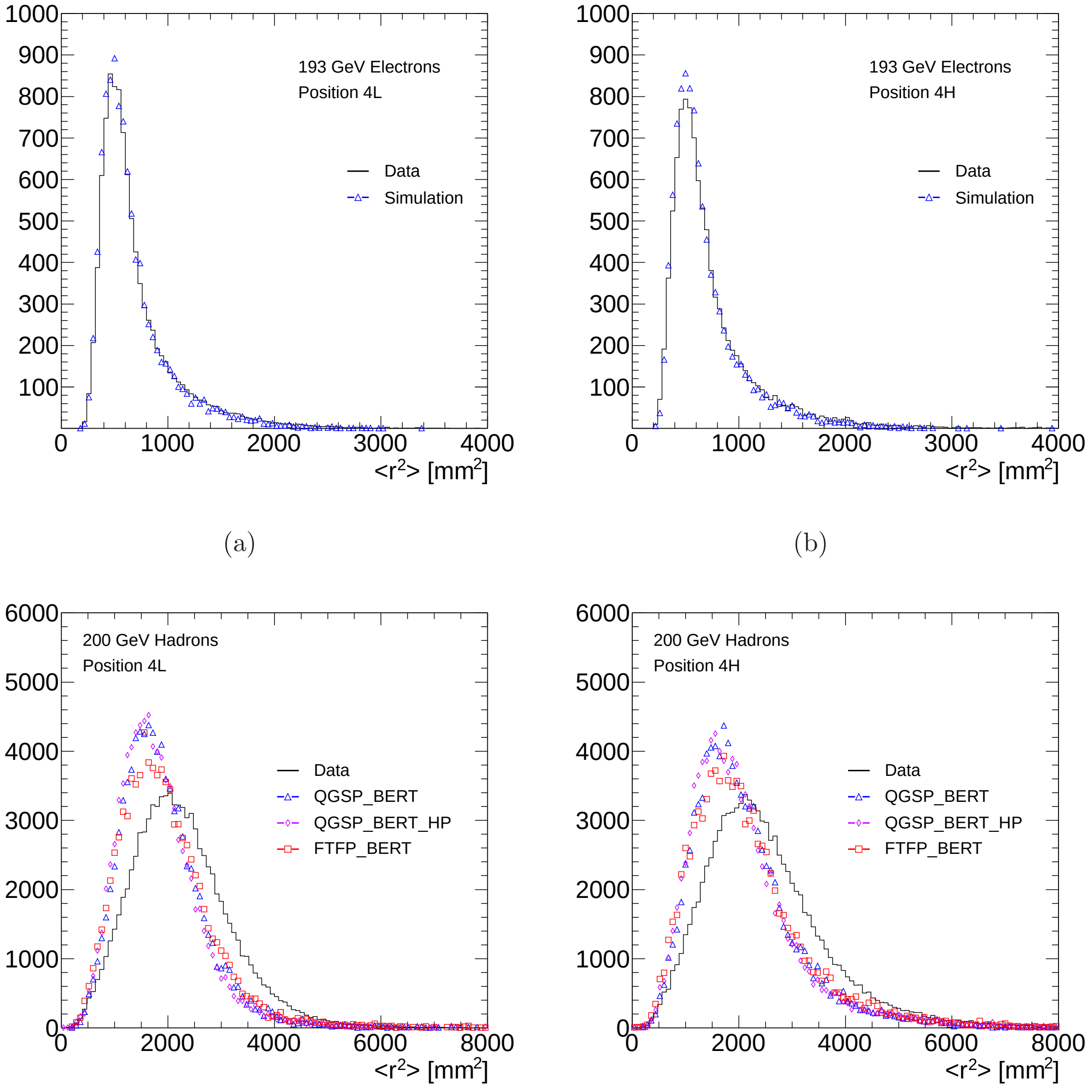

(a) (b)

(c) (d)

Figure 4.40: Shower moments derived from topological clusters. The upper plots show the distributions of $\langle r^2 \rangle$ obtained at position 4L (a) and 4H (b), from 193.1 GeV electrons. The lower plots show the same distributions obtained from 200GeV hadrons at position 4L (c) and 4H (d).

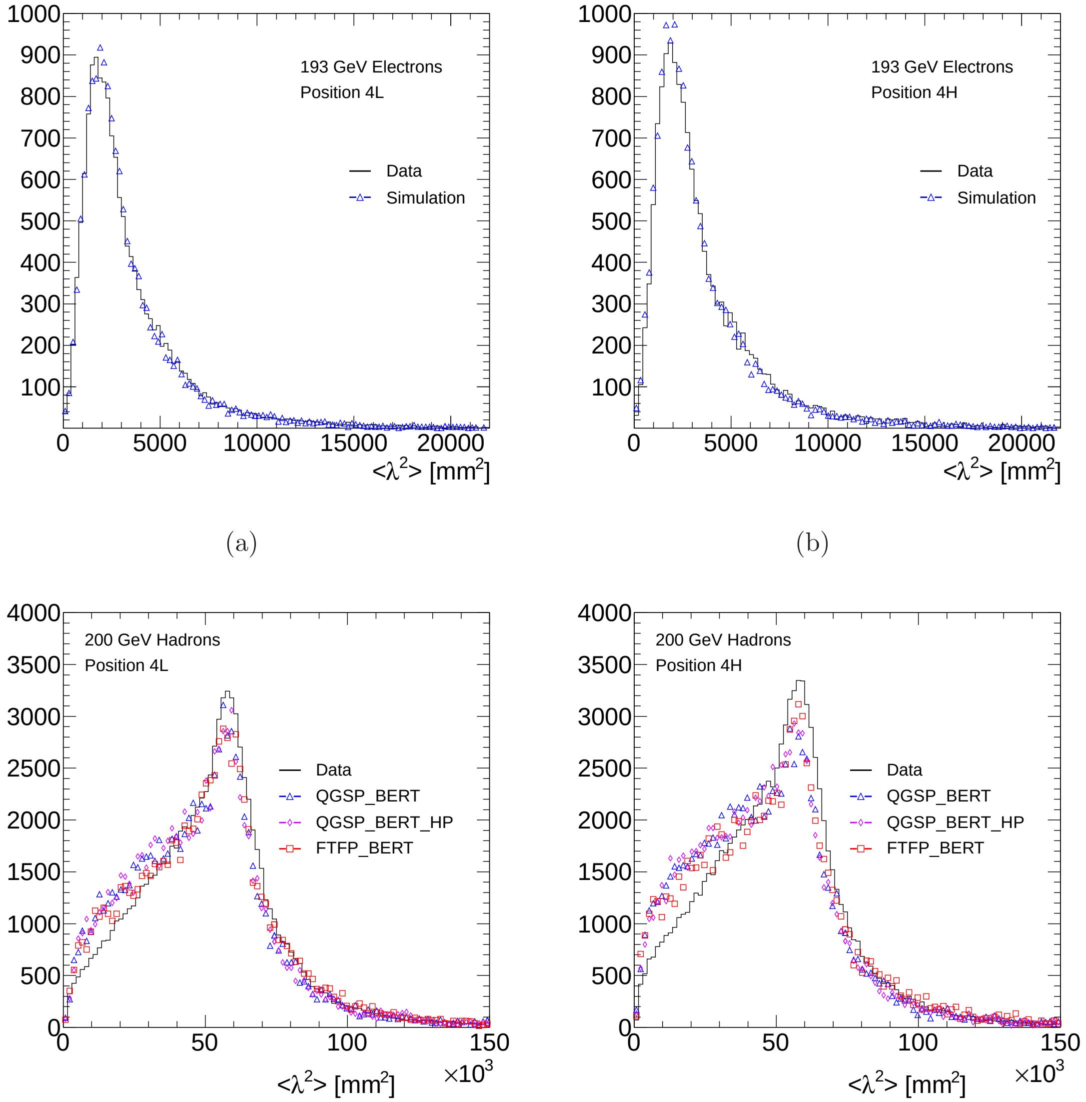

(a)

(b)

(c)

(d)

Figure 4.41: Shower moments derived from topological clusters. The upper plots show the distributions of $\langle r^2 \rangle$ obtained at position 4L (a) and 4H (b), from 193.1 GeV electrons. The lower plots show the same distributions obtained from 200GeV hadrons at position 4L (c) and 4H (d).

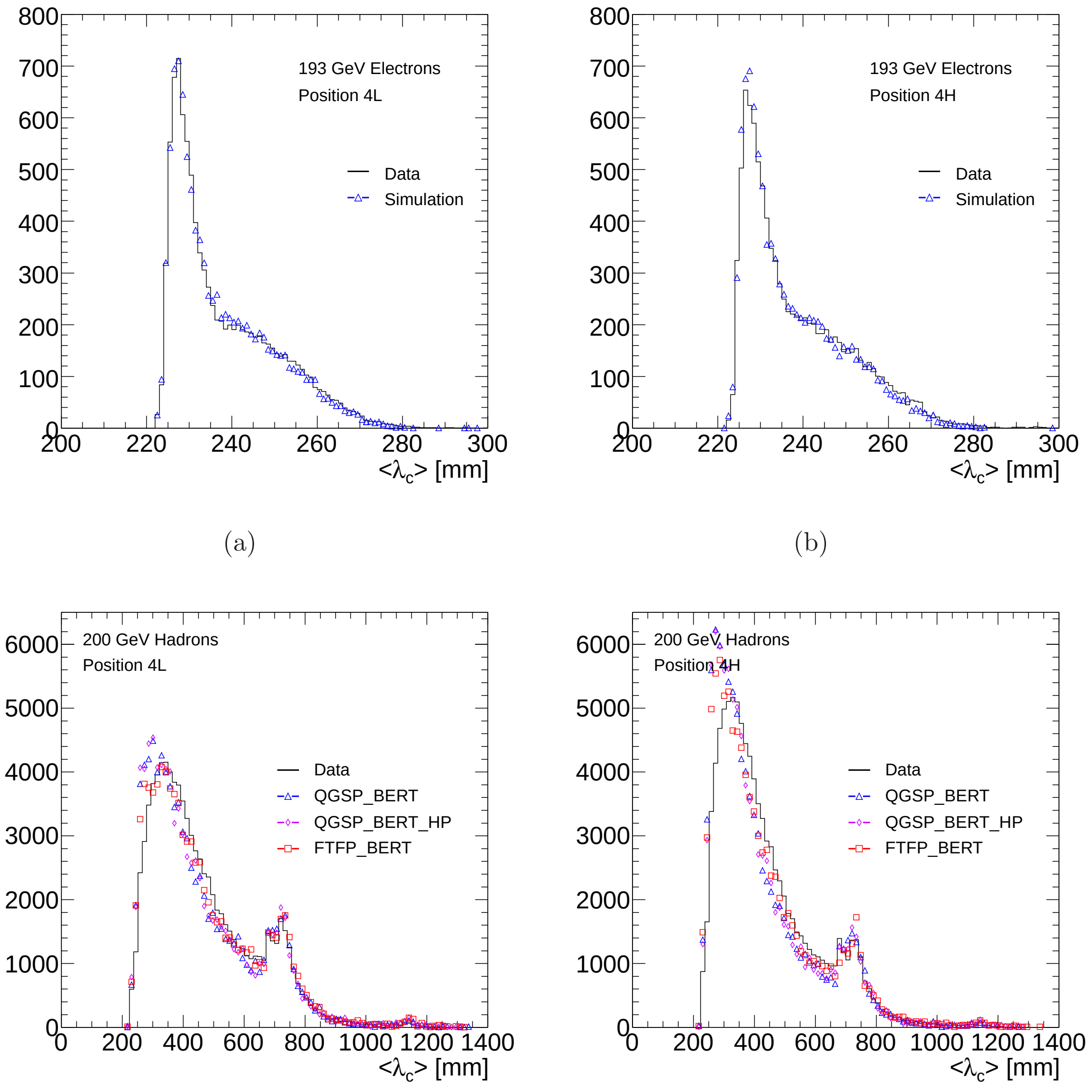

(a) (b)

(c) (d)

Figure 4.42: Shower moments derived from topological clusters. The upper plots show the distributions of λ_c obtained at position 4L (a) and 4H (b), from 193.1 GeV electrons. The lower plots show the same distributions obtained from 200GeV hadrons at position 4L (c) and 4H (d).

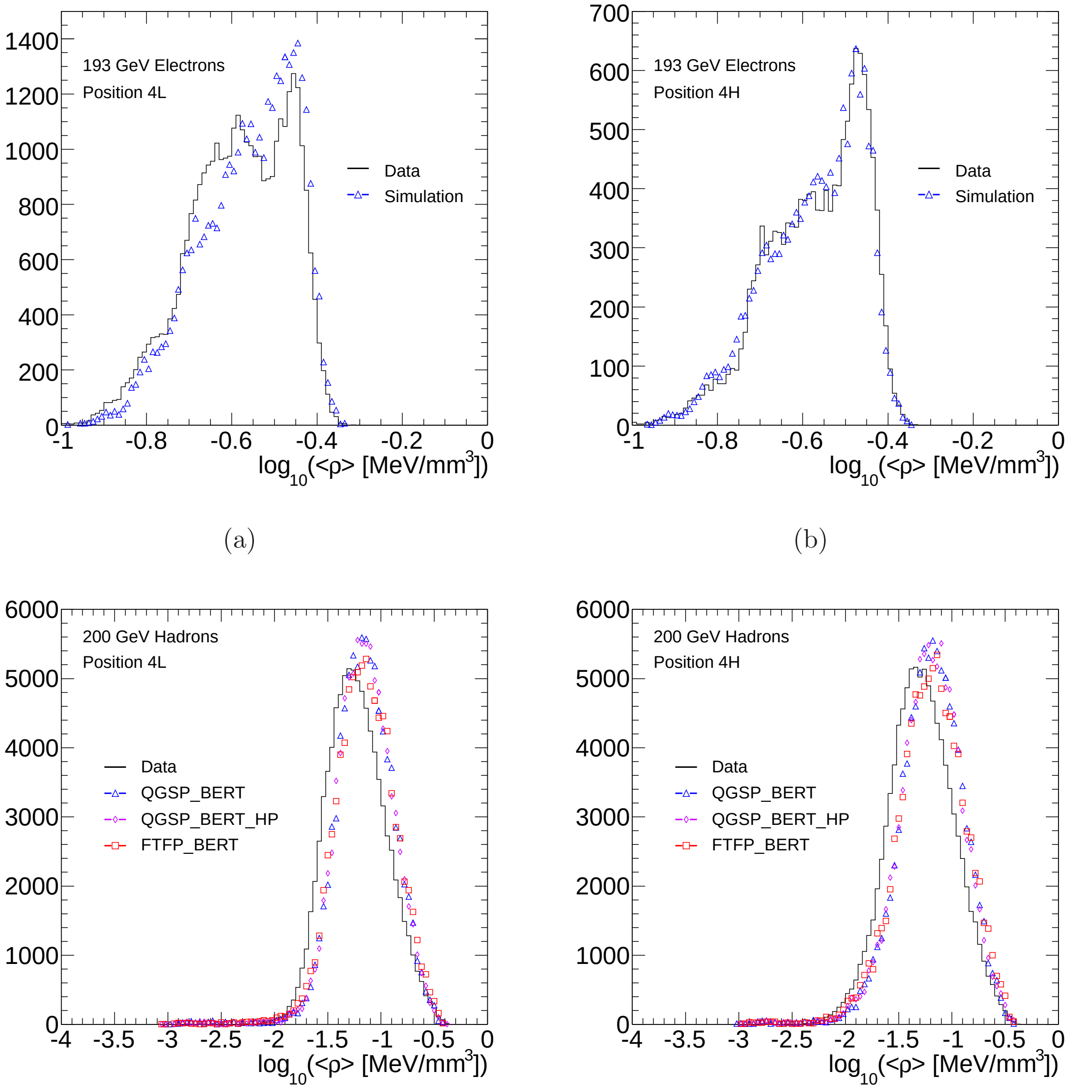

(a) (b)

(c) (d)

Figure 4.43: Shower moments derived from topological clusters. The upper plots show the energy density of clusters resulting from 193.1 GeV electrons at position 4L (a) and 4H (b). The lower plots show the same distributions from 200 GeV hadrons at position 4L (c) and 4H (d).

4.7 Beam Test studies in relation to ATLAS

During the 2003 beam test of the `ATLAS` forward calorimeter, beams of electrons and hadrons were directed at several positions on the front face of the calorimeter. Data taken at position 4L was used to obtain the EM scale calibration of the calorimeter [69], and is the basis of the calibration currently being used at `ATLAS`. Data taken at position 4H was compared to that at 4L, and used to study the effect of additional upstream material on the detector performance. These studies have been carried out using cylindrical clusters of calorimeter cells, and also using topological clusters, which are used heavily at `ATLAS`. Data taken at positions 1-3 were used to study the dependance of the FCal response on the beam particle impact point, near the inner (high $|\eta|$) edge of the calorimeter [67, 68]. A Monte Carlo simulation of the testbeam environment was developed, and results from the simulation were generally found to agree with those from data.

The 2004 beam test studied sections of the end-cap calorimeters (EMEC and HEC) and a prototype of the FCal (consisting of FCal1 and FCal2 modules). Data taken during the 2004 beam test was used to study the transition region between the end-cap and forward calorimeters. This allowed the combined response of these detectors to be studied in cases where the beam particles were impacting near the edges of the calorimeters (for the FCal, this is the outer/low $|\eta|$ edge) [64]. Data from the 2004 beam test was also used to evaluate the local hadronic calibration scheme [84], which is one of the calibration methods used at `ATLAS`. The local hadronic calibration scheme is derived purely from Monte Carlo simulations (as are all hadronic calibration schemes currently in use at `ATLAS`). In that study, one set of simulation results was used to obtain the calibration, while another set was compared to the data. Again, the simulation results agreed well with the data.

The 2003 beam test studies presented in this chapter represent the final set of testbeam results for the FCal*. The effects of additional upstream material on the detector performance have been studied, in both data and simulation. The simulation results agree well with the data, and the effects of the additional material are well modelled. Where comparable, both data and simulation results from the 2003 beam test are consistent with results obtained in other beam tests. This is important because only the 2003 beam test utilised the FCal modules that are currently in use at `ATLAS`, whereas other beam tests studied prototype FCal modules.

The extensive series of test beam studies have provided a solid understanding of the performance of the FCal, and the degree to which the `ATLAS` simulation models this performance. The energy resolution for electrons is slightly worse in the simulation than that seen in data, while simulated hadronic showers tend to be shorter and narrower than those in data (this effect has also been observed in other studies [81]). However, in most respects the simulation does a good job of modelling the FCal performance and the effects of additional upstream material.

4.8 Summary

The 2003 beam test subjected the `ATLAS` C-side forward calorimeter to beams of electrons and hadrons with energies of 10-200 GeV. A Monte Carlo simulation of the beam test has been developed, and results obtained from this simulation generally agree with those obtained from the data. The effects on the calorimeter performance from additional material introduced into the beam line have been studied, and these effects are also reasonably well-modelled by the simulation. Previously published testbeam results were found to be affected by a software bug that rounded down cell energies; this bug has since been corrected and the previously published results are superceded by those presented in this Chapter. Results have been obtained using a cylindrical cell clustering

---

* Analyses of the 2004 (and earlier) beam tests have already been completed.

method, as well as a topological clustering method frequently used at `ATLAS`. Shower shapes have been studied by varying the radius used to from cylindrical clusters, and by comparing the energy deposited in different FCal modules to obtain a longitudinal profile. Shower shapes have also been studied by obtaining distributions of shower shape moments from topological clusters. Shower shape moments are used to classify energy deposits in the local hadronic calibration method. The moment distributions obtained from the simulation generally agree well with those seen in data, and these results are consistent with those reported in other studies.

Chapter 5

Inclusive Jet and Dijet Cross-Sections

5.1 Introduction

The inclusive jet cross-section refers to the cross-section for jet production with no discrimination based on the final state, i.e. all jets in each event are considered. The cross-section measurement is binned in terms of the transverse momentum, p_{T}, and the jet rapidity, y. The cross-sections studied in this chapter are significant as they represent a precise measurement of QCD in a region of phase space that has not previously been explored*. Because QCD is the dominant process at the LHC, the inclusive jet and dijet cross-sections also allow jet production to be properly understood as a source of background in searches for more exotic processes, such as those presented in [86, 87].

The first `ATLAS` measurement of the inclusive jet and dijet cross-sections was made in 2010 [88, 89], using 17nb^{-1} of early data collected from 7 TeV collisions. The jet production cross-section was measured for jets with p_{T} from 60 to 600 GeV and with

---

[*] The inclusive jet cross-section measurement made by CDF covers $|y| < 2.1$ and in jet rapidity and 62 GeV $< p_{\mathrm{T}} <$ 700 GeV in jet p_{T} [85].

rapidities less than 2.8 in magnitude. This measurement was updated in early 2011 using the full 2010 `ATLAS` dataset ($37\,\text{pb}^{-1}$) to extend those results. This update expanded the kinematic coverage of the measurement to include jets with p_{T} from 20 GeV to 1.2 TeV, and the rapidity range was extended into the forward region to include jets with $|y| < 4.4^{*}$. Figure 5.1 shows the kinematic region covered by the initial measurement compared to that described in this analysis. The dijet mass spectrum has also been measured using 2010 data, and the rapidity coverage of this measurement has also been expanded to include the forward region. The results discussed here have been presented as a conference note [90] and were published in 2012 [91]. The inclusive jet cross-section has also been measured with the CMS detector using two independent analyses for 2010 data; the first of which covers the region $|y| < 3$ and uses a "particle flow" method to reconstruct jets [92], while the second covers the region $3.2 < |\eta| < 4.7$ and uses jets reconstructed from the CMS forward calorimeter [93]. The `ATLAS` measurement of the inclusive jet cross-section discussed in this chapter coherently uses the same jet reconstruction technique throughout the analysis, with no gaps in the rapidity coverage. The dijet mass spectrum has also been measured at CMS, though only for jets in the region $|y| < 2.5$ [94],whereas the `ATLAS` dijet analysis presented here has the same rapidity coverage as the inclusive analysis ($|y| < 4.4$).

Section 5.2 gives a brief overview of the operation of `ATLAS` and the LHC during 2010, while Section 5.3 describes how jets are defined and calibrated in `ATLAS` data. The event selection and triggers used for data collection are described in Section 5.4, while Section 5.5 describes the method used to correct for detector resolution effects in the measured data ("unfolding"). The treatment of experimental uncertainties is described in Section 5.6, and results are presented in Section 5.7.

---

[*] The FCal coverage extends out to $|\eta| < 4.9$, however an upper limit of 4.4 on the rapidity ensures that the jets under consideration were fully contained within the calorimeter

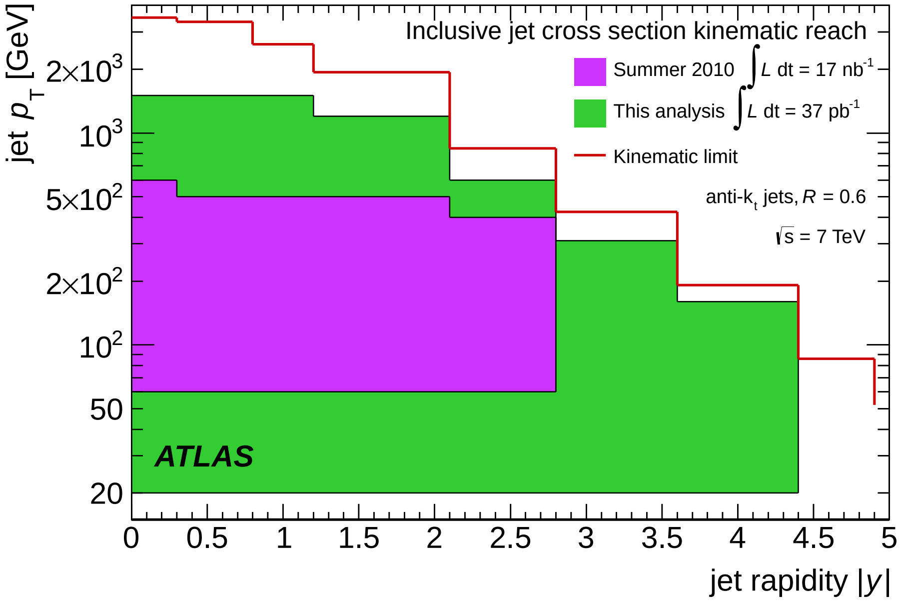

Figure 5.1: Diagram showing the kinematic range covered by the first inclusive jet cross-section measurement (purple) using $17\mathrm{nb}^{-1}$ of early data, and that covered when using the full $37\mathrm{pb}^{-1}$ from the 2010 dataset (green).

5.2 Overview of 2010 Running

Data taken during 2010 has been divided into nine data periods, A-I. Each period represents an interval during which there were no major changes to the configuration of the detector and trigger, or to that of the LHC. Each run is subdivided into a number of luminosity blocks (LB), each of which corresponds to ~2 minutes worth of recorded data. The instantaneous luminosity achieved by the LHC improved over the course of the year as the accelerator was commissioned, from $2 \times 10^{27}\text{cm}^{-2}\text{s}^{-1}$ early in the year to $2 \times 10^{31}\,\text{cm}^{-2}\,\text{s}^{-1}$ by the end of *pp* running.

The amount of data delivered by the LHC and recorded by `ATLAS` throughout 2010 is shown in Figure 5.2. In total `ATLAS` recorded 45 pb^{-1} of data from *pp* collisions. Note that this value is slightly lower than the integrated luminosity delivered by the LHC (48.1 pb^{-1}). The Inner Detector contains sensitive electronics, and so is only supplied with high voltage after stable running conditions have been established. This is the main reason for the discrepancy between the amount of data delivered and that recorded.

Certain data quality (DQ) requirements were put in place to ensure that the data used in this analysis was recorded when all relevant systems were functioning correctly. These criteria will be described in detail in Section 5.4. After imposing these conditions, the analysis is carried out using the remaining 37 pb^{-1} of data.

5.3 Jets in ATLAS

For the inclusive jet cross-section and dijet analyses, jets were reconstructed using the anti-k_t algorithm running on (EM scale) topological clusters of calorimeter cells. In this Section, jet finding algorithms will be presented, followed by a discussion of the jet calibration method and the uncertainty on the jet energy scale.

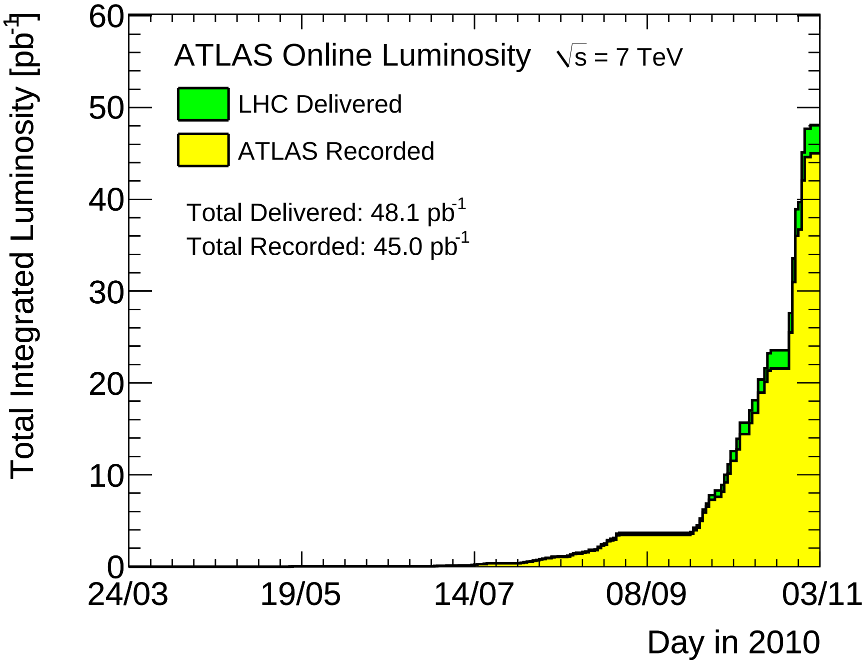

Figure 5.2: Integrated luminosity recorded by ATLAS over the course of 2010.

5.3.1 Jet Finding Algorithms

Jet finding algorithms are run on a set of input objects, which are referred to as constituents. In general any object with an associated four-vector may be used as a constituent; however for this analysis topoclusters (discussed in Section 4.6) are the only constituents considered*. The jets considered in this analysis are reconstructed using the anti-k_t algorithm [95]. The family of k_t-like jet algorithms operate by forming a list of all the constituents in the event. For all constituents and pairs of constituents, the jet resolution quantities

$$d_{ij} = \min(k_{ti}^{2p}, k_{tj}^{2p}) \frac{(y_i - y_j)^2 + (\phi_i - \phi_j)^2}{R^2} \tag{5.1}$$

---

* Although "track jets" are used for some systematic studies and "truth jets" are used in the derivation of the jet calibration and in the unfolding. These use tracks and "truth particles", respectively, as their constituents, and will be discussed later

and

$$d_i = k_{ti}^{2p} \tag{5.2}$$

are computed, where k_{ti}, ϕ_i and y_i are the transverse momentum, azimuthal angle and rapidity of the i-th constituent, respectively. The distance parameter R is related to the desired size of the jets being found, such that the reconstructed jets will be separated by no less than R in (y, ϕ)-space. In this analysis, jets with $R = 0.4$ and $R = 0.6$ are studied. The parameter p defines the jet-finding algorithm: $p = 1$ corresponds to the k_t algorithm [96], $p = -1$ gives the anti-k_t algorithm, and $p = 0$ corresponds to the Cambridge-Aachen cone algorithm [97].

Once the d_{ij} and d_i have been computed, the values are sorted. If the smallest value present corresponds to a d_{ij}, then the i-th and j-th constituents are formed into a proto-jet by summing their four momenta. The proto-jet is then added to the list of constituents and its components are removed. The d_{ij} and d_i values are then recomputed for all remaining constituents and proto-jets. This process is repeated, with each iteration either adding constituents to an existing proto-jet or merging constituents to form a new one. In the case where a d_i value is smaller than any d_{ij} value, this proto-jet is taken as a complete, final jet and is removed from the list. The process continues until the constituent list is empty, with all constituents having been used to form complete jets. The four momentum of a jet is obtained by summing the four momenta of its constituents. A jet mass may then be defined by calculating the invariant mass of the jet's four momentum.

In the k_t algorithm, d_{ij} is approximately equal to the relative difference in transverse momentum between the two constituents i and j, in the limit where the angle between them is small. The k_t algorithm thus clusters together constituents with similar momenta. As showering partons tend to radiate collinearly, the k_t algorithm thus acts to collect all of these radiated constituents and recombine them into a single jet. However, this procedure clusters constituents with the smallest transverse momenta first, such that

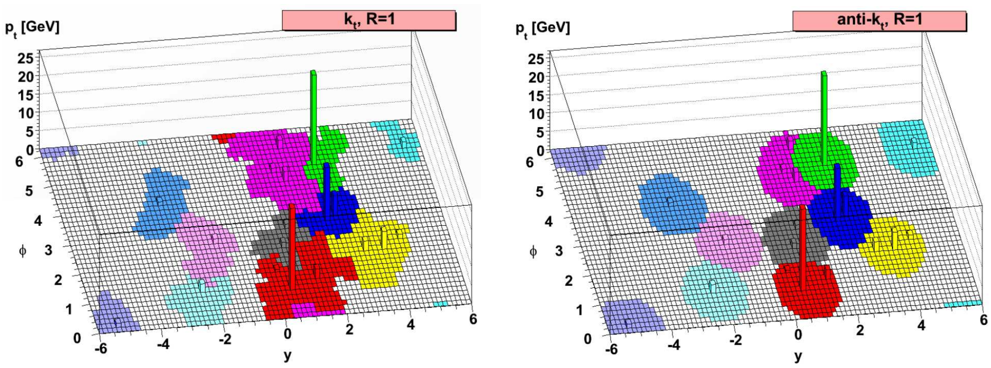

(a) (b)

Figure 5.3: Jets found by the k_t algorithm (a) and the anti-k_t algorithm (b). The event was generated using HERWIG [19], and contains some soft radiation in addition to the high-p_{T} constituents[95].

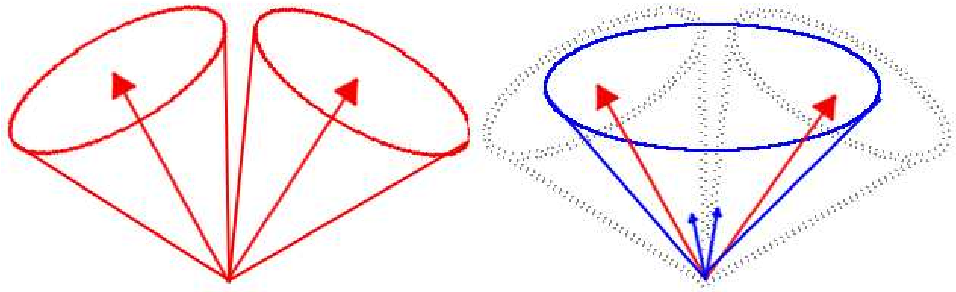

Figure 5.4: Illustration of a jet algorithm which is not IR safe. In the Figure on the left, two distinct jets are found around the high-p_{T} constituents. In the presence of soft radiation (right), the algorithm finds only a single jet.

high p_{T} constituents may be clustered around groups of low p_{T} constituents. This results in jets with irregularly shaped boundaries, as shown in Figure 5.3(a). Conversely, the anti-k_t algorithm considers the highest p_{T} constituents first and builds the proto-jets around those, resulting in conically-shaped jets (as shown in Figure 5.3(b)). This also means that jets found by the anti-k_t algorithm tend to be less sensitive to the effects of pile-up and the underlying event[95], as the jet is first built around high p_{T} constituents and the low p_{T} constituents are added to it later, whereas the k_t algorithm would do the opposite.

The k_t-like jet algorithms are favored because they are both infrared (IR) and collinear

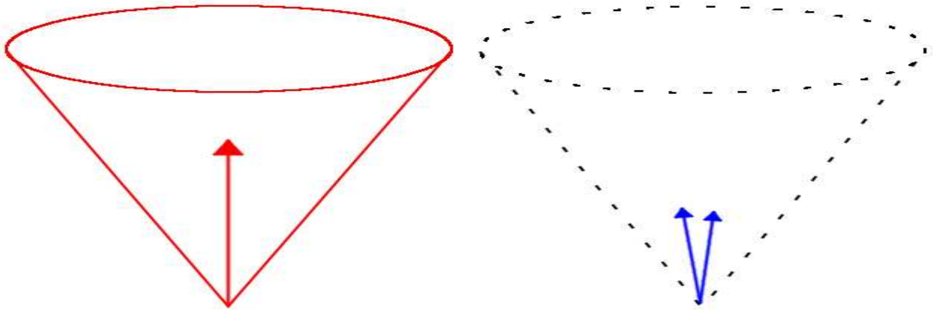

Figure 5.5: Illustration of an algorithm which is not collinear safe. On the left, a jet is found around a single high-p_{T} constituent. On the right, the single constituent is replaced by two constituents, each with half the p_{T} of the original. In this case, the algorithm fails to find a jet.

safe. IR safety means that the jets found are stable with respect to the presence of low p_{T} constituents arising from pile-up or the underlying event. For an algorithm to be IR safe, the presence of soft particles can not "confuse" the algorithm into mistaking two separate jets for a single large jet, as illustrated in Figure 5.4. Collinear safety requires that the algorithm will still find a jet if, for instance, a single high-p_{T} constituent is replaced by two (or more) close together constituents with lower p_{T} (Figure 5.5). The k_t-like algorithms have these properties, whereas most iterative cone algorithms (such as those presented in [98]) tend not to.

5.3.2 Jet Energy Scale Calibration

Once a jet has been reconstructed, its energy must be calibrated to the Jet Energy Scale (JES). For this analysis, this is done through an "EM+JES" scheme [99], whereby the EM scale energy of the jet is multiplied by a calibration factor to obtain the energy at the JES. The calibration is derived from Monte Carlo simulations using a numerical inversion process.

The calibration is done in three steps. First, the EM scale energy of the jet is adjusted in order to correct for pile-up effects. Additional proton-proton interactions from the same event can deposit energy in the calorimeter, affecting the energy of the high p_{T} objects from the hard scattering. Minimum bias data are used to determine the average energy deposited in the calorimeter as a function of pseudorapidity and the number of primary vertices reconstructed from the event. This information is used to subtract the average EM scale energy added to the jet as a result of pileup.

The second step is to correct the kinematics of the jet, still at the EM scale, based on the location of the hard scattering. Initially, jet kinematics are computed using the geometrical centre of `ATLAS` as the origin of the jet. The luminous region of `ATLAS` has a width of $\sim 40 - 70\mu$m in the transverse directions and $\sim$ 22 mm longitudinally [100], and it is within this volume that the hard scatterings occur. The vertex with the highest sum of squared transverse momenta from tracks ($\sum p^2_{\mathrm{T},track}$) is taken as the position of the hard scatter, and all jet kinematic quantities (p_{T}, y, ϕ, etc.) are recomputed using this vertex as the origin.

Finally, the JES correction is applied. The correction is derived exclusively from Monte Carlo, using samples generated without the inclusion of pile-up. An event generator is used to simulate a hard parton-parton scattering typical of proton-proton collisions, which outputs a set of final state particles and their four momenta. `GEANT4` is then used to simulate the interactions of these particles with the detector. The event is then reconstructed using the same methods that are used for the data: calorimeter cells are reconstructed and used to form topological clusters, on which jet finding algorithms are run. "Truth" jets are formed by running the jet finding algorithms on the final state particles output by the event generator.

The JES calibration accounts for the following effects:

- non-compensation of the calorimeter, i.e. the energy is calibrated to the hadronic scale;
- energy deposited in inactive (uninstrumented) regions of the detector, such as cryostat walls or support structures;

- leakage effects from particle showers not fully contained in the calorimeters;
- particles contained in the truth jet but not in the reconstructed jet;
- energy from showering particles that is not collected by the topoclustering algorithm (out of cluster corrections).

The calibration is derived by comparing the jets reconstructed from the (simulated) calorimeter information to the truth jets. A reconstructed jet is matched to a truth jet if the distance between them satisfies $\Delta R < 0.3$, where $\Delta R = (\Delta\eta^2 + \Delta\phi^2)^{1/2}$. Jets are only considered if they are isolated in order to avoid mis-matching in cases where multiple jets are close together. A reconstructed/truth jet must have no other jets with $p_{\mathrm{T,EM}} > 7\mathrm{GeV}$ within $2.5R$, or it is not used in the derivation of the calibration.

The matched reconstructed-truth jet pairs are then used to define the response R, such that

$$R = \frac{E_{\mathrm{reco}}^{\mathrm{EM}}}{E_{\mathrm{truth}}}, \tag{5.3}$$

where $E_{\mathrm{reco}}^{\mathrm{EM}}$ is the EM scale energy of the reconstructed jet and E_{truth} is the energy of the truth jet. The response is binned in E_{truth} and η_{det}, the pseudorapidity of the reconstructed jet at the EM scale. For each $(E_{\mathrm{truth}}, \eta_{\mathrm{det}})$ bin, the mean reconstructed jet energy, $\langle E_{\mathrm{reco}}^{\mathrm{EM}} \rangle$, is found, and a Gaussian fit is used to extract the mean response, $\langle R \rangle$.

The response is then parameterised as a function of $E_{\mathrm{reco}}^{\mathrm{EM}}$ for each η_{det} bin. For the k-th η_{det} bin, a fit is performed on the $(\langle E_{\mathrm{reco}}^{\mathrm{EM}} \rangle, \langle R \rangle)$ points obtained from each E_{truth} bin. The fitted function is of the form

$$F_{\mathrm{calib},k}(E_{\mathrm{reco}}^{\mathrm{EM}}) = \sum_{j=0}^{N_{\mathrm{max}}} a_j \left(\log E_{\mathrm{reco}}^{\mathrm{EM}}\right)^j, \tag{5.4}$$

where the a_j are free parameters and N_{max} is an integer between 1 and 6, depending on η_{det}.

The correction factor is then found by inverting $F_{\mathrm{calib},k}$, so the final EM+JES energy of a jet lying in the k-th η_{det} bin is given by

$$E_{\text{reco}}^{\text{JES}} = \frac{E_{\text{reco}}^{\text{EM}}}{F_{\text{calib},k}(E_{\text{reco}}^{\text{EM}})}. \tag{5.5}$$

5.3.3 JES uncertainty

The systematic uncertainty on the JES is an important quantity, and one of the dominant sources of uncertainty in the inclusive jet and dijet cross-section analyses. There are several sources that contribute to this uncertainty, outlined below:

- **Relative calibration of uncertainties between forward and central regions.** Contributions to the JES uncertainty from the sources discussed below have been calculated in the central region, $0.3 < |\eta| < 0.8$. This uncertainty is used as a baseline, and an intercalibration method [101] is used to extend the estimate of the JES systematic into other pseudorapidity regions. This method uses a p_{T} balancing technique applied to dijet events in order to obtain the ratio of the calibrated jet responses in different regions of pseudorapidity. This response was calculated for data and simulation, using several different MC event generators. The RMS of the differences in response between MC and data is then added in quadrature to the baseline uncertainty, yielding the uncertainty in higher pseudorapidity regions.

- **Uncertainty from the calibration method** The EM+JES method calibrates jets by applying a correction factor to the EM scale energy of the jet. This treats all of the jets constituents equally, i.e. each constituent is effectively scaled by the same calibration factor. Additionally, this same correction factor is used for both the energy and transverse momenta of the jet, which may bias the calibrated p_{T} in cases where the calibrated jet mass differs from the mass of the truth jet. The uncertainty arising from the calibration method is estimated by comparing the reconstructed jets at the EM+JES scale to their truth jet counterparts. The responses $\langle R_E \rangle = \langle E^{EM+JES}_{\rm reco}/E_{truth} \rangle$ and $\langle R_P \rangle = \langle p^{EM+JES}_{\rm T,reco}/p_{\rm T,truth} \rangle$ are computed, and binned in terms of $p^{EM+JES}_{\rm T,reco}$ and $|\eta|$. Any deviation of $\langle R_E \rangle$ or $\langle R_P \rangle$ from unity suggests that the kinematics of the reconstructed jets after calibration are not equal to those of the truth level jets (this is called "non-closure"). The estimated uncertainty associated with the calibration method is taken as the largest deviation of $\langle R_E \rangle$ or $\langle R_P \rangle$ from unity, and is found to be less than 1% for $p^{EM+JES}_{\rm T,reco} > 30$ GeV and less than 2% for 30 GeV $> p^{EM+JES}_{\rm T,reco} > 20$ GeV [102].

- **Uncertainty from calorimeter response** The contribution to the JES systematic from the uncertainty in the calorimeter response is derived from single particle measurements. The uncertainty in the response to charged hadrons is measured in E/p studies [103] and in testbeam data [104]. The simulation framework allows the particles in the truth jet to be associated with the energy they deposit in the calorimeter, and thus the single particle response uncertainties can be propagated to obtain an uncertainty for the response of the jet. When estimating this uncertainty, effects relating to the calorimeter acceptance, charged particles with $E > 400GeV^*$, and energy deposited by neutral hadrons are also considered. Effects related to the calorimeter response are found to contribute $1.5\% - 4\%$ to the JES systematic uncertainty.

- **Uncertainty due to noise thresholds in detector simulation** The noise present in the calorimeter electronics can change over time, whereas the noise used in the simulation is fixed when the MC sample is generated. The value of the noise RMS used influences which cells are grouped into topoclusters, and thus contribute energy to the jet. The effect of the noise threshold in the simulation was studied by increasing and decreasing the noise thresholds for the topoclustering algorithm by amounts of 5-10%. The uncertainty assigned to this effect was found to be neg-

---

[*] Charged particles at these energies could not be studied in beam tests, and so the uncertainties associated with particularly high energy densities or longitudinal leakage must be estimated.

ligible for jets with $p_{\mathrm{T}} > 45$ GeV, and is estimated as 1% for jets with momentum in the range 30 GeV $\leq p_{\mathrm{T}} \leq 45$ GeV. For jets with 20 GeV $\leq p_{\mathrm{T}} \leq 30$ GeV, the uncertainty was estimated as 1% (2%) for jets with radius 0.4 (0.6).

- **Effect of additional material in simulation** As the JES calibration is intended to correct for the effects of inactive material, it is sensitive to the material description of the detector in the simulation. The effects of this were estimated by adding additional material to the simulation geometry in several places, and comparing the response obtained with the modified geometry to that obtained using the nominal geometry.
- **MC event generators** The nominal MC sample used in the derivation of the JES was generated using `PYTHIA`, using the AMBT1 tune. Samples were also produced using `ALPGEN` [105] interfaced with `HERWIG` and `JIMMY`, and using the Perugia2010 tune for `PYTHIA`. The `ALPGEN` sample used the CTEQ6.1 PDF set, and treated parton showering and hadronisation effects differently than the nominal `PYTHIA` sample, whereas the Perugia2010 sample provided a different treatment of the underlying event. Deviations between the response obtained from the Perugia2010 and `ALPGEN` +`HERWIG` +`JIMMY` samples with respect to the nominal `PYTHIA` sample were used to estimate the uncertainty arising from the choice of physics models.

The total JES uncertainty, and its components, are plotted in Figure 5.6 for $R = 0.6$ jets. The uncertainty in the calorimeter response is the dominant contribution to the JES uncertainty for jets with $p_{\mathrm{T}} \geq 100$ GeV. In the central region ($0.3 < |\eta| < 0.8$), the uncertainties associated with alternative MC generators dominate below 100 GeV, while in other pseudorapidity regions intercalibration effects dominate at low p_{T}. At high p_{T} (near the kinematic limit) the JES uncertainty is around 3-5% in each rapidity region. The uncertainty associated with jets of radius $R = 0.4$ is generally similar to that associated with jets of radius $R = 0.6$.

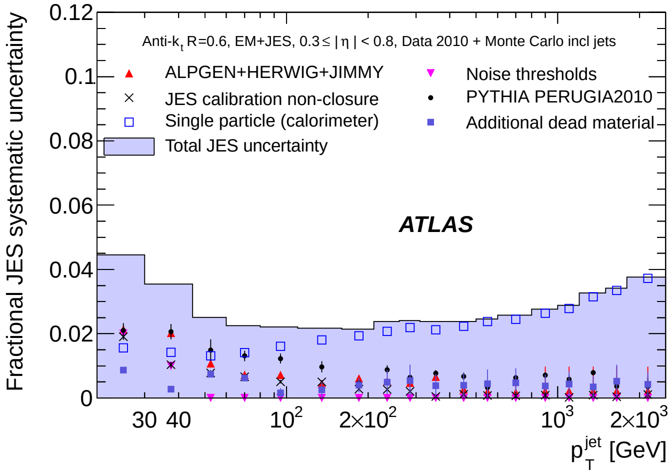

(a)

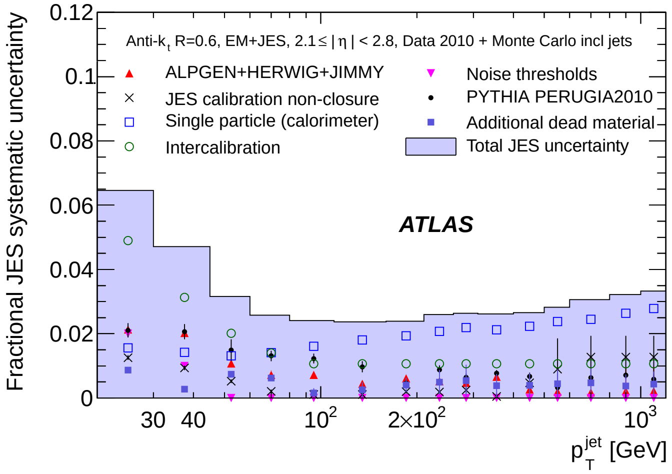

(b)

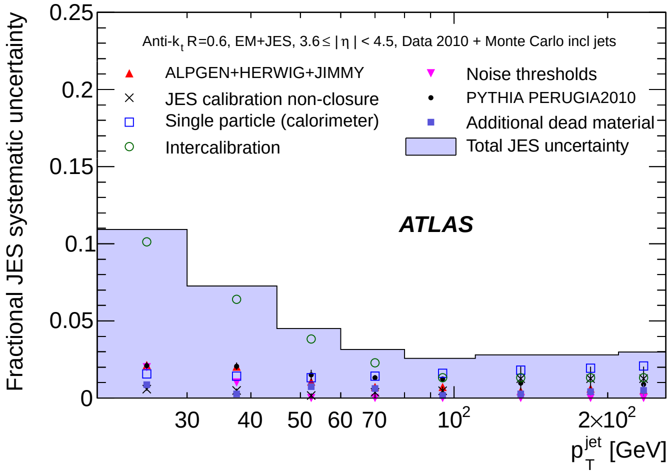

(c)

Figure 5.6: Systematic uncertainty on the Jet Energy Scale for jets in the regions (a) $0.3 < |\eta| < 0.8$, (b) $2.1 < |\eta| < 2.8$, (c) and $3.6 < |\eta| < 4.5$ [99]

5.3.4 Jet Selection

After jets have been calibrated, they are required to pass “cleaning cuts” before being included in the cross-section analysis. The cleaning cuts are intended to reject “fake” jets, which can be reconstructed from calorimeter signals that do not originate from proton proton collisions. The most significant sources of these fake jets are coherent noise in the EMB, noise bursts in the HEC, cosmic rays, and beam background events. The cleaning cuts used to reject fake jets are summarised below:

- **Coherent noise in the EM calorimeter:** Jet candidates with $|\eta| < 2.8$ were rejected if f_{em}, the fraction of the jet energy deposited in the EM calorimeter, exceeded 0.9 while the LAr quality variable exceeded 0.8. The LAr quality is defined as the fraction of jet cells located in the EM calorimeter that have a pulse shape significantly different to that expected.

- **Noise bursts (“spikes”) in the HEC:** Jet candidates were rejected if the fraction of the jet energy deposited in the HEC was greater than $1 - HECQ$, where $HECQ$ is the HEC quality variable, defined as the fraction of the jets cells located in the HEC that have a pulse shape significantly different to that expected. Jets were also rejected if the sum of negative energy cells exceeded 60 GeV in magnitude.

- **Cosmics rays/beam background:** Jet candidates were rejected if the average timing for jet cells was greater than 10ns from the average event time, or if 99% of the jet energy was deposited in a single layer of the calorimeter. For jets with $|\eta| < 2.0$, tracking information can be used to define the charged fraction, f_{ch}, which is the fraction of the jet p_{T} associated with tracks in the inner detector. In this case, jets were rejected if $f_{\mathrm{ch}} < 0.1$ and $f_{\mathrm{em}} < 0.05$ or if $f_{\mathrm{em}} > 0.95$ and $f_{\mathrm{ch}} < 0.05$. Jets with $|\eta| > 2.0$ were rejected if $f_{\mathrm{em}} < 0.05$.

Jet candidates which failed these cleaning cuts were excluded from the analysis. The efficiency of these cleaning cuts for real jets was at least 96% for jets with $p_{\mathrm{T}} > 20$ GeV, and greater than 99% for jets with $p_{\mathrm{T}} > 60$ GeV. In kinematic regions where the jet cleaning efficiency was less than 99%, the inefficiency is corrected for in the inclusive jet and dijet cross-section measurements.

5.4 Event Selection and Data Quality

In order for an event to be considered in the inclusive jet and dijet cross-section measurements, it was required to meet certain Data Quality (DQ) criteria. These criteria were expressed in terms of DQ flags. A green flag indicated that the corresponding system was operating normally, whereas a yellow flag indicated an issue that could be corrected for offline, or data that could be used with caution. Red flags were used to indicate data that had some problems and should not be used.

In order for an event to be included in the inclusive jet and dijet cross-section measurements, the following DQ flags were required:

- Trigger (L1Calo and L1 CTP) were required to be green. For periods G-I, the HLT flag was also required to be green.
- Magnets (toroid and solenoid) were required to be green.
- Inner Detector subsystems (pixel, SCT and TRT) were required to be green.
- Track, Missing E_{T} (from calorimeters), and Jet reconstruction performance were required to be green.
- Luminosity monitoring was required to be green.

The event was also required to have a primary vertex with at least 5 tracks. Events were also required to pass a trigger condition, which is discussed below.

These criteria were required for both the inclusive jet and dijet cross-section measurements. Both of these analyses considered jets in the rapidity range $|y| < 4.4$. The inclusive jet cross-section measurement considered jets with $p_{\mathrm{T}} > 20$ GeV, while the measurement of the dijet mass spectrum required that the leading jet in the event have $p_{\mathrm{T}} > 30$ GeV and the subleading jet have $p_{\mathrm{T}} > 20$ GeV.

5.4.1 Triggers used for the inclusive jet analysis

The inclusive jet cross-section measurement is performed in 7 bins of rapidity and 16 bins of p_{T}. A dedicated, fully efficient trigger is used to collect jets in each bin in order to maximise statistics. Each bin has an associated trigger condition that the event needed to satisfy before jets from the event could contribute to that bin. The three lowest p_{T} bins are populated using data taken from the MBTS1 (minimum bias) trigger, which required a hit signal from at least one of the MBTS tiles (described in Section 3.2.7). Minimum bias data from only the three earliest periods of running (A-C) were used for this purpose, as in these periods this trigger had a lower prescale (and so more data was recorded) and there was a minimal amount of pile-up. At higher p_{T} (above 60 GeV), data was taken using the central jet trigger for jets with $|y| < 2.8$. The rapidity bin from $2.8 < |y| < 3.6$ is referred to as the "transition bin", as it covers the transition region between the end-cap calorimeters and the FCal (Figure 4.3). In this region both the central and forward jet triggers were used, whereas in the forward region ($3.6 < |y| < 4.4$) only the forward jet trigger was used.

The performance of the jet trigger system needs to be understood before it can be used effectively in the analysis. This is achieved by measuring the trigger efficiency. The per-jet efficiency of a trigger represents the probability that the trigger condition will be satisfied by a given jet. It is defined as

$$\epsilon_{\mathrm{per-jet}} = \frac{N_{\mathrm{triggered}}}{N_{\mathrm{reference}}}, \tag{5.6}$$

where $N_{\mathrm{reference}}$ is the number of reconstructed jets obtained from a reference sample and

$N_{\text{triggered}}$ is the number of reconstructed jets from this reference sample that satisfy the trigger condition. These quantities are binned in terms of the p_{T} and rapidity of the reconstructed jets, which allows the efficiency to be determined as a function of these variables. For the trigger studies presented here, data taken from the MBTS1 trigger was used to obtain the reference sample.

In order to count $N_{\text{triggered}}$, the reconstructed jets that satisfy the trigger condition need to be identified. L1 jet triggers are satisfied provided that the transverse energy deposited in a given ROI exceeds a certain threshold (as discussed in Section 3.2.7). In order to determine whether a given jet satisfies the trigger condition, it must be matched to an ROI that is above the trigger threshold. A reconstructed jet is matched to an ROI from the central jet trigger if the jet lies within $\Delta R \leq 0.4$ of the ROI in $\eta - \phi$ space. The forward jet trigger relies only on data from the FCal, and the trigger towers in the FCal are summed such that there is no granularity in η. Reconstructed jets are matched to a forward jet trigger ROI if the jet lies within $\Delta\phi \leq 0.4$ of the ROI, provided the two are on the same side of the detector.

The per-jet efficiency describes the probability that the trigger will be satisfied by a given jet. However, for events containing multiple jets, only one jet needs to satisfy the trigger condition in order for all of the jets* to count towards the inclusive cross-section measurement. Consider an event in which there are two jets with equal and opposite momenta. If the relevant trigger has a per-jet efficiency of 90%, then each jet has a 10% chance of not satisfying the trigger condition. There is thus only a 1% chance that neither jet satisfies the trigger condition, and thus a 99% probability that the trigger condition is satisfied by one or both jets. For this reason, it is more appropriate to use the inclusive efficiency, ϵ_{inc}, which is defined as

$$\epsilon_{\text{inc}} = \frac{N_{\text{triggered,inc}}}{N_{\text{reference}}}. \tag{5.7}$$

---

* That is, all of the jets that have passed the jet selection criteria described earlier.

In this case, $N_{\text{triggered,inc}}$ is the number of jets contained in events (taken from the reference sample) in which the trigger condition is satisfied. The inclusive efficiency describes the efficiency of the trigger at the event level: if any jet in the event satisfies the trigger condition, then all jets in the event are counted. The inclusive efficiency is thus used to determine the p_{T} range in which data collected by a given trigger will be used.

In order to reduce the uncertainties on the cross-section related to the trigger efficiency, data are only used when collected above the trigger's "plateau" point. The plateau point is defined by integrating bins of $N_{\text{triggered,inc}}$ and $N_{\text{reference}}$ from high p_{T} towards low p_{T}, until reaching the point where the ratio of these sums drops below 99%. The high edge of this bin is then taken as the plateau point, as the trigger is at least 99% efficient at p_{T} values above it. On the plateau, the trigger is treated as fully efficient, and is used to collect data for the appropriate p_{T} bins.

While studying the forward jet triggers, it was observed that events containing high p_{T} jets in the region $3.4 < \eta < 3.9$ and $-\pi/8 < \phi < 0$ were not being selected by the trigger. The L1 trigger tower in this region was found to be producing no signal. This reduced the geometrical acceptance of the forward jet trigger by $\frac{1}{128}$[*], which is corrected for in the cross-section calculation. Consequently, the plateau points in the forward and transition bins are defined at an efficiency of 98%. It should be noted that while the trigger tower is considered "dead", the calorimeter cells (and hence jet reconstruction) are unaffected in this region, as the cell information is read off the FEB separately from the trigger signal (as described in Section 3.2.6.2).

The forward jet triggers were not commissioned when data taking began in 2010, however as the year progressed, the trigger system was commissioned further. The forward jet triggers were commissioned after run 161118 (during period E), and were used to collect data in the forward and transition regions from then on. The HLT system was

---

[*] The dead region consists of one of the four trigger towers in one of the sixteen ϕ-slices of one of the two forward calorimeters.

commissioned from period G on, which allowed event rejection to occur at L2. The EF remained in "pass-through" mode throughout the remainder of 2010, meaning that all events selected at L2 were recorded. Triggers at L1 were used to collect data until the HLT was commissioned, after which L2 triggers were used (periods G-I).

The inclusive efficiencies for the transition and forward bins are plotted in Figures 5.7 and 5.8, respectively, for several trigger thresholds at L1 and at L2. At L1, the trigger thresholds are based on the EM scale transverse energy reconstructed at L1, L1 $E_{\mathrm{T}}^{\mathrm{EM}}$. For the forward bin (Figures 5.7(a) and 5.7(b)) the efficiencies of the L1_FJ10, L1_FJ30, and L1_FJ55 triggers are plotted, which require L1 $E_{\mathrm{T}}^{\mathrm{EM}}$ to be greater than 10 GeV, 30 GeV, and 55 GeV, respectively. The lowest threshold, L1_FJ10, reaches its plateau point at 21 GeV for (calibrated) jets with $R = 0.4$ and at 23 GeV for jets with $R = 0.6$, and is thus used to collect data for the 30-45 GeV, 45-60 GeV, and 60-80 GeV p_{T} bins in the forward rapidity bin. For periods G-I, trigger thresholds at L2 were used instead of L1. The lowest threshold forward jet trigger at L2, L2_fj25, requires the L2 jet to have an EM scale transverse energy (L2 $E_{\mathrm{T}}^{\mathrm{EM}}$) of at least 25 GeV, while the higher thresholds, L2_fj45 and L2_fj70, require 45 GeV and 70 GeV, respectively. The L2_fj25 threshold reaches its plateau point at 43 (45) GeV for jets with $R = 0.4$ ($R= 0.6$), and is used to collect data for the 60-80 GeV and 80-110 GeV p_{T} bins of the forward rapidity bin during periods G-I. Triggers for the transition bin use an "OR" method that will be discussed below, such that the event may be accepted by either the forward jet or the central jet trigger. For example, the lowest threshold used at L1 in the transition bin (Figures 5.8(a) and 5.8(b)) requires that the event be selected by either the L1_FJ10 or the L1_J10 trigger, both of which require L1 $E_{\mathrm{T}}^{\mathrm{EM}} > 10$ GeV.

5.4.2 Trigger strategy for the Transition Bin

The transition bin covers the difficult region between the end-cap calorimeters and the FCal. The central jet trigger only uses information from the EMEC and HEC (which

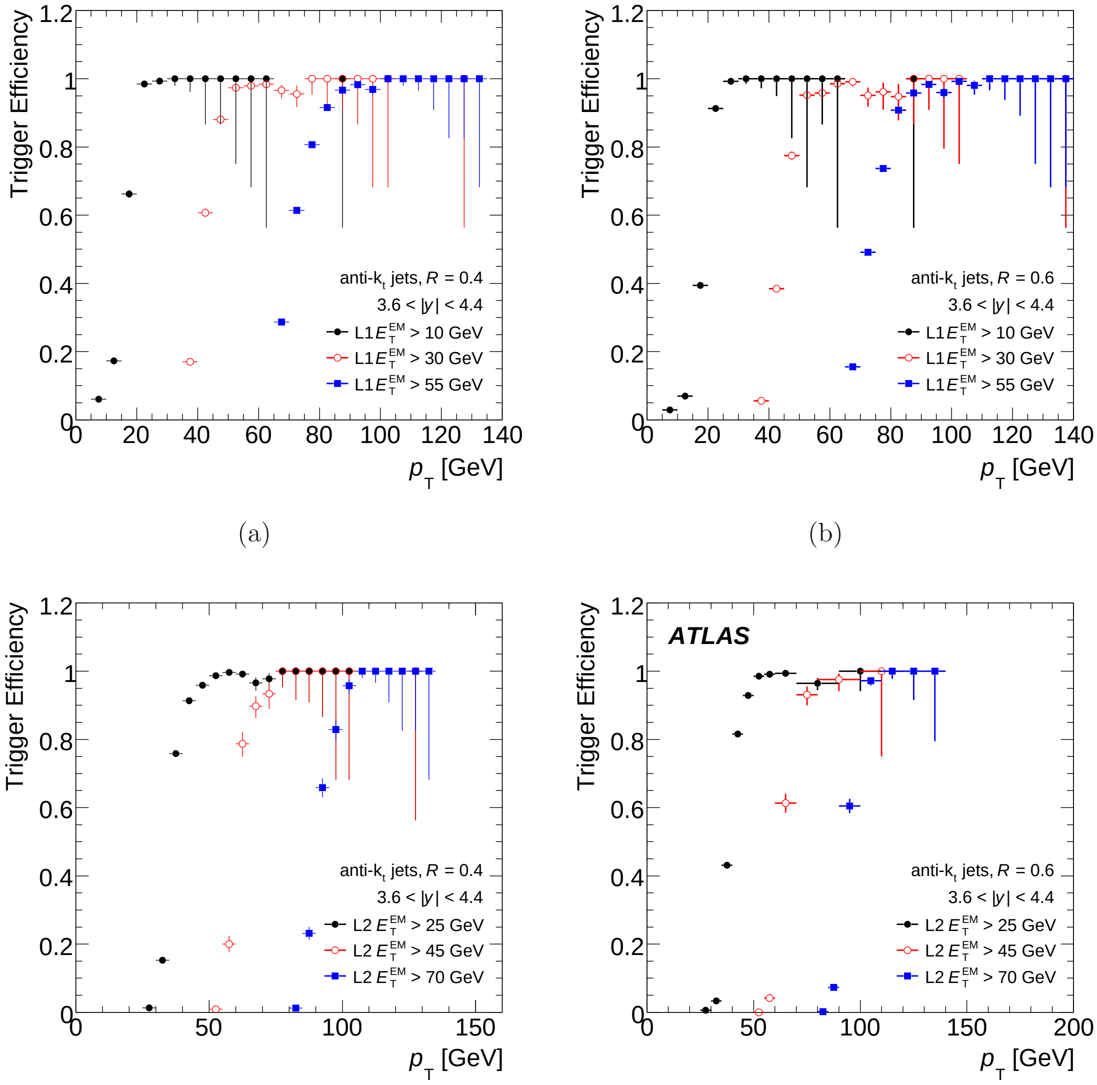

(a) (b)

(c) (d)

Figure 5.7: Efficiencies for L1 triggers (top) and L2 triggers (bottom) in the forward bin, for anti-k_t jets with R=0.4 (left) and R=0.6 (right).

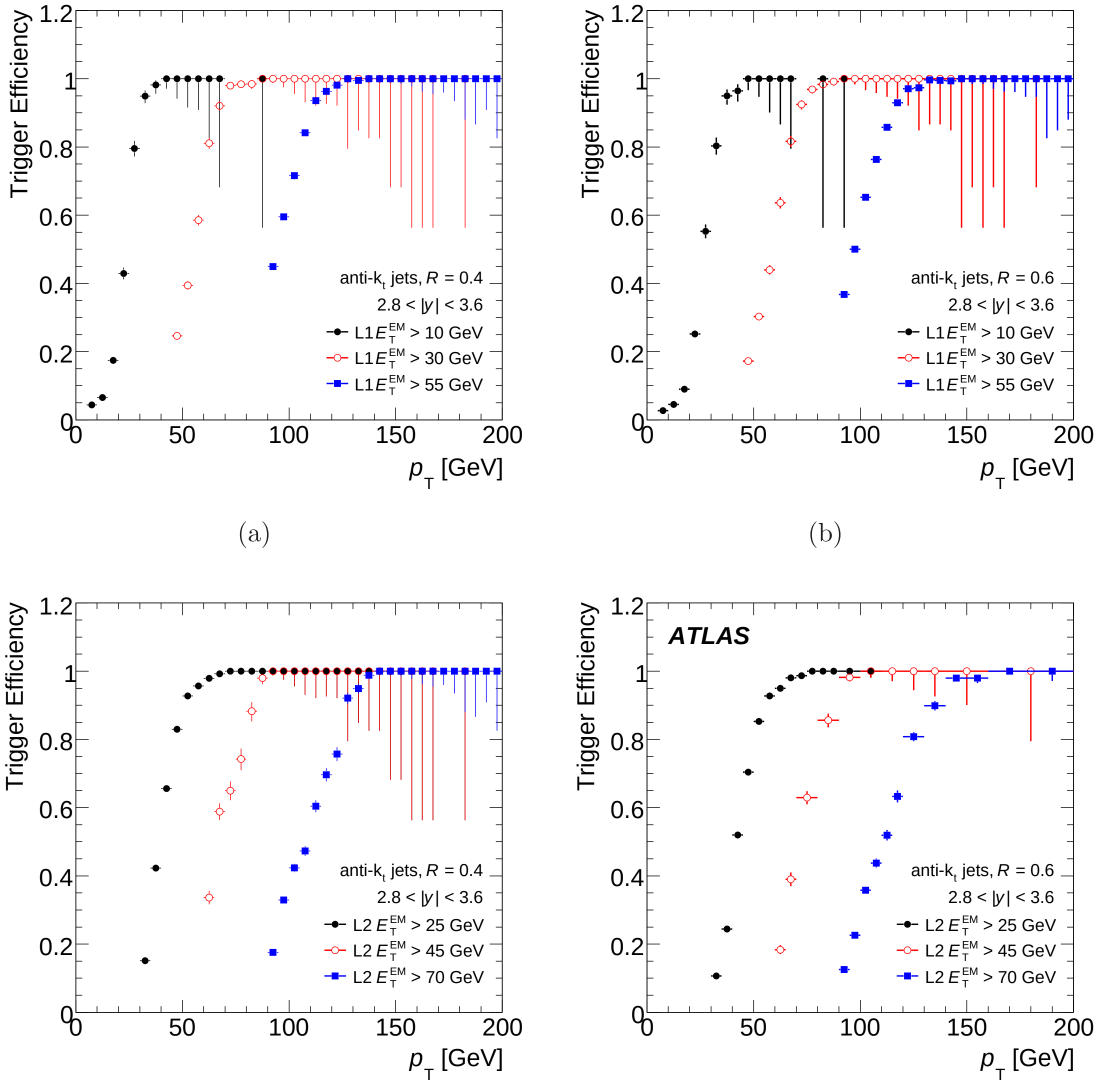

(a) (b)

(c) (d)

Figure 5.8: Efficiencies for L1 triggers (top) and L2 triggers (bottom) in the transition bin, for anti-k_t jets with R=0.4 (left) and R=0.6 (right).

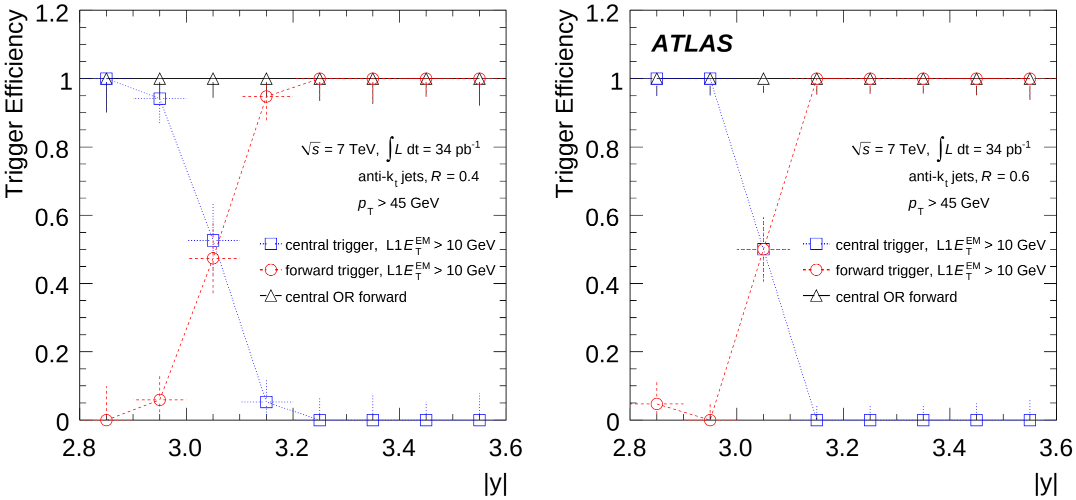

Figure 5.9: Per-jet efficiency of Level 1 forward (red) and central (blue) jet triggers as a function of jet rapidity for jets with $p_{\mathrm{T}} > 45$ GeV in the transition bin ($2.8 < |y| < 3.6$), for jets with $R = 0.4$ (a) and $R = 0.6$ (b). Note that the OR of the two triggers remains fully efficient throughout the rapidity range.

covers the region $|\eta| < 3.2$), while information from the FCal is only used by the forward jet trigger ($|\eta| > 3.2$). Note that as jets have a finite radius, jets in the transition region may deposit energy in both the FCal and in the EMEC/HEC. Thus, in order for the analysis to be sensitive to all jets in this region of rapidity, both the central and forward jet triggers need to be considered when collecting data. This is done by taking the logical "OR" of the two triggers, such that jets in the event are counted if either the central or forward trigger condition is met. The per-jet efficiency of each trigger throughout this rapidity range is shown in Figure 5.9. The "OR" of the two triggers is fully efficient throughout the rapidity range of the transition bin, although the individual triggers are not.

When only a single trigger is used, the measured cross-section is given by

$$\sigma = N_{jets} \left(\sum_i \frac{\mathcal{L}_i}{S_i} \right)^{-1}, \tag{5.8}$$

where N_{jets} is the number of jets observed and $\mathcal{L}_i$ and S_i are the integrated luminosity and trigger prescale for the ith luminosity block, respectively. The situation is more complex in the case where two triggers are employed [106]. In this situation events are classified as belonging to one of three classes, based on whether the event passed the forward trigger condition but not the central (case 10), the central trigger condition but not the forward (case 01), or both trigger conditions (case 11). When making these distinctions, it is important to consider whether the event satisfied a trigger condition before the prescale was applied, as events should be classified according to the triggers that they could potentially be accepted by rather than the triggers that actually selected the event. For L1 triggers the "Trigger Before Prescale" flag can be checked in `Athena`, but for L2 triggers the jets found at L2 must be checked to see if any exceed the trigger threshold.

Once the events have been divided into their respective classes, the cross-section may be written as

$$\sigma = \frac{N_{01}}{\mathcal{L}_{01}} + \frac{N_{10}}{\mathcal{L}_{10}} + \frac{N_{11}}{\mathcal{L}_{11}}, \tag{5.9}$$

where the integrated luminosities are given by

$$\mathcal{L}_{01} = \sum_i \frac{\mathcal{L}_i}{S_{i,01}} \tag{5.10}$$

$$\mathcal{L}_{10} = \sum_i \frac{\mathcal{L}_i}{S_{i,10}} \tag{5.11}$$

$$\mathcal{L}_{11} = \sum_i \frac{\mathcal{L}_i \left(S_{i,01} + S_{i,10} - 1\right)}{S_{i,01}\, S_{i,10}} \tag{5.12}$$

where $S_{i,10}$ ($S_{i,01}$) is the prescale of the forward (central) jet trigger for the i-th lumiblock.

5.4.3 Dijet Triggers

For the initial measurements made using data from `ATLAS` [88, 89] the dijet mas spectrum was binned in terms of the dijet mass, m_{12}, and the maximum rapidity of the two jets, $y_{\max} = \max(|y_1|, |y_2|)$. Dijet events were selected by triggering on the leading jet, using the same trigger thresholds as for inclusive analysis. These first measurements only considered cases where both jets were in the central region, with $y_{\max} < 2.8$.

For extension of the dijet analysis to the transition and forward regions, a new trigger scheme was initially considered. The intent was to bin the trigger efficiency in terms of the observables of interest. The central jet trigger would be used for $y_{max} < 2.8$, the forward jet trigger for $3.6 < y_{max} < 4.4$, and the OR of the two for $2.8 < y_{max} < 3.6$, with the trigger efficiency being described by a turn-on curve in m_{12}. Each trigger could then be considered fully efficient above some threshold value for the dijet mass, and used to collect data above this point. This trigger scheme was later abandoned, as the trigger system is based on jet p_{T} and thus inflates the minimum dijet mass at which the trigger becomes unbiased. Consider the case where both jets in the dijet system have transverse momenta well above the trigger threshold, but the separation between jets is small. The small separation between jets will yield a small mass, and the trigger will efficiently accept dijet events in this configuration. However, in cases where the separation between jets is large and the jet momenta are close to the trigger threshold, the resulting value for the dijet mass can still be quite large while the trigger is not fully efficient. For this reason, the observables of interest were changed to m_{12} and half of the jet rapidity separation[*], $y^* = |y_1 - y_2|/2$. The trigger scheme then reverted back to that used for earlier versions of the analysis wherein the leading jet was used to trigger the event, although this was extended to cover the forward and transition regions. The L1 trigger efficiencies obtained when using this method are plotted in Figures 5.10 and 5.11, for the transition bin and forward bin respectively, and are plotted as a function of the leading jet p_{T}. The trigger scheme was then expanded to consider the subleading jet, utilising a method similar to that used for the transition bin in the inclusive analysis. The kinematic region was divided into a number of bins in p_{T} and rapidity, each of which was associated with a

---

[*] In the parton-parton centre of mass frame, the scattered partons each have $p_{\mathrm{T}} = m_{12}/\cosh(y^*)$ and rapidity $\pm y^*$. For this reason y^* is considered a more desirable variable than $y_{\max}$.

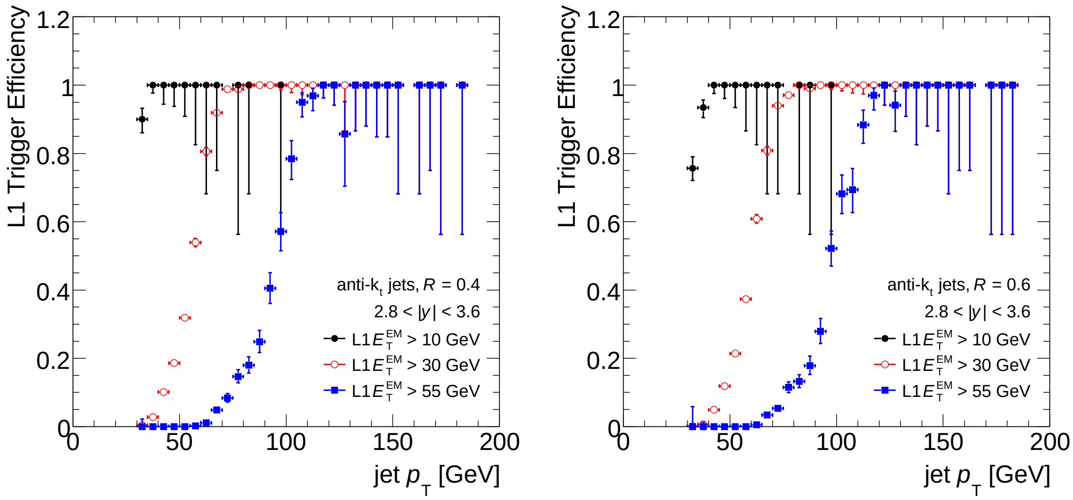

Figure 5.10: L1 trigger efficiencies for dijet events in which the leading jet lies in the transition bin, for anti-k_t jets with $R = 0.4$ (left) and $R = 0.6$ (right).

trigger threshold. Events were then divided into categories based on whether the trigger condition associated with the leading jet was met, or that for the subleading jet, or if both trigger conditions were satisfied. As there is some overlap between the forward and central jet triggers for jets in the region $3.0 < |y| < 3.2$ (Figure 5.9), jets in this region were matched to ROIs at L1 or trigger jets at L2 in order to determine whether the jet should be associated with the forward or central trigger. Events are then weighted based on the prescales of the triggers, using a generalised version of the method described in Section 5.4.2, in order to account for the larger number of trigger categories.

5.5 Unfolding

After the cross-section calculations have been carried out as described above, the data need to be corrected for acceptance and detector effects before it can be compared to any theoretical predictions. As the jet cross-section falls sharply with p_{T}, the non-zero resolution of the detector causes the measured spectrum to be skewed towards higher p_{T} relative to the “true” spectrum. Monte Carlo may be used to compare the p_{T} of truth jets with reconstructed jets in order to understand the effects of the detector resolution.

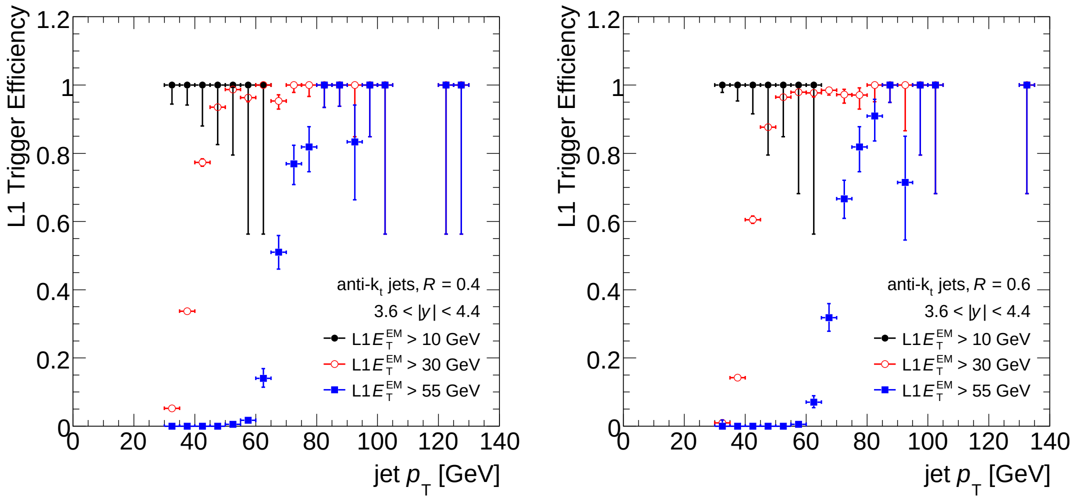

Figure 5.11: L1 trigger efficiencies for dijet events in which the leading jet lies in the forward bin, for anti-k_t jets with $R = 0.4$ (left) and $R = 0.6$ (right). Note that the 10 GeV trigger threshold is alwasy satisfied by the leading jet as dijet events are required to have a leading jet with $p_{\mathrm{T}} > 30$ GeV, which is greater than the plateau point for the 10 GeV trigger threshold.

These effects can then be “unfolded” from the measured spectrum in order to obtain the spectrum of jets prior to their interaction with the detector.

Information on detector related effects is contained in the transfer matrix, A_{ij}, which describes the influence that detector effects have on the measured results, and must be derived from simulation. The entry A_{ij} is equal to the number of truth jets in the j-th p_{T} bin which are reconstructed in the i-th p_{T} bin. This may be normalised to produce the folding matrix of probabilities, P_{ij}, given by

$$P_{ij} = \frac{A_{ij}}{\sum_{k=0}^{N_b} A_{kj}} \tag{5.13}$$

The spectrum at truth level, t_j, and the reconstructed spectrum r_j, are then related by

$$r_j = \sum_{k=0}^{N_b} P_{jk} t_k. \tag{5.14}$$

An unfolded result, u_j, may then be obtained from the measured data d_j, by solving the matrix equation

$$d_j = \sum_{k=0}^{N_b} P_{jk} u_k. \tag{5.15}$$

The solution to this may be found by inverting P_{ij}, such that $u_j = \sum_k P_{ik}^{-1} d_k$. However, this is undesirable as it yields large fluctuations in u_j [107]. Transfer matrices tend to have large condition numbers, meaning that the solution is sensitive to slight changes in the input. Small variations in d_j, which may be due to statistical fluctuations, can produce large spurious fluctuations in u_j.

In order to avoid this, the unfolding method must incorporate some form of regularisation. Typically equation 5.15 is solved numerically, and regularisation may be done, for example, by incorporating the smoothness of u_j into the optimisation method [107]. In this analysis, the unfolding is carried out using the Iterative, Dynamically Stabilised (IDS) method [108, 109], which is described below.

5.5.1 The Iterative, Dynamically Stabilised Unfolding Method

In the IDS method, the MC is re-weighted at each iteration such that the reconstructed MC spectrum is brought closer to that of the measured data, with the truth level spectrum and the transfer matrix adjusted accordingly. As the reconstructed MC is brought closer to the measured data spectrum through re-weighting, the truth level spectrum approaches the desired unfolded result. Any differences between the measured data spectrum and the reweighted reconstructed MC spectrum are then unfolded.

Regularisation is implemented through the use of a regularisation function, $f(\Delta x, \sigma, \lambda)$. This function determines how much unfolding should be carried out in a given iteration based on the difference between data and Monte Carlo, Δx, the uncertainty in this difference, σ, and a regularisation parameter λ. The regularisation function should take the ratio $\Delta x/\sigma\lambda$ as an argument, and return a value near zero at small values of this argument and approach one at higher values.

As the regularisation function depends on the difference between data and Monte Carlo, it is important that the Monte Carlo be normalised appropriately. The discrepancy is defined as

$$\Delta d_k = d_k - \frac{N_{\mathrm{dSmc}}}{N_{\mathrm{MC}}} r_k \tag{5.16}$$

where N_{MC} is the total number of jets in the MC sample and N_{dSmc} is the number of jets in the data spectrum that correspond to structures/shapes present in the MC spectrum. Normalising the MC in this way enables the unfolding to preserve features in the data, such as new physics signals, which were not simulated in the MC, while correctly scaling the MC in regions where it has a similar shape to the data. The total number of jets in the data sample may be taken as an initial estimate for N_{dSmc}. A better estimate may then be obtained using

$$N'_{\mathrm{dSmc}} = N_{\mathrm{dSmc}} + \sum_{k=1}^{N_B} \left(1 - f\left(\Delta d, \sigma, \lambda\right)\right) \Delta d_k. \tag{5.17}$$

This procedure may be repeated until the relative change in N_{dSmc} is less than a desired threshold.

5.5.2 Matching Efficiency

In order to obtain the transfer matrix from the Monte Carlo, reconstructed jets need to be matched with a corresponding truth jet. Jets are matched if they lie within a distance $\Delta R < 0.3$ in $y - \phi$ space. The spectrum of matched truth (or reconstructed) jets may be obtained by projecting the transfer matrix onto the appropriate axis. The matched spectrum may then be compared to the unmatched spectrum to obtain the matching efficiency for truth jets and for reconstructed jets. As the transfer matrix is derived using only matched pairs of jets, the effect of the matching efficiency should be taken into consideration. Prior to the unfolding, the measured data is multiplied by the matching efficiency for reconstructed jets, and after unfolding the result is divided by the matching efficiency for truth jets.

An initial unfolding may then be performed on the data, yielding the result

$$u_j = t_j \cdot \frac{N_{\mathrm{dSmc}}}{N_{\mathrm{MC}}} + \left[1 - f\left(\Delta d_k, \sigma d_k, \lambda_M\right)\right] \cdot \Delta d_j + \sum_{k=1}^{N_B} f\left(\Delta d_k, \sigma d_k, \lambda_M\right) \cdot \tilde{P_{kj}} \cdot \Delta d_k \quad (5.18)$$

where the unfolding matrix $\tilde{P_{ij}}$ is obtained from the transfer matrix:

$$\tilde{P_{ij}} = \frac{A_{ij}}{\sum_{k=0}^{N_b} A_{ik}} \quad (5.19)$$

The regularisation functions determine how much unfolding is done in a given bin, based on the regularisation parameter λ and significance of Δd_k. Only the difference between measured data and reconstructed MC is unfolded: in bins where Δd_k is small, the unfolded result is dominated by the truth level MC spectrum. In those bins where the discrepancy is significant, the regularisation parameter λ determines how much unfolding is carried out. For larger values of λ, less unfolding is performed on the data.

Once an initial estimate of u_j has been obtained, this may be used to reweight the MC at truth level, and thus improve the transfer matrix. The updated transfer matrix is given by

$$A'_{ij} = A_{ij} + f(|\Delta u_j|, \sigma u_j, \lambda) \cdot \frac{N_{\mathrm{MC}}}{N_{\mathrm{dSmc}}} \cdot P_{ij} \cdot \Delta u_j, \quad (5.20)$$

where

$$\Delta u_j = u_j - \frac{N_{\mathrm{dSmc}}}{N_{\mathrm{MC}}} \cdot t_j. \quad (5.21)$$

The new transfer matrix can then be used to update the folding and unfolding matrices, P_{ij} and $\tilde{P}_{ij}$. The procedure may then be carried out iteratively in the following sequence:

- Update the normalisation factor, N_{dSmc}, according to 5.17;
- Perform the unfolding;
- Use the unfolded data to update the transfer matrix, and the folding/unfolding

matrices.

5.6 Treatment of uncertainties

5.6.1 Statistical uncertainties

The statistical uncertainties on the final (unfolded) cross-section measurement are obtained using “toy” Monte Carlos. For each toy, Poisson fluctuations are applied to the measured data spectrum and to the transfer matrix. The fluctuated data is then unfolded using the fluctuated transfer matrix. The unfolded spectra from the toys are then used to compute a covariance matrix, from which the statistical uncertainty on the unfolded data is taken.

5.6.2 Systematic Uncertainties

The JES uncertainty is the dominant source of systematic uncertainty. Its effect on the final cross-section result is found by propagating each of the JES components listed in Section 5.3.3 through the unfolding procedure.

The uncertainty on the cross-section associated with a given component is obtained using Monte Carlo. For each rapidity bin of the MC spectrum, a modified spectrum is obtained by shifting the jet p_{T} up by one standard deviation of the JES uncertainty component being considered. A second modified spectrum is obtained by shifting jets down in p_{T} by the same amount. These modified spectra are then unfolded using the same technique as for data. The relative difference between the modified and nominal spectra (after unfolding) is then taken as the uncertainty on the cross-section associated with this JES component.

The effect of the jet energy resolution (JER) uncertainty is propagated through the unfolding in a similar fashion to the JES uncertainty. A modified Monte Carlo sample is produced by smearing the p_{T} of the reconstructed jets in the nominal MC sample. The reconstructed jets have their p_{T} smeared by a factor Δ, where Δ is a random variable with standard deviation σ_{Δ} and a mean of one. The standard deviation of Δ is chosen to satisfy

$$\sigma_{\Delta}^2 + \sigma_{\mathrm{nom}}^2 = \left(\sigma_{\mathrm{nom}} + \sigma_{\mathrm{JER}}\right)^2 , \tag{5.22}$$

where σ_{nom} is the nominal JER and σ_{JER} is its uncertainty. The additional smearing is thus applied in such a way as to increase the effective JER by one standard deviation. The data are then unfolded using the modified transfer matrix, and the difference between this result and that unfolded with the nominal transfer matrix is taken as the systematic uncertainty.

The matching between truth and reconstructed jets is another source of systematic uncertainty. As mentioned earlier, the transfer matrix is constructed by matching truth and reconstructed jets within $\Delta R < 0.3$ in rapidity and azimuthal angle. Transfer matrices are also constructed by matching jets within $\Delta R < 0.4$ and $\Delta R < 0.2$. The unfolding is carried out using these matrices, and the largest difference between either result and that obtained from the nominal transfer matrix is taken as the uncertainty.

Shape variations between the MC spectrum and the data will also introduce systematic uncertainties during the unfolding procedure. To estimate this effect, the truth level MC spectrum is reweighted in such a way to improve the agreement between the reconstructed MC and the measured data. The reweighted MC is then unfolded using the original transfer matrix (i.e., the one used to unfold the data). The difference between the result of this and the reweighted truth level MC is taken as a systematic uncertainty, as it reflects the effect of the MC shape on the unfolded spectrum.

The efficiency with which jets are reconstructed has also been considered. In Monte Carlo, this is equivalent to the matching efficiency. In data, the reconstruction efficiency may be estimated by matching reconstructed jets to track jets, which are formed by running jet-finding algorithms on tracks reconstructed using the inner detector. These two efficiencies may be compared in order to estimate the degree to which the jet reconstruc-

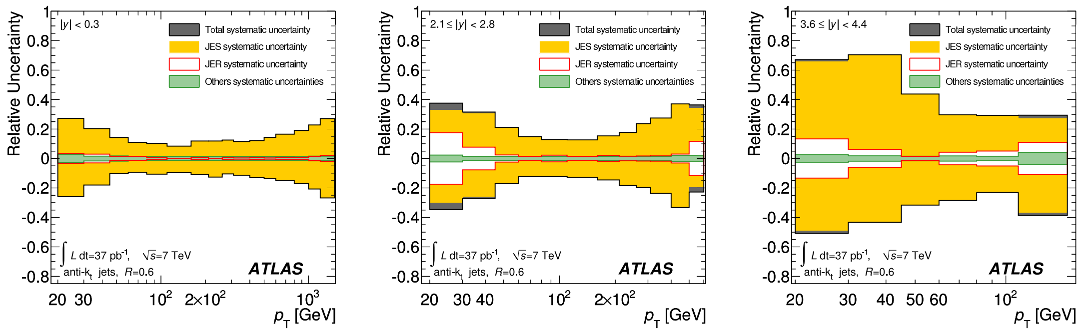

Figure 5.12: Systematic uncertainty on the inclusive jet cross-section for anti-k_t jets with $R = 0.6$, for jets in three rapidity regions.

tion efficiency is mis-modelled by the simulation. The difference is taken as a systematic uncertainty, and is 2% for jets with 20 GeV $< p_{\mathrm{T}} <$ 30GeV and less than 1% for jets with $p_{\mathrm{T}} >$ 30 GeV.

The relative systematic uncertainties for selected rapidity regions are plotted in Figure 5.12, showing the contributions from various components. In addition to these components, there is an additional uncertainty of 3.4% on the cross-section measurements due to the uncertainty associated with the luminosity measurement at `ATLAS`.

5.7 Results and discussion

5.7.1 Inclusive Jet Cross-Section

Results for the inclusive jet cross-section are plotted in Figure 5.13 for $R = 0.4$ jets and Figure 5.14 for $R = 0.6$. The overlaid theoretical predictions are obtained using NLOJet++ with the CT10 PDF set. Two of the parameters used by the event generator are the factorisation scale μ_f and the renormalisation scale μ_r. The renormalisation scale is the scale at which α_s is evaluated, while the factorisation scale is the scale at which the PDFs are sampled. For the theoretical predictions of the inclusive jet cross-section, both of these scales have been set to the p_{T} of the leading jet:

$$\mu_r = \mu_f = p_{\mathrm{T}}^{\mathrm{max}}. \tag{5.23}$$

The choice of scale is taken as a source of systematic uncertainty in the theoretical predictions. This uncertainty was estimated by varying μ_r and μ_f independently by factors of 2*, with the resulting variation in the observables taken as the systematic uncertainty associated with the scale choice.

The NLOJet++ event generator calculates (at NLO) the cross-section for partons produced in the hard scattering. Before this may be compared to data, it must be corrected for non-perturbative QCD effects (i.e. hadronisation and underlying event effects). These corrections are derived from `PYTHIA`. `PYTHIA` is run normally, using an LO matrix element for the hard scattering before showering the incoming/outgoing partons and incorporating hadronisation and UE effects. It is also run with the hadronisation and UE calculations turned off, essentially giving a parton level cross-section at LO. A correction factor, C_{NP} is then obtained by taking the ratio of these two results, such that

$$C_{\mathrm{NP}} = \frac{\sigma_{\mathrm{full}}}{\sigma_{\mathrm{sans-UE/had}}}, \tag{5.24}$$

where $\sigma_{\mathrm{sans-UE/had}}$ is the cross-section obtained from `PYTHIA` with hadronisation and UE calculations turned off and σ_{full} is the cross-section obtained from `PYTHIA` with these effects enabled. The correction factor C_{NP} is computed bin by bin in p_{T} and y, and used to scale the NLOJet++ result to obtain the theoretical prediction for the cross-section with non-perturbative effects included. The agreement between data and theory is generally good.

In Figures 5.15 ($R = 0.4$) and 5.16 ($R = 0.6$), the ratios of the data and theory results

---

*Scenarios in which one scale is reduced by half while the other is doubled were not considered, in order to avoid introducing large logarithms.

are plotted as a function of p_{T} in bins of $|y|$. The CT10 PDF set is used as a baseline, such that cross-sections are plotted relative to those obtained from NLOJet++ with CT10 PDFs. Theoretical results obtained using NLOJet++ with other PDF sets (MSTW2008, NNPDF 2.1, and HERAPDF 1.5) are also shown. NLOJet++ tends to predict a higher cross-section than seen in data when using any of the PDF sets considered here, with the discrepancy becoming worse at high p_{T} or high rapidity. Of the PDF sets considered, MSTW2008 follows the data best in these regions. In all cases, the differences between data and theory are similar in magnitude to the combined systematic uncertainties from theory and data.

Figures 5.17 and 5.18 again show the ratios of the data and theory results, but also include theoretical predictions obtained from `POWHEG`. In these cases, `POWHEG` is used to compute the matrix element for the hard scattering at NLO using the CT10 PDF set, and is interfaced to either `PYTHIA` (with either the AUET2B or Perugia2011 tune) or `HERWIG` (AUET2 tune). In these cases, `POWHEG` interacts with the parton shower event generators in such a way that NLO accuracy is maintained throughout the calculation. The pink curves in Figures 5.17 and 5.18 show the results obtained from `POWHEG` when it is run with the hadronisation and underlying event calculations switched off, with non-perturbative corrections applied in the same manner used for NLOJet++ as discussed above. The `POWHEG` results vary significantly depending on the method used for parton showering and UE effects. These variations are on the order of 30%, whereas the theoretical uncertainty due to non-perturbative effects is less than 10% for jets with $R = 0.4$. The results obtained by interfacing `POWHEG` with the AUET2B tune of `PYTHIA` show fairly good agreement with the data over the entire kinematic range studied.

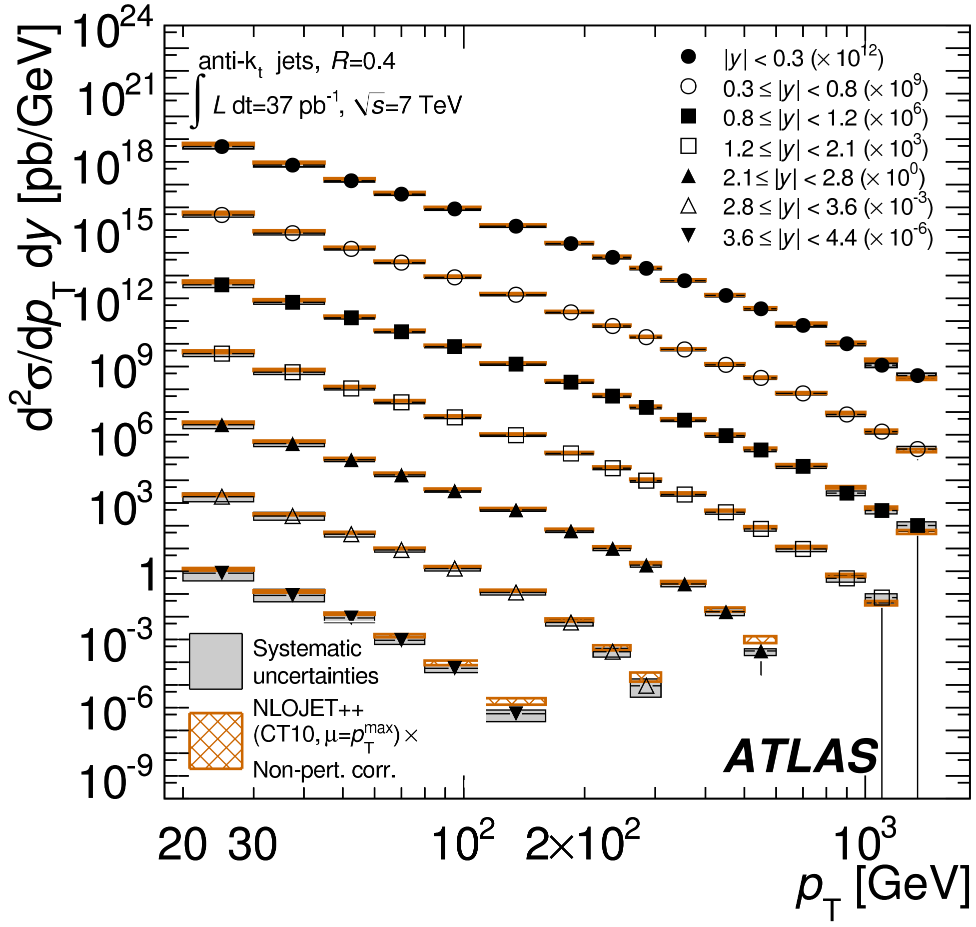

Figure 5.13: Inclusive jet cross-section for anti-k_t jets with $R = 0.4$.

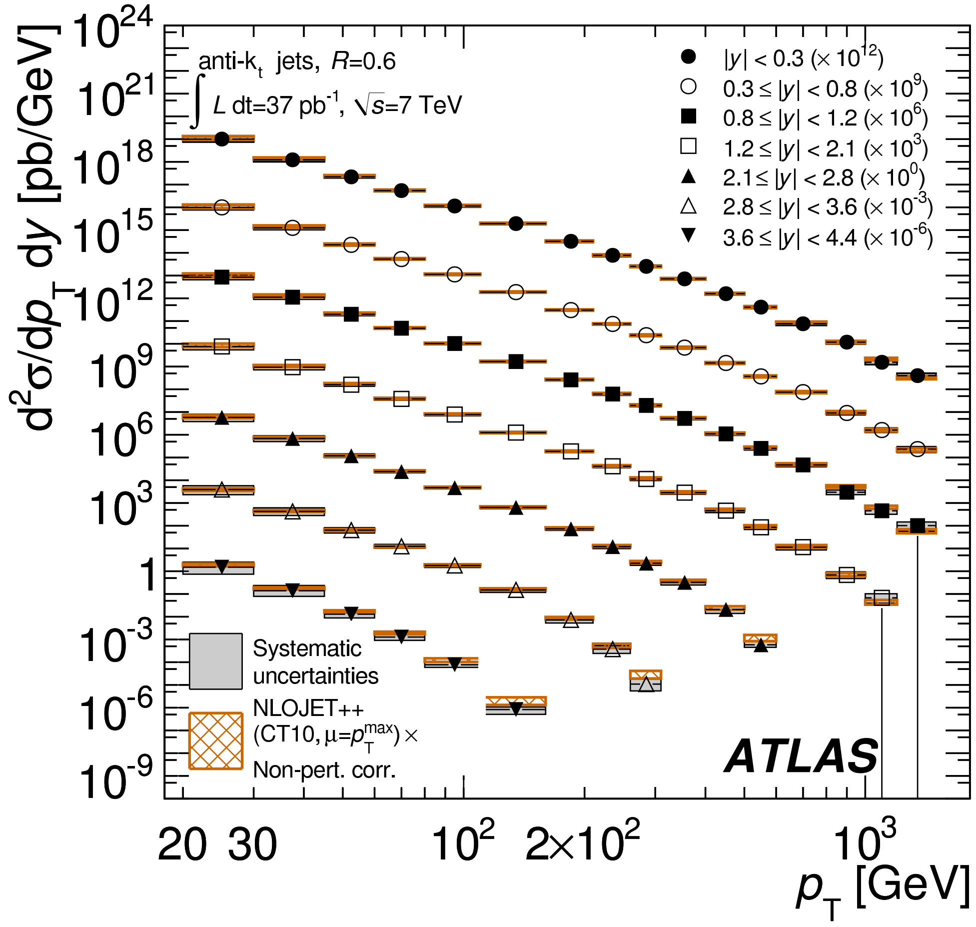

Figure 5.14: Inclusive jet cross-section for anti-k_t jets with $R = 0.6$.

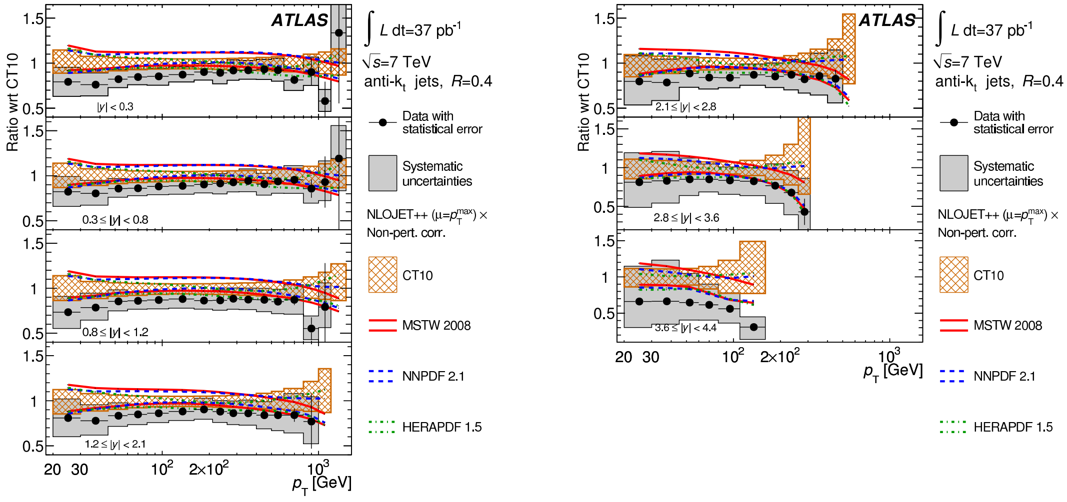

Figure 5.15: Ratio of the inclusive jet cross-section to the NLOJet++/CT10 prediction, for different rapidity bins using anti-k_t jets with $R = 0.4$. Other PDFs are also shown.

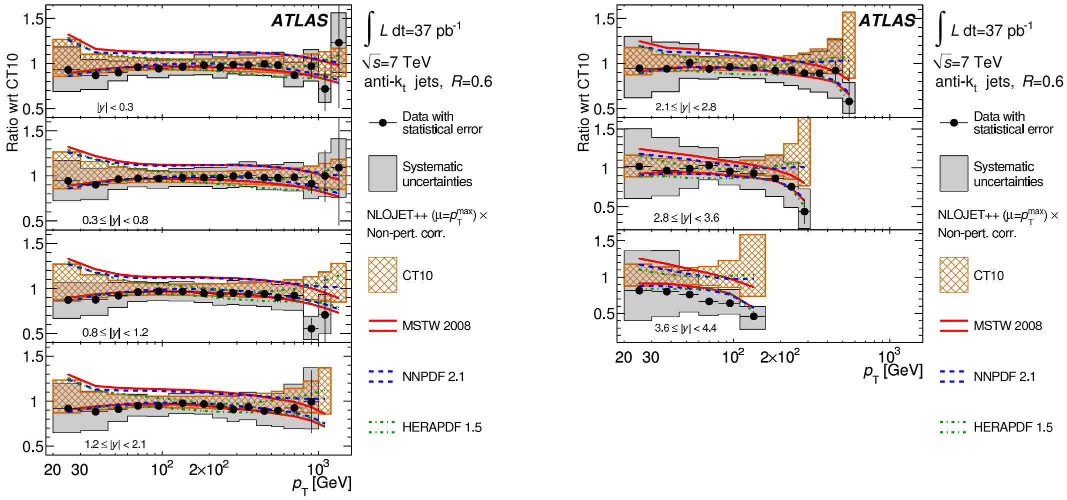

Figure 5.16: Ratio of the inclusive jet cross-section to the NLOJet++/CT10 prediction, for different rapidity bins using anti-k_t jets with $R = 0.6$. Other PDFs are also shown.

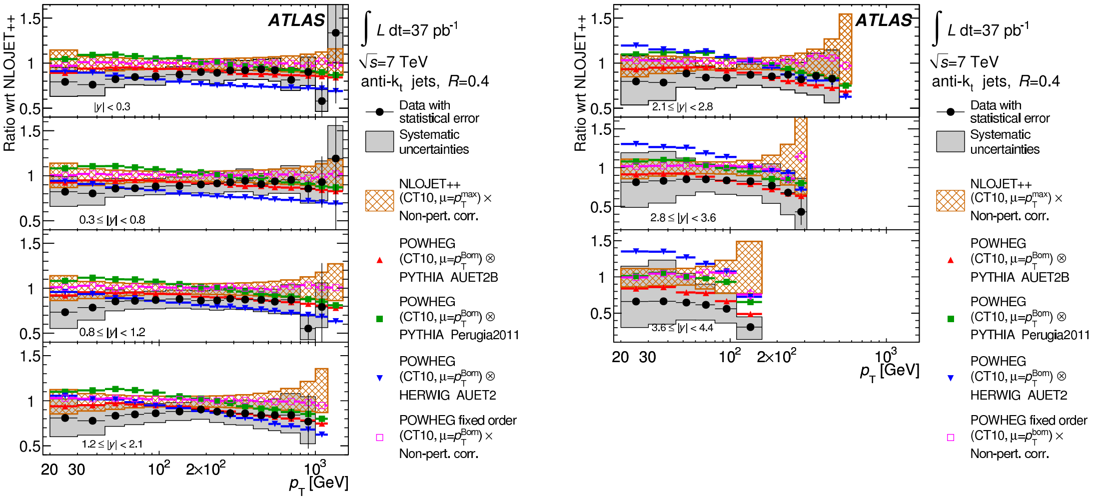

Figure 5.17: Ratio of the inclusive jet cross-section to the NLOJet++/CT10 prediction, for different rapidity bins using anti-k_t jets with $R = 0.4$. Theoretical predictions made using `POWHEG` are also shown.

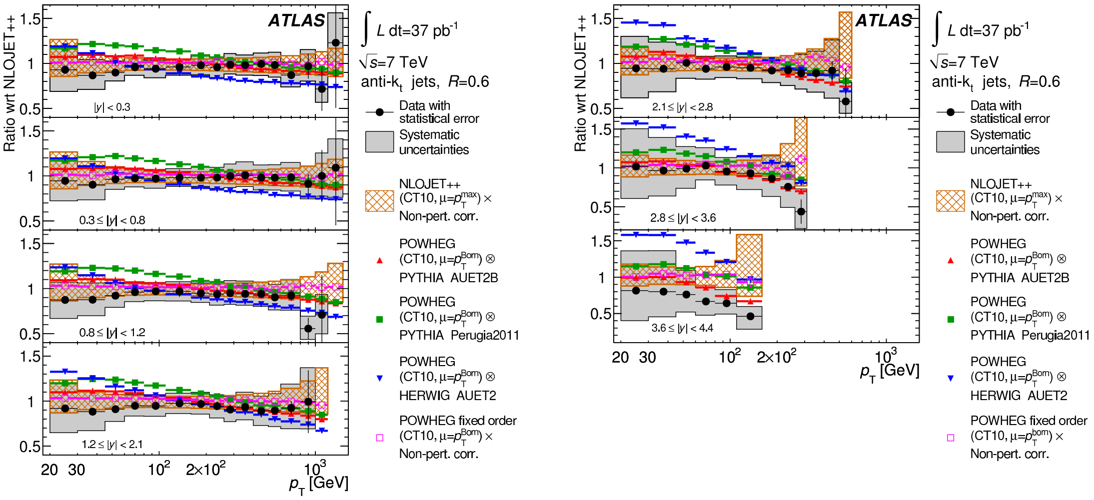

Figure 5.18: Ratio of the inclusive jet cross-section to the NLOJet++/CT10 prediction, for different rapidity bins using anti-k_t jets with $R = 0.6$. Theoretical predictions made using `POWHEG` are also shown.

5.7.2 Dijet Mass Spectrum

The dijet mass spectrum, after unfolding, is plotted in Figures 5.19 for jets with $R = 0.4$, and 5.20 for $R = 0.6$. The overlaid theoretical results are again obtained using NLOJet++ with the CT10 PDF set and non-perturbative corrections obtained from `PYTHIA`. In this case, the scales

$$\mu_r = \mu_f = p_{\mathrm{T}}^{\max} e^{0.3y^*}, \tag{5.25}$$

(motivated in Reference [110]), were chosen for renormalisation and factorisation. For the scale choice given in equation 5.23, NLOJet++ and `POWHEG` gave results that agreed with each other and were consistent with the data for small values of y^*. However for $y^* \gtrsim 3$ the cross-sections obtained from NLOJet++ were unstable and significantly smaller (in some cases negative) than those obtained from `POWHEG`. When using the scales given in equation 5.25, NLOJet++ gave stable results that were in agreement with those obtained from `POWHEG`.

Theoretical results obtained using NLOJet++ with different PDF sets are plotted in Figures 5.21 and 5.22, shown as a ratio to the result obtained using CT10. Data and theory are seen to agree well at small values of y^*. At larger values of y^*, fluctuations appear in the data/theory ratio. The data spectrum is smooth in this region, and fluctuations are due to lack of statistics in the theoretical predictions. As with the inclusive jet cross-section, the best agreement between data and NLOJet++ is obtained with the MSTW2008 PDF set.

Results obtained from `POWHEG` are plotted in Figures 5.23 and 5.24. `POWHEG` did not exhibit the instabilities seen in the NLOJet++ results at high values of y^*, and so the scales $\mu_r = \mu_f = p_{\mathrm{T}}^{\max}$ are again used with `POWHEG`. The best agreement between data and the `POWHEG` results is seen when using the AUET2B tune of `PYTHIA` (as was also seen in the inclusive jet cross-section), with Perugia2011 and the AUET2 tune of `HERWIG` yielding

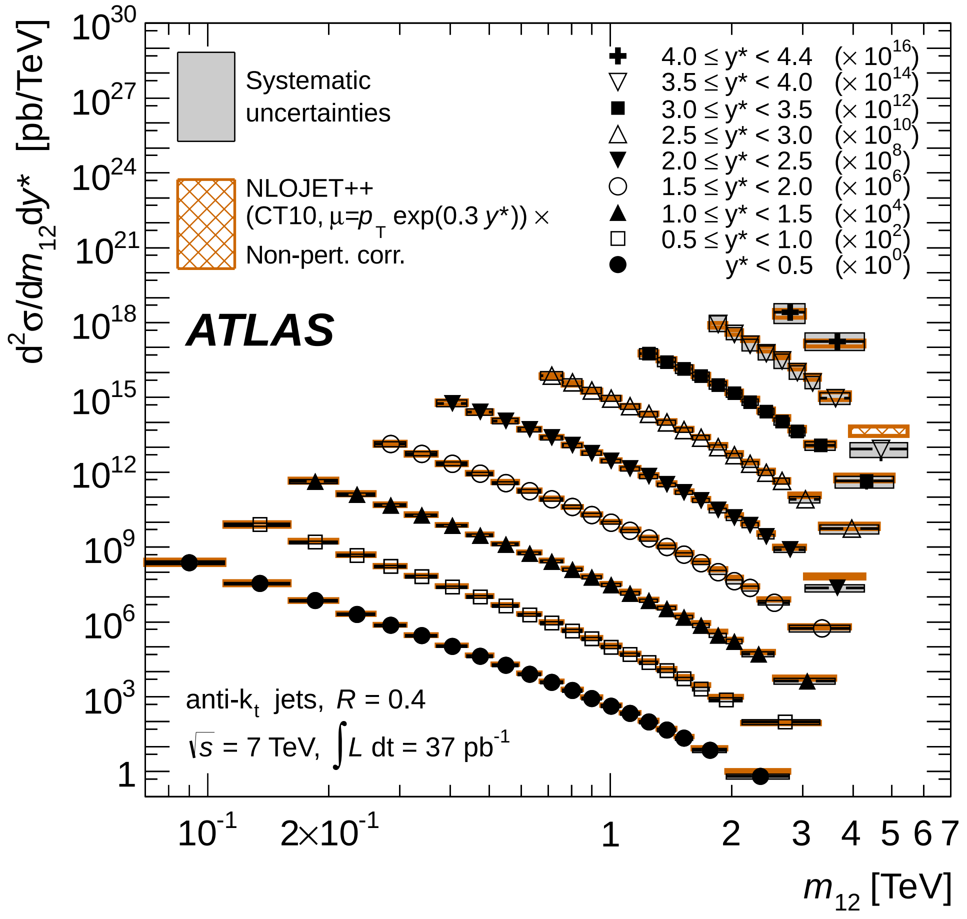

Figure 5.19: Dijet mass spectrum for anti-k_t jets with $R = 0.4$.

cross-sections higher than that seen in data.

5.8 Summary

The inclusive jet and dijet cross-sections have been measured with 37pb^{-1} of data recorded in 2010. For the most part the theoretical predictions agree with the measured data, although there are some discrepencies at high p_{T} and high $|y|$ (i.e. in the kinematic regions where the cross-section has not been previosuly measured). Of the theoretical predictions obtained using NLOJet++, those using the MSTW2008 PDF set have the best agreement with the measured data. Of the predictions obtained from `POWHEG` inter-

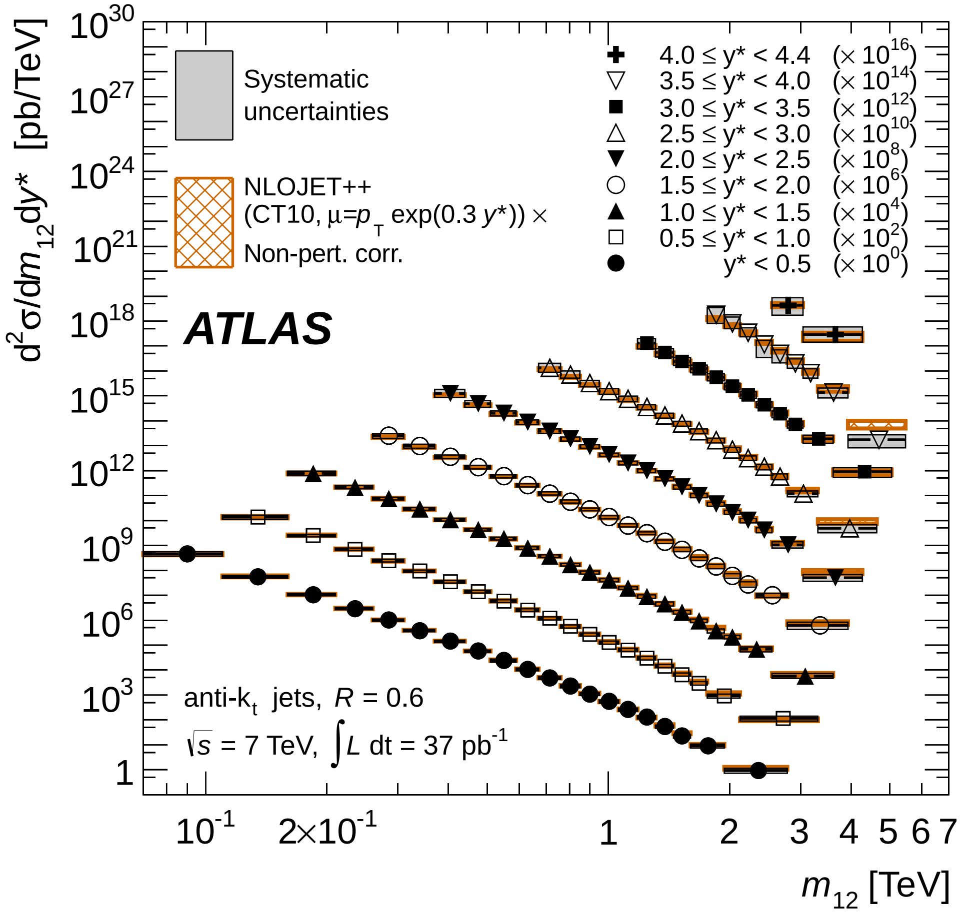

Figure 5.20: Dijet mass spectrum for anti-k_t jets with $R = 0.6$.

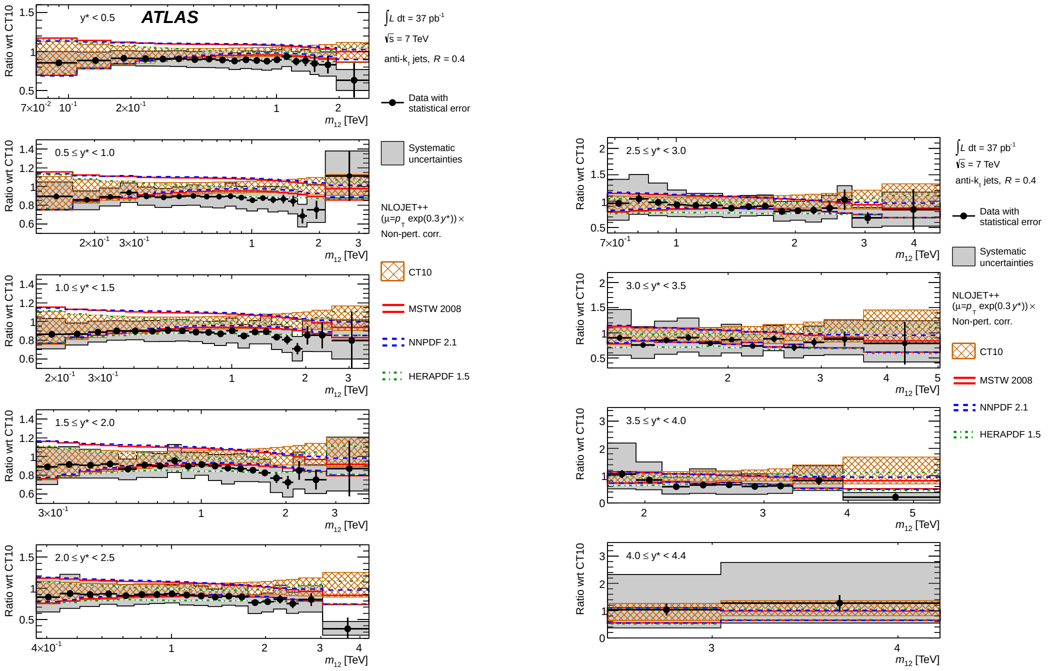

Figure 5.21: Ratio of measured dijet mass spectrum to theoretical prediction obtained using NLOJet++ with various PDF sets, for anti-k_t jets with $R = 0.4$.

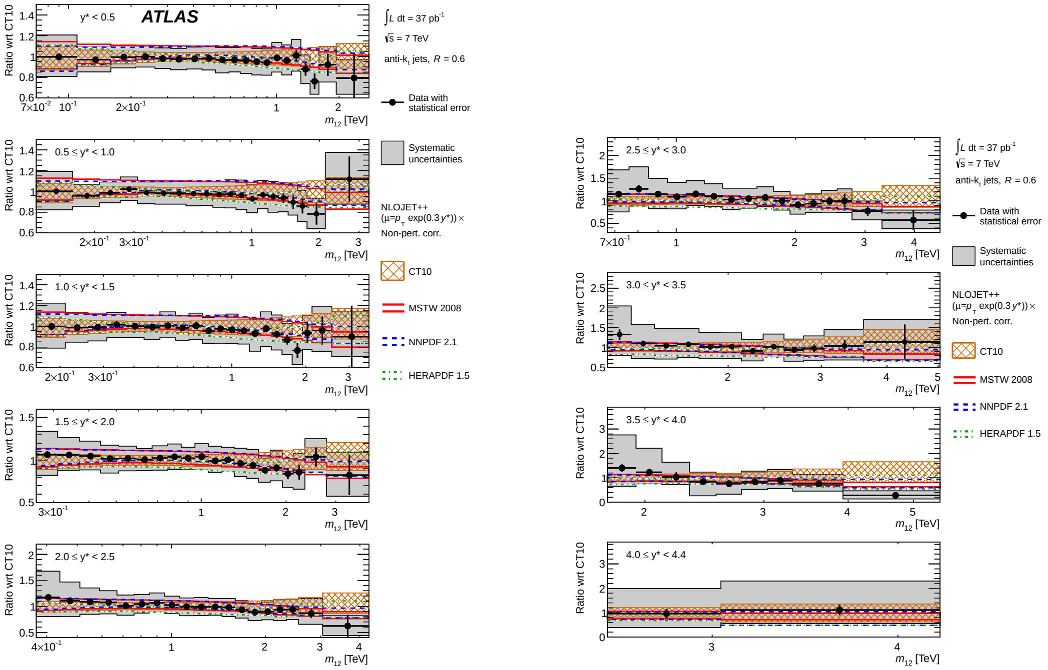

Figure 5.22: Ratio of measured dijet mass spectrum to theoretical prediction obtained using NLOJet++ with various PDF, for anti-k_t jets with $R = 0.6$.

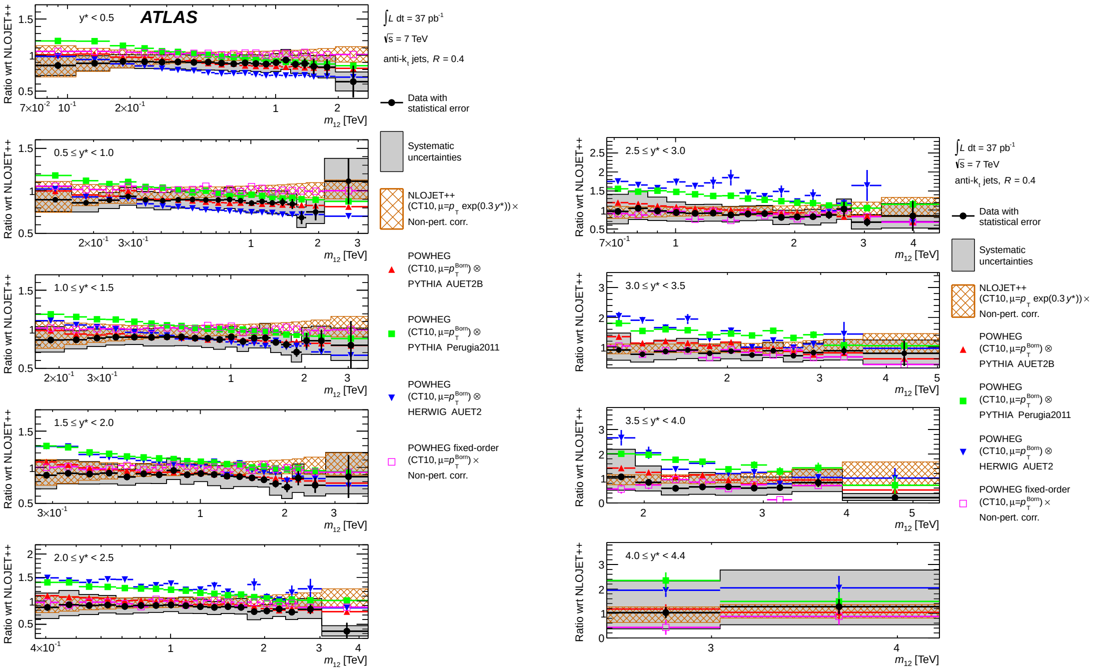

Figure 5.23: Ratio of measured dijet mass spectrum to theoretical prediction obtained using `POWHEG`, for anti-k_t jets with $R = 0.4$.

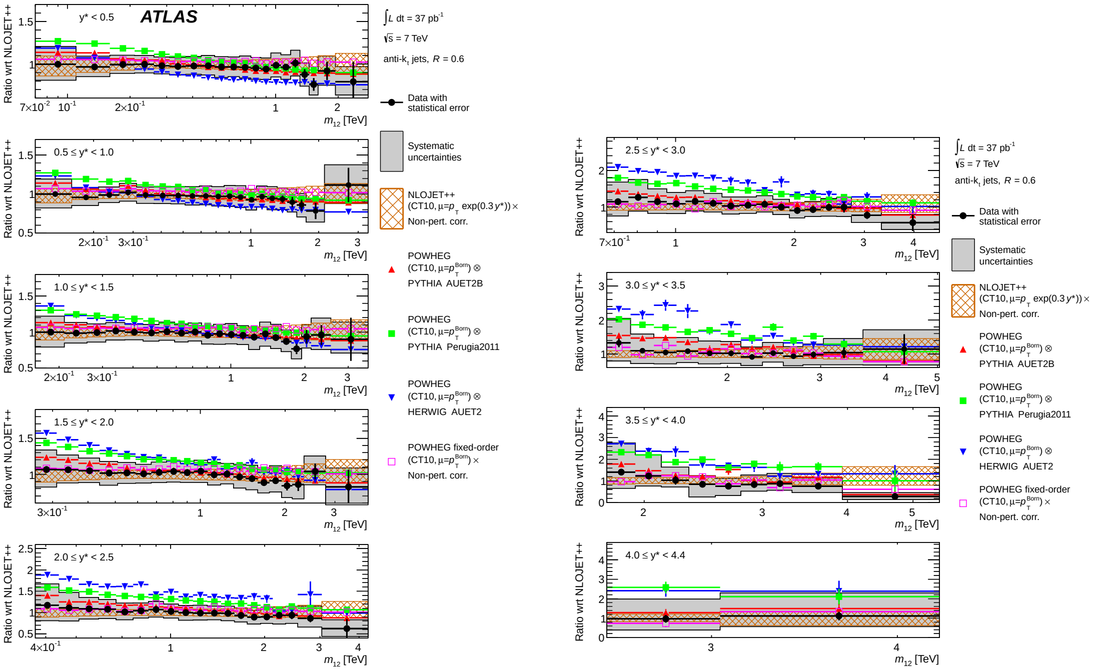

Figure 5.24: Ratio of measured dijet mass spectrum to theoretical prediction obtained using `POWHEG`, for anti-k_t jets with $R = 0.6$.

faced to `PYTHIA` or `HERWIG`, the AUET2B tune of `PYTHIA` yields the best agreement with the measured data; this agreement persists in regions of high p_{T} and/or $|y|$. These measurements represent a coherent QCD measurement made over a large kinematic region, which seamlessly covers forward rapidities that have not previously been studied at a hadron-hadron collider. These measurements are suitable for use in the computation of next-generation PDF sets, and thus may provide some insight into the non-perturbative structure of the proton. Similar studies have been made using the CMS detector; however separate analyses using different jet definitions were used for the central and forward regions, and a gap exists in the rapidity regions covered by these analyses.

Chapter 6

Conclusion

Data taken during the 2003 beam test of the `ATLAS` forward calorimeter has been analysed. A software bug affecting data reconstruction was fixed, and thus the results presented here supercede those that were previously published. The effects of additional upstream material on the calorimeter response and resolution have been studied. The results of Monte Carlo simulations of the beam test have been compared to the results obtained from data, and the agreement between the two is typically good. Good agreement between data and simulation is also found when studying the topological cluster moments used in local hadronic calibration, and these results are consistent with those obtained from other studies. These studies play a key role in the validation of Monte Carlo simulations for the `ATLAS` forward calorimeter, which is important because all the hadronic calibration schemes used by `ATLAS` are derived from Monte Carlo studies.

The inclusive jet and dijet cross sections have been measured using 37pb^{-1} of data collected with the `ATLAS` detector during 2010. While the CMS measurements from the same time period contain a gap in the rapidity coverage, the measurements presented here fully cover the rapidity region $0 < |y| < 4.4$. This was accomplished through the use of a sophisticated trigger scheme, which allowed jets in the transition region to be accepted by either the central or the forward jet trigger system. Theoretical predictions generally agree well with the measured cross sections, with the `POWHEG` generator giving results that agree well even at high p_{T} and rapidity. These measurements constitute a new measurement of QCD in a region of phase space that had not previously been explored, spanning two orders of magnitude in jet p_{T} (dijet mass) and eleven orders of magnitude in cross section.

Bibliography

[1] F. Spano. *Standard model electroweak measurements at LEP*, arXiv: hep-ex/0605093, 2006.

[2] T. Aaltonen et al. *Combination of the top-quark mass measurements from the Tevatron collider*, Phys. Rev. D86, 092003, 2012.

[3] CERN experiments observe particle consistent with long-sought Higgs boson, July 2012, http://press.web.cern.ch/press/PressReleases/Releases2012/PR17.12E.html.

[4] G. Aad et al. *Observation of a new particle in the search for the Standard Model Higgs boson with the ATLAS detector at the LHC*, Phys. Lett. B716, 1 – 29, 2012.

[5] G. Flugge. Future Research in High Energy Physics. In *1993 European School of High-Energy Physics*, pages 117–163, Zakopane, Poland, September 1993. CERN-94-04.

[6] C. Burgess and G. Moore. *The Standard Model: A Primer*. Cambridge University Press, 2007.

[7] J. Beringer et al. *Review of particle physics. Particle Data Group*, Phys. Rev. D86, 2012.

[8] J. C. Collins, D. E. Soper, and G. Sterman. *Factorization for short distance hadron-hadron scattering*, Nucl. Phys. B261, 104 – 142, 1985.

[9] W. Greiner, S. Schramm, and E. Stein. *Quantum Chromodynamics*. Springer, 2007.

[10] G. Altarelli and G. Parisi. *Asymptotic freedom in parton language*, Nucl. Phys. B126, 298 – 318, 1977.

[11] H.-L. Lai et al. *New parton distributions for collider physics*, Phys. Rev. D82, 074024, 2010.

[12] G. Voss and B. Wiik. *The electron-proton collider HERA*, Annual Review of Nuclear and Particle Science 44, 413–452, 1994.

[13] L. Lederman. *The Tevatron*, Sci. Am. 264, 26–33, 1991.

[14] D. University, The Durham HepData Project, April 2013, http://hepdata.cedar.ac.uk/pdf/pdf3.html.

[15] J. Campbell, J. W. Huston, and W. J. Stirling. *Hard interactions of quarks and gluons: a primer for LHC physics*, Reports on Progress in Physics 70, 89, 2007.

[16] S. Catani and M. Seymour. *A general algorithm for calculating jet cross-sections in NLO QCD*, Nucl. Phys. B485, 291–419, 1997.

[17] P. Nason. *A New method for combining NLO QCD with shower Monte Carlo algorithms*, JHEP 0411, 040, 2004.

[18] T. Sjöstrand, S. Mrenna, and P. Skands. *A brief introduction to PYTHIA 8.1*, Computer Physics Communications 178, 852–867, 2008.

[19] G. Corcella et al. *HERWIG 6.5 release note*, arXiv: hep-ph/0210213, 2002.

[20] T. Sjöstrand. *Monte carlo generators*, arXiv preprint hep-ph/0611247 , 2006.

[21] S. Frixione and B. R. Webber. *Matching NLO QCD computations and parton shower simulations*, JHEP 0206, 029, 2002.

[22] J. Butterworth et al., Jimmy generator: multiparton interactions in HERWIG, July 2012, http://jimmy.hepforge.org/.

[23] G. Aad et al. Further ATLAS tunes of PYTHIA6 and Pythia 8. Technical Report ATL-PHYS-PUB-2011-014, ATL-COM-PHYS-2011-1507, 2011.

[24] P. Z. Skands. *Tuning Monte Carlo Generators: The Perugia Tunes*, Phys. Rev. D82, 074018, 2010.

[25] S. Frixione, P. Nason, and C. Oleari. *Matching NLO QCD computations with Parton Shower simulations: the POWHEG method*, JHEP 0711, 070, 2007.

[26] Z. Nagy, NLOJET++ home page, July 2012, http://www.desy.de/˜znagy/Site/NLOJet++.html.

[27] S. Alioli et al. *A general framework for implementing NLO calculations in shower Monte Carlo programs: the POWHEG BOX*, JHEP 1006, 043, 2010.

[28] S. Alioli et al. *Jet pair production in POWHEG*, JHEP 1104, 081, 2011.

[29] L. Evans and P. Bryant. *LHC Machine*, JINST 3, S08001, 2008.

[30] M. Benedikt et al., A walk through the LHC injector chain, 2005, http://cdsweb.cern.ch/record/794393/pages, CERN, Geneva, 21 - 23 Mar 2005.

[31] G. Aad et al. *The ATLAS Experiment at the CERN Large Hadron Collider*, JINST 3, S08003, 2008.

[32] S. Chatrchyan et al. *The CMS experiment at the CERN LHC*, JINST 3, S08004, 2008.

[33] G. Aad et al. Performance of primary vertex reconstruction in proton-proton collisions at $\sqrt{s} = 7$ TeV in the ATLAS experiment. Technical Report ATLAS-CONF-2010-069, CERN, Geneva, Jul 2010.

[34] G. Aad et al. Muon Momentum Resolution in First Pass Reconstruction of pp Collision Data Recorded by ATLAS in 2010. Technical Report ATLAS-CONF-2011-046, CERN, Geneva, Mar 2011.

[35] R. Wigmans. *Calorimetry: Energy Measurement in Particle Physics*. International Series of Monographs on Physics. Clarendon Press, 2000.

[36] C. Caso et al. *Review of particle physics. Particle Data Group*, Eur. Phys. J. C3, 1–794, 1998.

[37] R. Wigmans. *Calorimetry*, Scientifica Acta 2, 18, 2008.

[38] M. Derrick et al. *Design and construction of the ZEUS barrel calorimeter*, Nucl. Inst. Meth. A309, 77 – 100, 1991.

[39] C. W. Fabjan and F. Gianotti. *Calorimetry for particle physics*, Rev. Mod. Phys. 75, 1243–1286, Oct 2003.

[40] ATLAS liquid-argon calorimeter: Technical Design Report. Technical Report ATLAS-TDR-2, CERN-LHCC-96-041, CERN/LHCC 96-41, Geneva, 1996.

[41] B. Aubert et al. *Development and construction of large size signal electrodes for the ATLAS electromagnetic calorimeter*, Nucl. Inst. Meth. A539, 558–594, 2005.

[42] ATLAS tile calorimeter: Technical Design Report. Technical Report ATLAS-TDR-3 ; CERN-LHCC-96-042, Geneva, 1996.

[43] D. M. Gingrich et al. *Construction, assembly and testing of the ATLAS hadronic end-cap calorimeter*, JINST 2, P05005, 2007.

[44] J. Colas, M. Pripstein, and W. A. Wenzel. *The electrostatic transformer*, Nucl. Inst. Meth. pages 583–590, September 1990.

[45] A. Artamonov et al. *The ATLAS Forward Calorimeter*, JINST 3, P02010, 2008.

[46] J. P. Archambault et al. The simulation of the ATLAS liquid argon calorimetry. Technical Report ATL-LARG-PUB-2009-001-1, ATL-COM-LARG-2008-002, 2009.

[47] N. J. Buchanan et al. *Design and implementation of the Front End Board for the readout of the ATLAS liquid argon calorimeters*, JINST 3, P03004, 2008.

[48] W. Cleland and E. Stern. *Signal processing considerations for liquid ionization calorimeters in a high rate environment*, Nucl. Inst. Meth. A338, 467 – 497, 1994.

[49] L. W. Nagel and D. Pederson. SPICE (Simulation Program with Integrated Circuit Emphasis). Technical Report UCB/ERL M382, EECS Department, University of California, Berkeley, Apr 1973.

[50] J. Ye. Electronics of the Atlas Liquid Argon Calorimeter and its Precision Calibration. Technical Report ATL-LARG-PROC-2009-006. ATL-COM-LARG-2009-020, CERN, Geneva, Jun 2009. June 17, 2009.

[51] D. Banfi, M. Delmastro, and M. Fanti. *Cell response equalisation of the ATLAS electromagnetic calorimeter without the direct knowledge of the ionisation signals*, JINST 1, P08001, 2006.

[52] M. Bruschi. *The ATLAS luminosity monitor*, Nucl. Inst. Meth. A623, 371 – 373, 2010. 1st International Conference on Technology and Instrumentation in Particle Physics.

[53] P. Jenni et al. *ATLAS Forward Detectors for Measurement of Elastic Scattering and Luminosity*. Technical Design Report. CERN, Geneva, 2008.

[54] V. Cindro et al. *The ATLAS beam conditions monitor*, JINST 3, P02004, 2008.

[55] L. Tompkins. *Performance of the ATLAS Minimum Bias Trigger in p-p collisions at the LHC*, arXiv: 1009.6133, 2010.

[56] G. Aad et al. *Charged-particle multiplicities in pp interactions measured with the ATLAS detector at the LHC*, New J. Phys. 13, 053033, 2011.

[57] N. J. Buchanan et al. *ATLAS liquid argon calorimeter front end electronics*, JINST 3, P09003, 2008.

[58] R. Achenbach et al. *The ATLAS level-1 calorimeter trigger*, JINST 3, P03001, 2008.

[59] U. Schäfer and S. Silverstein, ATLAS level-1 Calorimeter Trigger Jet/Energy Module Project Specification, October 2012, https://edms.cern.ch/file/326674/1.2d/JEMspec12d.pdf.

[60] M. Ferguson et al. *Electron testbeam results for the ATLAS liquid argon forward calorimeter prototype*, Nucl. Inst. Meth. A383, 399 – 408, 1996.

[61] J. Armitage et al. *Results for electrons from the 1995 ATLAS forward calorimeter prototype testbeam*, Nucl. Phys. B61, 101 – 105, 1998. Proceedings of the Fifth International Conference on Advanced Technology and Particle Physics.

[62] P. Loch. Testbeam results for the ATLAS forward calorimeter module 0. In *proceedings of the 8th International Conference on Calorimetry in High Energy Physics*, pages 184–191, Lisbon, June 1999. June 1999.

[63] J. Armitage et al. *Electron signals in the forward calorimeter prototype for ATLAS*, JINST 2, P11001, 2007.

[64] J. Pinfold et al. *Performance of the ATLAS liquid argon endcap calorimeter in the pseudorapidity region $2.5 < |\eta| < 4.0$ in beam tests*, Nucl. Inst. Meth. A593, 324 – 342, 2008.

[65] J. Colas et al. *Position resolution and particle identification with the ATLAS EM calorimeter*, Nucl. Inst. Meth. A550, 96–115, 2005.

[66] J. Colas et al. *Response Uniformity of the ATLAS Liquid Argon Electromagnetic Calorimeter*, Nucl. Inst. Meth. A582, 429–455, 2007.

[67] L. Heelan. *Calibration of the ATLAS Forward Calorimeter and a Study of the Top Quark Production Cross-section Measurement in the Dilepton Channel.* PhD thesis, Carleton University (Canada), 2011.

[68] J. P. Archambault et al. *Performance of the ATLAS Liquid Argon Forward Calorimeter in beam tests*, submitted to JINST .

[69] J. P. Archambault et al. *Energy calibration of the ATLAS liquid argon forward calorimeter*, JINST 3, P02002, 2008.

[70] C. Bovet et al. The CEDAR counters for particle identification in the SPS secondary beams: a description and an operation manual. Technical Report CERN-82-13, Geneva, 1982.

[71] S. Agostinelli et al. *GEANT4: A Simulation toolkit*, Nucl. Inst. Meth. A506, 250–303, 2003.

[72] G. Folger and J. P. Wellisch. *String Parton Models in Geant4*, arXiv: nucl-th/0306007, 2003.

[73] H. Fesefeldt. The simulation of hadronic showers Physics and applications. Technical Report PITHA–85/02, Aachen Technische Hochschule, Germany, 1985.

[74] V. Barashenkov et al. *Medium energy intranuclear cascade calculations: a comparative study*, Nucl. Phys. A187, 531 – 544, 1972.

[75] H. W. Bertini. *Low-Energy Intranuclear Cascade Calculation*, Phys. Rev. 131, 1801–1821, Aug 1963.

[76] P. Speckmayer. Impact of the choice of physics list on GEANT4 simulations of hadronic showers in tungsten. Technical Report LCD-Note-2010-00, CERN, Switzerland, 2010.

[77] B. Andersson, G. Gustafson, and B. Nilsson-Almqvist. *A model for low-*p_{T}*hadronic reactions with generalizations to hadron-nucleus and nucleus-nucleus collisions*, Nucl. Phys. B281, 289 – 309, 1987.

[78] J. Rutherfoord. The Shape of the ATLAS Forward Calorimeter Current Pulse. Technical Report ATL-LARG-PUB-2006-004. ATL-COM-LARG-2006-005, CERN, Geneva, Jun 2006.

[79] J. Rutherfoord. Electrode Transmission Line Corrections to the ATLAS Forward Calorimeter Pulse. Technical Report ATL-LARG-PUB-2006-005. ATL-COM-LARG-2006-006, CERN, Geneva, May 2006.

[80] K.-J. Grahn et al. *Tests of Local Hadron Calibration Approaches in ATLAS Combined Beam Tests*, Journal of Physics: Conference Series 293, 012032, 2011.

[81] E. Abat et al. Response and Shower Topology of 2 to 180 GeV Pions Measured with the ATLAS Barrel Calorimeter at the CERN Test-beam and Comparison to Monte Carlo Simulations. Technical Report ATL-CAL-PUB-2010-001, CERN, Geneva, May 2010.

[82] W. Lampl et al. Calorimeter Clustering Algorithms: Description and Performance. Technical Report ATL-LARG-PUB-2008-002, ATL-COM-LARG-2008-003, CERN, Geneva, Apr 2008.

[83] T. Barillari et al. Local Hadronic Calibration. Technical Report ATL-LARG-PUB-2009-001-2, ATL-COM-LARG-2008-006, CERN, Geneva, Jun 2008.

[84] J. Pinfold et al. *Evaluation of the Local Hadronic Calibration with Combined Beam-Test Data for the Endcap and Forward Calorimeters of ATLAS in the Pseudorapidity Region* $2.5 < |\eta| < 4.0$, Nucl. Inst. Meth. A693, 74–97, 2012.

[85] T. Aaltonen et al. *Measurement of the Inclusive Jet Cross Section at the Fermilab Tevatron p anti-p Collider Using a Cone-Based Jet Algorithm*, Phys.Rev. D78, 052006, 2008.

[86] Search for New Phenomena in Monojet plus Missing Transverse Momentum Final States using 10fb^{-1} of pp Collisions at $\sqrt{s} = 8$ TeV with the ATLAS detector at the LHC. Technical Report ATLAS-CONF-2012-147, CERN, Geneva, Nov 2012.

[87] Search for New Phenomena in the Dijet Mass Distribution updated using $13.0\ \text{fb}^{-1}$ of *pp* Collisions at $\sqrt{s} = 8$ TeV collected by the ATLAS Detector. Technical Report ATLAS-CONF-2012-148, CERN, Geneva, Nov 2012.

[88] G. Aad et al. *Measurement of inclusive jet and dijet cross sections in proton-proton collisions at 7 TeV centre-of-mass energy with the ATLAS detector*, Eur. Phys. J. C71, 1512, 2011.

[89] ATLAS Collaboration. Measurement of jet production in 7 TeV proton-proton collisions with the ATLAS Detector. Technical Report ATLAS-COM-CONF-2010-052, CERN, Geneva, Jun 2010. See back up note for full author list.

[90] Measurement of inclusive jet and dijet cross sections in proton-proton collision data at 7 TeV centre-of-mass energy using the ATLAS detector. Technical Report ATLAS-CONF-2011-047, CERN, Geneva, Mar 2011.

[91] G. Aad et al. *Measurement of inclusive jet and dijet production in pp collisions at* $\sqrt{s} = 7$ *TeV using the ATLAS detector*, Phys. Rev. D86, 014022, 2012.

[92] S. Chatrchyan et al. *Measurement of the Inclusive Jet Cross Section in pp Collisions at* $\sqrt{s} = 7$ *TeV*, Phys. Rev. Lett. 107, 132001, 2011.

[93] CMS Collaboration. *Measurement of forward jets in proton–proton collisions at* $\sqrt{s} = 7$ *TeV*, CDS: CMS-PAS-FWD-10-003, 2011.

[94] S. Chatrchyan and others. *Measurement of the differential dijet production cross section in proton-proton collisions at* $\sqrt{s} = 7$ *TeV*, Phys. Lett. B700, 187–206, 2011.

[95] M. Cacciari, G. P. Salam, and G. Soyez. *The anti-*k_{T} *jet clustering algorithm*, JHEP 04, 063, 2008.

[96] S. Catani et al. *Longitudinally invariant* k_{T} *clustering algorithms for hadron hadron collisions*, Nucl. Phys. B406, 187–224, 1993.

[97] Y. L. Dokshitzer et al. *Better jet clustering algorithms*, JHEP 9708, 001, 1997.

[98] G. C. Blazey et al. *Run II jet physics*, pages 47–77, 2000.

[99] G. Aad et al. *Jet energy measurement with the ATLAS detector in proton-proton collisions at* $\sqrt{s} = 7$ *TeV*, arXiv: 1112.6426, 2011.

[100] Characterization of Interaction-Point Beam Parameters Using the pp Event-Vertex Distribution Reconstructed in the ATLAS Detector at the LHC. Technical Report ATLAS-CONF-2010-027, CERN, Geneva, May 2010.

[101] In-situ pseudorapidity intercalibration for evaluation of jet energy scale uncertainty using dijet events in proton-proton collisions at $\sqrt{s} = 7$ TeV. Technical Report ATLAS-CONF-2011-014, CERN, Geneva, Mar 2011.

[102] G. Aad et al. Jet energy scale and its systematic uncertainty in proton-proton collisions at $\sqrt{s} = 7$ TeV in ATLAS 2010 data. Technical Report ATLAS-CONF-2011-032, CERN, Geneva, Mar 2011.

[103] ATLAS Calorimeter Response to Single Isolated Hadrons and Estimation of the Calorimeter Jet Scale Uncertainty. Technical Report ATLAS-CONF-2011-028, CERN, Geneva, Mar 2011.

[104] E. Khramov et al. Study of the Response of the Hadronic Barrel Calorimeter in the ATLAS Combined Test-beam to Pions of Energies from 20 to 350 GeV for Beam Impact Points from 0.2 to 0.65. Technical Report ATL-TILECAL-PUB-2009-007. ATL-COM-TILECAL-2009-006, CERN, Geneva, Apr 2009.

[105] M. L. Mangano et al. *ALPGEN, a generator for hard multiparton processes in hadronic collisions*, JHEP 0307, 001, 2003.

[106] V. Lendermann et al. *Combining Triggers in HEP Data Analysis*, Nucl.Instrum.Meth. A604, 707–718, 2009.

[107] V. Blobel. *An Unfolding method for high-energy physics experiments*, arXiv: hep-ex/0208022, 2002.

[108] B. Malaescu. *An Iterative, dynamically stabilized method of data unfolding*, arXiv: 0907.3791, 2009.

[109] B. Malaescu. *An Iterative, Dynamically Stabilized(IDS) Method of Data Unfolding*, arXiv: 1106.3107, 2011.

[110] S. D. Ellis, Z. Kunszt, and D. E. Soper. *Two jet production in hadron collisions at order alpha-s**3 in QCD*, Phys.Rev.Lett. 69, 1496–1499, 1992.

Appendix A

Additional Simulation results

Some simulation results were omitted from chapter 4, specifically response plots relating to the various physics lists. These have been included in this appendix.

A.1 Results Obtained using Cylindrical Clusters

Figures A.1 (A.2), A.3 (A.4), and A.5 (A.6) show the responses obtained from beams of pions directed at position 4L (4H), for the QGSP_BERT, QGSP_BERT_HP, and FTFP_BERT physics lists, respectively. The simulation results are analysed using the same method as for data, that is, cylindrical clusters of radius 16 cm are formed around the beam impact point, and the clustered energy is calibrated to the hadronic scale using a simple flat-weighting method (described in Chapter 4). The weights used for the calibration are derived from data, at a beam energy of 200 GeV.

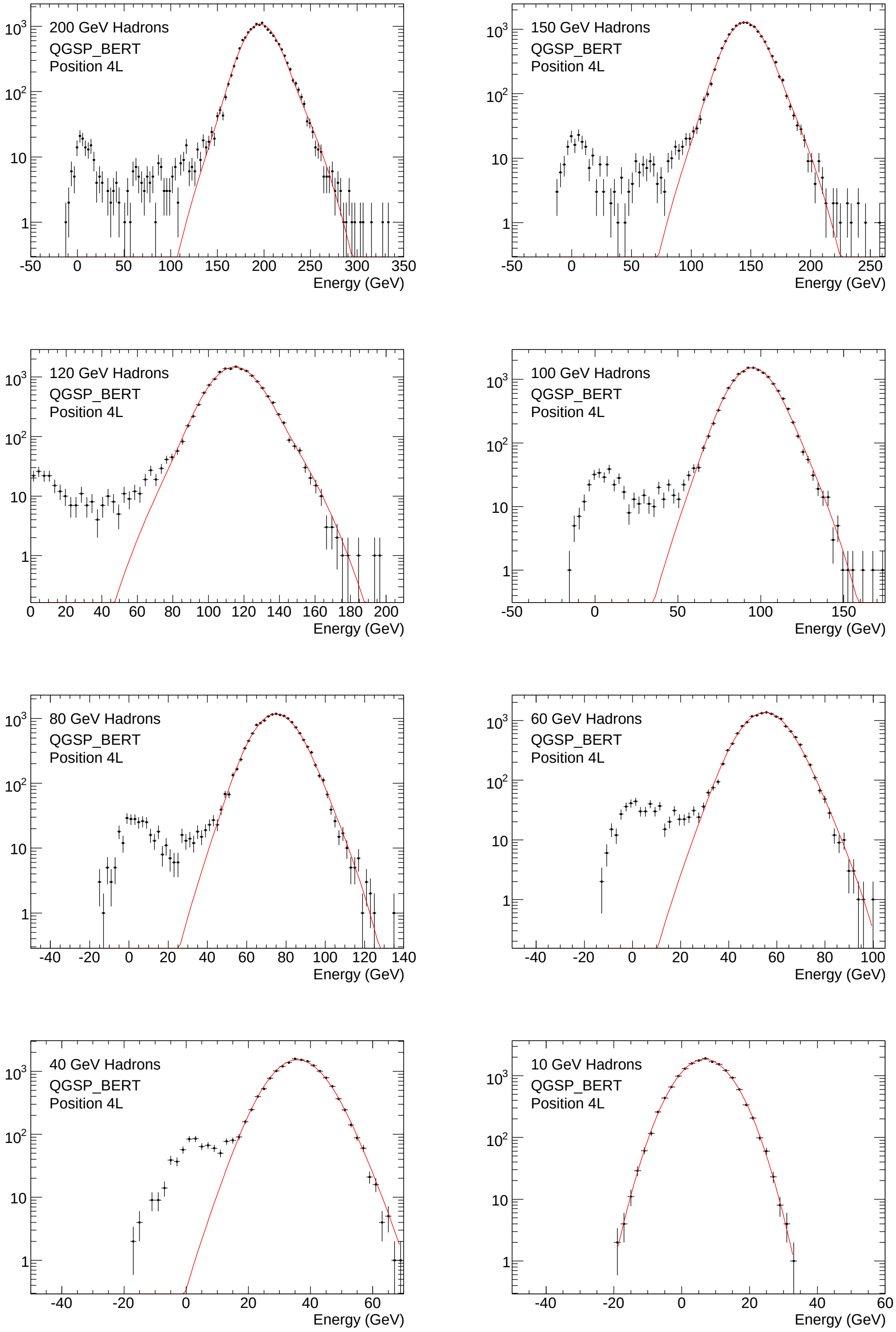

Figure A.1: Response plots for pions directed at position 4L, simulated using the QGSP_BERT physics list.

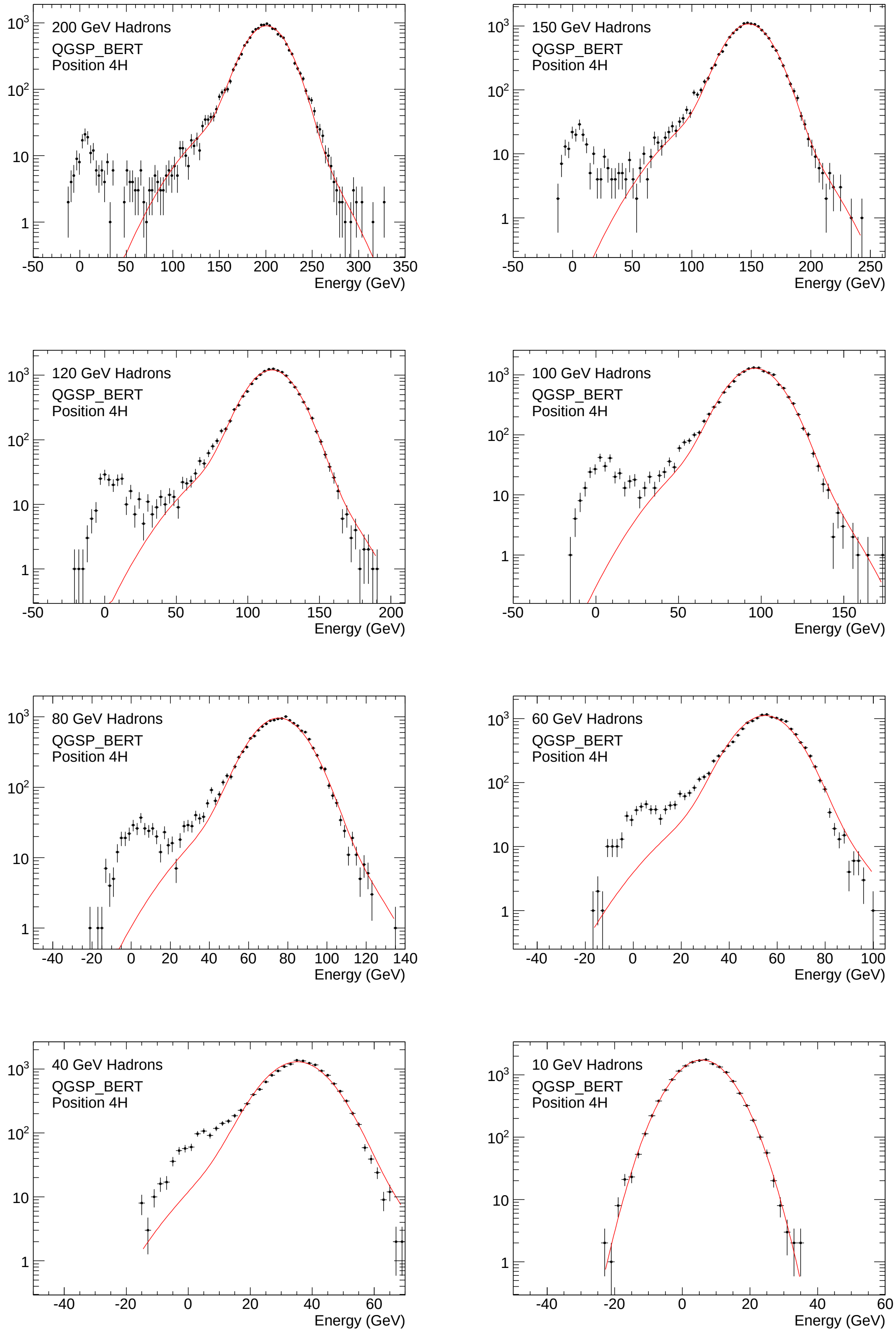

Figure A.2: Response plots for pions directed at position 4H, simulated using the QGSP_BERT physics list.

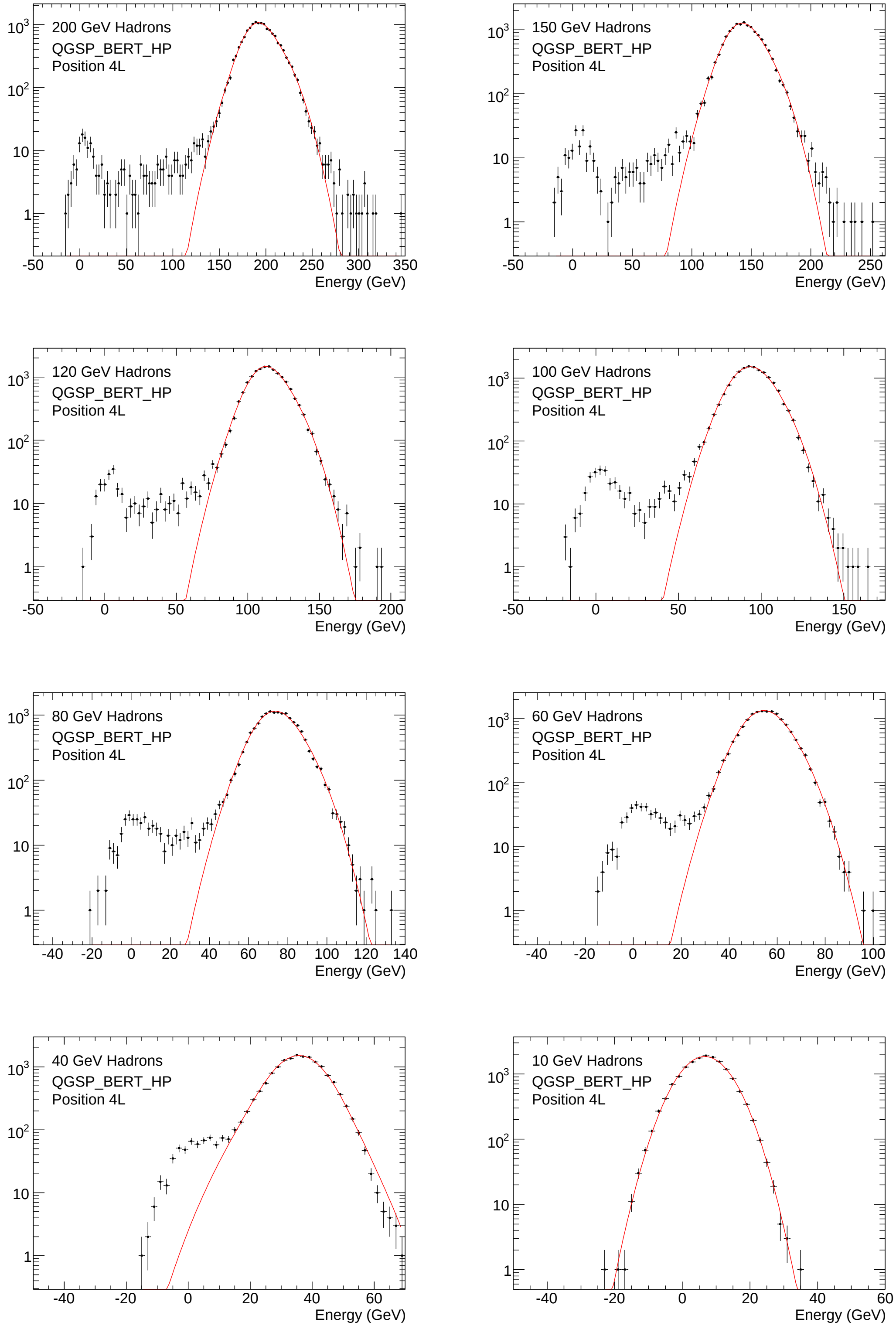

Figure A.3: Response plots for pions directed at position 4L, simulated using the QGSP_BERT_HP physics list.

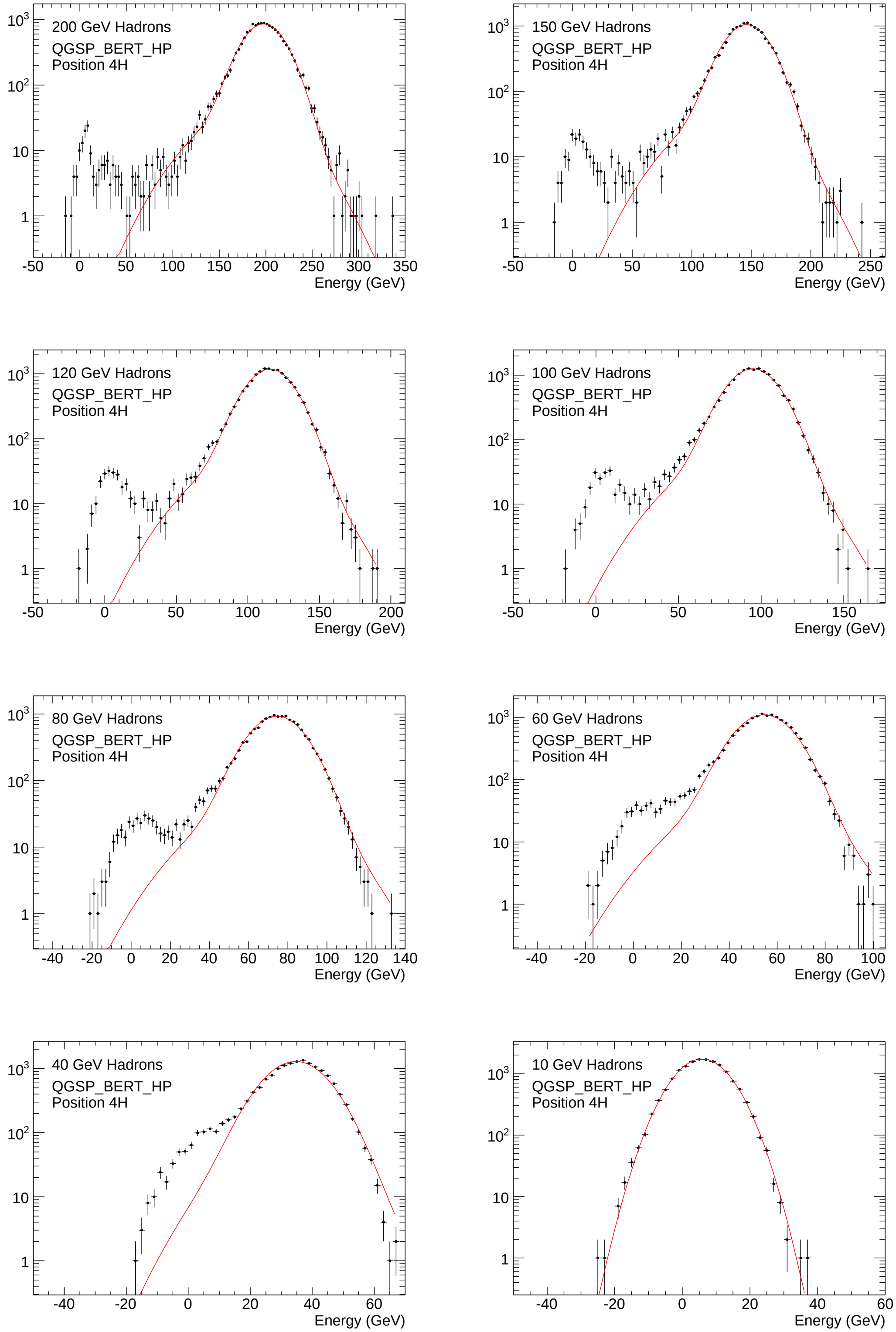

Figure A.4: Response plots for pions directed at position 4H, simulated using the QGSP_BERT_HP physics list.

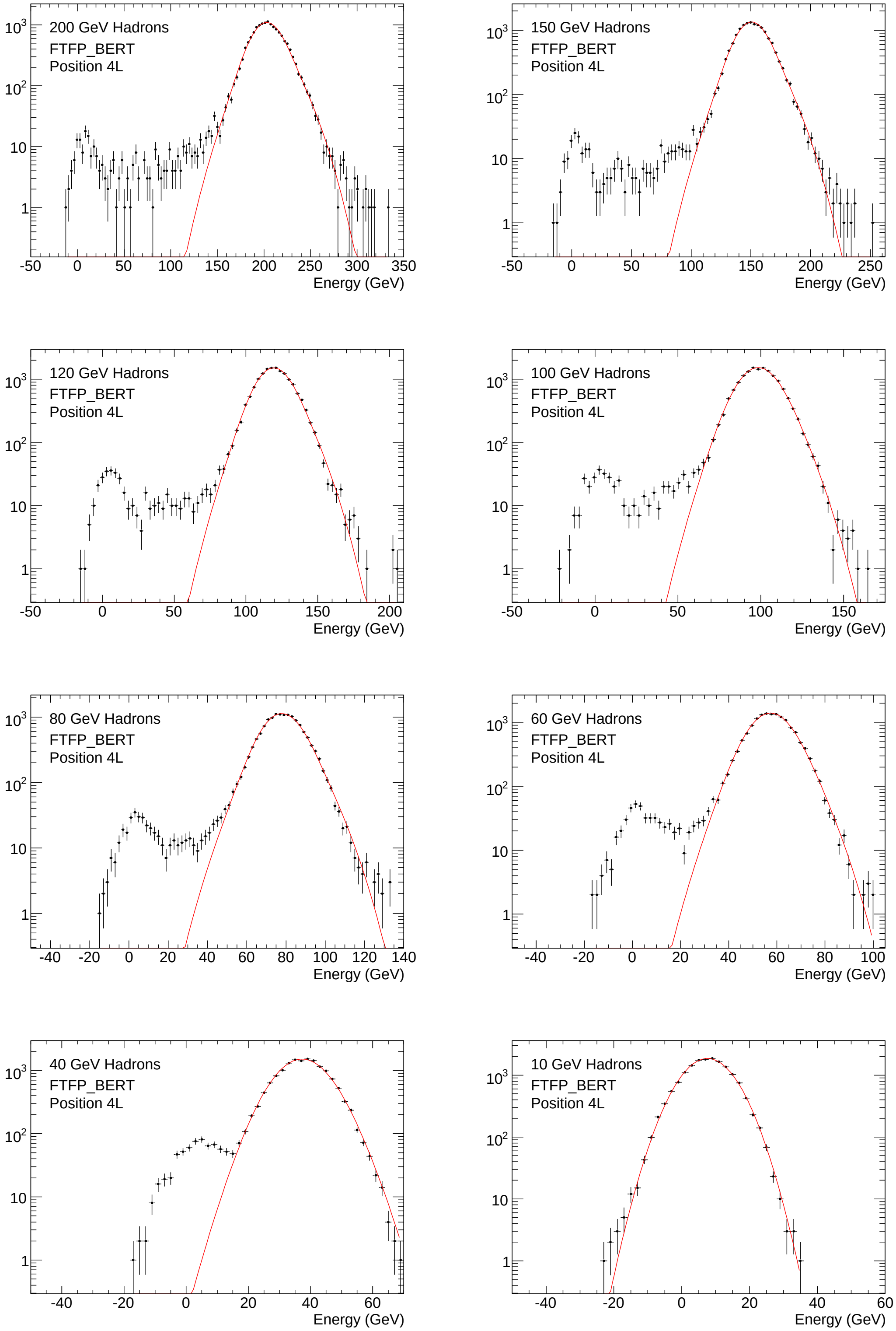

Figure A.5: Response plots for pions directed at position 4L, simulated using the FTFP_BERT physics list.

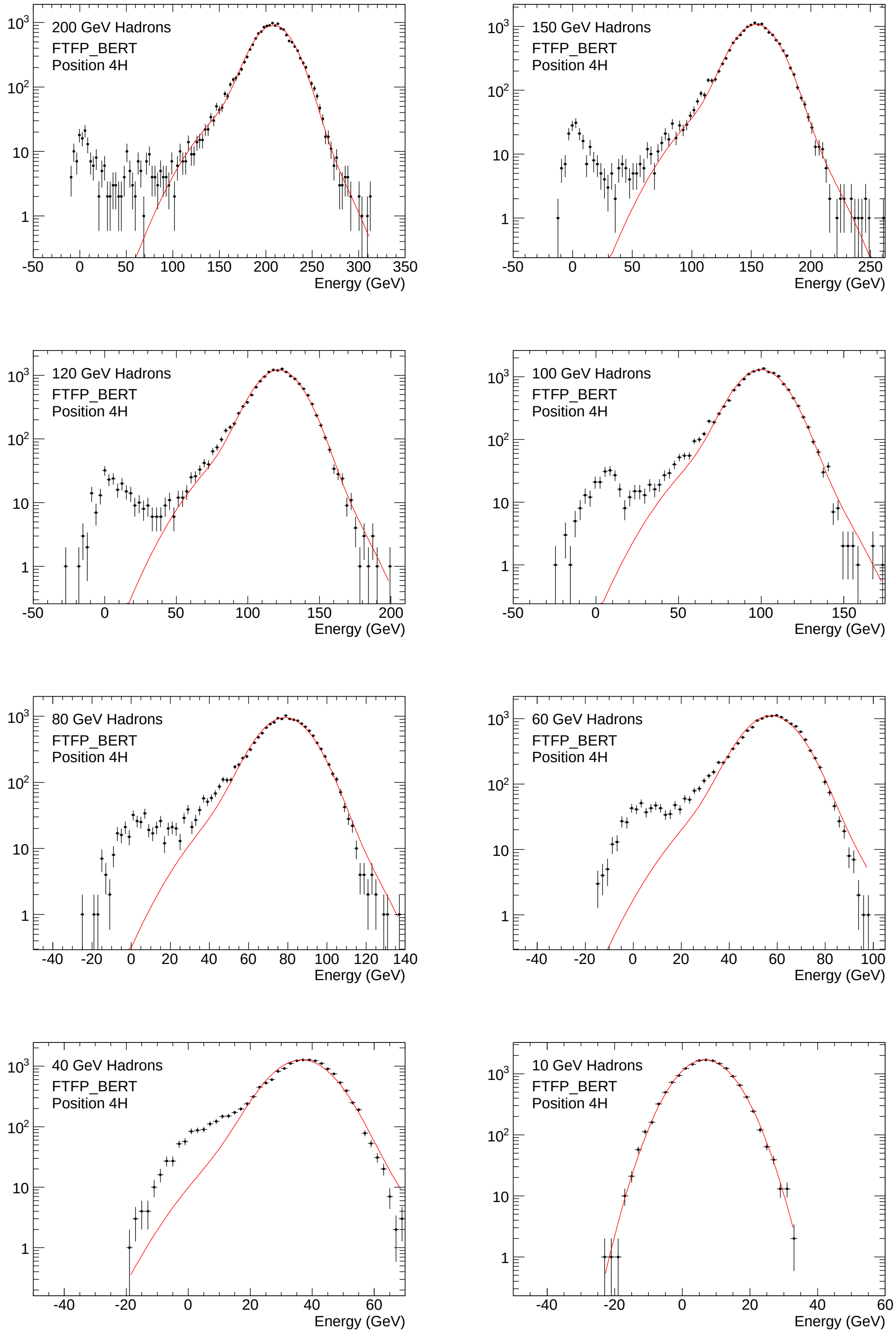

Figure A.6: Response plots for pions directed at position 4H, simulated using the FTFP_BERT physics list.

A.2 Results Obtained using Topological Clusters

Figures A.7 (A.8), A.9 (A.10), and A.11 (A.12) show the responses obtained from beams of pions directed at position 4L (4H), for the QGSP_BERT, QGSP_BERT_HP, and FTFP_BERT physics lists, respectively. The results presented here are obtained using a topological clustering method, with "420" thresholds. Hadronic calibration is again carried out using the flat-weighting method, with the weights derived from 200 GeV data.

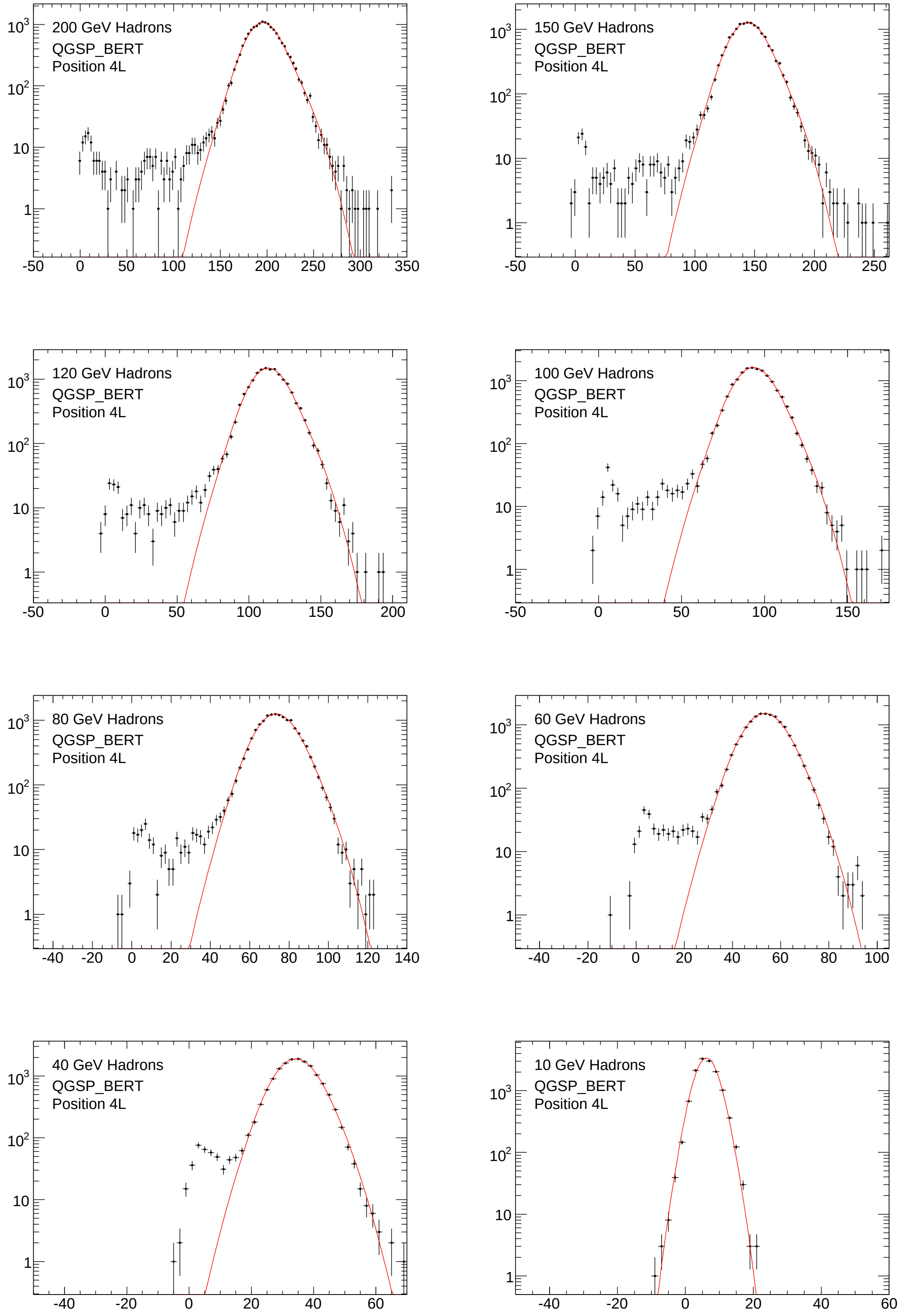

Figure A.7: Response plots for pions directed at position 4L, simulated using the QGSP_BERT physics list.

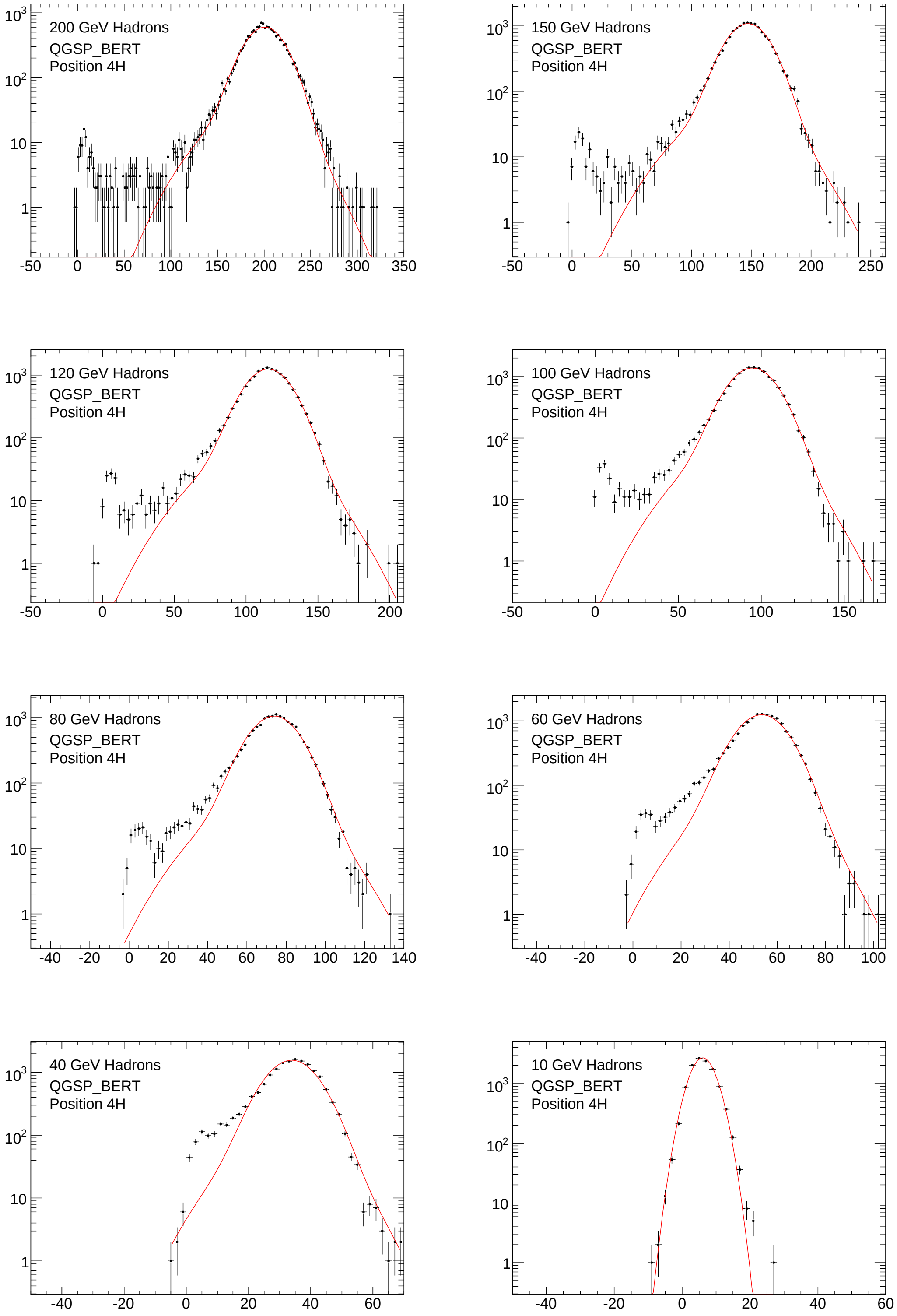

Figure A.8: Response plots for pions directed at position 4H, simulated using the QGSP_BERT physics list.

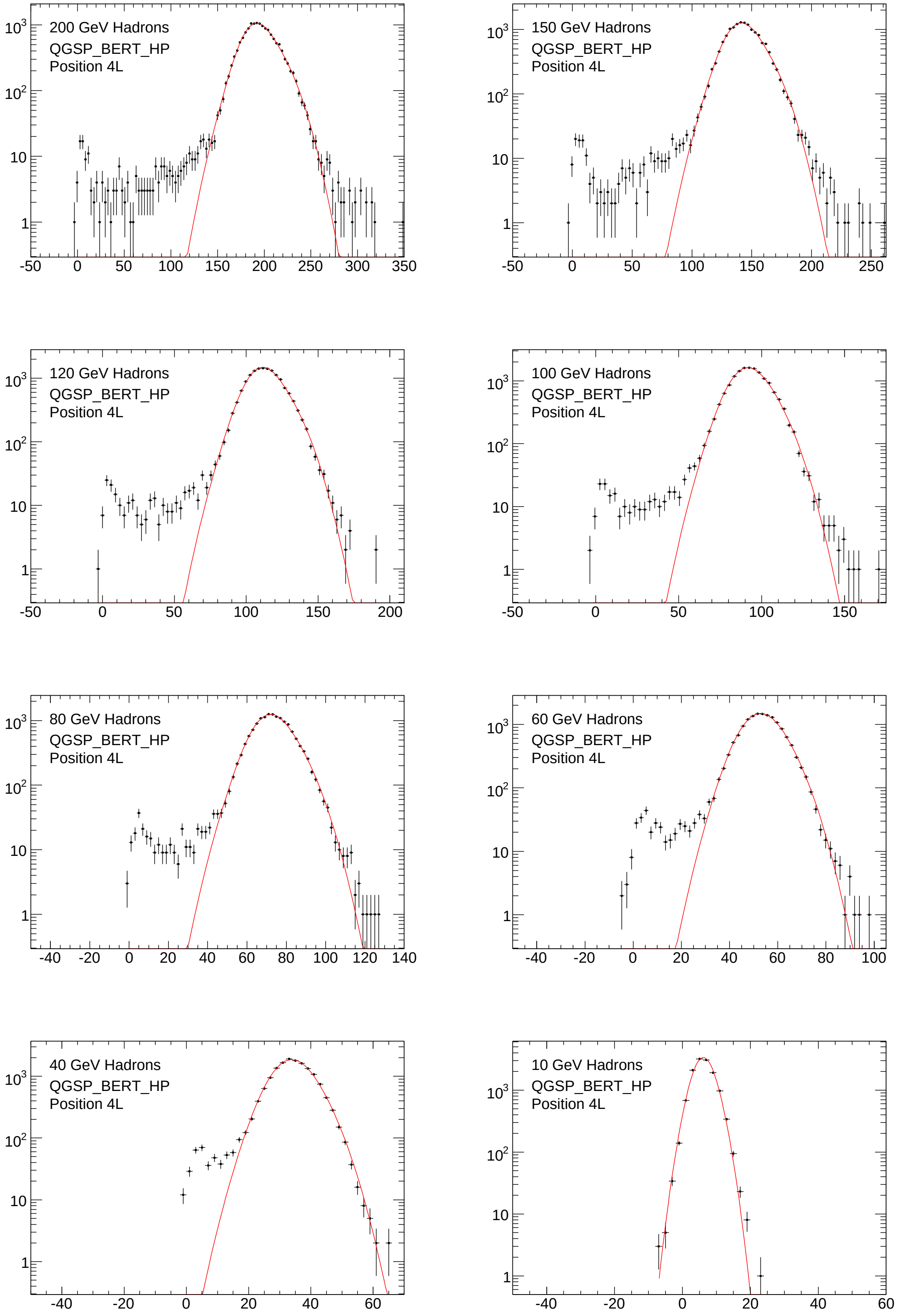

Figure A.9: Response plots for pions directed at position 4L, simulated using the QGSP_BERT_HP physics list.

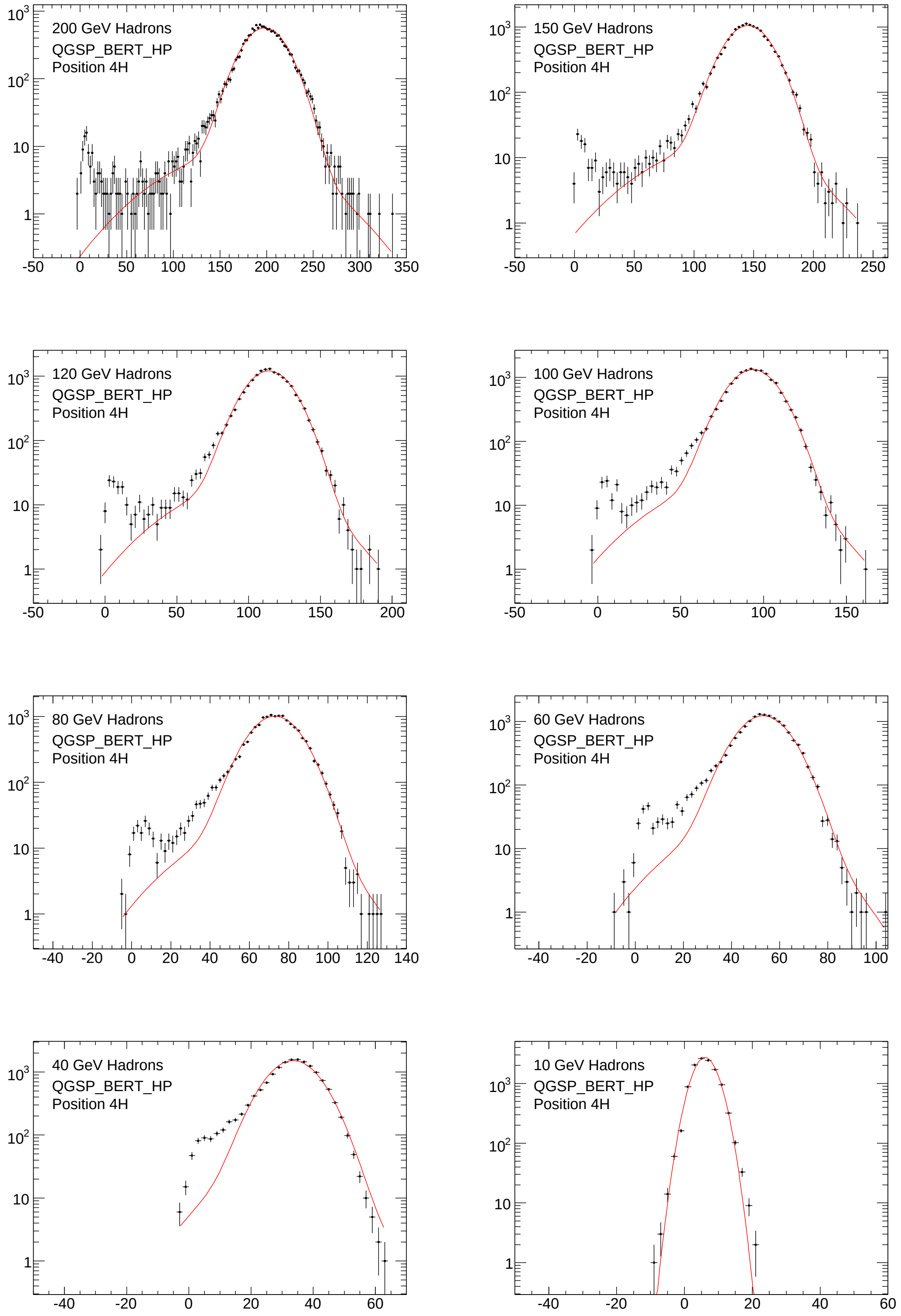

Figure A.10: Response plots for pions directed at position 4H, simulated using the QGSP_BERT_HP physics list.

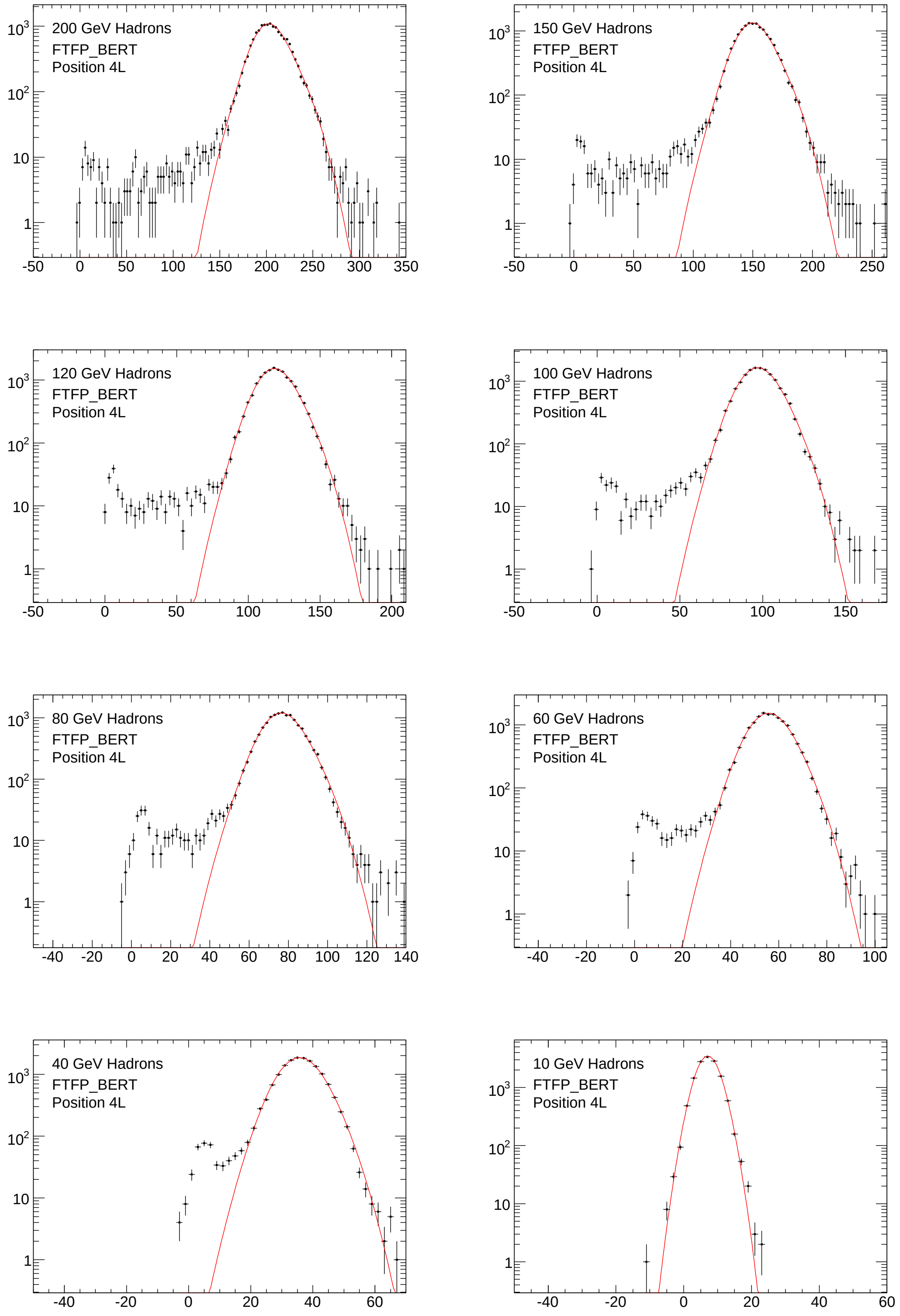

Figure A.11: Response plots for pions directed at position 4L, simulated using the FTFP_BERT physics list.

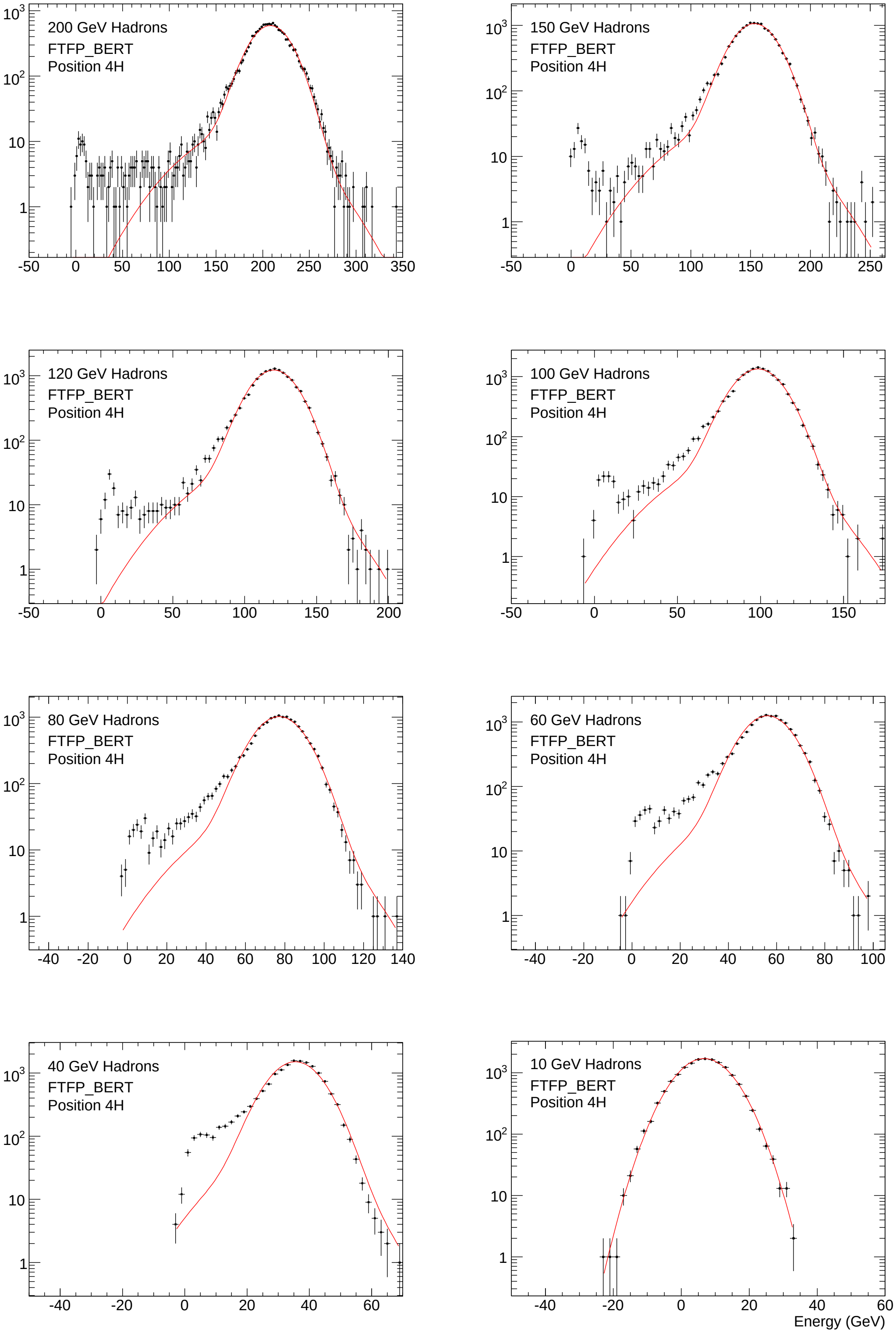

Figure A.12: Response plots for pions directed at position 4H, simulated using the FTFP_BERT physics list.

Appendix B

Data Calibrated using Weights Derived from Monte Carlo

The results presented in Chapter 4 use weights derived from data to calibrate the simulation results. In figure B.1 the response to hadrons, obtained from data, is plotted as a function of beam energy, for cylindrical and topological clusters at positions 4L and 4H. These plots include results obtained when the weights used for hadronic calibration are derived from the simulation, rather than data. This is analogous to the hadronic calibration schemes used at `ATLAS`, in that the data is calibrated using results obtained from simulations.

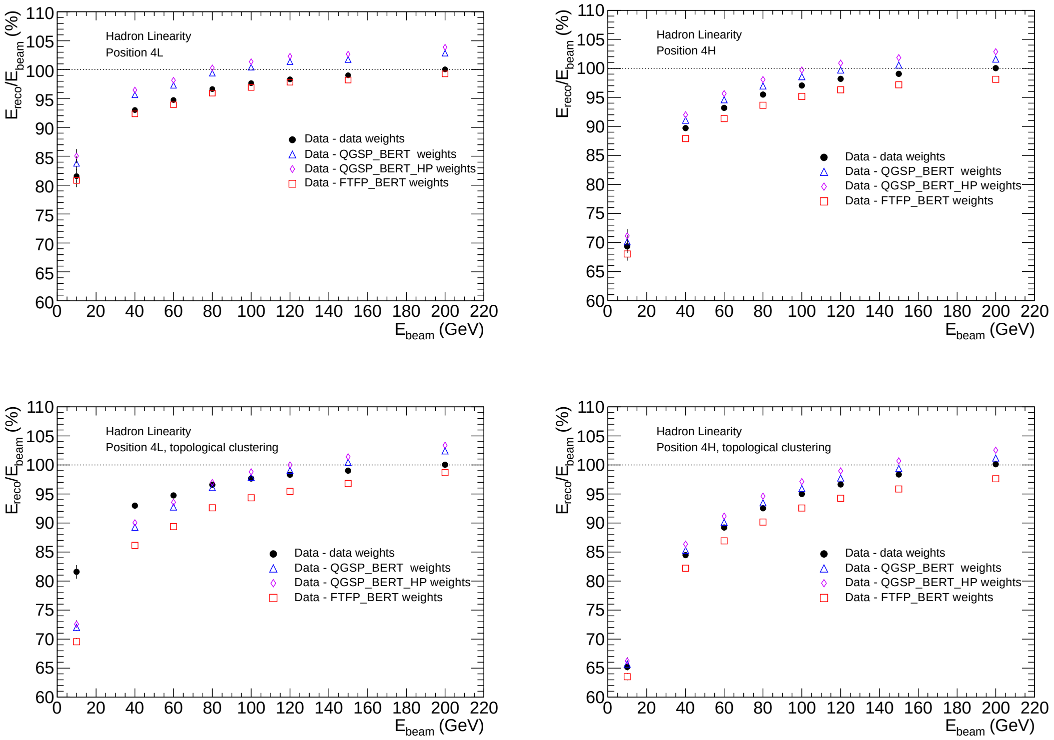

Figure B.1: The FCal response to hadrons at positions 4L (a,c) and 4H (b,d), using cylindrical (a,b) and topological (c,d) clusters. The solid black markers show the results obtained from data, in which the flat weights used for hadronic calibration are also derived from data. The open markers show the results obtained when weights derived from Monte Carlo are used to calibrate the data.